Microelectrochemical Studies of Atom Transfer and Chain Transfer Catalysts

by

Rebecca Jane Haskins

Thesis

Submitted to the

University of Warwick

for the degree of

Doctor of Philosophy

Department of Chemistry

September 2001

For Μιχάλη μου, (ευχαριστώ για την αγάπη και το τσάι ☺) and the rest of my family for their love and support.

"Sit down before fact as a little child, be prepared to give up every preconceived notion, follow humbly wherever and whatever abysses nature leads, or you will learn nothing"

Thomas H. Huxley

"I love deadlines, I like the whoosing sound they make as they fly by"

Douglas Adams

Acknowledgements

The first person who deserves to be and indeed must be mentioned here is my supervisor, Patrick Unwin, a man who inspires others with his ever present enthusiasm for electrochemistry. Additionally, his group at Warwick deserve a huge thank you for being friendly, willing to help out and fun to work with. Thanks to Phil for his inventiveness when it comes to cocktail mixing (long live "The Dave!"), Lou, Nikki and Naf for helping me to get through all those tea bags. A very special thank you must go to Anna, who knows more than I could ever imagine about electrochemical simulation. Additionally, none of the research described in this thesis would have been possible without the mechanical, electrical and glassblowing workshops. The staff within these facilities work tirelessly to manufacture the ultimate piece of experimental apparatus to exacting standards.

The work described within this thesis utilised catalysts made within the polymers group of Prof. D. M. Haddleton at Warwick University. Therefore I would like to thank Drs Alex Hemming, Jennifer Waterson and Richard Harrison for their synthetic skill and Prof Haddleton for the helpful discussions. I would also like to thank the EPSRC for financial support via a quota studentship.

A final note of thanks to my family, who got me here and to Mike for inspiring me as well as listening to the moaning and keeping me in tea and toast!

Declaration

The work contained in this thesis is entirely original and my own work, except where otherwise acknowledged. The electrochemical simulations were written by either Prof. P. R. Unwin or Dr. A. L. Barker.

I confirm that this thesis has not been submitted for a degree at another university.

List of Abreviations

ADIFDM	Alternating direction implicit finite-difference method
AgQRE	Silver quasi-reference electrode
AIBN	2,2'-azo-bis-isobutyrylnitrile
aq	Aqueous
ATP	Atom transfer polymerisation
ATRC	Atom transfer radical cyclisation
bipy	2,2'-bipyridyl
BN	Benzonitrile
CCTA	Catalytic chain transfer agent
CCTP	Catalytic chain transfer polymerisation
CV	Cyclic voltammetry / cyclic voltammogram
DBCH	Dibromocyclohexane
DCE	1,2-dichloroethane
DMF	Dimethylformamide
DPSC	Double potential step chronoamperometry
E_2	Second-order elimination reaction
E2IBB	Ethyl-2-isobromobutyrate
EC	Electron transfer followed by a chemical reaction
EC'	Electron transfer followed by a chemical reaction, in which the initial electroactive species is regenerated
EPR	Electron paramagnetic resonance
ESR	Electron spin resonance
ET	Electron transfer

Fc	Ferrocene
GC	Generation collection
HOPG	Highly orientated pyrolic graphite
i.d.	Inner diameter
i.s.e.t.	Inner sphere electron transfer
IT	Ion transfer
ITIES	Interface between two immiscible electrolyte solutions
kid	Kinetic indicator diagram
L	Ligand
LSV	Linear sweep voltammetry or linear sweep voltammogram
MeCN	Methyl cyanide (acetonitrile)
MJE	Microjet electrode
mma	Methyl methacrylate
MO	Molecular orbital
o.d.	Outer diameter
Ox	The oxidised form of a redox couple
o.s.e.t.	Outer sphere electron transfer
PDI	Polydispersity index
PSC	Potential step chronoamperometry
PTFE	Polytetrafluoroethane
RBr	Alkyl bromide
Red	The reduced form of a redox couple
RFMRE	Radial flow microring electrode
RRDE	Rotating ring disc electrode
RX	Alkyl halide

SCE	Saturated calomel electrode
SECM	Scanning electrochemical microscope or scanning electrochemical microscopy
SECMIT	Scanning electrochemical microscope induced transfer
SG-TC	Substrate generation – tip collection
S_N2	Second-order nucleophilic substitution reaction
SWV	Square wave voltammetry
TBAP	Tetrabutylammonium perchlorate
TEACl	Tetraethylammonium chloride
TEAP	Tetraethylammonium perchlorate
TG-SC	Tip generation – substrate collection
UME	Ultramicroelectrode
wwwda	World Wide Web Data Analysis service (www.physchem.ox.ac.uk/~rgc)

List of Symbols

α	Transfer coefficient
a	Electrode radius
A	Electrode area
c	Concentration
C	Normalised concentration
C^*	Bulk concentration
d	Distance
D	Diffusion coefficient
E	Potential
E^0	Standard electrode potential
$E^{0'}$	Formal potential
$E_{3/4}$	Potential at $3/4i_{lim}$
$E_{1/2}$	Potential at $1/2i_{lim}$
$E_{1/4}$	Potential at $1/4i_{lim}$
$\Delta E_{1/4}$	Difference between $E_{1/4}$ and $E_{1/2}$
$\Delta E_{3/4}$	Difference between $E_{1/2}$ and $E_{3/4}$
E_S	Substrate potential
E_T	Tip potential
F	Faraday's Constant
i	Current
i_1	Current of wave 1
i_2	Current of wave 2
$i(1)$	The limiting current for wave 1

$i(2)$	$i_{lim}(2)$ is the total current at the plateau of wave 2 minus the limiting current for wave 1
i_c	Catalytic diffusion-limited current
i_{lim}	Diffusion-limited current
i_S	Substrate current
i_T	Tip current
$i_{T\infty}^{0}$	Tip current at infinite tip-substrate separation for a heterogeneous electron transfer (no coupled chemical reactions)
i_∞	Current at infinite tip-substrate separation
k_1	First-order rate constant
k_c	Rate constant of a chemical reaction coupled to a heterogeneous electron transfer
k_b	Rate constant for a reverse reaction
k_f	Rate constant for a forward reaction
k_i	Rate constant for a pseudo first-order interfacial process
k_r	Rate constant
k_r'	Rate constant for a pseudo first-order process
k_t	Rate constant for heterogeneous electron transfer
K	Normalised rate constant
λ	Dimensionless rate constant
mM	Milli molar, 10^{-3} mol dm^3
n	Number of electrons
N_{eff}	Effective number of electrons
r	Radial coordinate of the axisymmetric geometry that defines SECM
R	Gas constant

RG	Characteristic dimension of an UME
r_{glass}	Radius of glass sheath surrounding a disc microelectrode.
ρ	Ratio of substrate concentration to catalyst
t	Time
τ	Normalised time
T	Temperature
t_d	Diffusion time to an electrode
t_{switch}	The time at which the second potential step of a DPSC experiment occurred.
υ	Scan rate
z	Axial coordinate of the axisymmetric geometry that defines SECM

Chapter 1 - Introduction

This thesis is concerned with the measurement of the kinetics of both heterogeneous electron transfer reactions and coupled homogeneous reactions using ultramicroelectrode (UME) techniques. Two different types of ligated metal-centred catalysts were studied; copper-centred atom transfer polymerisation (ATP) catalysts and cobalt-centred catalytic chain transfer agents (CCTA). This introductory chapter outlines the systems of interest and the techniques used to investigate them. Notably, both microelectrode voltammetry and scanning electrochemical microscopy (SECM) are examined in some detail. The principles and applications of both are discussed, with particular attention paid to the role of these techniques in determining both heterogeneous and homogeneous reaction rates. More detailed aims of the work described in this thesis are outlined at the end of this chapter. For clarity, the full chemical name of each copper or cobalt complex is not used. Rather, appendix 1 provides an explanation of the nomenclature used and the structures of each species described herein.

1.1 Copper-centred macrocyclic catalysts

The [Cu^{I}] complexes under examination are used as ATP or atom transfer radical cyclisation (ATRC) catalysts. In this section, an outline is given of ATP and the investigations of the catalytic mechanism that preceded this study.

1.1.1 Atom Transfer Polymerisation

ATP is a type of controlled polymerisation; the terms "living" and controlled are often interchanged when used to describe this system, but the term "living" is inaccurate as this describes a polymerisation that only concludes when all of the reactant has been expended. In addition, polymerisation can continue once further fresh monomer has been added to the reaction vessel, thus providing an easy route[1] to block copolymers, dendrimers and star polymers. In the case of ATP, free radicals are believed to be involved in the propagation step and, as such, a certain amount of termination is destined to occur, thus implying that the process is not truly living. ATP shows many of the facets usually associated with truly living processes. Most notably, it has a very narrow polydispersity index (PDI), typically in the range 1.1 - 1.2. It is robust, operates over a wide range of temperatures and is not sensitive to a large range of impurities or functional groups[2].

1.1.1.1 Catalysts

During an ATP reaction, a catalyst is used to aid the transfer of alkyl groups onto a growing polymer chain. During the inception of ATP, ruthenium[3] or copper[4] centred complexes were utilised as catalysts. It was found that catalysts based on Schiff base complexes of copper, where the central Cu was bonded to two identical ligands, were efficient catalysts for this reaction[5]. Later, Granel et al[6] showed that Ni centred complexes also made efficient catalysts. Recently, an abundance of publications have appeared that utilise one of a family of catalysts based on the ligated copper complexes described earlier. In such complexes the purpose of the ligands is three fold. First, they must withdraw electron density from the central metal in order to stabilise its low oxidation state. Second, they must allow conversion from the

tetrahedral configuration of the Cu^{I} species to the distorted square based pyramid of the Cu^{II} species[5]. Last and perhaps most importantly, Cu^{I} halides are insoluble in the organic solvents and monomers in which polymerisations are carried out; thus the ligands must be able to solubilise Cu^{I} in these solvents.

Manufacture of the required complex is a simple affair, the complex is generated in situ by adding ligand to a solution of CuCl. Figure 1.1 shows a typical catalyst comprising a central Cu^{I} surrounded by two ligands, the particular ligand (ligand 5; see appendix 1) shown in Figure 1.1 has an eight carbon chain alkyl group attached to one of the two nitrogens. The properties of such complexes may be adjusted by varying either the length or composition of the carbon chain[7], or by using a different ligand, such as bipyridyl (bipy) which may also be derivatised with additional groups[8].

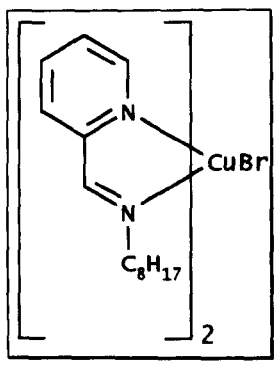

Figure 1.1. The copper complex formed by the reaction of CuBr with ligand 5.

1.1.1.2 Mechanism

As with any polymerisation, three main aspects constitute the entire process. First, there must be initiation, which creates a source of initiating species such as ions or free radicals. Initiation of ATP occurs via three routes:

1) reaction of an alkyl bromide (RBr) with a catalyst[9] or,
2) generation of initiating species from a universal initiator, such as an alkyl or arylsulfonyl halide[10], or
3) initiation with a standard initiator, such as 2,2'-azo-bis-isobutyrylnitrile (AIBN) and use of reverse ATP where the catalyst is introduced to the reaction vessel in the M^{n+1} state[11].

Following initiation, propagation occurs, which results in growing polymer chains. Probability governs the propagation process and, after a certain time, termination by disproportionation or combination occurs, resulting in deactivation of the growing polymer chain. ATP seeks to control the amount of termination that can occur by controlling the amount of actively growing chains present at any time[12]. This is achieved by means of a reversible redox process between M^n and M^{n+1} that deactivates growing chains. A halogen (or pseudo halogen) is transferred between an organic radical (the growing chain) and the metal complex during the redox process. As there are less active radicals present in the solution at any given point in time, the probability of a termination event occurring is greatly reduced.

It is generally held that the mechanism of this reaction is free radical in nature[12], but further investigation[13] has cast doubt upon the solidity of this claim. The main point of contention arises as there is no direct evidence for the involvement of free radicals in the process. It might be expected that electron paramagnetic resonance (EPR) spectroscopy could provide such evidence, but the spectrum of propagating carbon centred radicals is rather similar to that of Cu^{II}. Hydrophilic[14] and coordinating

groups, as well as radical inhibitors[15], have been shown to influence the kinetics of ATP, whilst they do not affect "normal" free radical polymerisations. Whatever the exact details of the mechanism, the process is likely to occur via a radical or radical-like pathway such as that shown in scheme 1.1, where Pol-X is the growing initiated chain, $L[Cu^{I}]$ is the catalyst in oxidation state +I, Pol^{*} is the active end of the growing polymer chain and $[Cu^{II}]$-X is the catalyst in oxidation state +II.

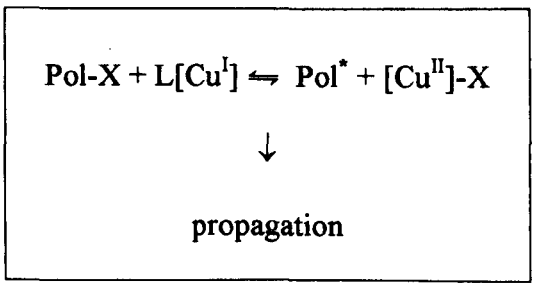

Scheme 1.1. The propagation of reaction via ATP, using $[Cu^{I}]$ as a catalyst.

Many steps which result in propagation are to be found between the two extremes shown in Scheme 1.1. These steps are not yet fully understood, but it is known that for the catalyst to be most effective in producing polymer of narrow PDI and at an acceptable rate, it must easily undergo oxidation to $[Cu^{II}]$-X, and yet the kinetics should be sufficiently slow to allow propagation to occur before two Pol^{*} units react together in a termination step[16].

This thesis, in part, describes the measurement of the kinetic and thermodynamic parameters, electron transfer coefficient (α), standard rate constant (k^{0}) and the formal electrode potential ($E^{0'}$) for the redox couple $[Cu^{I}]/[Cu^{II}]$ in a range of catalyst structures. The ultimate goal is to provide an understanding of such properties, to aid comprehension of the behaviour of the catalyst in ATP systems.

1.1.1.3 Refinements to the basic system

A further problem associated with ATP, and the reason why it has yet to be adopted as a commercial process, is retention of catalyst within the product polymer. The catalysts are usually dark green or brown species, which results in a highly coloured product. Polymer chemists have made efforts to contain the catalyst on solid supports and hence prevent it from contaminating the product. So far, growth has been achieved on silicon wafers[17] and silica gel particles[18]. The catalysts supported on silica gel have also been used in ATRC reactions[19]. It was found[20] that addition of pure copper to the polymerisation system, (i.e. in the Cu^0 state) in the form of a fine powder or even a "penny", increased the rate of reaction. This suggested that, in the absence of metallic copper, a portion of Cu^{II} did not convert back to Cu^{I} and therefore catalyst was lost over time, further evidence that ATP is not truly living. This apparent comproportionation process was not examined in any detail and would benefit from investigation in a well defined system.

1.2 [Co] catalysts

Like other transition metals, Co centred macrocycles ([Co]) are well suited as catalysts due to their ability to be stabilised by a range of ligands and to exist in many oxidation states. Vitamin B_{12} and its analogues are used as catalysts in carbon-carbon bond forming reactions[21], both in simple syntheses and more recently as CCTA in catalytic chain transfer polymerisation (CCTP)[1]. The studies described in this thesis were carried out with one particular family of catalysts, based upon cobaloxime ($[Co(dmgH)_2]$), which itself is a B_{12} analogue. There are, however, many analogues of B_{12}, each with remarkably similar properties. Therefore, a generic nomenclature

will be used herein. Designations and details of the structures for particular complexes are given in appendix 1.

1.2.1 Structure and reactivity

1.2.1.1 Structure

The basic structure of the [Co] under investigation comprises a large equatorial ligand system arranged in a square planar manner around a central Co. The two axial positions are usually occupied by solvent but substitution may occur with species such as alkyl groups. The number of these axial type ligands is related to the oxidation state of the metal[22], [Co^{III}] having two axial ligands, [Co^{II}] one and [Co^{I}] none.

1.2.1.2 Cobaloximes

[$Co(dmgH)_2$] is a model complex of B_{12r} (the Co^{II} state of vitamin B_{12}). Cobaloximes may be prepared from oximes[22] and are mild reducing agents. Figure 1.2 shows the structure of [$Co(dmgH)_2$]; many derivatives are possible by replacing the Me groups shown with various R groups. Figure 1.3 and Figure 1.4 show that derivatives are also possible by altering one or more of the two O-H-O bridging groups.

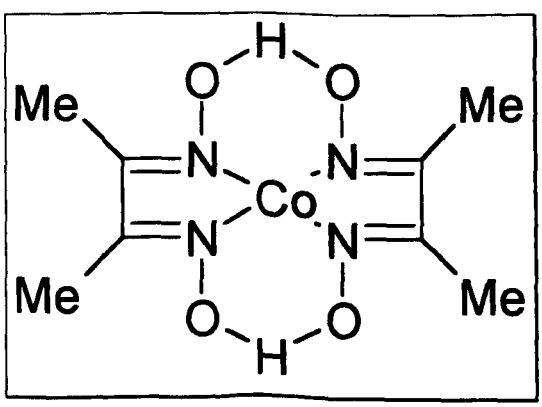

Figure 1.2. The structure of [$Co(dmgH)_2$].

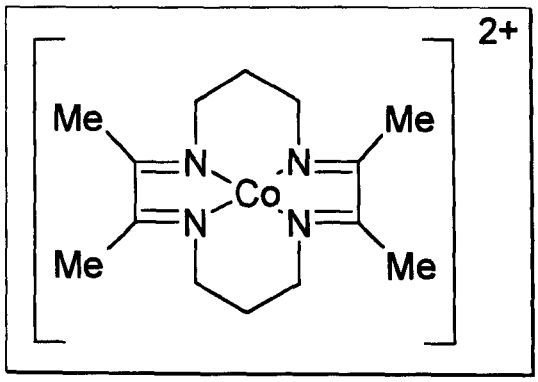

Figure 1.3. The structure of $[Co(tim)^{2+}]$[23].

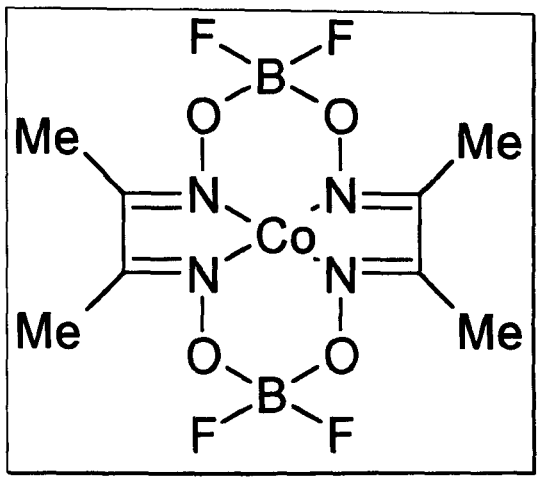

Figure 1.4. The structure of $[Co(dmgBF_2)_2]$.

The purpose of the synthesis and subsequent investigation of these "variations on a theme" is to understand, and ultimately, increase the selectivity of a particular catalyst. With selectivity in mind, Bedioui et al[24] manufactured and studied the electrochemical properties of a $[Co^{II}(salen)]$ complex embedded in a Y type zeolite.

Shi and Anson[25] used electroactive ligands to examine the mechanism and kinetics of formation of [M]. During this study, ligand was adsorbed onto either basal plane or

edge plane pyrolytic graphite electrodes. Cyclic voltammograms (CVs) for the reduction of the ligand were recorded, showing one peak in each sweep direction. On addition of Co^{2+} to the solution in which the electrode was immersed, the peak on the reverse sweep split into two. The first, most negative, peak was as seen for the solution that contained no Co^{2+} and hence was assigned to the oxidation of the free ligand, whilst the newer more positive peak was assigned to the oxidation of newly formed complex, [Co]. By varying the sweep rate the kinetics of complex formation were examined.

1.2.1.3 Spin States

Rockenbauer et al[26] applied electron spin resonance (ESR) spectroscopy to $[Co(dmgH)_2]$. They determined that the central Co^{II} was in the low spin state and that after reduction to Co^{I} the unpaired electron was predominantly located in the d_z^2 orbital. This orbital is the highest occupied orbital in the $[Co^{I}]$ form and is slightly antibonding in character. The orbital is highly directional and has a high charge density, which leads to a large nucleophilicity in a direction that is perpendicular to that of the equatorial ligand (i.e. axial)[27]. Haddleton et al[28] investigated the efficacy of low and high spin [Co] as CCTAs and concluded that only low spin [Co] are active as CCTA.

1.2.1.4 Electrochemical Detection

[Co] can undergo a range of redox reactions depending on the initial state of the complex. Spectroscopic[29,113] and electrochemical evidence[30] suggest that redox processes occur at the central Co atom. The overall stability of the complex depends on the ability of the ligands to stabilise the various oxidation states of cobalt.

Commonly, both Co^{III} and Co^{II} states are stable, thus allowing either two one-electron reductions of Co^{III} to Co^{I} or an oxidation and reduction from an initial Co^{II}.

As in many electrochemical reactions, the ability to measure the voltammetric characteristics of a particular couple may be influenced by the choice of electrode material and experimental conditions, e.g. whether the species of interest is adsorbed onto the electrode surface or resides in the solution phase. Shi and Anson[31] have introduced a method to overcome the problem of cobalt tetraphenylporphyrins not giving well defined redox behaviour when adsorbed onto graphite, by containing a layer of organic solvent/electroactive species between a graphite electrode and an aqueous solution. Supporting electrolyte diffuses from the aqueous solution into the organic phase, and because the layer is so thin, ohmic distortion is very small and undistorted voltammograms may be recorded with relatively low supporting electrolyte concentrations. The technique has subsequently been used to examine electron transfer at the immiscible organic/aqueous interface, and represents a useful technique provided that mass transfer is treated correctly[32].

1.2.2 [Co^{I}] as catalysts.

The reason that [Co] make good catalysts for C-C bond forming reactions is that many [Co] species form labile [Co]-C bonds and thus are an excellent source of alkyl free radicals ($R^{\cdot}$). The standard synthetic route to the formation of alkylcobalt ($R[Co^{III}]$) involves generation of $[Co^{I}]$ by the reduction of $[Co^{II}]$ by $NaBH_4$ in basic or alcoholic solutions. Subsequent alkylation by an alkyl halide (RX) produces an $R[Co^{III}]$ species. However, this route has proven to be slow, with very poor yields. Moreover, in complicated systems, further side reactions, due to the presence of

$NaBH_4$, can occur. Electrochemical generation of [Co^I], before subsequent alkylation, is becoming increasingly utilised[33]. Overall, there are three possible pathways that give rise to alkylcobalt formation; the pathway is dependent on the oxidation state of the starting [Co]. [Co^{III}] may be reacted with grignard reagents or enol ethers[34]. [Co^{II}] will react with organic radicals, whilst [Co^I] may be reacted with alkyl halides[35]. Not all combinations of [Co^I] and RX will form a stable R[Co^{III}] bond. In particular, the C-Co^{III} bond can easily be broken to form a radical or anion alkyl group.

1.2.2.1 Mechanism of the reaction of [Co^I]with RX.

Various methods have been used to study the mechanism[22] of oxidative addition of RX to [Co^I]. The reason that [Co^I] readily attacks electrophiles is that as a supernucleophilie[27], it will react with many different electrophilies especially[27]: alkylating agents[36,37,38,39] (tosylates and halides), acetylene[40,41], oxirans[42,43], alkenes activated by electron-withdrawing groups and vinyl halides[44,45] to form R[Co^{III}]. The reaction of [Co^I] with RX can proceed via two mechanisms: S_N2 or E_2 elimination. Figure 1.5 and Figure 1.6 show typical S_N2 and E_2 reactions respectively.

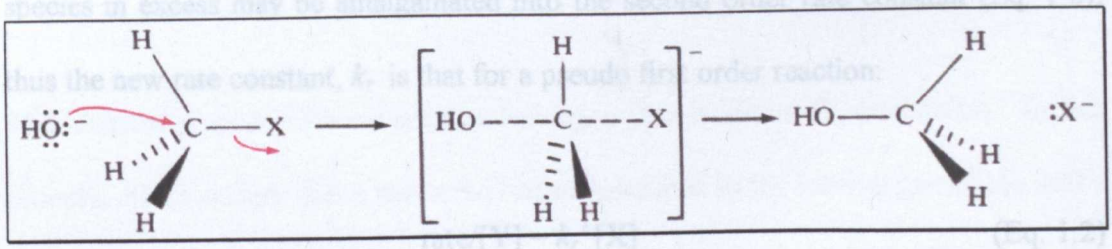

Figure 1.5. An S_N2 mechanism[46].

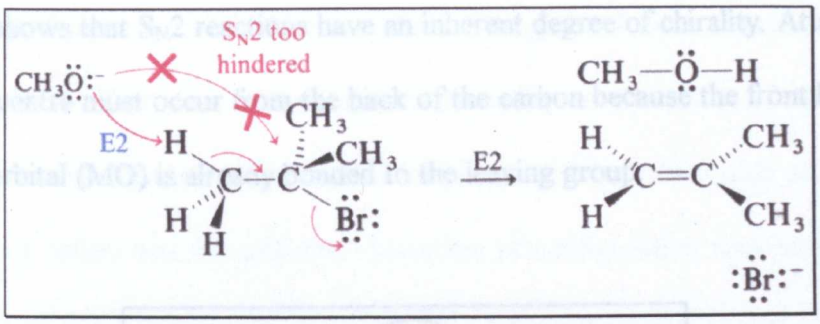

Figure 1.6. An E_2 mechanism[46].

The S_N2 mechanism is concerted, second order overall and obeys the normal rate equation for a second order process:

$$\text{rate} = k_r[X][Y] \qquad \text{(Eq. 1.1)}$$

where k_r is the rate constant of the reaction, X and Y are two reactants.

Obviously, if the concentration of one of the species were high enough, there would be very little change in rate with change in its concentration. Under these conditions the process may be regarded as pseudo-first order and thus the concentration of the species in excess may be amalgamated into the second order rate constant (Eq. 1.2), thus the new rate constant, k_r' is that for a pseudo first order reaction:

$$\text{rate}/[Y] = k_r'[X] \qquad \text{(Eq. 1.2)}$$

Figure 1.7 shows that S_N2 reactions have an inherent degree of chirality. Attack on the sp^3 carbon centre must occur from the back of the carbon because the front lobe of the molecular orbital (MO) is already bonded to the leaving group.

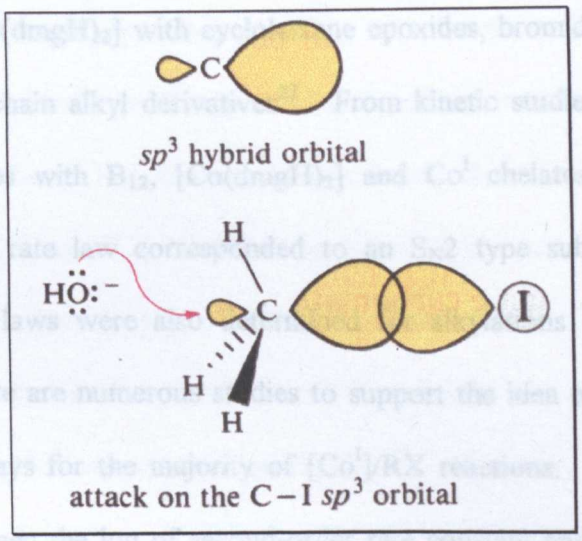

Figure 1.7. S_N2 reaction: attack must occur from behind the sp^3 orbital already bonded to the leaving group[46].

The result is that where the attacking nucleophilie is particularly bulky, or the carbon centre is hindered, the steric hindrance of the process will slow the rate of reaction and in certain cases will actually prevent attack from occurring in an S_N2 manner.

The alternative route of eliminating a leaving group is via an E_2 mechanism. In this process, attack occurs not at the carbon centre attached to the leaving group, but at the β position. Clearly, the product from this coplanar attack is wholly different to that from an S_N2 reaction.

For electron transfer between RX and [Co^I], Wang and Jordan concluded that the transfer could be either inner or outer sphere depending on the nature of the oxidant[47]. Scheffold found that the stereoelectrochemical course of the substitution of R by [Co^I] at a saturated cation was not uniform. Inversion of configuration was determined for the reaction of [$Co^I(dmgH)_2$] with cyclohexane epoxides, bromides and tosylates, as well as with open chain alkyl derivatives[22]. From kinetic studies of the reaction of various alkyl halides with B_{12}, [$Co(dmgH)_2$] and Co^I chelates, Schrauzer et al[27] concluded that the rate law corresponded to an S_N2 type substitution at carbon. Second order rate laws were also determined for alkylations of many B_{12} model compounds[48]. There are numerous studies to support the idea of a predominance of inner sphere pathways for the majority of [Co^I]/RX reactions. Rusling[30] found a linear relation between the log of second-order rate constant and $E^{0'}$ for [Co^{II}]/[Co^I] for reactions in dimethyl formamide (DMF) and microemulsions. Data recorded in both solutions fell on the same line, as if it were one series. His study showed that kinetic differences were controlled by activation free energies, dependent on the reduction potential of [Co^{II}]/[Co^I]. To further prove an inner sphere pathway, Rusling[30] compared the $E^{0'}$ of the [Co^{II}]/[Co^I] couple to a correlation of first-order rate constant (k_1) vs. $E^{0'}$ for outer-sphere catalysts reacting with *trans*-1,2-dibromocyclohexane (t-DBC). A rate constant of 0.02 M^{-1} s^{-1} was predicted for the outer sphere reaction of [Co^I] and RX, whereas the value measured was 5 x10^6 M^{-1} s^{-1}. This proved that catalysis by B_{12r} is much more efficient than expected for an outer sphere reaction, supporting the inner-sphere mechanism.

The reaction of alkylmonohalide species with [Co] has been shown to occur via an S_N2 mechanism[49,50] Schrauzer and Deutsch[27] used the low energy d-d transitions of

Co^{I} species (blue - blue/green depending on axial ligation) to measure reaction progress for a wide range of RX species with either B_{12} or $[Co(dmgH)_2]$. They also found that secondary alkyl halides formed very unstable [alkyl-Co] species with $[Co(dmgH)_2]$. While tertiary alkyl halides reacted, no [*tert*-alkyl-Co] species could be detected due to their instability. This instability was thought to be brought about by steric hindrance, which in larger Co species (such as B_{12}) would undoubtedly lead to each [RCo] species being less stable. It was found that a second-order reaction occurred between $[Co^{I}]$ and RX, but either an S_N2 or an electron transfer process may have given this order of reaction. $[Co^{II}(CN)_5]^{3-}$ has been shown to react with RX by an electron transfer mechanism[51]. Further work has shown that $[Co^{II}(dmgH)_2]$ reacts with PhBr in aprotic solvents by this mechanism[52]. However, this evidence is for $[Co^{II}]$; Schrauzer and Deutsch argued that the S_N2 mechanism may be proven by reaction of a $[Co^{I}]$ species with a chiral RX group. The resultant complex showed a complete inversion of configuration in line with the S_N2 mechanism. Further evidence occurred from measurements of the rates of displacement of the halogen leaving group. It was found that[35] the $[Co(dmgH)_2]$ and B_{12} reactions were about 10 times more sensitive to leaving group than a "typical" S_N2 process, but the reaction of $[Co^{II}(CN)_5^{3-}]$ (which had already been shown to proceed via an electron transfer mechanism) with RX was 100 times more sensitive. The body of evidence suggests that the majority of $[Co^{I}]$ react with RX by an S_N2 mechanism that may be treated as either second or pseudo first-order, depending on the concentration of RX.

When either or both of the reactants are too sterically hindered to allow an S_N2 reaction to proceed, reaction can occur via an E_2 elimination mechanism. Iwunze et al[48] showed that vicinal dibromides (RBr_2) were reduced to alkenes at the potential at

which [Co^{I}] was formed at the electrode. The reaction pathway involved rate determining inner sphere electron transfer (iset) between [Co^{I}] and RBr_2. This occurred by kinetically indistinguishable radical or E_2 elimination mechanisms.

1.2.2.2 Effect of changing pH

Rusling[48] observed that without pH control, the rate of heterogeneous electron transfer to [Co^{II}] (of B_{12} in this case) was quite slow. Moreover, the [Co^{II}]/[Co^{I}] electrochemistry of B_{12} was pH dependent, requiring pH < 3 for the reversibility desired as a redox catalyst. This was attributed to two factors, first, the interaction of H^+ with [Co^{I}], which hindered the reaction of RX with [Co^{I}]. Second, specifically for B_{12}, the structure depends on the acidity of the solution, as B_{12} can exist in either a "base on" or "base off" form, depending on the acidity of the media. When Schrauzer and Windgassen[40] synthesised fifty different alkylcobaloximes they found that in neutral solutions only α-alkyl complexes were formed, whereas in basic solutions β-forms were also produced.

1.2.3 Structure and bonding of R[Co^{III}] species.

[Co] and R[Co^{III}] are very closely related, in that the cobalt complex has two axial ligands that are both solvent molecules, while the alkylcobalt complex has a single solvent molecule and an R group. As such, the properties and reactivity of these two types of complex are very similar.

1.2.3.1 Electrochemistry

R[Co^{III}] complexes undergo a multitude of redox processes; both oxidations and reductions are possible. A one electron oxidation, to produce [Co^{IV}], has been

confirmed by ESR spectroscopy[53]. This state may be attacked by nucleophilies as shown in Scheme 1.2, for R = Me.

$$Me[Co^{III}] + IrCl_6^{2-} \rightarrow Me[Co^{IV}]^+ \quad \textbf{(a)}$$

$$Me[Co^{IV}]^+ + H_2O \rightarrow MeOH + [Co^{III}] \quad \textbf{(b)}$$

Scheme 1.2[54]. Nucleophilic attack on R[Co^{III}] species.

Two one-electron reductions from [Co^{III}] to [Co^{II}] to [Co^{I}] are also possible. Ph[Co^{II}(salen)] has been shown to be stable, but other R[Co^{II}(salen)] decompose spontaneously by homolysis[55], as shown in Scheme 1.3.

$$Me[Co^{III}(salen)] + e^- \rightarrow Me[Co^{II}(salen)]^- \quad \textbf{(a)}$$

$$Me[Co^{II}(salen)]^- \rightarrow Me^{\cdot} + [Co^{I}(salen)]^- \quad \textbf{(b)}$$

Scheme 1.3. Homolysis of the R-Co bond brought about by reduction.

Zhou et al[56] have studied a range of alkylcobalamines and alkylcobyrinates. They found that as there was an increase in the electron-withdrawing nature of the R group, or an increase in the degree of substitution at the Co bound C, $E^{0'}$ for the reduction of [Co^{III}] to [Co^{II}] shifted towards more positive potentials.

1.2.3.2 Ligand/metal centre interactions

The electronic and steric interactions between the central cobalt and any attached R groups have been shown to cause activation in the R group, promoting reaction within itself rather than at the central cobalt. For example, back donation occurs between a

π^* orbital of the diene and the full Co d orbital in the Diels Alder reaction of 2-(butadienyl)cobaloxime with various dienophilies, as investigated by Welker[57,58,59,60] and Tada[61].

The standard potential (E^0) for the various redox transitions has been shown to depend on the axial ligands, the solvent and the square planar macrocycle[22]. In particular, a strongly co-ordinating axial ligand resulted in a more negative potential for Co metal reduction than with a weakly co-ordinating ligand[67]. Further evidence of the effect of axial ligands on the redox properties of [Co] has been found by examination of $[Co^{II}]/[Co^{III}]$ couples. Kang and Anson[62] have examined the $[Co^{II}(hmc)]/[Co^{III}(hmc)]$ couple and compared their results to those previously obtained for $[Co^{II}(cyclam)]/[Co^{III}(cyclam)]$[63]. They found that the transition: $[Co^{III}] \rightarrow [Co^{II}]$ was more easily accomplished than the oxidation of: $[Co^{II}] \rightarrow [Co^{III}]$. It was postulated that this difference was due to axial ligand binding effects with oxidation requiring the prior coordination of a suitable axial ligand to the metal centre.

$$[(H_2O)Co^{II}(hmc)] + X \leftrightharpoons [(H_2O)Co^{II}(hmc)X] \quad \textbf{(a)}$$

$$[(H_2O)Co^{II}(hmc)X] - e^- \leftrightharpoons [(H_2O)Co^{III}(hmc)X] \quad \textbf{(b)}$$

Scheme 1.4. The reaction of [Co(hmc)] with axial ligand aids reduction.

Scheme 1.4 shows the mechanism that was used to explain the experimental findings, where X is a ligand that must occupy an axial position before oxidation of $[(H_2O)Co^{II}(hmc)]$ can occur. X has been shown to be either an anion present in solution or a functional group from the surface of a polished or oxidised glassy carbon

electrode. Fendler et al[64] have shown that this type of investigation may also be carried out in mixed solvents, specifically micelles.

Clearly, the choice of equatorial ligand also influences the formal potential ($E^{0'}$), for both the [Co^{III}]/[Co^{II}] and [Co^{II}]/[Co^{I}] redox couples. Bigotto et al[41] conducted a survey involving six different equatorial ligands and, whilst maintaining constant axial ligation, measured $E^{0'}$ for each species. They found that for the [Co^{III}]/[Co^{II}] couple, the polarographic half-wave potentials indicated that the electron affinity increased in the order bae<7,7'-$(CH_3)_2$salen<salen<salophen[65]<$(DH)_2$. In addition, for the [Co^{II}]/[Co^{I}] couple it was concluded that the half-wave potential ($E_{1/2}$) decreased with increasing nucleophilicity of [Co^{I}] (decreasing electron affinity of [Co^{II}]). They found that $E_{1/2}$ was very sensitive to changes in the equatorial ligand and that the trend was bae<7,7'-$(CH_3)_2$salen<salen<salophen<$(DH)_2$, the same trend as obtained for the [Co^{III}]/[Co^{II}] couple. Further studies were carried out with different equatorial ligands[66] and supplementary information was gained by examination of the effect of a range of different R groups as axial ligand[67], with constant equatorial ligand. It was found that $E_{1/2}$ of R[Co^{III}]B was more cathodic than that of [Co^{III}]B_2 but much less cathodic than $E_{1/2}$ for the reduction of R (where this could be detected). It was found that $E_{1/2}$ increased in the order $PhCH_2$<Ph<Me=Et. Bottcher et al[68] tested a range of [Co^{III}(acacen)] derivatives and surmised that the effect on $E_{1/2}$ of change in the equatorial ligand was much less than that of change in the axial ligand. Where an activating group is present at the β position of the alkyl chain an agostic interaction[69] causes elimination to occur, whereas it was shown, by NMR spectroscopy[70], that the presence of a hydrogen in the β position created a three-centre two-electron interaction that stabilised the complex[71].

As the R[Co^{III}] complex has groups bonded in one axial and four equatorial positions, it has been described as five coordinate[244]. The literature corroborates the evidence that both axial and equatorial ligands affect the stability of the whole complex. When an alkyl group is bonded into one of the axial positions, strain is caused in that axial group by the equatorial ligand system[34]; the bulkier the group(s) the greater the strain. The two axial groups exhibit a large cross-influence, through the central Co atom. If the lower axial group is bulky it will impact on the strength of the upper axial bond[54], thereby introducing different stabilities in different solvents. The alkyl-cobalt σ bond was described by Tada[54] in the way shown in Figure 1.8.

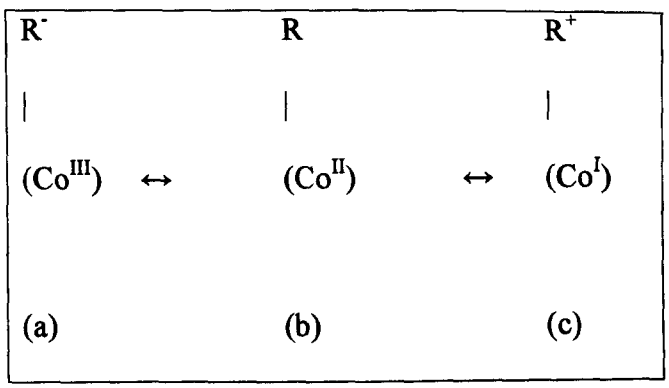

Figure 1.8. Resonance structures of the R-Co σ bond[54].

Structure (a) of Figure 1.8 is the major contributor and hence alkylcobalt species are described as R[Co^{III}]. However, the central cobalt displays a wide of diversity of reactions, such as those with anions, cations or radical species and this behaviour is explained by the presence of the other resonance forms. Schrauzer and Windgassen[72] showed that the axial base ligand could easily be replaced if the incoming ligand had greater donor-acceptor properties than that of the ligand already attached. They observed the electron affinity towards cobalt to decrease in the

following order $(n\text{-}C_4H_9)_3P \approx (C_6H_5)_3P > py > (C_2H_5)_2S > H_2O > CH_3OH$. It is known that the rate of exchange of this axial base group affects the reactivity of the σ bond between Co and the upper R group[73]. Jensen and Kiskis[74] investigated the mechanism of base ligand exchange. They postulated that the reaction could proceed via a dissociative interchange (I_d), as shown in Scheme 1.5, or a purely dissociative mechanism (D_i), as shown in Scheme 1.6. They also showed that the mechanism could be altered by changing the reaction conditions.

$$M(L)_nX + Y \rightleftharpoons M(L)_nXY$$

$$M(L)_nXY \rightarrow M(L)_nYX$$

$$M(L)_nYX \rightarrow M(L)_nY + X$$

Scheme 1.5. The I_d mechanism.

$$M(L)_nX \rightleftharpoons M(L)_n + X$$

$$M(L)_n + Y \rightarrow M(L)_nY$$

Scheme 1.6. The D_i mechanism.

The mechanisms for axial base exchange in a range of $Me[Co(dmgH)_2]B$ complexes in chloroform were investigated. In all cases it was found that the D_i mechanism was operative. Endicott et al[75] described the bonding in $R[Co^{III}]B$ complexes as being of X-Co-Y type with a three centre 4→5→6 electron bonding model. This combined the metal orbitals, which are d_{z^2} in nature with the σ orbitals of the axial ligands. Figure 1.9 shows the molecular orbital description for a three centre four electron bond along the axial axis, modified by the π orbital of the equatorial ligand.

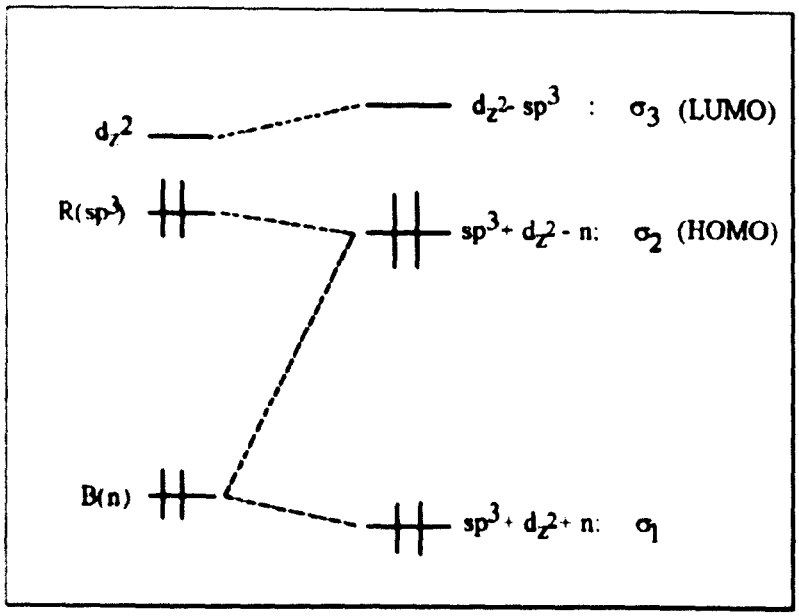

Figure 1.9. Molecular orbital description of the Co-C bond.

The excited state of this species is $[(\sigma_2)^1(\sigma_3)^1]$, therefore the Co-C bond has a degree of antibonding nature, and as such is characterised by weakness and softness[34]. Insertion products of the type R-Y-[Co][76] can be synthesised, where Y can be nitrogen, halogen, sulfur, selenium, halogen or oxygen. Scheme 1.7 highlights the thermal or photochemical insertion of oxygen that can occur between the alkyl group and cobalt centre of a macrocycle. This process has been shown to take place without stereoselectivity[77,78,79]

$$R[Co] + O_2 \xrightarrow{h\nu\ \Delta} R\text{-}O\text{-}O\text{-}[Co]$$

Scheme 1.7. Insertion of O_2 into a C-Co bond.

This type of bond, like that between carbon and cobalt, may be cleaved by irradiation with UV or visible light[79] [Co] (with or without R groups attached) are also involved in the reduction of carbon dioxide. This is of major synthetic interest, because the products may be useful organic compounds such as methanol, methane, etc[80]. The insertion of CO occurs in the same way as described previously for oxygen. Insertion reactions may also take place with sulfur, ultimately leading to an R-S_4-R species. The reduction of nitrate to ammonia has also been reported[81].

The inherent lability of the C-Co bond means that R[Co^{III}] can spontaneously dissociate into a radical pair[82,83,84,85,86,87], usually promoted by exterior influences such as heat or light. However, this radical pair has been shown to recombine readily[88] and so the efficient homolytic cleavage does not necessarily lead to radical generation. The rate of recombination depends on cobalt species, temperature, solvent viscosity and other systematic factors. Evidence of this recombination was gained from studies[89,90] which involved asymmetric groups attached to cobalt. In the case of an asymmetric α carbon, isomerisation occurred under irradiation, even in the crystal form. The rate of racemisation was shown to depend on the energy of the Co-C bond. Homolysis in the Co-C bond can occur due to determinants such as[22]:

- electrophilic, nucleophilic or radical attack,
- modification within R,
- charge transfer interactions of macrocycles with axial ligands,
- axial ligand exchange,
- heat or light,
- steric interaction between equatorial and axial ligands.

Schrauzer and Grate[91] studied the homolysis of benzylcobalamin under both atmospheric and oxygen-free environments. The products formed by each reaction led them to conclude that bond breaking was a homolytic process. Nome et al[92] investigated the effect of changing the substituent on the benzyl ring on the rate of homolysis. They concluded that changes in ring substituents had a far smaller effect on the rate of homolysis than changes in axial ligand. In a comparison of the redox behaviour of various trans[14]diene macrocyclic species of the series iron to zinc, Rillema et al[93] found that the [Co^{I}] species generated did not produce stable R[Co^{III}] species. This was attributed to insufficient electron delocalisation in the complex to stabilise such a species. In the case of RX having an activating group in the β position, any R[Co^{III}] species produced will be short-lived. This is due to the extremely weak bond resulting in the spontaneous decomposition of the complex[30].

1.2.3.3 Effect of light on the breakdown of C-Co bonds

Particular C-Co bonds can be broken down by the application of heat or light.

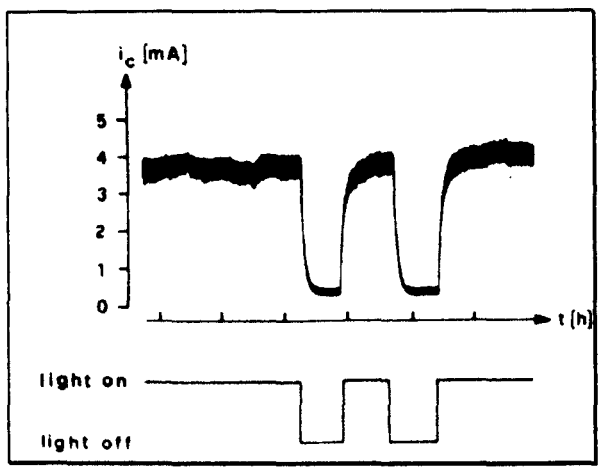

Figure 1.10. Current fluctuation as a function of applied light[22].

Figure 1.10 shows how Scheffold[22] investigated the effect of light on the diffusion-limited current for the reduction of $[Co^{III}] \rightarrow [Co^{II}]$. This reduction was shown to only induce catalytic coupling of acetanhydride and acrylonitrile during periods of illumination.

Scheffold and Orlinski found that the addition of acyl anion equivalents to activated olefins was assisted by the application of visible light to the reaction cell[94]. The reaction, catalysed by B_{12}, was found to occur at -0.95V to -1V in the presence of light and at -1.5V to -2V (both vs. SCE) in the dark. Rusling[95] found that $R[Co^{III}]$ produced from the reaction of $[Co^{I}]$ with RX could be broken down at two different potentials, that depended on the intensity of illumination. A potential of –0.85V vs. SCE was used with irradiation by visible light and a potential of –1.45V was required in the dark. Further proof of the promotion of the breakdown of Co-C bonds was obtained by Pagenkopf and Livinghouse[96] when they used $[Co_2(CO)_8]$ to catalyse [2+2+1] cycloadditions. It was discovered that the choice of source and magnitude of illumination was vital to ensure an efficient process. However, in a comprehensive study Rangel et al[97] measured the effect of exposing samples of pyridine and phosphine (as axial base) $[Co(dmgH)_2]$ to a range of visible and UV light sources. It was found that Co-C bond homolysis was not necessarily triggered by exposure to visible light, while the stability of the bond was dependent on the nature of both axial and equatorial ligands.

1.2.4 Interaction with oxygen

Whilst this thesis is not concerned with study of the interaction of [Co] with O_2, it is important to be aware of the potential complications that O_2 can introduce. In particular R[Co^{III}] are susceptible to homolysis by visible light, so specific [Co] and R[Co^{III}] are susceptible to interaction with O_2. Additionally, there are many similarities between the reactions of [Co^{I}] with RX and [Co^{I}] with O_2. A large range of cobalt species will interact with oxygen, therefore studies in which oxygen interaction is undesirable must be conducted in an oxygen-free atmosphere.

Costa[65] performed a simple study into the formation of the [Co(salen)O_2] complex from a solution of [Co(salen)] in anhydrous pyridine, containing tetraethylammonium perchlorate (TEAP). A wave due to the one electron reduction of [Co^{II}] to [Co^{I}] was found at -1.38V. Oxygen (effectively a radical trapping agent) was then bubbled through the system and the reduction wave recorded at various time intervals. Over time the wave at -1.38V decreased, with the simultaneous appearance of another wave at -0.6V. This change was reversible, as on bubbling dry nitrogen through the solution the original wave returned. The new wave was attributed to the reduction of [Co^{II}(salen)O_2] to [Co^{II}(salen)O_2]$^-$. Oxygen adducts were also found in the cases of [Co^{II}BAE] and [Co^{II}saloph]. ESR was used to show that the adducts formed were best described as Co^{III} superoxides, with O_2^- acting as the ligand. The interaction of oxygen with [Co(dmgH)$_2$][98] was also investigated by Costa et al. Scheme 1.8 was proposed for the formation of [O_2Co^{III}] adducts of this type.

$$[Co^{III}L]^{n+} + e^- \rightarrow [Co^{II}L]^{(n-1)+} \quad \textbf{(a)}$$

$$[Co^{II}L]^{(n+1)} + O_2 \rightarrow [CoL\text{-}O_2]^{(n-1)+} \quad \textbf{(b)}$$

$$[CoL\text{-}O_2]^{(n-1)+} + H^+ \rightarrow [Co^{III}L]^{n+} + OOH^- \quad \textbf{(c)}$$

Scheme 1.8. Reaction of electrogenerated $[Co^{II}(dmgH)_2]$ with O_2.

Again, it was found that after controlled-potential electrolysis of the Co^{III} complex, $[Co(dmgH)_2]$, to generate the Co^{II} complex, exposure to O_2 gave a new wave which could be removed by purging the system with N_2. Steps (a) – (b) of Scheme 1.8 were considered to explain this behaviour.

The catalytic reduction of oxygen can produce either H_2O_2 or H_2O as product; the former of these species attacks [Co] catalysts and is thus undesirable. Mechanistic studies have revealed that the environment of the Co species has a large influence over the mechanism of reaction. Geiger and Anson[99] showed that the concentration of reactants influenced the reaction pathway. Figure 1.11(a) and (b) show the proposed mechanism for excess Co and excess O_2 respectively.

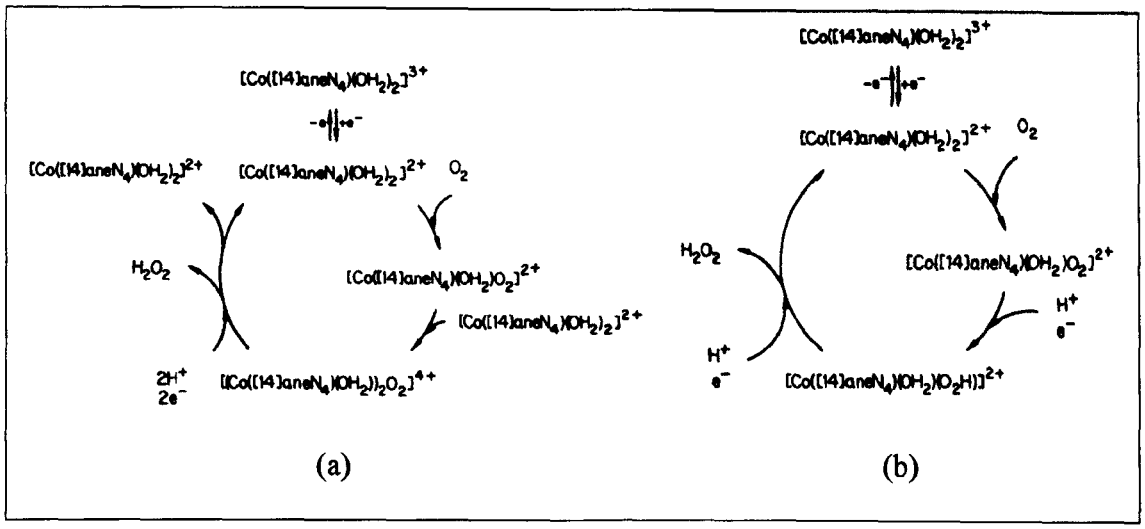

Figure 1.11. Variation of mechanism with change in concentration ratios: (a) excess [Co] and (b) excess O_2.

Adsorption of the [Co] catalyst onto an electrode has been found to promote the four electron reduction of O_2 to H_2O. Kobayashi et al[100] adsorbed a cobalt crown phthalocyanine onto a highly orientated pyrolytic graphite (HOPG) electrode. It was found that the method of adsorption, surface coverage, pH and changes in the ionic strength of the solution influenced the reduction process. Anson[101] demonstrated that the reduction of O_2 catalysed by $[Co(tim)]^{2+}$ may be enhanced from a relatively slow two-electron reduction to a fast four-electron reduction to H_2O, by adsorbing the cobalt complex onto the surface of a graphite electrode. This enhancement was attributed to interaction of [Co] with functional groups on the electrode surface causing an increase in the affinity of the complex for O_2. The method of adsorbing [Co] onto graphite electrodes was studied further via investigation of cobalt porphine[102], and the same species substituted with four methyl groups[103]. This behaviour was attributed to the propensity to form dimeric, cofacially disposed ring structures, thereby allowing the two ends of an O_2 molecule to each interact with Co simultaneously during the transition state. It has been shown that this leads to

reduction of O_2 to H_2O[104,105]. This observation led to the synthesis of Co(DPD) and Co(DPX)[106], which were specifically designed to react with both ends of an O_2 molecule. The complexes are cofacial cobalt bisporphyrins that incorporate either a dibenzofuran or xanthene molecule as a "hinge" between the two porphyrin rings. This makes the entire structure highly flexible and is described by Anson as having a "pac-man" mode of action, whereby the rings can open to allow O_2 to coordinate between the upper and lower cobalt.

In addition to adsorbing catalyst onto the electrode surface, other methods have been employed to encourage the four-electron reduction of O_2 by [Co], that generally show the two-electron reduction of O_2 to H_2O_2. Marchaj et al found that addition of Fe^{2+} to a solution of [$Co(tim)^{2+}$] changed the reduction of O_2 from a two-electron path to a four-electron process[107]. The two-electron electrocatalytic reduction of O_2 that usually occurs at a particular cobalt porphyrin (even when adsorbed on graphite), was enhanced to a four-electron reduction by addition of $Ru(NH_3)_5$-groups to the structure[108]. The enhanced activity was this time attributed to the back bonding nature of the Ru species, causing the transmission of electron density into the porphyrin ring, thereby enhancing the electronic interaction between Co and O_2. This, in turn, increased the affinity of Co for O_2. Further to these studies, it has been discovered that a specific number of Ru species must be present. Each porphyrin ring has four possible sites of substitution with respect to a Ru species and therefore an investigation was made into the differences between mono, di- and tri-substituted porphyrins,[109] compared to previous work with tetra- substituted rings. It was found that with only one or two Ru species attached to the porphyrin ring, the catalyst acted in two-electron mode, but for tri, or higher, substitution the four-electron mechanism

operated. A polymerised film of cobalt porphyrins linked together with ruthenium bridging species was also proposed as a catalyst for O_2 reduction[29]. The catalyst resulted in the reduction of O_2 to H_2O and, as a film, remained integral with the electrode surface for a longer time.

1.2.4.1 Electron Transfer

In related studies examining the interaction between the central cobalt atom and the surrounding ligand(s), fast transient absorption techniques have been utilised to examine the electron transfer between metal and ligand[110]. The charge separation and recombination were recorded for four different cobalt porphyrin complexes, by measuring decay profiles with a pump wavelength of 530 nm and a probe wavelength of 610 nm. The rate of decay was found to parallel the differences in the electrocatalytic activity of the complexes. Charge transfer from Co (d-π) to O_2 is involved in the transition state of the reaction of these complexes with oxygen leading to the conclusion that there is clear evidence of a link between the dynamics of the charge transfer state of cobalt porphyrins and their electrocatalytic activity.

1.2.5 Cobalt dinuclear interactions

Different oxidation states of cobalt complexes may form dinuclear species. It has been shown[47] that [Co^{II}] species can be oxidised by either an inner or outer sphere electron transfer mechanism, depending on the nature of the oxidant and bridging bond. Adin and Espenson[111] examined the reduction of $[Co(dmgH)_2](OH_2)_2$ with $[Co^{III}(NH_3)_5]X^{2+}$ (where X is Br^-, Cl^- or N_3^-) and postulated an inner sphere electron transfer mechanism. The same type of reaction was examined by Wang and Jordan[47], but $[Co(dmgBF_2)_2]$ was used in place of $[Co(dmgH)_2]$. An analogous inner sphere

mechanism operated, but the rate of reaction was approximately three orders of magnitude smaller than for $[Co(dmgH)_2]$, which was attributed to a smaller driving force of the reaction. A study was also made of the outer sphere oxidation of cobalt^{II} sepulchrate by $[Co^{III}(dmgH)_2]^+$ and $[Co^{III}(dmgBF_2)_2]^+$. Gupta and Qanungo investigated the formation of organobridged cobaloximes from dihalides[112]. The proposed reaction scheme involved a haloakylcobaloxime, which was also found in the final reaction mixture under certain conditions.

1.2.6 Ion pairing of [Co] with solution species.

A study by Pletcher[113] et al investigated the effects of varying the concentration and cation of the supporting electrolyte during voltammetric studies of a single cobalt-centred macrocycle, $[Co^{II}(salen)]$. Voltammograms were recorded at gold microdisc electrodes in DMF for the redox couples $[Co^{II}(salen)]/[Co^{III}(salen)]^+$ and $[Co^{II}(salen)]/[Co^{I}(salen)]^-$. It was found that the potential for the Co^{II}/Co^{III} transition altered very little with either change in concentration of supporting electrolyte or with change in electrode diameter. However, as the electrode diameter decreased (equivalent to an increase in mass transport rate as discussed later), the irreversibility of the wave increased. A common anion, bromide, was used in all cases and the conclusion was drawn that there was no interaction between it and the Co^{II} species, as the wave position was unaffected by bromide concentration.

Rather different results were obtained for the Co^{II}/Co^{I} transition. It was found that change in electrode radius (a) had no effect on the position of the wave, but when the concentration of supporting electrolyte was altered, a significant shift in wave position was observed. In particular, $E_{1/2}$ became more negative by between 60 and 90mV for

a 10-fold increase in electrolyte concentration (Na^+). This was attributed to ion pairing between this cation and $[Co^I(salen)]^-$. The investigation was extended to a range of cations, namely tetrabutylammonium, sodium and lithium (all bromides). It was found that the strength of the ion pairing interaction increased in the order $Bu_4N^+<Na^+<Li^+$. The conclusion drawn was that significant ion pairing occurred when the cation was classified as being small and hard.

Since alkyl halides are known to react with $[Co^I]$, butyl bromide (BuBr) was added to the electrochemical cell during the aforementioned experiments. This allowed the effects of ion pairing on the following chemical reaction of $[Co^I]$ with BuBr to be studied. When BuBr was added two waves were reported, the first for the reduction of $[Co^{II}]$ and the second the reduction of $R[Co^{III}]$. Again, the concentration of supporting electrolyte was varied, with a similar result to that described above. The first wave of the pair shifted to a more positive value, with $E_{1/2}$ increasing with decreasing electrolyte concentration. This was attributed to $[Co^I(salen)]^-$ having greater nucleophilic character when there was less electrolyte present to ion pair to it and hence reduce its nucleophilicity.

With larger microdiscs it was found that the second wave was also affected by change in electrolyte concentration, the diffusion-limited current increased as the electrolyte concentration decreased. Pletcher postulated that one of two things had occurred: (i) a change in reaction, with more than one electron involved in the reduction or; (ii) a change in mechanism to a catalytic EC' type.

A similar investigation was carried out by Reisenhofer and Costa[114] where four different [Co] and six different electrolytes were investigated to determine the effect of ion pairing with different cations. It was found that tetraalkylammonium salts had a negligible effect on the reduction Co^{II}/Co^{I}, although small cations, such as Li^{+} formed a strong ion pair. The ion pair formation constants were measured by altering the concentration of Li^{+} (whilst keeping the ionic strength constant) and measuring the positive shift in $E_{1/2}$. It was found that in the presence of PhBr the formation of an ion pair with Li^{+} reduced the nucleophilic character of the Co^{I} species, hence decreasing the rate at which it reacted with PhBr. Once formed, it was postulated that the resulting $Ph[Co^{III}]$ complex underwent reduction to $[RCo^{II}]^{-}$, which decomposed more readily in the presence of Li^{+}.

1.3 Microelectrodes

Microelectrodes, more commonly known as ultramicroelectrodes (UMEs) are characterised by having at least one dimension of the order of 50 μm or smaller, such that edge diffusion becomes significant on the voltammetric timescale. Their small size means that they show increased mass transfer compared to conventionally sized electrodes, fast response and a diversification in the range of environments in which they can be used (including poorly conducting media). When the polarity of a solvent is low, measurement of the voltammetric characteristics of a particular system becomes impossible with conventional electrodes[115], due to problems of adding sufficient electrolyte, in order to carry current in the cell. UMEs[116] cause very little current to flow in solution and are thus very well suited to work in conditions of low ionic strength[117]. They have been used in many systems to study species in challenging solvents[118] such as toluene, and benzene. Some examples of the use of

UMEs in classically "unusual" media include: measurements made in low temperature solvent glasses[119] and measurement of the $E^{0'}$ for the oxidation of pyrrole[120]. This latter reaction causes irreversible formation of a polymer. Fast voltage scan rates were used in conjunction with an UME so that the reaction of interest was observed before a polymer formed, and thus fouled the electrode.

It has been established that the amperometric characteristics, such as steady-state current and ohmic distortion, of UMEs are quite different to those of conventional-sized electrodes. An UME shows two limiting cases of behaviour, dependent on the time scale of the experiment. If a sufficiently fast scan speed is used, species diffuse to the UME in a planar manner and thus the diffusion field is the same as in the case of a conventional electrode. An advantage of UMEs over conventional-sized electrodes is that very fast scan speeds can be employed[121], up to 2 x 10^6 V s^{-1} [122]. This is because UMEs suffer less from ohmic and capacitative charging effects compared to conventional electrodes. If one operates the UME at a more conventional scan speed, diffusional edge effects become increasingly dominant which, at sufficiently slow scan speeds, result in a steady-state current. The transport of species to the electrode in this situation is via a hemispherical diffusion field.

These limiting mass transport situations are depicted in Figure 1.12. The steady-state diffusion-limited current observed at a disc-shaped UME in bulk solution, i_{lim}, is given by Eq. 1.3 for a simple electron transfer process[123].

$$i_{lim} = 4nFDac^* \qquad \text{(Eq. 1.3)}$$

where n is the number of electrons transferred per redox event, a is the electrode radius and c^* is the bulk concentration of the electroactive species.

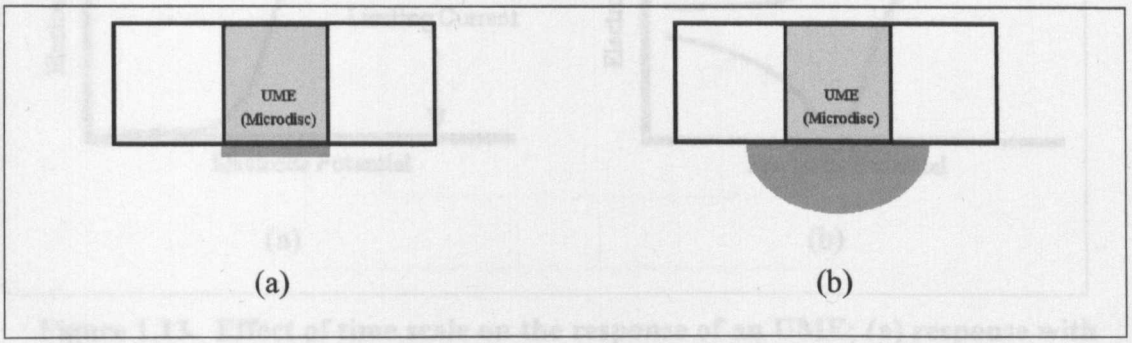

Figure 1.12. Limiting mass transport regimes at an UME: (a) planar diffusion at short times; (b) hemispherical diffusion under steady-state conditions.

A characteristic of these small electrodes is a high rate of mass transfer to the electrode. The efficiency of mass transport to the electrode can be increased by reducing the size of the electrode (diameter if the UME is a disk), which has led to much research on the development and fabrication of ultra-small electrodes[124, 125, 126, 127, 128]. The time-dependent nature of mass transport to an UME implies the shape of a voltammogram will change with timescale of the measurement, as shown in Figure 1.13. At sufficiently slow scan speeds, a current plateau, similar to that seen at a rotating disk electrode is observed, because a limiting rate of steady-state mass transfer is attained (Figure 1.13a). In contrast, fast scan speeds will produce a peak shaped response, as observed at large electrodes (Figure 1.13b).

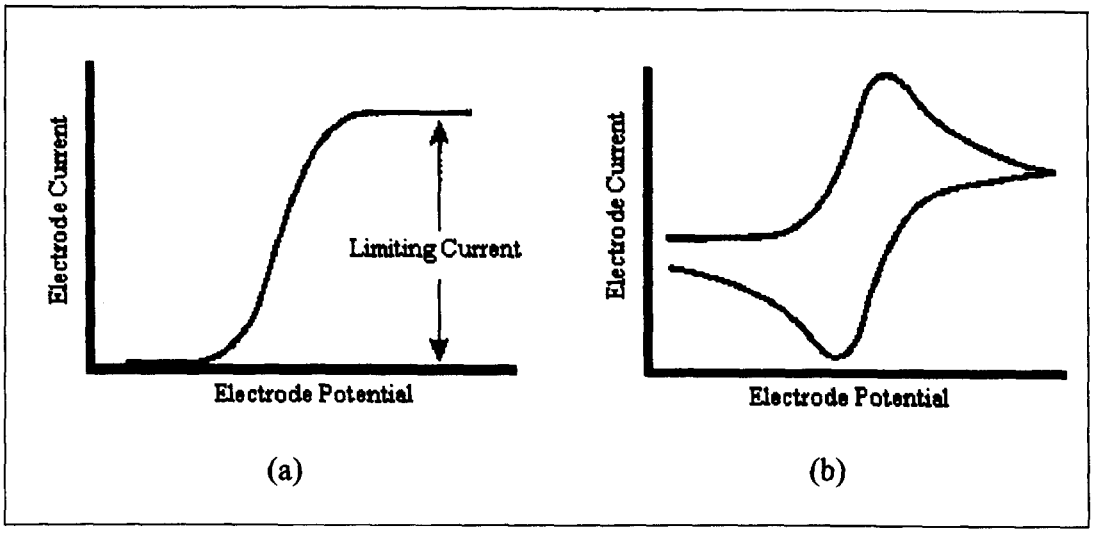

Figure 1.13. Effect of time scale on the response of an UME; (a) response with spherical diffusion to a UME and (b) response with planar diffusion to a UME.

1.3.1 Measurement of electrochemical kinetics with UMEs

Both the kinetics of electron transfer and those of any preceding or following, coupled chemical reaction(s) may be measured. Either transient or steady-state methods may be employed in conjunction with UMEs for measuring heterogeneous or homogeneous kinetics. The approaches used to measure the heterogeneous kinetics of electron transfer are reviewed briefly in the following sections, as background to later chapters which discuss the measurement of kinetics in greater detail.

1.3.1.1 Transient techniques

Both fast scan cyclic voltammetry (CV) and rapid transient methods can be employed with UMEs, as discussed in the following sections.

1.3.1.1.1 Fast Scan CV

During a CV experiment the potential applied across a working and reference electrode, is swept between two limits in a triangular fashion as shown in Figure 1.14.

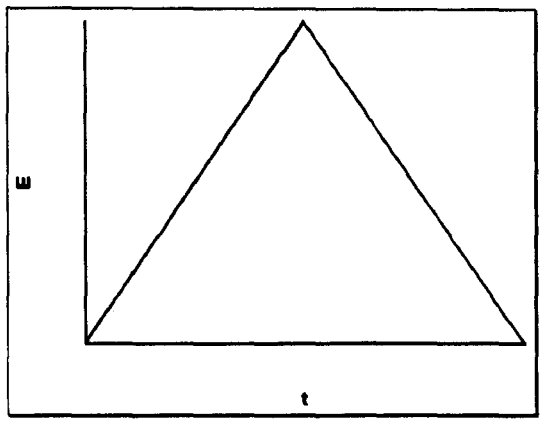

Figure 1.14. Applied potential (*E*) as a function of time (*t*), during CV.

The current at the working electrode is measured as a function of applied potential and the resultant voltammogram resembles that shown in Figure 1.13(b). At best, macroscopic electrodes can only be used practically up to a scan speed of approximately 1000 V s^{-1}; above this value ohmic distortion affects the shape of the response. However, as just mentioned, UMEs can be scanned at rates up to 2 x 10^6 V s^{-1} [129]. A three-electrode system, comprising working, reference and counter electrodes, all controlled by a potentiostat, is generally employed. There are three main applications of fast scan CV: (i) detection of short lived species (and their lifetime; i.e. the rate of chemical reactions); (ii) determination of $E^{0'}$ for couples where the product of electron transfer is relatively unstable and; (iii) the measurement of rate constants of fast interfacial electron transfer.

1.3.1.1.2 Potential step chronoamperomentry (PSC)

In PSC the potential applied to the working electrode is stepped from a value where no redox process occurs to one where the process of interest (either an oxidation or reduction) occurs at a diffusion-controlled rate. The current at the electrode is

measured as a function of time. The potential may also be reversed in a subsequent step to collect back the electrogenerated species, i.e. double potential step chronoamperometry (DPSC). At UMEs, this technique can be used to measure rapid solution kinetics[130,131] and to measure the diffusion coefficient of both species in a redox couple[132].

1.3.1.2 Steady-State Measurements

This type of measurement does not suffer from the charging currents[133], normally associated with transient methods, and relatively simple potentiostats or current followers used in a two-electrode circuit with working and reference electrodes will suffice for experimental measurements[121]. The factor governing the magnitude of the rate constant that may be measured is the electrode size. The mass transfer coefficient (k^t) for a microdisc electrode under steady-state conditions is:

$$k^t = 4D/\pi a \qquad \text{(Eq. 1.4)}$$

where D is the diffusion coefficient of the electroactive species.

There has been considerable effort to develop increasingly smaller UMEs to enhance the range of kinetics that may be studied[124]. Mass transport to micrometer-sized electrodes can be enhanced by employing convection, as in the microjet electrode (MJE)[134,135,136,137,138], radical flow mircoring electrode (RFMRE)[139,140,141,142] and high-speed channel electrode[143,144,145]. These techniques deliver high k^t values (in excess of 2 cm s^{-1} in the case of the RFMRE), allowing the study of both rapid heterogeneous and homogeneous kinetics.

The voltammetric characteristics of a particular system may be measured in order to gain access to various thermodynamic and kinetic parameters for heterogeneous electron transfer. Here the applied potential is swept between two limits in a linear sweep voltammogram (LSV). Figure 1.15 is a diagrammatic representation of the way in which the applied potential changes with time during a LSV.

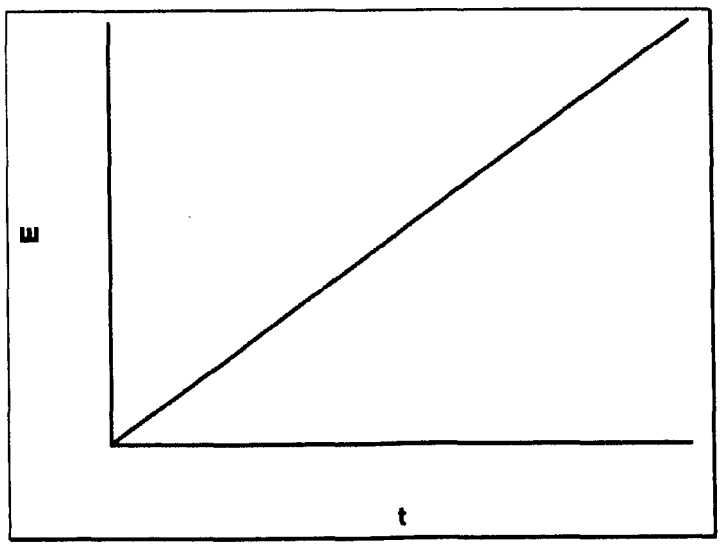

Figure 1.15. E is swept linearly with time during a LSV.

The resultant voltammogram resembles that shown in Figure 1.13(a). As discussed later in this thesis (chapter 3), the shape of the voltammogram changes, depending on the relative magnitude of the standard heterogeneous rate constant (k^0) and k^f. The wave becomes more elongated as k^0 decreases compared to k^f (increasing irreversibility)[146]. Figure 1.16 shows schematically three voltammograms that illustrate the difference between reversible, quasi-reversible and irreversible systems.

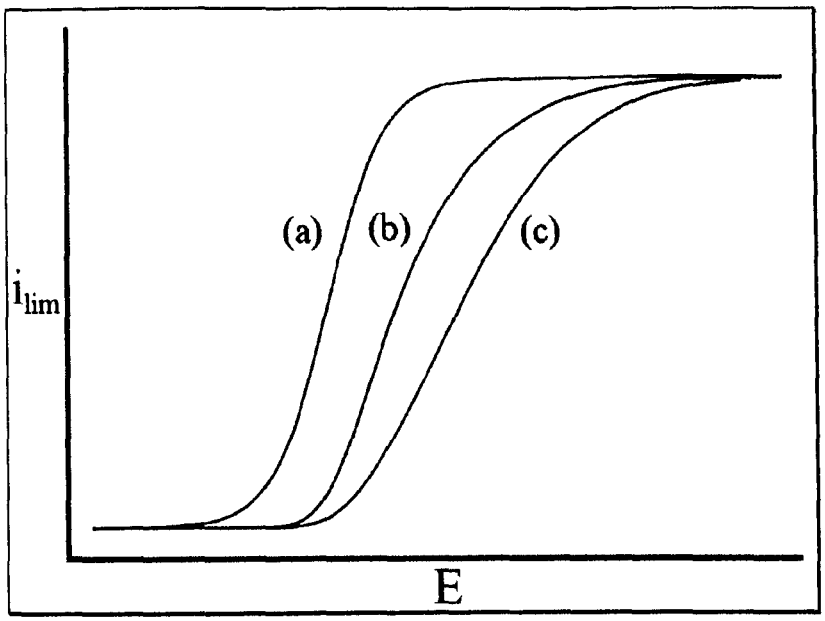

Figure 1.16. Voltammograms for (a) reversible, (b) quasi reversible, (c) irreversible systems.

The general methodology employed to measure kinetics is to set the heterogeneous or homogeneous reactions of interest in competition with mass transfer and to deduce the kinetics from the voltammetric response. The approaches and methods utilised are discussed in much greater detail in chapter 3. For systems that involve homogeneous chemical reactions, as well as heterogeneous electron transfer, the resolution of rate constants is a more complicated matter, involving comparison of experimental results to analytical or simulated results, a subject which forms the basis of chapter 5.

1.4 SECM

SECM was first introduced in 1989 by Bard and co-workers[147], following earlier work by Engstrom[148, 149], and is one of a family of scanned probe microscopes. Bard et al produced a series of papers which described the principles[147], instrumentation[147, 150] and theoretical formulation[151] of SECM. SECM employs a UME probe, which is

operated in close proximity to a target interface submerged in a solution, such that the electrochemical response of the UME is governed by mass transport between the interface and UME, as well as by chemical reactions at the interface (and in solution). In this way, the SECM reveals both topographical and kinetic information as a function of a surface position. The spatial resolution is comparable with the dimensions of the UME tip, typically of the order of 1 - 25 μm.

SECM has been used widely to investigate reactions that occur at solid/liquid interfaces[152,153], showing particular promise in determining the kinetics of rapid interfacial processes. A number of reviews have recently been published covering the range of SECM measurements[121,154,155,156,157]. SECM has more recently been applied to studies of liquid/liquid[132] interfaces, with the first report in 1995[158]. These experiments have concentrated mainly on kinetic studies of ion and electron transfer[159,160] at immiscible liquid/liquid interfaces. Additionally SECM has proved a powerful tool for the investigation of biologically important materials[159,161].

1.4.1 Basics of Operation

The tip used in SECM is most commonly a disc UME. The electrochemical cell contains an electroactive mediator, which may be either oxidised or reduced at the UME, along with supporting electrolyte and the target substrate or interface of interest. The tip may be operated in either an amperometric or potentiometric mode. For the studies described herein, amperometry is used and this configuration will be reviewed here. A typical SECM set-up is shown in Figure 1.17. The UME is positioned in three axes, *x*, *y* and *z*, using either piezoelectric elements or a combination of a piezoelectric element in the *z* axis and high resolution stepper

motors for the x and y axes. These devices expand or contract on the application of a voltage, so allowing positioning with sub-micron level resolution.

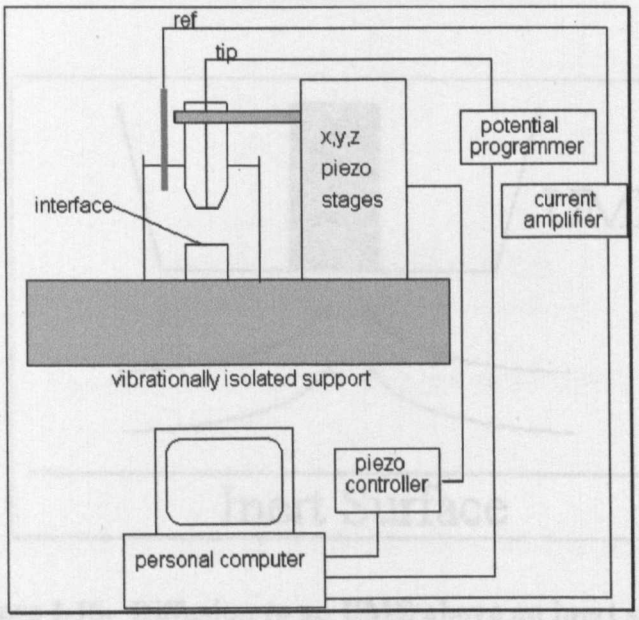

Figure 1.17. Schematic of a typical SECM set-up.

As shown in Figure 1.17, a simple two-electrode set up, usually suffices for UME measurements, with the UME operating as the working electrode, together with a reference electrode. The interface of interest can be formed between the solution containing the tip and either a solid[152,153], a liquid of a different (immiscible) phase[132], or even a gas[132,162]. When the tip is positioned a long way from the interface it behaves as if it were an ordinary UME in a solution. The diffusion-limited steady-state current is now referred to as i_{∞}, rather than i_{lim}, Eq. 1.3 applies.

1.4.2 The feedback mode

With the electrode positioned close to an interface, within about two electrode radii, the flux of material to the electrode is perturbed from the normal hemispherical

diffusion case described earlier (Figure 1.12). The effect on the current depends on the nature of the interface (i.e. its reactivity) and the distance of the electrode from the surface.

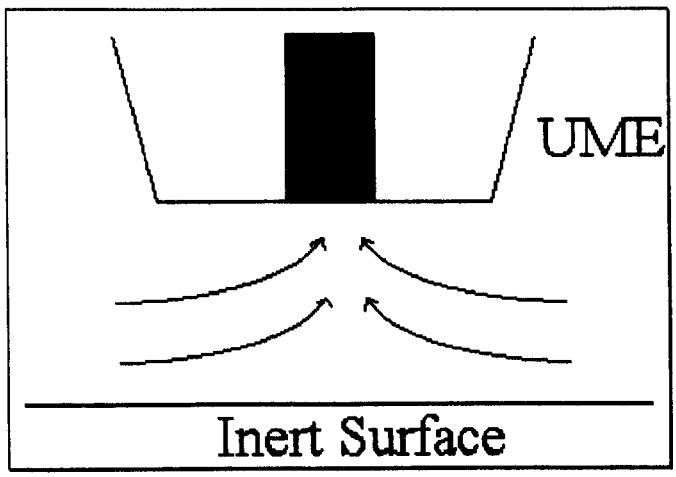

Figure 1.18. Diffusion to an UME above an inert surface.

For the case where the interface is inert to the electrogenerated species, Figure 1.18 shows that the interface perturbs the hemispherical diffusion field; the flux of species to the tip UME is hindered and thus decreases. Consequently, a decrease in the diffusion-limited steady-state current at the tip (i_T) is observed as the UME approaches the surface such that $i_T < i_\infty$. This effect is termed negative feedback[151].

Opposite to this effect is positive feedback[151], where the electrogenerated species interacts with the substrate and is converted back to the original solution precursor (Figure 1.19). This results in an enhanced flux of species to the electrode, compared with the bulk, infinite separation case, and the observed current increases, such that $i_T > i_\infty$. This effect is termed positive feedback[151].

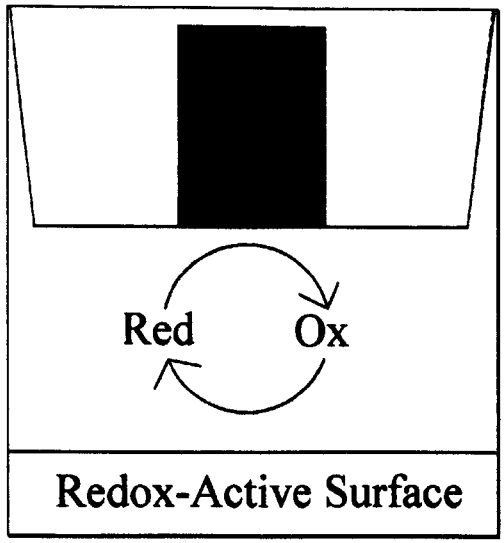

Figure 1.19. Positive Feedback at an UME.

The size of the negative or positive feedback effect seen is dependent on the tip-substrate separation, and the rate of the interfacial redox reaction. The dependence of the positive feedback current on distance can be used to record topographical data for a particular surface. In particular, at close distances the current changes significantly with only small changes in separation. During such topographical studies, the SECM is scanned across the surface of a substrate in a line scan pattern whilst the current is monitored. Currents can be converted to tip-interface separations, which in turn gives topographical information, if the surface reactivity is known[163,164]. Alternatively, an image of the reactivity of the substrate can be built up, where the topography is known[165]. SECM images can be obtained in a solution containing two different mediators to record both topography and reactivity in subsequent passes.

The kinetics of reactions that occur at an interface can be measured from "approach curves", where the normalised current, (i_T/i_∞) is measured as a function of the tip-substrate separation (d). The limiting cases, described as negative and positive

feedback, are plotted in Figure 1.20; these correspond to surface reaction kinetics where the rate is zero, and where the rate of the interfacial redox reaction is controlled by mass transport.

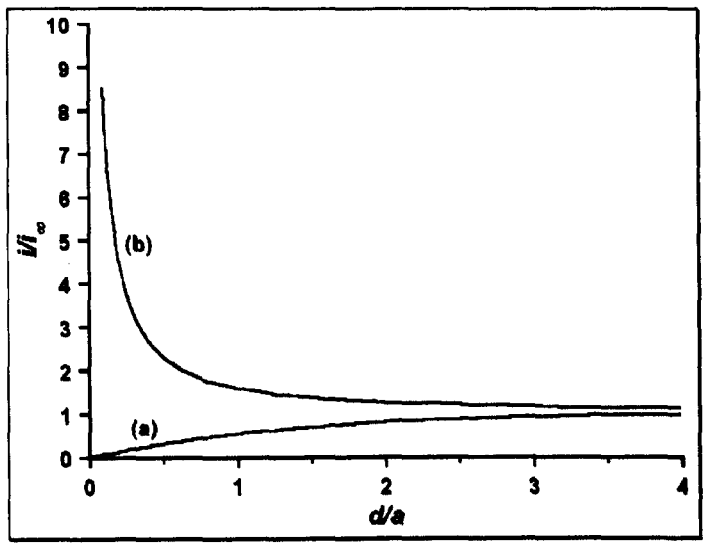

Figure 1.20. Feedback curves for negative (a, lower curve) and positive (b, upper curve) feedback. Data from Kwak and Bard[151].

Kinetic cases for reaction rates between these two limits can be measured with this technique by fitting experimental data to simulated working curves[166]. Since diffusion is fast for the SECM configuration, measurements of fast kinetics can be made, in the cm s^{-1} domain[167,168], for heterogeneous processes. Approach curves may also be used to measure homogeneous kinetics, as outlined later in this chapter.

1.4.2.1 Substrate size effects

When the interface under examination is formed between the solution containing the electroactive mediator and a solid substrate, the size of the substrate relative to the tip electrode influences the results seen at the tip. Feedback at a solid substrate is due to

the substrate potential (E_S), which may be biased externally, or via the redox couple present in solution, as shown in Figure 1.21[169].

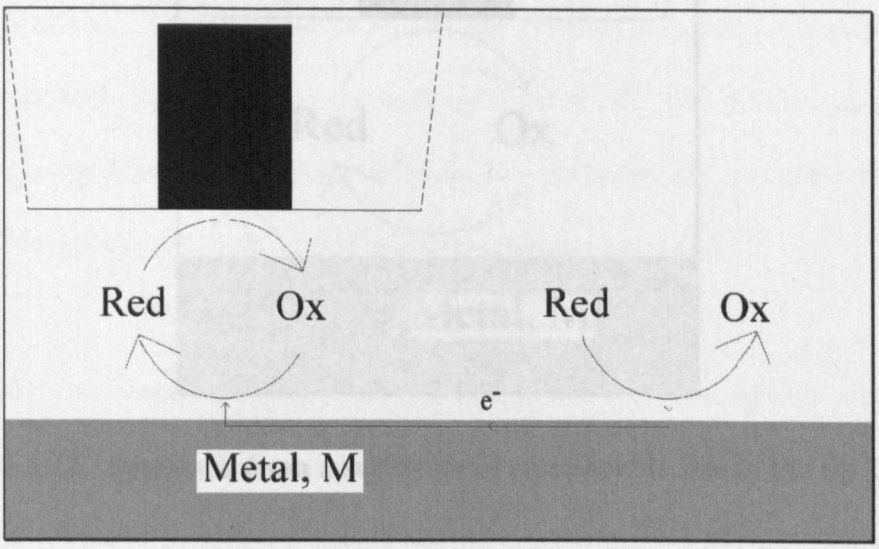

Figure 1.21. Feedback for the case where the substrate is much larger than the tip UME.

If the portion of the substrate, probed by the tip, is relatively small (compared to the tip size) then the substrate is predominately surrounded by Red. This fixes the substrate at a potential where the conversion of Ox to Red occurs spontaneously[170]. In this case oxidative etching of the substrate (Figure 1.22) may also occur if Ox is a sufficiently powerful oxidant, compared to the base metal, and the kinetics are fast enough.

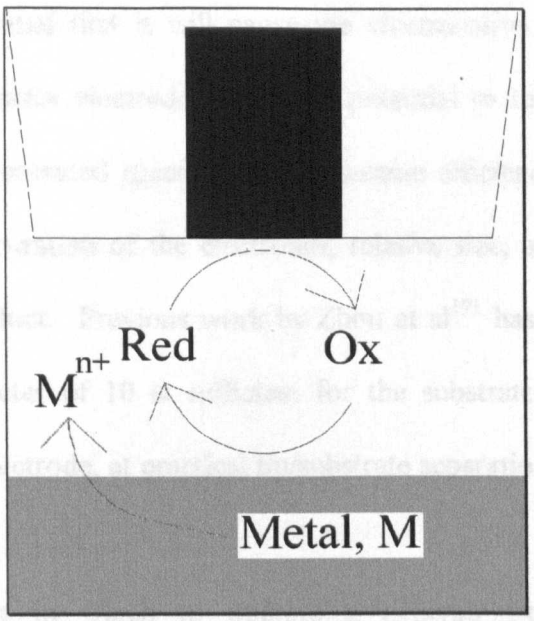

Figure 1.22. Feedback from a substrate of comparable size to the tip UME.

Both processes cause the flux of species to the tip to be increased resulting in a larger i_T than might otherwise be seen. However, it is difficult to determine whether this increase in i_T is due to substrate potential driven feedback, or oxidative etching of the substrate, or even a combination of the two. If one wishes to make quantitative measurements of oxidative etching processes then the contribution of substrate potential driven feedback must be eliminated, the bathing of the substrate in Red can be made negligible by reducing the size of the substrate, making it equal to that of the tip[169].

1.4.3 Generation collection (GC) modes.

GC experiments involve two externally biased electrodes, one as tip and the other as substrate. The tip is generally a UME but the substrate can be of any size. The SECM is set up with the substrate electrode located directly below the tip electrode, in an electrochemical cell with electroactive mediator present. The generator electrode

is set at such a potential that it will cause the electroactive mediator to undergo electrolysis. The collector electrode is set at a potential to reverse this change and "collect" the electro-generated species. The collection efficiency (*CoEf*) is governed by several factors: separation of the electrodes, relative size, and the stability of the electro-generated product. Previous work by Zhou et al[171] has shown that a ratio of substrate to tip diameter of 10 is sufficient for the substrate to collect all that is generated by the tip electrode, at practical tip/substrate separations.

There are two ways in which to operate a generation-collection experiment: electrogeneration may occur at either the tip or the substrate UME. This has led to the terms tip generation-substrate collection (TG-SC) and substrate generation-tip collection (SG-TC)[171]. SECM may be employed in the study of homogeneous kinetics coupled to electron transfer, as discussed in section 1.45.

1.4.3.1 The TG-SC mode of SECM.

TG-SC involves electro-generation of a species of interest from a solution precursor at a tip UME, at a diffusion-controlled rate. The electrogenerated species then diffuses into solution, where it may undergo reaction in solution before being collected at an externally-biased substrate electrode. The main attributes of the TG-SC mode are: a) high collection efficiencies, approaching 100%, when the electrogenerated species is stable in solution; b) measurements may be made under steady-state conditions[172,171] and; c) mass transport is well-defined and modellable.

1.4.3.2 The SG-TC mode of SECM.

The SG-TC mode was introduced by Engstrom and co-workers[148, 149] in which an

amperometric tip UME was used to collect both stable and transient species generated at a larger substrate electrode. The SG-TC mode has also been used to identify subtle differences between the diffusion coefficients for the reduced and oxidised forms of a simple redox couple[173]. This mode has also been used to study an electrochemical reaction followed by an irreversible chemical reaction, known as an EC-type mechanism[174,175].

1.4.4 Studies of biphasic liquid systems with SECM

The interface of interest need not be formed between a solution and a solid; studies may be made of the interface between two immiscible liquids. Amperometric measurements have mainly been made to study electron or ion transfer in biphasic liquid systems[176,130,177,158,178,179,180,181,182]. A brief description of methods involving amperometric UMEs to initiate and monitor interfacial reactions follows.

1.4.4.1 Equilibrium perturbation mode

SECM has been used to induce and monitor reversible interfacial phase transfer processes through the perturbation of an equilibrium. In general, the UME is positioned in a liquid phase close to an interface at which the chemical process is initially at equilibrium. Electrolysis is employed to remove a target solution species adjacent to the interface, driving the interfacial process in the direction of interest. The basic operation of this mode is shown schematically in Figure 1.23. This technique has been used to study both the desorption of protons from a titanium dioxide, rutile (100), surface[152], and the dissolution of ionic single crystals[183,184,185,186,187,188,189]. The first example demonstrated the ability of SECM to resolve adsorption/desorption processes, solution diffusion and the lateral surface diffusion of protons[152].

Dissolution from a copper sulphate single crystal was a further example of the use of the method of induced dissolution[190]. Most recently this technique has been used to study transfer across liquid/liquid[191] and liquid/gas[162] interfaces, and lateral diffusion in Langmuir monolayers[192].

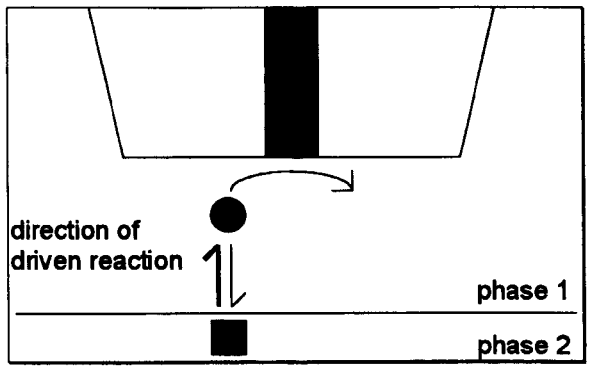

Figure 1.23. Schematic illustration of the equilibrium perturbation mode of the SECM.

1.4.4.2 Investigation of reactions at liquid/liquid interfaces using the feedback mode of SECM

SECM operating in the feedback mode, has been applied to a number of processes at liquid/liquid interfaces. Figure 1.24 shows the complex nature of the application of the feedback mode of the SECM. Ion transfer is associated with the electron transfer reaction in order to maintain electroneutrality[158] in the two phases. A generalised schematic of the processes occurring is shown in Figure 1.24. Four stages have been identified as having an effect on the observed current, namely; mediator diffusion in the phase containing the UME, the interfacial electron transfer reaction, diffusion of the redox species in the organic phase, and charge compensation by ion transfer[158].

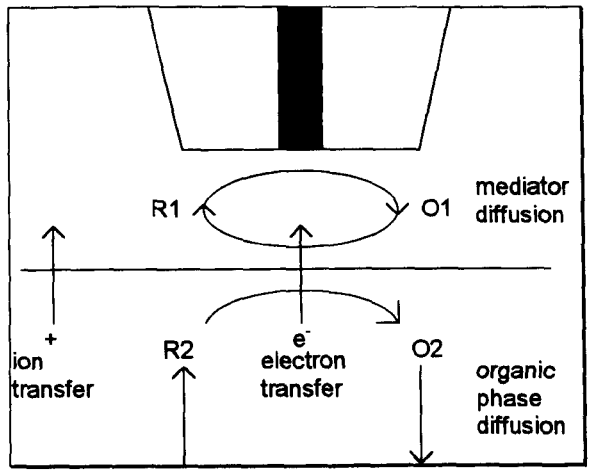

Figure 1.24. Schematic showing the processes occurring during SECM feedback experiments at a liquid/liquid interface.

Due to the in-plane homogeneity of liquid/liquid interfaces, approach curve measurements have generally been used in these investigations[193,194]. A further technique employed to initiate and study interfacial processes is double potential step chronoamperometry (DPSC)[132], a technique discussed in greater detail in chapter 6.

1.4.5 Mechanistic studies with SECM

The use of UMEs to measure homogeneous kinetics was introduced earlier in this chapter. The range of reaction rates that may be measured can be extended compared to a stationary UME, by placing the electrode into an SECM configuration. SECM is established for the study of solution kinetics of chemically unstable electrogenerated species[195,171,196]. Many mechanisms involving following chemical reactions have already been studied. These include first-order EC[195,197] and second-order EC_{2i}[171,198,199] mechanisms. Chemical reactions that follow an electrochemical step can also lead to a further electrochemical step, as in the ECE-DISP1 reaction[196].

The investigation of electrode processes involving coupled homogeneous kinetics with SECM has largely been based on the feedback mode[154,195-199] or closely related TG-SC mode[171,172,196,198-199]. With these approaches, the tip UME is positioned directly over a larger substrate electrode, effectively creating a variable gap ultra thin layer cell[126]. The tip is held at a potential to electro-generate the species of interest from a solution precursor at a diffusion-controlled rate. A competition is then established between the diffusion of the electrogenerated species to the collector electrode, maintained at a potential to promote regeneration and feedback of the initial precursor, and the solution kinetics. By measuring either the tip feedback current, i_T, or tip and substrate currents, i_S, as a function of the tip-substrate separation, the kinetics of the solution process can be determined with high precision over a wide dynamic range[195-199]. The behaviour of i_T and i_S are governed by the tip to substrate diffusion time, t_d, (Eq. 1.6);

$$t_d = d^2/D \qquad \text{(Eq. 1.5)}$$

The rate of the coupled homogeneous reaction (k_c) may be elucidated by varying the system parameters. When t_d is small compared to the lifetime of the electro-generated species, the majority of electrogenerated species reaches the substrate electrode and is converted back to its original form. However, when $t_d >> 1/k_c$, the tip generated species is consumed by solution reaction and little reaches the substrate. Consequently, i_T and i_S show behaviour, dependent on k_c. The tip and substrate currents approach that for normal positive feedback in the first case, while i_T shows negative feedback and i_S approaches zero for the second case described. The two

cases considered here are clearly extremes; to elucidate k_c for this type of reaction, it must lie somewhere between the two limits described above, at a range of d.

The TG-SC mode requires that d is well-defined and variable. This parameter can be obtained by approaching the tip to contact the substrate, and then withdrawing the two precisely aligned electrodes[174,200], measuring the solution resistance[201], or by use of an internal mediator[202,203] as a calibrant of the tip-substrate separation. The SG-TC mode is an alternative, albeit less used, approach for investigating homogeneous kinetics[148,149,204]. SG-TC has been shown, in conjunction with feedback measurements[205], to be a powerful method for highlighting slight differences in the diffusion coefficients of redox couples[173,205]. The technique can also be used to measure the kinetics of follow-up chemical reactions[174]. Generally, a large substrate electrode with diameter of the order of millimeters[126,148,149,174,] is used, so that alignment of tip and substrate in the x-y plane can be accomplished by eye, negating the need for a high resolution x-y stage.

1.5 Aims

The aims of this work were to explore the applicability of existing UME techniques to investigate a range of heterogeneous electron transfer processes and, where appropriate, the kinetics of coupled chemical reactions(s), for a series of redox-active cobalt and copper based catalysts. Further understanding of these systems was then advanced through the development of SECM methods to study kinetics of processes either in homogeneous solution, or at liquid/solid and liquid/liquid interfaces.

Following an overview in chapter 2, of the experimental methods used, chapter 3 describes the use of steady-state UME voltammetry as a tool for the elucidation of the redox potentials and heterogeneous electron transfer kinetics for several novel [Cu^{I}] examined in dichloroethane (DCE). These studies were extended in chapter 4 via an SECM investigation of the comproportionation reaction between a range of [Cu^{II}] and Cu^{0}, as used in ATP to reduce the proportion of [Cu^{I}] catalyst needed at the outset of an ATP reaction.

Chapter 5 introduces a range of [Co^{II}] CCTAs, and describes investigations of their voltammetric characteristics. Studies of the catalytic reaction of electrogenerated [Co^{I}] with an alkyl bromide were also undertaken. The reactions were examined in a number of solvents: acetonitrile (MeCN), DMF and the polymerisation monomer, methyl methacrylate (mma).

Chapter 6 outlines the development of a model for EC' reactions in an SECM configuration under TG-SC conditions. This new experimental approach was examined through studies of two model systems: $FeCl_3/H_2O_2$ and $K_4Fe(CN)_6$/amidopyrine in aqueous solution. The method was subsequently applied to study the reaction of [$Co(dmgBF_2)_2$] with an alkyl bromide in MeCN. This approach was extended to study the [$Co(dmgBF_2)_2$]/alkyl bromide reaction in a two phase-system of H_2O/DCE. Finally, the overall outcomes of the studies undertaken are highlighted in chapter 7, with suggestions for further work.

Chapter 2 - Experimental

This chapter provides details of the experimental techniques utilised in the studies described herein. UMEs were applied extensively, and so their manufacture and usage is described in some detail. The apparatus and instrumentation for SECM is also described in full, with particular attention given to the feedback and TG-SC modes of operation. In addition to studies performed at solid/liquid interfaces, SECM has been used to study two-phase liquid systems. The slight modifications to the apparatus required for these investigations are outlined. The simple potentiometric methodology used to measure the potentials of various copper metal/copper complex couples and the redox potentials of copper complexes, where the central copper is in oxidation state +I or +II, is also described. Further details on specific experimental procedures are considered in greater detail in each of the subsequent chapters, where appropriate. The final section describes the reagents used and the protocols employed to prepare solutions.

2.1 Microelectrode Studies.

2.1.1 Fabrication of Ultramicroelectrodes.

2.1.1.1 Discs of diameter 10μm and larger.

The general method introduced by Wightman and Wipf[206] and Bard et al[207] for the fabrication of UMEs was followed. A glass capillary (borosilicate glass, 2mm od, 1.16mm id, Clark Electrochemical Instruments, Reading) was pulled to a fine point, by application of heat and suspended weight, by use of a micropipette puller (PB-7 Narishighe Co. Ltd, Japan). The end of the capillary was then sealed in the flame of a Bunsen burner. A length of wire, approximately 10mm (Pt 99.99% purity, 125, 25 or

10μm diameter; Ag 99.99% purity, 125 or 10μm diameter all from Goodfellow, Cambridge), was placed into the open end of the capillary, and the capillary was tapped gently on the laboratory bench until the wire reached the sealed end. The capillary was placed in a purpose-built "sealing" apparatus, shown schematically in Figure 2.1, such that the tapered end of the capillary, containing the wire, was located centrally in a heater coil of annealed nichrome wire (Goodfellow). The open end was connected via a length of plastic tubing to a vacuum pump (RE-2, Vacuubrand GMBH and Co., Germany). After a good vacuum had been achieved (15 minutes) the sealer was used to apply heat to the tapered end of the capillary. The microwire generally sealed in place without air bubbles, which would otherwise prevent a good seal between the glass and the wire.

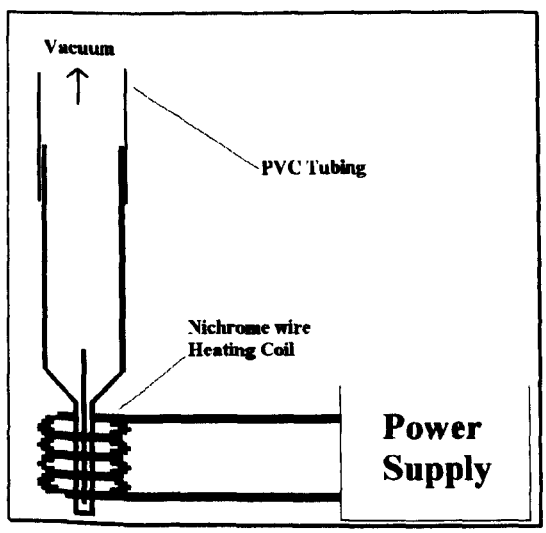

Figure 2.1. The manufacture of an UME.

After sealing, a conducting connection to the microwire was made by melting a slug of solder (60:40 tin:lead alloy, RS Components, Corby) between the microwire and a length of tinned copper wire. The melting was achieved by placing the tip of a hot

(440°C) soldering iron onto the side of the capillary adjacent to the solder slug and pulling the upturned capillary onto the copper wire held vertically in a vice. The open end of the capillary was sealed with Araldite Rapid (Ciba-Geigy, Cambridge).

After exposing the end of the microdisc, and testing for electrical connection, with a resistance meter, the electrode was polished to a smooth finish. Polishing of the end of the electrode began with rough (240 grit, Buehler, Coventry) then progressively finer grades (600 grit, diamond film 30μm, 15μm, 6μm, 1μm, Buehler) of polishing surface (dry paper/cloth respectively). This series was followed by wet alumina micropolish (slurry of 0.05μm alumina in millipore water) on a microcloth polishing pad (both Buehler) yielding a smooth flat surface with an exposed disk of radius *a*. Polishing was achieved manually for the dry paper and wet alumina slurry polishing materials. A polishing wheel (built in-house), that held the electrode at precisely 90° to the polishing surface, was employed for the diamond film polishing surface. The flatness of the disc and its dimensions were assessed by optical microscopy with an Olympus BH2 microscope.

When the UME was to be used to measure voltammetric characteristics, the radius of the glass sheath was relatively unimportant, provided it was sufficiently large that back diffusion to the electrode was prevented. For SECM measurements, a ratio of glass sheath to electrode diameter (RG) of approximately 10 was required, which was achieved by a process termed "coning". This involved removing the excess glass surrounding the electrode with 240, followed by 600 grit polishing paper, by holding the axis of the electrode at an angle of approximately 45^0 to the polishing paper. By rotating the electrode between the thumb and index finger it was possible to achieve a

consistent rate of glass removal. This process was continued and frequently checked by optical microscopy to ensure uniform glass removal until the desired geometry was achieved. A schematic of a typical electrode is shown in Figure 2.2.

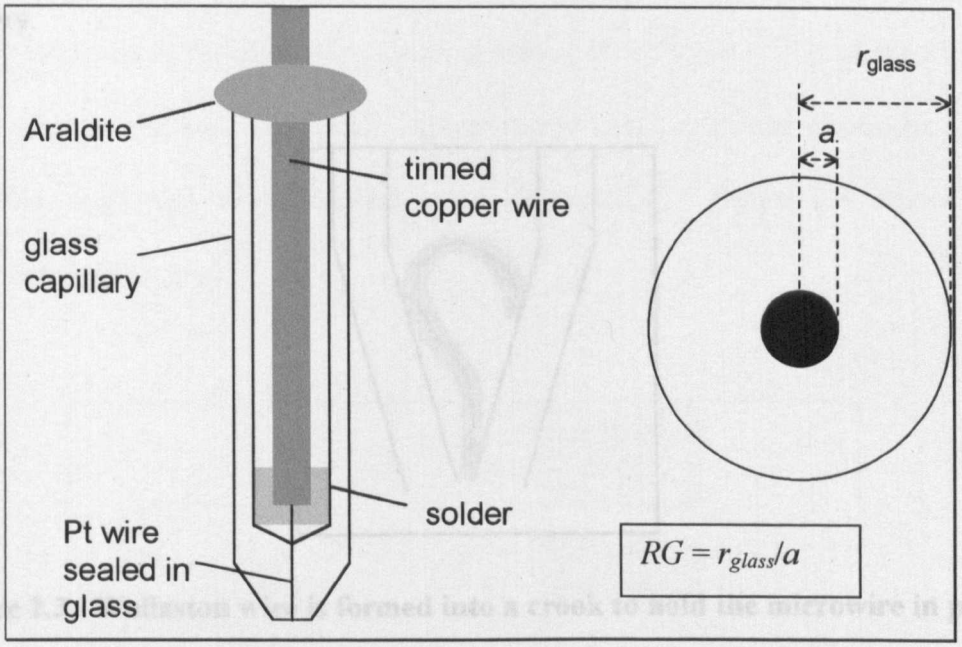

Figure 2.2. Schematic of a glass sealed microdisc electrode.

2.1.1.2 Discs of diameter 5μm and smaller.

A slightly modified method[208] was used to prepare UMEs of smaller diameter, 5μm and less. As wires of this diameter are difficult to manufacture and handle, the material is supplied coated in silver metal to give an overall total diameter of approximately 50μm; this is referred to as Wollaston wire. The capillaries were also prepared in a different manner, in view of the need to remove the outer silver coating during the process of electrode manufacture. After one end of the capillary had been "pulled" to a fine point, the subsequent fine hole was left unsealed i.e. there was no application of flame to seal the end of the capillary into which the microwire would be

placed. An approximately 15mm length of Wollaston wire was fashioned into a crook shape as shown in Figure 2.3 and inserted into the large open end of the capillary. The side of the capillary was gently tapped on a bench until the hook reached the tapered end of the capillary, where it was held in place on the side walls of the capillary.

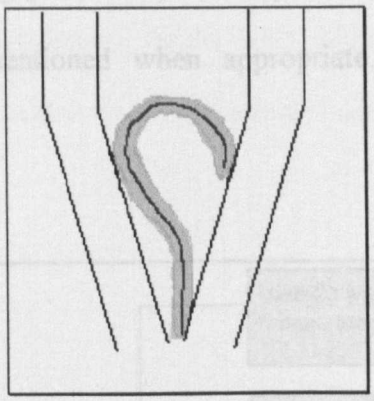

Figure 2.3. Wollaston wire is formed into a crook to hold the microwire in place.

The silver coating was then etched from the wire by placing the tapered, open end of the capillary consecutively into concentrated nitric acid and then water. After etching, the tapered end of the capillary (containing the etched wire) was thoroughly rinsed in water, then acetone by repeatedly dipping the end into the liquid and then draining the liquid onto a tissue. The final procedure was to place the capillary into in an oven to ensure that the capillary and the wire were completely dry. The tapered end of the capillary was sealed in the flame of a Bunsen burner and finished as described previously.

2.1.2 Experimental Setup

The measurement circuit for studies of the voltammetric characteristics of a particular system, consisted of a simple two-electrode configuration with a Pt UME as the working electrode and a silver wire (1mm diameter, 99.99% purity, Goodfellow) as a quasi reference electrode (AgQRE). Occasionally other reference electrodes were used, and these will be mentioned when appropriate. Figure 2.4 shows the experimental set-up used.

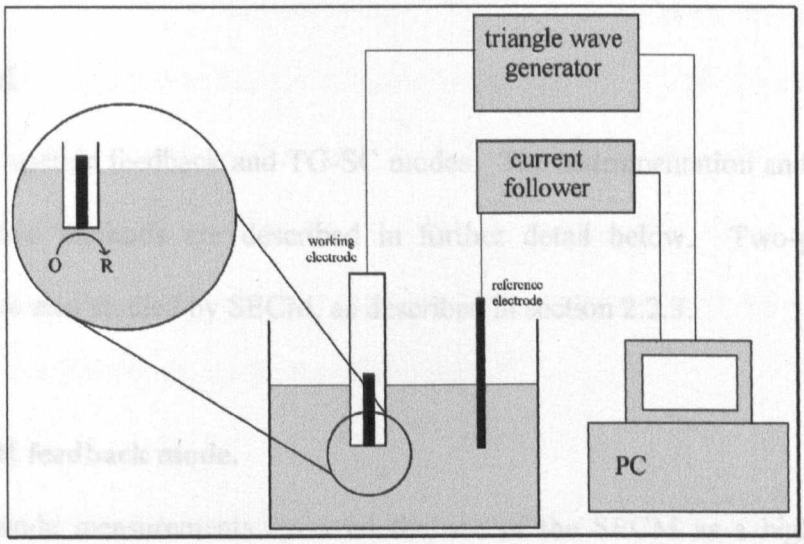

Figure 2.4. The simple set up used to record the voltammetric characteristics of a redox couple.

A potential was applied between the working and reference electrodes, which was swept via a purpose-built triangular wave and pulse generator (Colburn Electronics, Coventry, UK). The resulting current was amplified by a current follower with gains of 10^{-5} to 10^{-9} A V^{-1} (built in-house) before being measured by an IBM compatible PC, equipped with a Lab-PC data acquisition card (National Instruments, Austin,

USA). LSV experiments were performed by sweeping the applied potential between two limits in a linear fashion as shown earlier in Figure 1.15. Data was collected from the card via a Quick Basic programme (written in-house). All apparatus was housed in a Faraday cage (built in-house) to prevent interference. Where an oxygen free atmosphere was required a glove box, modified by addition of copper mesh across the viewing window (built in-house) was used in place of the faraday cage. The box was purged with nitrogen (BOC Chemicals, Poole, UK) before use and the provision of a separate chamber, which could also be purged allowed small items to be added and/or removed as necessary.

2.2 SECM

SECM was used in feedback and TG-SC modes. The instrumentation and procedures for these two methods are described in further detail below. Two-phase liquid systems were also studied by SECM, as described in section 2.2.3.

2.2.1 SECM feedback mode.

Feedback mode measurements involved the use of the SECM as a highly accurate positioning apparatus capable of locating an unbiased substrate UME of the same diameter as the tip. This was the basis for the experiments reported in chapter 4, which were carried out in a six-electrode arrangement. Two circuits allowed the tip current (amperometric circuit) and substrate potential (potentiometric circuit) to be measured simultaneously[209]. The three-electrode amperometric tip circuit utilised a Pt (25 μm) working electrode, an AgQRE reference electrode and a Pt gauze counter electrode. This three-electrode circuit was controlled by a potentiostat (Colburn Electronics). Insertion of a current follower (made in-house) and a 10 kΩ resistor box

(made in-house) in line with the working electrode allowed currents to be measured with gains of 10^{-5} to 10^{-9} A V^{-1} [210]. The three-electrode system used to measure the potential of the substrate electrode was simpler; an instrument amplifier (made in-house) was used to measure the potential difference between the substrate (25 μm Cu UME) and AgQRE, with a counter electrode (Pt gauze) being common.

The position of the UME tip was controlled by mounting on a high accuracy *xy* positioning system, encompassing Heidenhain (model MT25) linear encoders and signal processors, controlled by combined DC micrometer drives and limit switches (model 223.21, PI, Waldbronn, Germany). On the *z* axis, a manual screw gauge was used for general control and a piezoelectric (model E-112.10) controller linked to a piezoelectric element (model P-173.07, both PI) for fine positional control. The above apparatus was controlled via an IBM compatible PC with a Quick Basic programme (written in-house). The instrument and software were developed by Dr. N. J. Evans; further details can be found elsewhere[211].

The electrochemical cell comprised a fully detachable Teflon base (made in-house), a cylindrical glass body (precision bore cylindrical glass, 40mm id, Chance Bros., Malvern) and a Teflon lid (made in-house). The base contained one hole in the centre such that the substrate electrode could be securely accommodated parallel to the face of the tip. The lid contained five holes, one in the centre that allowed the tip to move freely and four surrounding the central hole that held the two reference and two counter electrodes securely in place.

The stages and cell were all mounted on an aluminum holder, raised above a Newport CSD series breadboard by two stainless steel legs (made in-house). The entire assembly was placed inside a Faraday cage (built in-house) and upon a granite-topped vibration isolation table (built in-house). The experimental set up is shown in further detail in Figure 2.5.

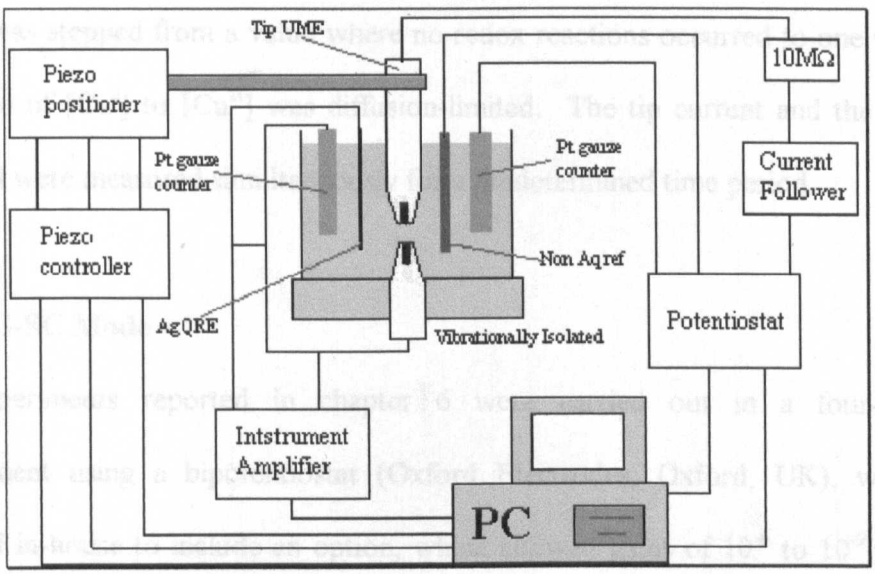

Figure 2.5. SECM set up for feedback measurements, with an unbiased UME as the substrate.

Linear sweep voltammograms were recorded to establish the potential of the redox process (e.g. Cu^{I} to Cu^{II} complex oxidation). This allowed determination of the potential at which the redox process was diffusion-limited, for subsequent SECM measurements. Once the tip had been set to this potential, the tip and the substrate were aligned by eye, so that the tip was positioned over the insulating part of the substrate. The tip electrode was then moved towards the substrate until the diffusion-limited current at the tip dropped to approximately half its bulk solution value, due to hindered diffusion. Subsequently, the tip was scanned in a "line scan" pattern across

the substrate in order to locate the centre of the disc. On passing over the substrate an increase in diffusion-limited current was observed. This increase in current was used to precisely align the centres of the tip and substrate electrodes. Once aligned, an approach curve was used to determine the closest distance that the tip and substrate could be approached to one another before contact was made. A series of single potential step chronoamperometric transients was recorded, whereby the potential at the tip was stepped from a value where no redox reactions occurred to one where the oxidation of $[Cu^{I}]$ to $[Cu^{II}]$ was diffusion-limited. The tip current and the substrate potential were measured simultaneously for a predetermined time period.

2.2.2 TG-SC Mode

The experiments reported in chapter 6 were carried out in a four-electrode arrangement using a bipotentiostat (Oxford Electrodes, Oxford, UK), which was modified in-house to include an option, which allowed gains of 10^{-6} to 10^{-9} A V^{-1}, as well as the conventional 10^{-3} to 10^{-6} A V^{-1} range.

The SECM instrumentation and cells used were as described previously. The cell base contained an additional hole, with a plastic tube sealed in place, to serve as a drain. This allowed the solution in the cell to be changed as needed, without disturbance to the positions of the tip and substrate electrodes.

Ferric chloride (2 mM) solution was prepared immediately prior to each experiment using Milli-Q reagent water (Millipore Corp.), with potassium chloride (0.2 mol dm^{-3}) as supporting electrolyte. The pH of the solution was adjusted to 2 using conc. HCl (Sigma). Hydrogen peroxide (30% w/w, BDH) was added, as required, by a

Finnpipette (200 – 1000 µl, Labsystems, Helsinki, Finland). A stock solution of ferrocyanide (1 mM) with KOH (1 mol dm^{-3}) as supporting electrolyte, was also prepared with Milli-Q reagent water immediately prior to use. Solid amidopyrine was weighed directly into volumetric flasks and made up to the required volume with the ferrocyanide stock solution. A steady stream of nitrogen was bubbled through each solution directly prior to use to remove any dissolved oxygen.

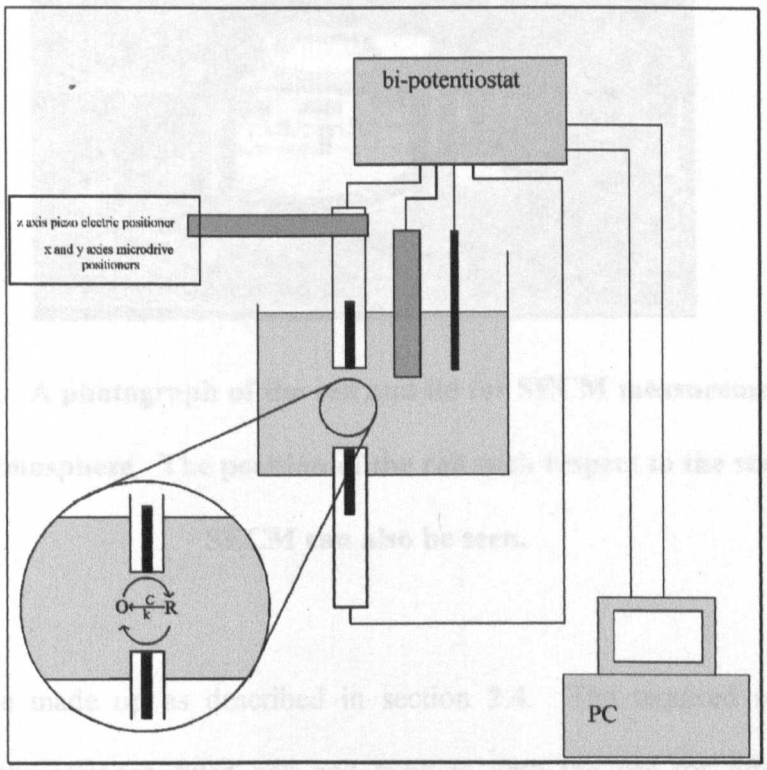

Figure 2.6. Arrangement for TG-SC mode SECM measurements.

For the reasons highlighted in chapter 1, it was important to measure the voltammetric characteristics of [Co] in an oxygen free atmosphere. A dedicated lid was designed to fit the existing cells, which allowed SECM experiments to be carried out in a nitrogen atmosphere, without having to contain the entire set up within a glove box. This lid and the other apparatus is shown in Figure 2.7. The working electrode was sealed in

place by a flexible seal joined to a Teflon collar by an O ring. Two gas inlets and two gas outlets provide a constant N_2 atmosphere. Gas from the latter outlet passed through a Dreschle bottle to ensure that only gas from the inlet entered the cell.

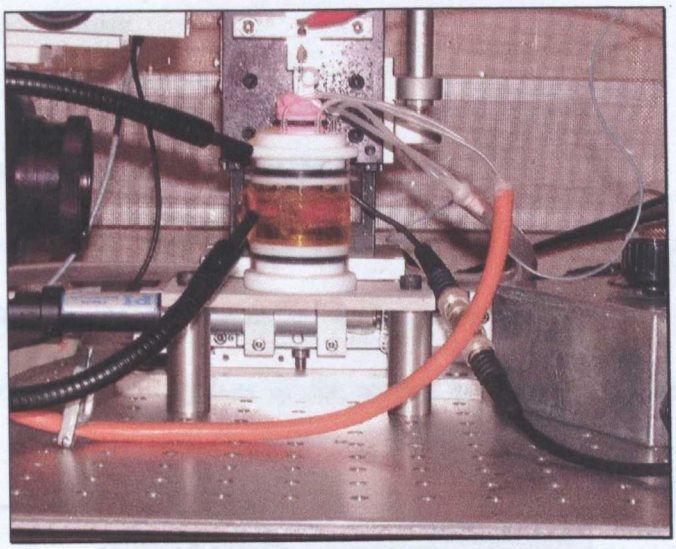

Figure 2.7. A photograph of the cell and lid for SECM measurements in a controlled atmosphere. The position of the cell with respect to the stages of the SECM can also be seen.

Solutions were made up as described in section 2.4. The required solution was injected into the nitrogen filled cell and bubbled with the gas for fifteen minutes before an experiment commenced. This ensured thorough mixing of solution components and removal of any dissolved oxygen.

As described previously for the feedback mode measurements, the imaging capabilities of the SECM instrumentation were used to align the tip with the centre of the substrate. For TG-SC experiments, the substrate UME was 125 μm in diameter and the tip was a 10 μm diameter UME, to ensure optimal collection efficiencies. Au

UMEs were utilised in the study of the Fe/H_2O_2 system, whilst Pt UMEs were utilised to study the Fe/amidopyrine and $[Co^I]$/E2IBB systems. For these measurements, carried out by LSV at set *d*, both the potential dependent current at the tip and the corresponding diffusion-limited collection current at the substrate electrode were monitored simultaneously.

2.2.3 Two-phase (liquid/liquid) SECM

A simple two-electrode system was used to make steady-state and potential step chronoamperometric measurements in bulk solution and close to a liquid/liquid interface[212]. The methodology was similar to that described elsewhere[191,213,214,215,216].

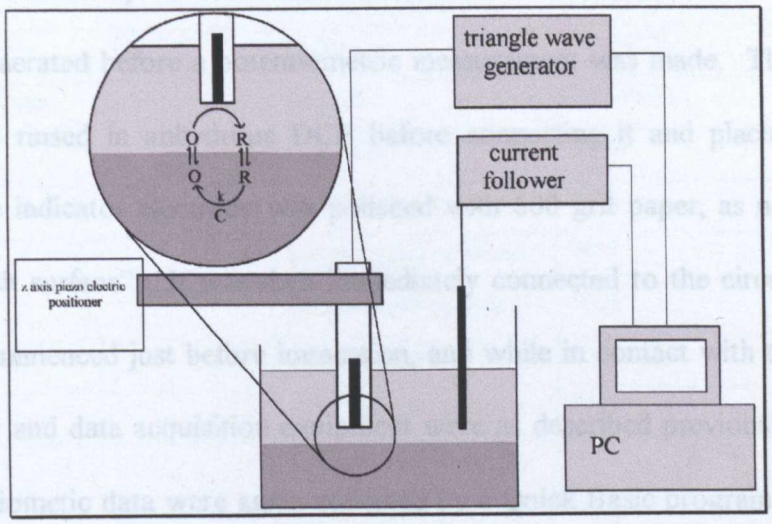

Figure 2.8. Two phase liquid SECM set up.

A Pt UME (25μm diameter) was used as working electrode, whilst the reference was a saturated calomel electrode (SCE). An N_2 atmosphere was provided by using a half size lid containing gas in and out lines and sealing the remaining portion of the cell

with parafilm. By maintaining a gentle, but constant, flow of N_2 over the liquid surface, it was possible to exclude O_2 from the system.

2.3 Potentiometric Measurements

A 20 mm x 10 mm piece of 0.25 mm thick metal (Cu or Pt) foil was soldered to a piece of tinned copper wire, which constituted the indicator electrode for potentiometric measurement, while a Ag/Ag^+ non-aqueous reference electrode (CH Scientific Instruments Inc, Austin, USA) was used as the second electrode. All potentiometric measurements were made in DCE.

Solutions were made up as described in section 2.4. The solution was mixed and thoroughly deaerated before a potentiometric measurement was made. The reference electrode was rinsed in anhydrous DCE before connecting it and placing it in the solution. The indicator electrode was polished with 600 grit paper, as necessary, to ensure a "fresh surface". It was then immediately connected to the circuit and data acquisition commenced just before immersion, and while in contact with the solution. The computer and data acquisition equipment were as described previously in section 2.1.2. Potentiometic data were again collected by a Quick Basic program (written in-house), typically at a rate of 5 points per second and each datum was the result of averaging 100 measurements. The potentials reported are those relating to a steady reading, which was generally attained within half a minute.

2.4 Reagents

Chemical	Source	Grade
Acetonitrile	BDH	HPLC
Dichloroethane	Aldrich	HPLC
Dimethyl formamide	BDH	HPLC
Methyl methacrylate	Aldrich	99%
Basic Alumina	Aldrich	1
Nitrogen	BOC	White Spot
Tetrabutyl ammonium perchlorate	Sigma	99%
Tetraethyl ammonium chloride	Fluka	99%
Tetra-n-hexyl ammonium perchlorate	Alfa	99%
Lithium perchlorate	Aldrich	ACS
Potassium chloride	BDH	AnalR
Hydrochloric acid	Sigma	Conc AnalR
Ferric chloride	Aldrich	ACS
Copper (I) chloride	Fluka	99.999%
Copper (II) chloride	Aldrich	99.999%
$[Co(dmgH_2)_2]$	Avocado	98%
$[Co(dmgBF_2)_2]$	Synthesised in-house	N/A
$[Co(megBF_2)_2]$	Synthesised in-house	N/A
$[Co(degBF_2)_2]$	Synthesised in-house	N/A
Tbutyl ligand	Synthesised in-house	N/A
Octo ligand	Synthesised in-house	N/A
Penta ligand	Synthesised in-house	N/A
Tris ligand	Synthesised in-house	N/A
Bpy ligand	Synthesised in-house	N/A
Nonylbpy ligand	Synthesised in-house	N/A
Tmeda	Fluka	≤98%
Hydrogen peroxide	BDH	30%
Amidopyrine	Sigma	99%
Ferrocyanide	Fischer	Analytical

Table 2.1. Summary of Grades and Sources of all chemicals used.

All syntheses were carried out by Drs A. Hemming (Cu ligands), J. Waterson and R. Harrison (Co complexes) in the polymer group at Warwick University. The procedures employed and analysis of the material are outlined elsewhere[5].

Chapter 3 - Study of the voltammetric characteristics of a range of copper ATP catalysts.

This chapter describes work undertaken to measure the redox properties of a range of copper complexes. The aim was to establish whether there was a link between the redox properties of a particular species and its effectiveness as a catalyst in atom transfer reactions[13]. The family of complexes described herein is used as the catalyst in atom transfer reactions for either organic synthesis or polymerisation. Steady-state voltammetric data were obtained for all of the complexes of interest; values of $E^{0'}$, α and k^o were obtained, from the data, by two methods of data analysis. The Mirkin and Bard method[217] required $E_{3/4}$, $E_{1/2}$ and $E_{1/4}$ to be measured from a single LSV and tables were subsequently used to obtain $E^{0'}$, k^0 and α from these values. The method of Oldham et al[146] required knowledge of $E_{3/4}$, $E_{1/2}$ and $E_{1/4}$ to elucidate α and k^o from kinetic indicator diagrams (kids). A comparison of the merits and drawbacks of the two methods is made, and voltammetric characteristics of the complexes are reported.

3.1 Introduction

The structure and reactivity of a range of ATP catalysts based around a central copper atom has already been described, although the exact mechanism of ATP is yet to be determined. However, it is known[16] that the least efficient [Cu^I] catalysts (in terms of rate of polymerisation[218]) are those that cause the position of the equilibrium shown in Scheme 3.1 to be at either extremity.

$$\text{Pol-X} + M^{n} \rightleftarrows \text{Pol}^{*} + M^{(n+1)}\text{-X}$$

Scheme 3.1. Schematic of ATP.

where Pol-X is a polymer with a terminal halogen, M^n is the metal catalyst in oxidation state n, Pol* is a growing polymer chain.

The motivation for this work was based on the desire to be able to measure the redox properties of the catalysts and correlate these with data previously accumulated for the efficacy of each species as an ATP catalyst.

3.1 Analysis of voltammetric data

UMEs and techniques, such as LSV, that may be used to obtain voltammetric characteristics have already been described. However, chapter 1 only touched briefly on how the results of such experiments may be interpreted. Here, a more thorough explanation is given of the use of steady-state voltammetry to obtain the kinetic and thermodynamic parameters of heterogeneous electron transfer.

A number of methods have been devised for analysing steady-state voltammetric data at an UME to obtain information about the system under study. For heterogeneous electron transfer Butler-Volmer kinetics may be considered:

$$Ox + e^{-} \underset{k_b}{\overset{k_f}{\rightleftharpoons}} Red \qquad \text{(Eq. 3.1)}$$

where Ox is the electroactive species in its oxidised state, e^- is an electron, Red and Ox are the reduced and oxidised forms of the redox couple. The rate constants are:

$$k_f = k^0 \exp\left(\frac{-\alpha nF\left(E - E^{0'}\right)}{RT}\right) \qquad \text{(Eq. 3.2)}$$

and

$$k_b = k^0 \exp\left(\frac{(1-\alpha)nF\left(E - E^{0'}\right)}{RT}\right) \qquad \text{(Eq. 3.3)}$$

In Equs. 3.2 and 3.3, k_f is the rate constant of the forward reaction, k_b is the rate constant for the back reaction, k^0 is the standard rate constant, α is the transfer coefficient, E is potential and $E^{0'}$ is the formal potential of the couple, F is Faraday's constant, R and T have their usual meaning.

The equation that describes the current at any point of a steady-state voltammogram of a fully reversible process is:[219]

$$i = \frac{i_{lim}}{1 + \frac{D_O}{D_R}\exp\frac{nF\left(E - E^{0'}\right)}{RT}} \qquad \text{(Eq. 3.4)}$$

where: i is current, i_{lim} is the steady-state diffusion-limited current, D_o is the diffusion coefficient of the oxidised form of the species, D_R is the diffusion coefficient of the reduced form of the species, and all other symbols have their usual meanings.

It follows that:

$$n\left(E^{0'} - E_{1/2}\right) = \left(\frac{RT}{F}\right)\ln\left(\frac{D_O}{D_R}\right) \qquad \text{(Eq. 3.5)}$$

Tomes[220] related Eq. 3.5 to the difference between the potential at a quarter and three quarters of the wave height, which introduced a way of quantifying the slope of voltammograms and therefore the degree of reversibility of a redox process. For a totally reversible process $E^{0'}$ and $E_{1/2}$ are identical and therefore $n(E_{1/4} - E_{3/4}) =$ 56.5mV at $T = 298$ K. If a system is examined under quasi-reversible conditions, Eq. 3.6, developed by Oldham and Zoski[221], may be applied.

$$i = i_{lim}/\theta\{1 + \pi/\kappa\theta[(2\kappa\theta + 3\pi)/(4\kappa\theta + 3\pi^2)]\}^{-1} \qquad \text{(Eq. 3.6)}$$

where:

$$\theta = 1 + (D_O/D_R)exp[nF(E - E^{0'})/RT] \qquad \text{(Eq. 3.7)}$$

$$\kappa = \kappa^0 exp[-\alpha nF(E - E^{0'})/RT] \qquad \text{(Eq. 3.8)}$$

$$\kappa^0 = (k^0 \pi a/4D_O) \qquad \text{(Eq. 3.9)}$$

Oldham et al[146] developed a method for determining the kinetic parameters, k^0 and α, of a particular reaction, as well as the thermodynamic quantity, $E^{0'}$. Their method

contained a range of protocols to be followed, which depended on the reversibility of the system under study. For quasi-reversible systems, two variations were presented. First, a single-steady state voltammogram could be used to determine α and k^0 if $E^{0'}$ was known. When $E^{0'}$ was unknown, a series of voltammograms at UMEs of various diameters were used to obtain all three parameters. "Kinetic indicator diagrams" were presented, which were built from iterative solving of a series of equations. The method was capable of modification to include situations such as differences in the diffusion coefficients of oxidised and reduced forms of the species. Quite simply if $E^{0'}$ is known, $n(E^{0'} - E_{1/2})$ and $n(E_{1/4} - E_{3/4})$ are measured from a voltammogram and compared to kinetic indicator diagram 1 (kid1), shown in Figure 3.1. The loci, in turn give values for α and log κ^0.

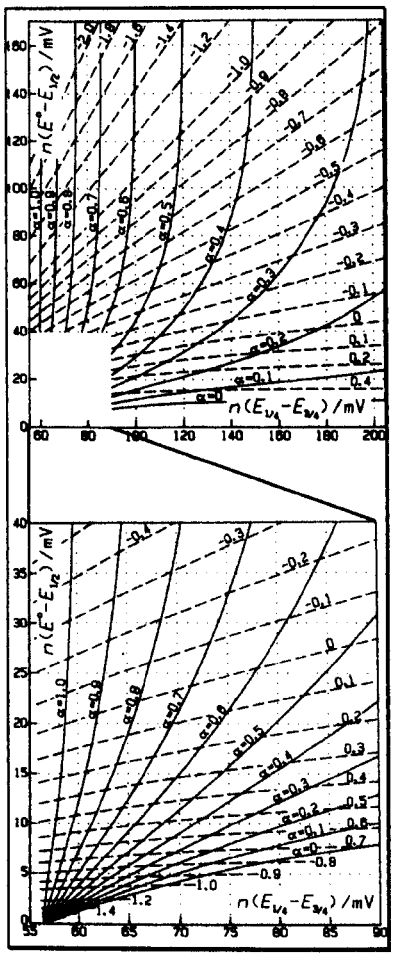

Figure 3.1. Kinetic Indicator Diagram 1[146].

If $E^{0'}$ is unknown, a range of voltammograms must be recorded at UMEs with different radii in order to elucidate the required parameters. Points are located on kinetic indicator diagram 2 (kid2), shown in Figure 3.2, of $n\mathrm{d}E_{1/2}/\mathrm{dlog}(a)$ vs. $n(E_{1/4} - E_{3/4})$.

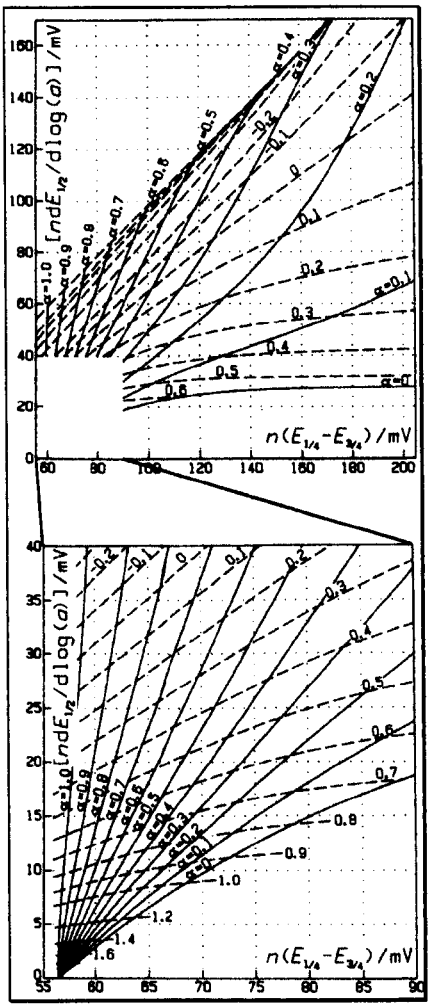

Figure 3.2. Kinetic Indicator Diagram 2[146].

A summary was presented that allowed a systematic analysis, of a series of voltammograms, recorded at a range of different electrodes. Protocols were presented

for five different cases plus totally reversible and totally irreversible (cases O and VI respectively). The relationship of these cases is shown in Figure 3.3.

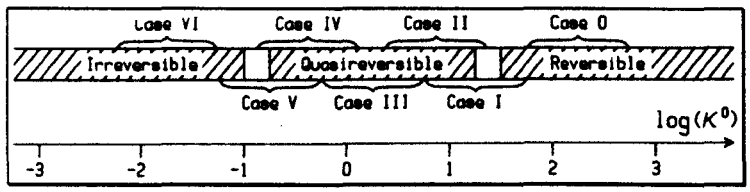

Figure 3.3. The classification of reversibility.

If a system is totally reversible, i.e. $(E_{1/4} - E_{3/4}) = 56.5\text{mV}$ for all electrodes then $E_{1/2} = E^{0'}$ and k^0 exceeds $51D/a_{min}$, where a_{min} is the diameter of the smallest electrode used, while α cannot be determined. Alternatively, for an irreversible system, $E_{1/2}$ shifts to a greater over-potential as the diameter of the electrode is decreased, but $(E_{1/4} - E_{3/4})$ remains constant. In this case $\alpha = 60.2/(E_{1/4} - E_{3/4})$, $E^{0'}$ and k^0 are inaccessible. Between these two limiting cases are the five cases were all three parameters may be determined. These cases were as described as:

I. reversible/near-reversible

II. near-reversible/quasi-reversible

III. quasi-reversible

IV. near-irreversible

V. near-irreversible/irreversible.

Case	Behaviour of ($E_{1/4}$ - $E_{3/4}$)	Protocol used to obtain α, k^0 and $E^{0'}$
I	G = 56.5mV at LE G > 56.5mV at SE	Assume $E_{1/2} = E^{0'}$ at larger electrodes, locate points of α and log κ on kid1. Points should lie along constant α, calculate k^0 for each point.
II and III.1	G > 56.5mV $G \Rightarrow$ 56.5mV at LE	Plot $E_{1/2}$ vs. $1/a$. Intercept = $E^{0'}$, k^0 = (-51.4D/slope), elucidate α from kid1
III.2	As above but previous method is unsuccessful.	Plot $E_{1/2}$ vs. G, $E_{1/2} = E^{0'}$ when G = 56.5mV, slope = $(3^{\alpha-1} - 3^{\alpha+1})^{-1}$, elucidate k^0 from kid1.
IV	G varies with disc size but does not tend to a limit.	Plot $E_{1/2}$ vs. log(a), draw a smooth curve through points and measure slope at each point. Knowing G and d$E_{1/2}$/dlog(a) locate these points on kid2. Elucidate α, and k^0 for each point, transfer points to kid1, to obtain $E^{0'}$.
V	As above but previous method is unsuccessful.	Plot $L^{\dagger}$ vs. G draw best fit straight line through points for SE, α = 60.2/(intercept at L = 0), $nE^{0'} = nE_r$ + 25.7 ln[-(25.7)(slope)/α], elucidate log κ and hence k^0 from kid1.
VI	G is constant at the SE but decreases with increasing disc size.	α = 60.2/[limiting G], locate points on kid1 for LE (knowing α), read off ($E^{0'} - E_{1/2}$) and calculate k^0 in the usual manner.

† Note: L = 0.3654exp{$n(E_{1/4} - E_r)$/25.7} - 3.472exp{$n(E_{3/4} - E_r)$/25.7} and E_r is any constant reference potential in the vicinity of the wave (typically $E_{1/2}$ of one of the voltammograms). $G = (E_{1/4} - E_{3/4})$, LE = largest electrode(s), SE = smallest electrode(s) and $\Rightarrow$ indicates tends to.

Table 3.1. Protocols for determination of α, k^0 and $E^{0'}$.

($E_{1/4}$ - $E_{3/4}$) varies between 56.5mV for electrodes with large diameters for case II and 60.2mV/α for small electrodes in case VI. Between these two limits several protocols are available for use in order to determine α, k^0 and $E^{0'}$. The protocol used depends on the variation of ($E_{1/4}$ - $E_{3/4}$) with electrode diameter as summarised in table 3.1.

Mirkin and Bard[217] also presented a method that may be used to obtain the kinetic parameters, k^0 and α, and the thermodynamic parameter, $E^{0'}$, for simple electron transfer processes, using a single voltammogram. As with the Oldham method, this approach involved the determination of inter-quartile separations, but did not require knowledge of $E^{0'}$. The potential at $3/4i_{lim}$, ($E_{3/4}$), at $1/2i_{lim}$, ($E_{1/2}$), and at $1/4i_{lim}$, ($E_{1/4}$) are determined from a voltammogram. From the potentials at these points the differences $\Delta E_{1/4}$ (= $E_{1/2}$ - $E_{1/4}$) and $\Delta E_{3/4}$ (= $E_{3/4}$ - $E_{1/2}$) are compared to calculated values. Utilisation of extensive tables enables the coefficients α, λ = (ak^o/D) and $n\Delta E^0$ and hence k^o and $E^{0'}$ to be determined[217]. Mirkin and Bard[217] stated "since the above analysis and that by Oldham et al are based on the same approximate equation...they should extract the same values of kinetic parameters from experimental data". This statement is examined later in this chapter.

3.2 Experimental

Full details of the experimental protocols for steady-state UME voltammetry were given in chapter 2. All [Cu] utilised in these studies were formed in situ. A solution of CuCl (0.5 mM) and TEACl (50 mM) was made up with anhydrous DCE, the required amount of ligand (1.25 mM) was added and the contents mixed by shaking.

3.3 Results and Discussion

LSVs of [Cu] were made versus AgQRE, as reference electrode, but to convert to a universal potential scale, voltammograms were also recorded for the ferrocene/ferricinium (Fc/Fc^+) couple under the same conditions, directly prior to each experiment. The two different methods of interpretation of steady-state data described earlier, namely those of Oldham[146] and Mirkin and Bard[217], were applied to the voltammetric data in order to determine $E^{0'}$, k^0 and α. The motivation behind the work described in this chapter was to elucidate $E^{0'}$, k^0 and α, for various [Cu]. As no such measurements had been made previously it was important to use a range of methods of data interpretation to ensure that any facets of the interpretation method did not introduce error into the results. In order to check the validity of each data interpretation method, the Fc/Fc^+ couple was subjected to the same interpretation. To illustrate the basic approach, this system is considered first in the following section.

3.3.1 Oxidation of Ferrocene

LSVs were recorded at Pt microdisc electrodes with four different diameters, 25μm, 10μm, 5μm and 2μm. A typical LSV is shown in Figure 3.4. As the potential applied across the working and reference electrodes is swept between two limits, a current flows which is controlled by the redox processes occurring at the electrode and mass transport.

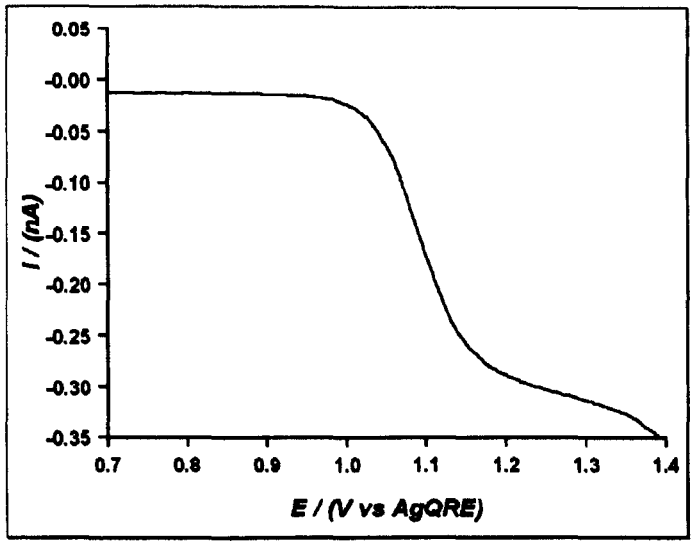

Figure 3.4. The oxidation of Fc (0.5 mM) at a Pt microdisc UME (2μm), with THACl (80 mM) as supporting electrolyte in DCE.

Values of i_{lim}, $E_{1/4}$, $E_{1/2}$, $E_{3/4}$ were measured from a each of a series of voltammograms, by use of a data visualisation program named "visualiser" (written in-house by Dr. M. K. Steliaros). These data are shown in Table 3.2.

$2a$ / (μm)	i_{lim} / (nA)	$E_{1/4}$ / (V vs. AgQRE)	$E_{1/2}$ / (V vs. AgQRE)	$E_{3/4}$ / (V vs. AgQRE)
25	3.38	1.03	1.06	1.08
10	1.28	1.03	1.06	1.09
5	0.53	1.03	1.06	1.10
2	0.23	1.04	1.07	1.11

Table 3.2. Experimental results from the oxidation of Fc to Fc^+.

3.3.1.1 Application of the Mirkin and Bard method.

Data from Table 3.2 were transformed into values of $\Delta E_{1/4}$ (= $E_{1/2} - E_{1/4}$), and $\Delta E_{3/4}$ (= $E_{3/4} - E_{1/2}$) to enable comparison to the tables of Mirkin and Bard. These data are

shown in Table 3.3. Notice that the electrodes with 5μm and 2μm diameter are fabricated from Wollaston wire, and the resulting electrodes are not perfectly circular. This may introduce some error in measuring D from the limiting current.

$2a$ / (μm)	D / (10^{-5} cm^2 s^{-1})	$\Delta E_{1/4}$ / (mV)	$\Delta E_{3/4}$ / (mV)
25	1.4	28.5	29.0
10	1.32	30.0	31.5
5	1.09	32.0	35.0
2	1.18	34.5	40.0

Table 3.3. Data required for interpretation via Mirkin and Bard method.

The Mirkin and Bard tables display various allowable combinations of $\Delta E_{1/4}$ and $\Delta E_{3/4}$, which permit λ, α and $n\Delta E^{0'}$ to be determined and converted to k^0, α and $E^{0'}$, respectively. Two sets of tables are available, which show $\Delta E_{1/4}$ or $\Delta E_{3/4}$ for either uniformly or non-uniformly accessible electrodes. The tables for microelectrodes (non-uniformly accessible) were used. Values of either $\Delta E_{1/4}$ or $\Delta E_{3/4}$ of <30mV or <31mV respectively were considered to indicate a fully reversible process, i.e. one that allows no determination of kinetic parameters. Where values fell between quoted column heading figures, e.g. the table has columns for $\Delta E_{1/4}$ = 41mV and 42mV but the value of $\Delta E_{1/4}$ was actually 41.5mV a linear interpolation was carried out to estimate the value. From the values of $\Delta E_{1/4}$ and $\Delta E_{3/4}$ shown in Table 3.3, the values of α, λ and $n\Delta E^{0'}$ shown in Table 3.4 were obtained.

$2a$/(μm)	α	λ	$N\Delta E^{0'}$/(mV)
25	too close to reversible to analyse		
10	too close to reversible to analyse		
5	0.54	4.1	9.8
2	0.49	2.6	15.1

Table 3.4. Parameters obtained from the tables of Mirkin and Bard.

In turn, the values of λ and $n\Delta E^{0'}$ were converted to $E^{0'}$ and k^0, Table 3.5 summaries the results obtained via this method.

$2a$/(μm)	$E^{0'}$/(V vs. AgQRE)	α	k^0/(cm s^{-1})
25	1.06	too close to reversible	
10	1.06	too close to reversible	
5	1.05	0.54	0.18
2	1.06	0.49	0.31

Table 3.5. Thermodynamic and kinetic parameters obtained for the oxidation of Fc at Pt microdisc electrodes in DCE.

3.3.1.2 Oldham method of analysis.

One can elucidate values for α, k^o and $E^{0'}$ based on ($E_{1/4}$ - $E_{3/4}$) and the change in half-wave potential with change in electrode diameter, using kids of the type shown earlier in this chapter. Where data includes voltammograms recorded at a range of electrode sizes, a full analysis may be performed (i.e. no assumption as to the position of $E^{0'}$ is needed). The analysis assumes that $D_O = D_R$, although arbitrary diffusion coefficients for the oxidised or reduced forms of the redox couple may be considered, when necessary. At the microelectrode level, most electron transfer systems may be

described as quasi-reversible, as total reversibility and irreversibility are only limits, "in practice, however, the useful range of quasi-reversibility embraces only about two orders of magnitude"[146]. Table 3.6 is taken from ref 146 and shows the range of radii of electrode that may be used to access particular rate constants.

k^o /(m s^{-1})	a /(μm)
10^{-1}	0.0025 - 0.25
10^{-2}	0.025 - 2.5
10^{-3}	0.25 – 25
10^{-4}	2.5 – 250
10^{-5}	25 – 2500

Table 3.6. Radii of microdisc required to measure particular rate constants[146]. Assuming $D = 1 \times 10^{-5}$ cm^2 s^{-1}

Experimental values may be placed directly onto specific points on kid1, which enables α and k^o to be determined. However, $E^{o'}$ is not always known (as in the cases of interest in this chapter) and thus kid1 cannot be utilised immediately. As discussed earlier, an alternative method is based on the change in $E_{1/2}$ with electrode radius, in which values of $ndE_{1/2}/d(\log a)$ are plotted against $n(E_{1/4} - E_{3/4})$, referred to as kid2. Where $E^{o'}$ is unknown, further analysis must be implemented (Table 3.1). Two methods were available to analyse data that fell within case III of Table 3.1 and were first applied to the Fc/Fc^+ data as a trial system.

3.3.1.2.1 Application of method III.1

Method III.1 involved plotting $E_{1/2}$ vs. $1/a$. The slope of the resultant line was equal to $(-51.4D/k^o)$ and hence was used to deduce k^o. Such a plot is shown in Figure 3.5.

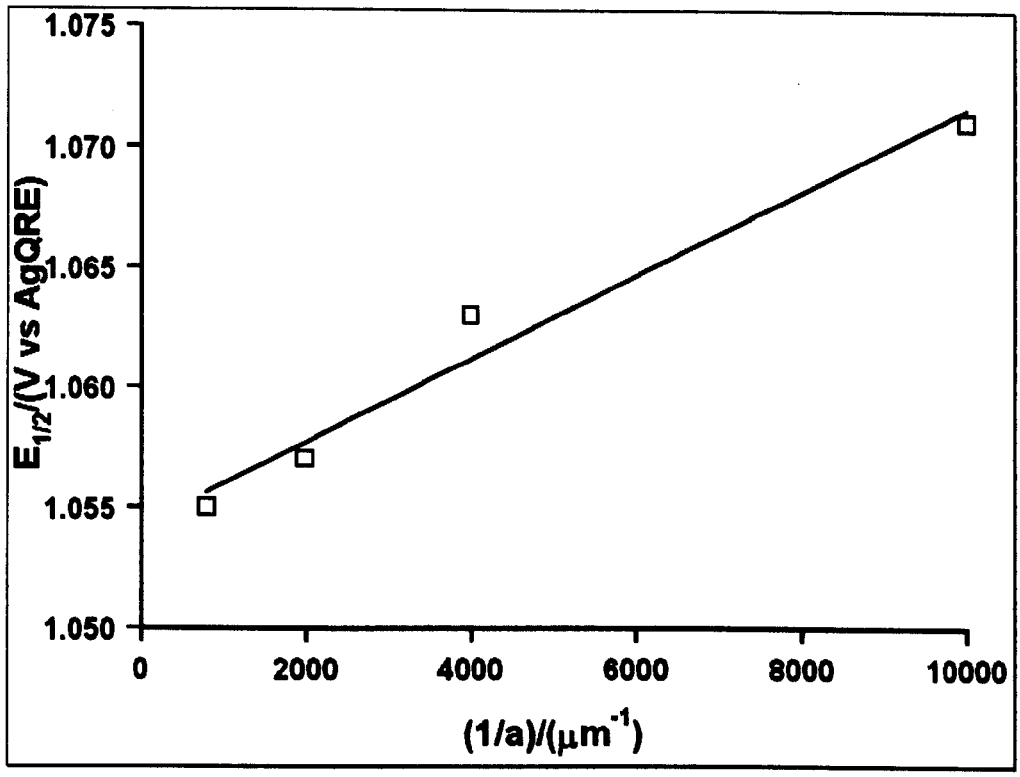

Figure 3.5. A plot of $E_{1/2}$ vs. $1/a$ for the oxidation of Fc (0.5 mM) in DCE with THACl (50 mM) present as supporting electrolyte.

$E^{0'}$ is the intercept of Figure 3.5. This method gave direct access to $E^{0'}$ and k^0 but reference was made to kid1 to elucidate α. Values of $(E^{0'} - E_{1/2})$ and $(E_{1/4} - E_{3/4})$ for each of the four electrodes were calculated and used to find points on kid1, which were positioned along a contour of constant α. Figure 3.6 shows how kid1 was used to yield a value for α, while Table 3.7 summarises the results obtained from this analysis protocol.

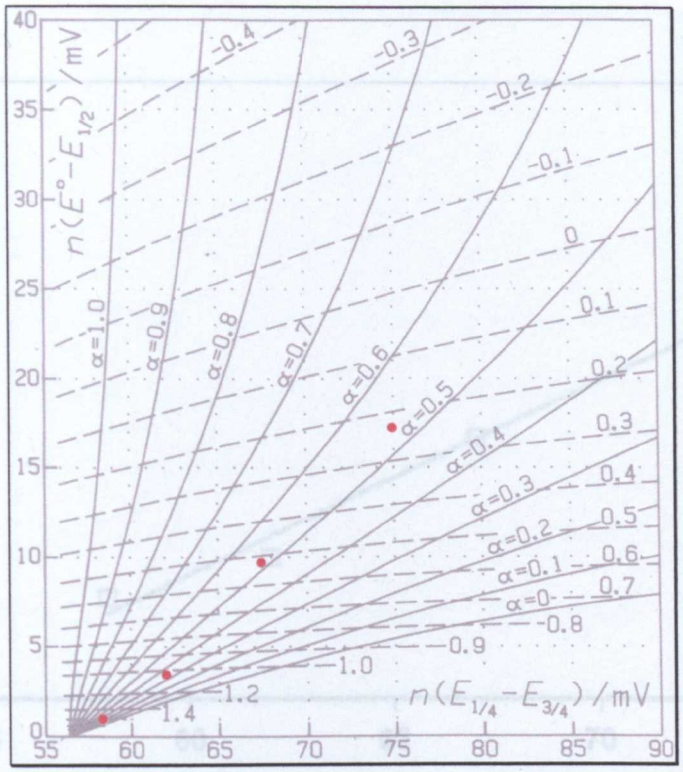

Figure 3.6. Results from analysis III.1 superimposed onto kid1.

Equation of plot of $E_{1/2}$ vs. $1/a$	y =1.733 x 10^{-6} +1.054
$E^{o'}$/(V vs. AgQRE)	1.05
α	0.5
k^0/(cm s^{-1})	0.4

Table 3.7. Results of analysis of data for the oxidation of Fc using method III.1.

3.3.1.2.2 Application of method III.2

By way of a further test of this method, the data were analysed via the second of the case III routes. Method III.2 utilised a plot of $E_{1/2}$ vs. ($E_{1/4}$ - $E_{3/4}$). The slope of the resultant line was equal to $[(3^{\alpha-1} - 3^{\alpha+1})^{-1}]$ and hence was used to deduce α. $E^{o'}$ was found from the intercept at ($E_{1/4}$ - $E_{3/4}$) = 56.5mV. Figure 3.7 shows a plot of $E_{1/2}$ vs. ($E_{1/4}$ - $E_{3/4}$) for the oxidation of Fc.

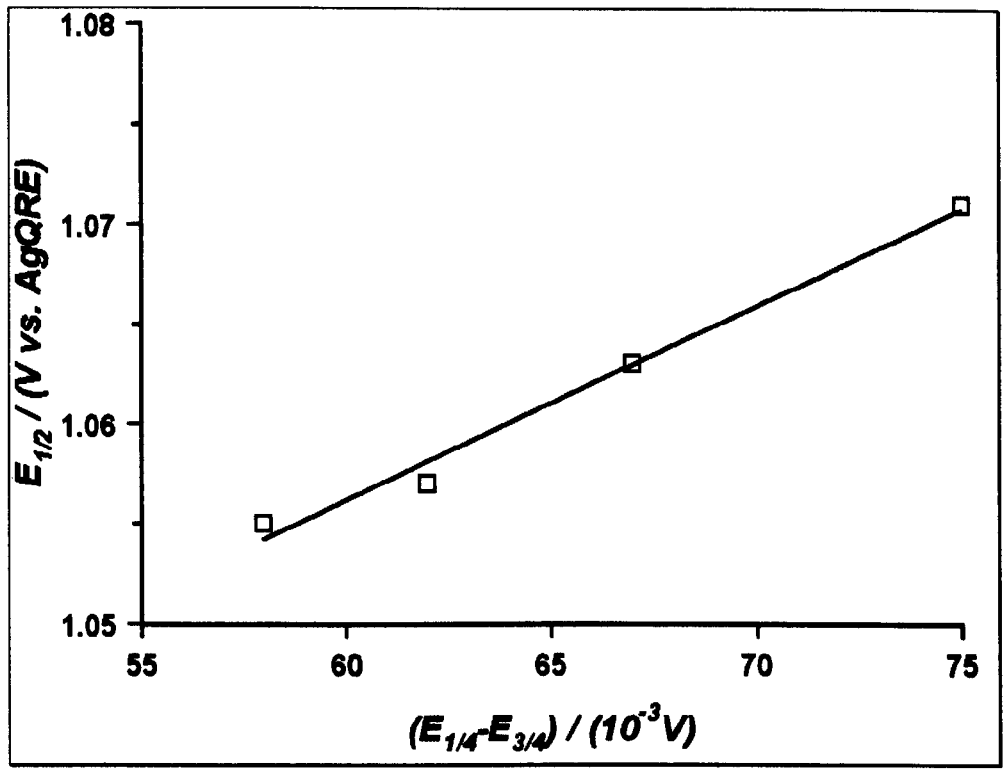

Figure 3.7. A plot of $E_{1/2}$ vs. $(E_{1/4} - E_{3/4})$ for the oxidation of Fc (0.5 mM) in DCE with THACl (50 mM) present as supporting electrolyte.

This method gives direct access to $E^{0'}$ and α, but reference must be made to kid1 to elucidate k^0. Values of $(E^{0'} - E_{1/2})$ and $(E_{1/4} - E_{3/4})$ were then used to find points on kid1, which indicated the value of k^0. Figure 3.8 demonstrates how kid1 was used to elucidate k^0. Table 3.8 is a summary of the results obtained from this analysis protocol.

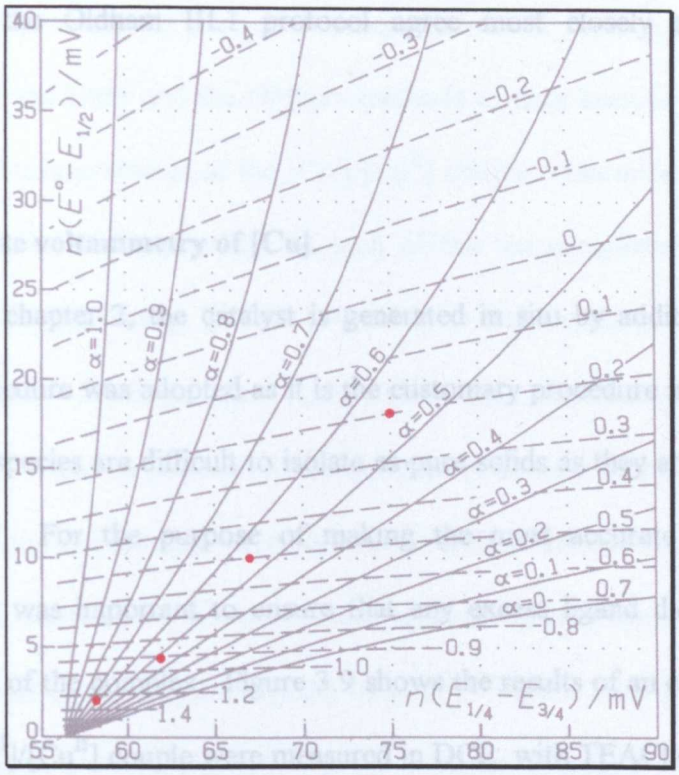

Figure 3.8. Results from analysis III.2 superimposed onto kid1.

Equation of line of plot of $E_{1/2}$ vs. ($E_{1/4}$ - $E_{3/4}$)	y = 0.9752x + 997.63
$E^{0'}$/(V vs. AgQRE)	1.05
α	0.55
k^0/(cm s^{-1})	0.3

Table 3.8. Results of analysis of method III.2 (data from Figure 3.8).

The above analysis shows that all three interpretation protocols are consistent to a good degree. $E^{0'}$ is the most consistently reported value, which is not surprising because the voltammograms are close to reversible. The greatest variation is found within the deduced values of k^0, which again is expected because the kinetics of the process are fast and comparable to the rate of mass transfer. The method of Mirkin

and Bard and the Oldham III.1 protocol agree most closely across all three parameters.

3.3.2 Steady-state voltammetry of [Cu].

As described in chapter 2, the catalyst is generated in situ by addition of ligand to CuCl. This procedure was adopted as it is the customary procedure in ATP reactions. Generally these species are difficult to isolate as pure solids as they are sensitive to air and moisture[222]. For the purpose of making the most accurate electrochemical measurements it was important to ensure that any excess ligand did not inhibit the electrochemistry of the complex. Figure 3.9 shows the results of an experiment where LSVs of the $[Cu^{I}]/[Cu^{II}]$ couple were measured in DCE, with TEACl (50 mM) present as supporting electrolyte, at a Pt UME (a = 12.5 μm) with various concentrations of ligand 1. Clearly, as an increasing amount of ligand was added the $E_{1/2}$ of the wave shifted to a smaller over-potential before attaining a limit. After this plateau a further decrease in over-potential was observed.

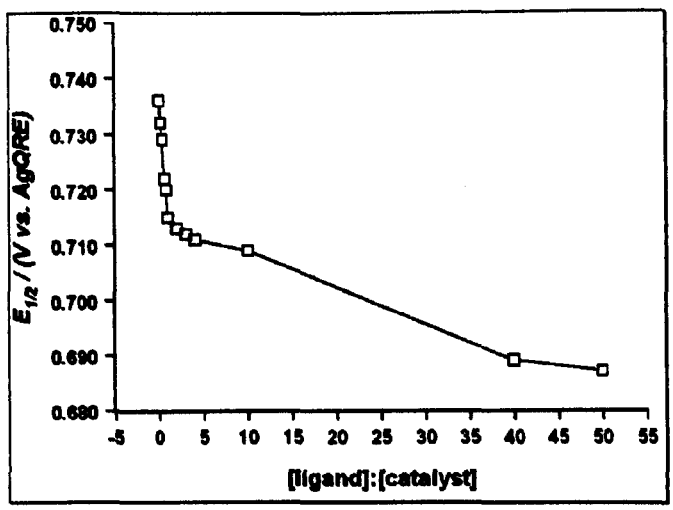

Figure 3.9. The variation of $E_{1/2}$ with change in [ligand 1]:$[Cu^{I}]$. $[Cu^{I}]$ = 0.5 mM.

All ligands were subsequently used at a concentration 2.5 times greater than CuCl. Both the Mirkin and Bard and the Oldham methods of data analysis were applied to the voltammetric measurements of the $[Cu^{I}]/[Cu^{II}]$ couple. Ten different ligands were used; the voltammetric characteristic of each of the ten complexes plus CuCl was measured in DCE (containing TEACl [50 mM] as supporting electrolyte), at two different UMEs ($2a$ = 25μm and $2a$ = 2μm). These data were analysed by the Mirkin and Bard method. Later, a sub-set of four different [Cu] were investigated at a larger range of UME sizes and the data interpreted according to the methods of Oldham and Mirkin and Bard. Each of the waves recorded showed a quasi-reversible, one electron oxidation representing the transition $[Cu^{I}] \rightarrow [Cu^{II}]$. Figure 3.10 shows an example LSV for the oxidation of $[Cu^{I}]$ to $[Cu^{II}]$ in the presence of ligand 1. The complex is referred to herein as [1_Cu].

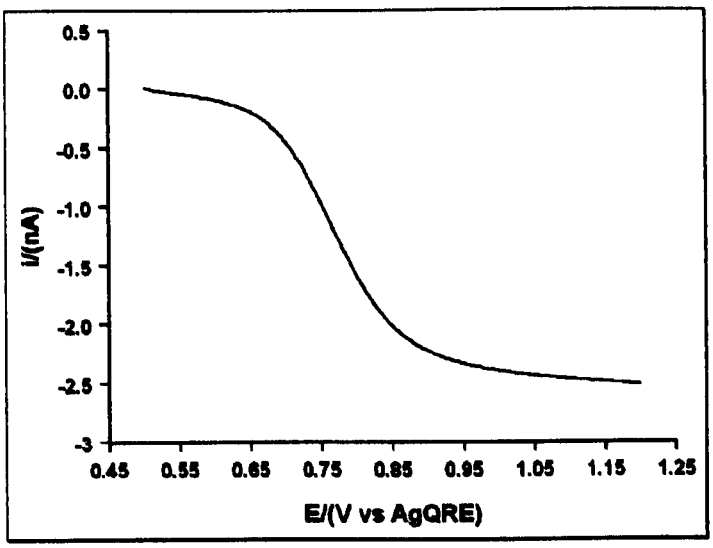

Figure 3.10. Oxidation of [1_Cu]; CuCl (0.5 mM) in the presence of ligand 1 (1.25 mM) at a 25μm diameter Pt microdisc electrode in a solution of THACl (50 mM) in DCE.

3.3.2.1 Preliminary studies of a range of [Cu].

The aim of recording LSVs for the eleven complexes was to measure $E^{0'}$, k^0 and α for a range of [Cu]. Given the large volume of data, LSVs were analysed by the Mirkin and Bard method in the first instance. The experimental data obtained are shown for each electrode size, a = 12.5μm and a =1μm, in Table 3.9 and Table 3.10 respectively. All potentials are reported with respect to the Fc/Fc^+ couple, to avoid any discrepancies that might have arisen from day to day drift in the AgQRE. The method of Mirkin and Bard that was previously described for the analysis of data for the Fc/Fc^+ couple was followed. Specifically, values of i_{lim}, $E_{1/4}$, $E_{1/2}$ and $E_{3/4}$ were measured for each voltammogram, as shown in Table 3.9 and Table 3.10.

The experimental data, extricated from voltammograms, calculated values needed for analysis and resultant kinetic and thermodynamic parameter derived from the analysis are given in three separate tables, for each electrode size (6 tables in total). The first pair of tables (Table 3.9 and Table 3.10) give data for i_{lim}, $E_{1/4}$, $E_{1/2}$ and $E_{3/4}$ as measured directly from the voltammograms, the second tables (Table 3.11 and Table 3.12) begin the analysis by showing the calculation of D, $\Delta E_{1/4}$ and $\Delta E_{3/4}$. The values of $\Delta E_{1/4}$ and $\Delta E_{3/4}$ are quoted to the nearest 0.5mV, which was considered to be a reasonable measure of the accuracy of the experiment. Finally, the third pair of tables (Table 3.13 and Table 3.14) show the parameters α, λ and $n\Delta E^{0'}$ and hence the subsequent calculation of the required kinetic and thermodynamic parameters, α, k^0 and $E^{0'}$.

Ligand	i_{lim} /(nA)	$E_{1/4}$/(V vs. Fc/Fc$^+$)	$E_{1/2}$/(V vs. Fc/Fc$^+$)	$E_{3/4}$/(V vs. Fc/Fc$^+$)
None	1.805	-0.338	-0.298	-0.253
1	2.011	-0.351	-0.310	-0.264
2	1.896	-0.354	-0.313	-0.268
3	1.799	-0.366	-0.325	-0.280
4	1.563	-0.381	-0.336	-0.287
5	1.890	-0.344	-0.299	-0.249
6	1.903	-0.345	-0.302	-0.253
7	1.901	-0.342	-0.299	-0.254
8	1.916	-0.299	-0.251	-0.196
9	1.953	-0.355	-0.312	-0.266
10	1.954	-0.324	-0.278	-0.227

Table 3.9. Voltammetric data recorded at a 25μm diameter Pt UME.

Ligand	i_{lim} /(nA)	$E_{1/4}$/(V vs. Fc/Fc$^+$)	$E_{1/2}$/(V vs. Fc/Fc$^+$)	$E_{3/4}$/(V vs. Fc/Fc$^+$)
None	0.148	-0.245	-0.189	-0.124
1	0.154	-0.209	-0.143	-0.060
2	0.151	-0.268	-0.218	-0.159
3	0.114	-0.296	-0.245	-0.180
4	0.134	-0.302	-0.250	-0.184
5	0.150	-0.268	-0.212	-0.146
6	0.150	-0.253	-0.195	-0.131
7	0.138	-0.270	-0.214	-0.147
8	0.150	-0.235	-0.173	-0.101
9	0.151	-0.249	-0.197	-0.132
10	0.153	-0.258	-0.206	-0.143

Table 3.10. Voltammetric data recorded at a 2μm diameter UME.

Ligand	$D/(10^{-5}cm^2\ s^{-1})$	$\Delta E_{1/4}/(mV)$	$\Delta E_{3/4}/(mV)$
None	0.74	40.0	44.5
1	0.83	41.5	45.5
2	0.77	41.0	45.5
3	0.73	41.0	44.0
4	0.65	45.5	49.5
5	0.77	45.5	49.5
6	0.80	43.5	48.5
7	0.77	42.0	46.0
8	0.78	48.0	55.0
9	0.81	43.0	46.5
10	0.79	46.5	50.5

Table 3.11. Values of D, $\Delta E_{1/4}$ and $\Delta E_{3/4}$ calculated from the data in Table 3.9 (25 μm diameter Pt UME).

Ligand	$D/(10^{-5}cm^2\ s^{-1})$	$\Delta E_{1/4}/(mV)$	$\Delta E_{3/4}/(mV)$
None	0.74	56.5	65.0
1	0.80	66.0	82.5
2	0.77	50.5	59.0
3	0.66	50.5	64.5
4	0.69	52.0	65.5
5	0.76	56.5	65.5
6	0.76	58.0	64.5
7	0.72	56.0	67.0
8	0.76	61.5	72.5
9	0.78	52.0	64.5
10	0.78	52.0	63.0

Table 3.12. Values of D, $\Delta E_{1/4}$ and $\Delta E_{3/4}$ calculated from the data in Table 3.10 (2 μm diameter Pt UME).

Ligand	α	λ	$n\Delta E^{0'}/(mV)$	$k^0/(10^{-3}$ cm $s^{-1})$	$E^{0'}$/(V vs. Fc/Fc^+)
None	0.62	0.68	40.4	4.0	-0.239
1	0.63	0.48	52.0	3.2	-0.362
2	0.62	0.59	44.6	3.6	-0.358
3	0.67	0.31	60.9	1.8	-0.387
4	0.60	0.31	69.3	1.6	-0.405
5	0.60	0.31	69.4	1.9	-0.367
6	0.59	0.51	51.7	3.2	-0.354
7	0.62	0.45	52.3	2.8	-0.352
8	0.52	0.50	56.1	3.1	-0.307
9	0.64	0.32	64.2	2.1	-0.376
10	0.59	0.29	73.4	1.8	-0.351

Table 3.13. Kinetic and thermodynamic parameters for the oxidation of various $[Cu^I]$ (0.5 mM) in THACl (50 mM)/DCE at a 25 μm diameter Pt microdisc UME.

Ligand	α	λ	$n\Delta E^{0'}/(mV)$	$k^0/(10^{-3}$cm $s^{-1})$	$E^{0'}$/(V vs. Fc/Fc^+)
None	0.45	0.41	73.0	30	-0.262
1	0.36	0.51	75.7	41	-0.218
2	0.49	0.52	58.2	40	-0.276
3	0.42	0.75	48.3	50	-0.293
4	0.43	0.68	52.1	47	-0.302
5	0.45	0.43	71.4	32	-0.282
6	0.47	0.31	85.5	23	-0.278
7	0.43	0.50	65.1	36	-0.279
8	0.41	0.43	76.8	32	-0.250
9	0.44	0.64	53.6	50	-0.250
10	0.45	0.59	56.0	36	-0.262

Table 3.14. Kinetic and thermodynamic parameters for the oxidation of various $[Cu^I]$ (0.5 mM) in THACl (50 mM)/DCE at 2μm diameter Pt microdisc UME.

Obviously there is some discrepancy between the two sets of data, within the kinetic and the thermodynamic parameters derived. Specifically, α was found to be larger, k^0 to be smaller and $E^{0'}$ to occur at a smaller over-potential for the 25 μm diameter electrode. A possible drawback of the Mirkin and Bard method is that small errors in the measurement of $\Delta E_{1/4}$ and $\Delta E_{3/4}$ may produce large errors in the extracted values of $E^{0'}$, k^0 and α. These experimental errors may be significant particularly if the initial and final plateaux currents, associated with each LSV, deviate from the ideal of zero gradient.

Figure 3.11 shows voltammograms, recorded at a range of sizes of UME. As each voltammogram has been normalised it is clear that as a decreased the voltammetric wave becomes irreversible for the smallest electrodes. The diffusion-limited current plateau is not ideal, which makes the determination of i_{lim} less precise.

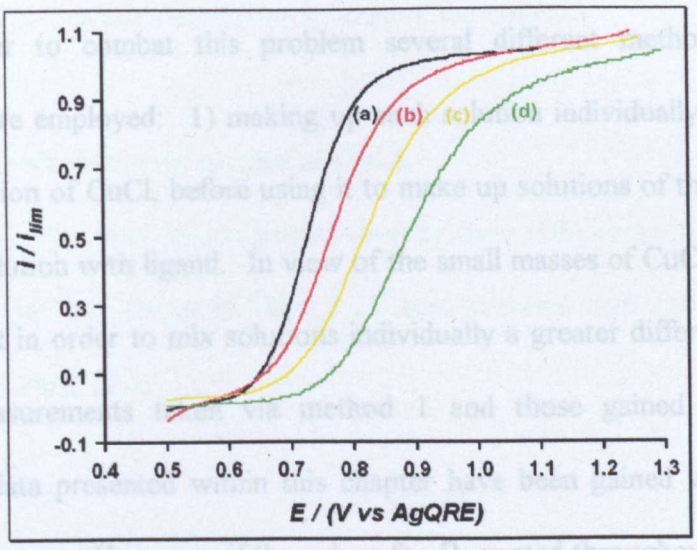

Figure 3.11. Voltammetric data for the oxidation of [1_Cu^I], in a solution of DCE with TEACl (50 mM) present as supporting electrolyte. Data recorded at Pt UMEs of diameter (a) 25 μm, (b) 10 μm, (c) 5 μm and (d) 2 μm.

Where values of $\Delta E_{1/4}$ and $\Delta E_{3/4}$ were close, whilst still allowing analysis, the values of α, λ and $nE^{0'}$ obtained from the tables were quite different for those where the value of $\Delta E_{1/4}$ was mid-way in the range of possible values for a specific value of $\Delta E_{3/4}$. For example, the tables in ref 217 indicate that when $\Delta E_{3/4}$ = 58 mV and $\Delta E_{1/4}$ = 53 mV, then α = 0.52, λ = 0.27 and $n\Delta E^{0'}$ = 97.9 mV. However, if $\Delta E_{1/4}$ = 55 mV then, α = 0.53, λ = 0.09 and $n\Delta E^{0'}$ = 135.0 mV. Thus it is clear that small errors in the measured values of $\Delta E_{1/4}$ and $\Delta E_{3/4}$, when they are of similar magnitude may produce large errors in the extracted values of $E^{0'}$ and k^0, although, α remains largely unaffected. As much of the data reported herein has values in this regime, this could be a major source of error. The data shown for the experimental parameters $E_{1/4}$, $E_{1/2}$ and $E_{3/4}$ were taken from a single series of voltammograms, recorded in quick succession. Whilst, these studies were being carried out, it was noticed that the day-to-day reproducibility of not only potentials, but also i_{lim} (and subsequently D) was poor. In order to combat this problem several different methods of solution manufacture were employed: 1) making up each solution individually and 2) making up a stock solution of CuCl, before using it to make up solutions of the complexes by mixing stock solution with ligand. In view of the small masses of CuCl that needed to be weighted out in order to mix solutions individually a greater difference was found within the measurements taken via method 1 and those gained via method 2. Therefore, all data presented within this chapter have been gained via method 2 of solution manufacture. However, if the values for D, quoted throughout this chapter in are examined in detail, it will be noted that those for CuCl are smaller than might be expected, additionally, they are smaller than observed for some complexes. This is particularly unusual, especially if the relative sizes of the two molecules are taken into

account. It is likely that in fact D_{CuCl} is larger than measured, due to a lack of solubility of CuCl in DCE, the concentration of CuCl may be much lower than calculated. Therefore, when ligand is added to the solution, the process of complexation, increases the solubility of the species of interest and hence increases the apparent value of D. Therefore, by making solutions via a stock solution method, it is likely that the concentration of each species is actually lower than calculated, especially for solutions of CuCl alone.

Given the large variation in the kinetic and thermodynamic parameters between the two UME sizes (Table 3.13 and Table 3.14) for each Cu complex, a more thorough investigation was undertaken with UMEs of four different diameters. Each complex was subjected to examination by 25μm, 10μm, 5μm and 2μm diameter Pt UMEs, and the results are discussed in the following sections. The results displayed are for a single set of experiments, however, within each section an indication is given of D and associated error, as calculated from a range of experiments.

3.3.2.2 Further voltammetric studies of CuCl.

The values of i_{lim}, $E_{1/4}$, and $E_{3/4}$ measured directly from voltammetric data are shown in Table 3.15. The data shown in Table 3.15 were analysed with Table 3.16 showing values of D, $\Delta E_{1/4}$ and $\Delta E_{3/4}$.

a/(μm)	i_{lim} /(nA)	$E_{1/4}$/(V vs. Fc/Fc^+)	$E_{1/2}$/(V vs. Fc/Fc^+)	$E_{3/4}$/(V vs. Fc/Fc^+)
12.5	1.82	-0.343	-0.299	-0.249
5.0	0.78	-0.317	-0.267	-0.209
2.5	0.46	-0.292	-0.240	-0.179
1.0	0.14	-0.255	-0.196	-0.122

Table 3.15. Voltammetric data for the oxidation of CuCl (0.5 mM) in DCE, containing THACl (50 mM) as supporting electrolyte.

a/(μm)	D^*/(10^{-5} cm^2 s^{-1})	$\Delta E_{1/4}$/(mV)	$\Delta E_{3/4}$/(mV)	$E_{1/4} - E_{3/4}$/(mV)
12.5	0.75	43.5	50.0	93.5
5.0	0.80	50.5	57.0	107.5
2.5	0.95	51.0	61.0	112.0
1.0	0.73	59.0	74.0	133.0

Table 3.16. Interquartile separations required for voltammetric analysis.

a /(μm)	α	λ	$n\Delta E^{0'}$/(mV)	k^0/(10^{-3}cm s^{-1})	$E^{0'}$/(V vs. Fc/Fc^+)
12.5	0.55	0.67	44.25	4.0	-0.343
5.0	0.52	0.41	56.60	6.6	-0.332
2.5	0.46	0.57	55.60	22	-0.296
1.0	0.39	0.56	64.60	41	-0.261

Table 3.17. Application of the method of Mirkin and Bard to yield values of the required thermodynamic and kinetic parameters.

---

* The value of D was found to be 0.81 ± 0.12 from 9 measurements, according to solution preparation method 2.

This further experimental evidence confirmed the preliminary findings in that there were systematic variations in the values of $E^{0'}$, k^0 and α with electrode size.

The data were also analysed with the Oldham method. From Table 3.16 it can be seen that the values of ($E_{1/4}$ – $E_{3/4}$) are sizable, approaching the irreversible limit. The Oldham method provides a number of protocols, the choice depending on the likely kinetic regime of the experimental data. The data were examined with reference to the criteria in Table 3.1, for which case III seemed most appropriate, in that ($E_{1/4}$ – $E_{3/4}$) increased with decrease in electrode diameter. ($E_{1/4}$ – $E_{3/4}$) for the largest electrode (a = 12.5μm) is somewhat larger than 56.5mV, however, the trend is as described in Table 3.1 and ($E_{1/4}$ – $E_{3/4}$) would be expected to attain the reversible value at a sufficiently large electrode. The data was analysed via protocol III.1, which involved plotting $E_{1/2}$ vs. $1/a$ as shown in Figure 3.12. If this protocol were appropriate, the plot shown in Figure 3.12 would yield a straight line, allowing analysis of $E^{0'}$ from the intercept of the y axis and k^0 from the slope. As the plot was curved, it was evident that this protocol was not applicable to this system as it was too irreversible.

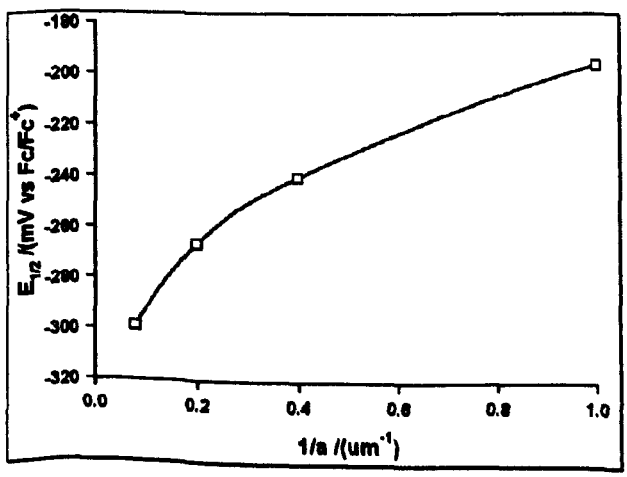

Figure 3.12. A plot of $E_{1/2}$ vs. $1/a$ for the oxidation of CuCl.

Application of protocol III.2, yielded a plot of $E_{1/2}$ vs. $(E_{1/4} - E_{3/4})$, as shown in Figure 3.13.

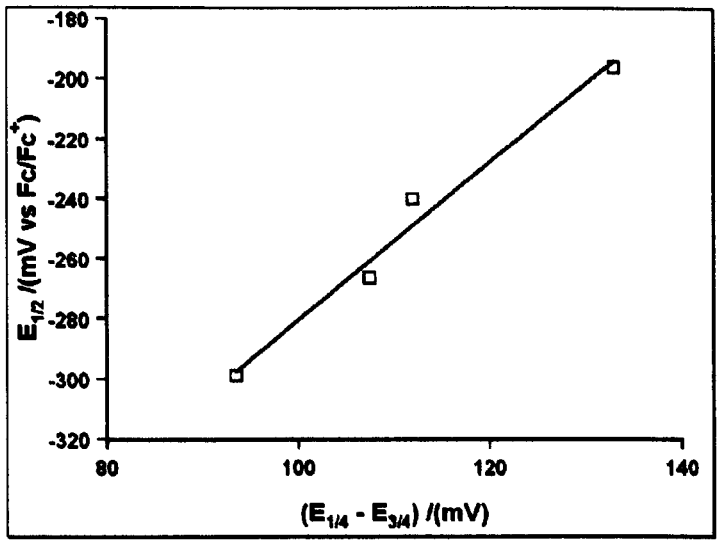

Figure 3.13. A plot of $E_{1/2}$ vs. $(E_{1/4} - E_{3/4})$ for the oxidation of CuCl.

A linear relation was expected that would allow $E^{0'}$ to be determined via the intercept at $(E_{1/4} - E_{3/4})$ = 56.5mV, slope = $(3^{\alpha-1} - 3^{\alpha+1})$ and recourse to kid1 to yield k^0. The procedure yielded $E^{0'}$ = -0.3951V vs. Fc/Fc^+, which is quite different to that resulting from the Mirkin and Bard analysis earlier. A numerical solution was used to elucidate α as 0.82. These values were then used to calculate $E^{0'} - E_{1/2}$ for each point, enabling the points to be located on kid1 as shown in Figure 3.14.

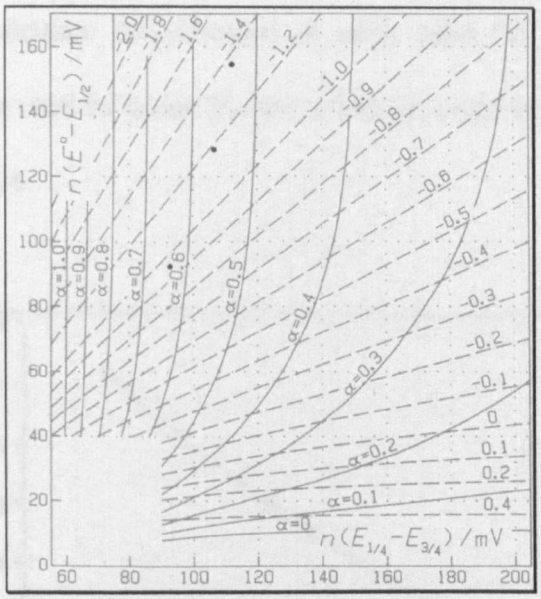

Figure 3.14. Analysis of k^0 from kid1.

Only the first three of the four points may be located on kid1, giving log κ = -0.95, -1.19 and –1.38, respectively, corresponding to k^0 of 8.6 x 10^{-4}, 1.3 x 10^{-3} and 2.0 x 10^{-3} cm s^{-1}, respectively. Via use of the elucidated $E^{0'}$, it appears that the values of α obtained from the plot shown in Figure 3.13 and the points superimposed onto kid1 as shown in Figure 3.14 do not match. If this were the most appropriate protocol to use, there would only be one possible combination of E^0, k^0 and α, whereas, it has been shown that a number of different possibilities have been obtained, negating this protocol.

To use protocol IV, a plot of $E_{1/2}$ vs. log(a) was constructed, as shown in Figure 3.15. The first differential of the equation of the best fit curve was found to be:

$$dE_{1/2}/d\log(a) = 42.4 (\log a) - 116.6 \qquad \text{Eq. 3.6}$$

This was used to calculate $dE_{1/2}/d\log(a)$ at each value of $(E_{1/4} - E_{3/4})$. These coordinates were then used to locate points on kid2 in order to elucidate α and log κ, as shown in Figure 3.16.

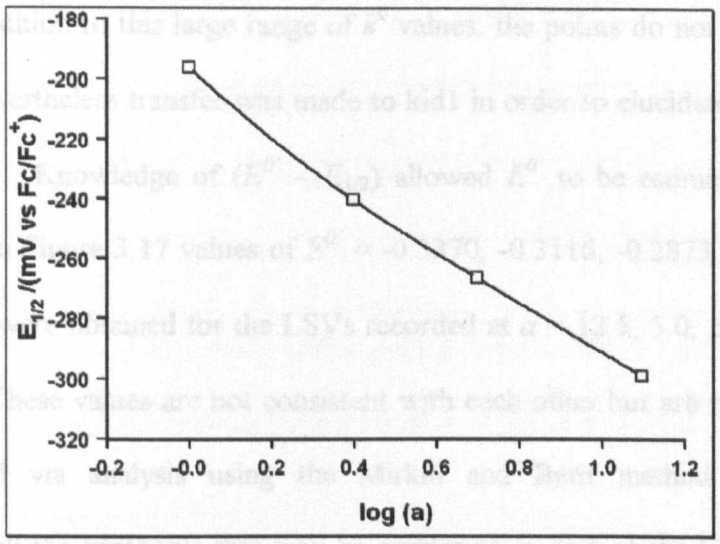

Figure 3.15. A plot of $E_{1/2}$ vs. log (a) for the oxidation of CuCl.

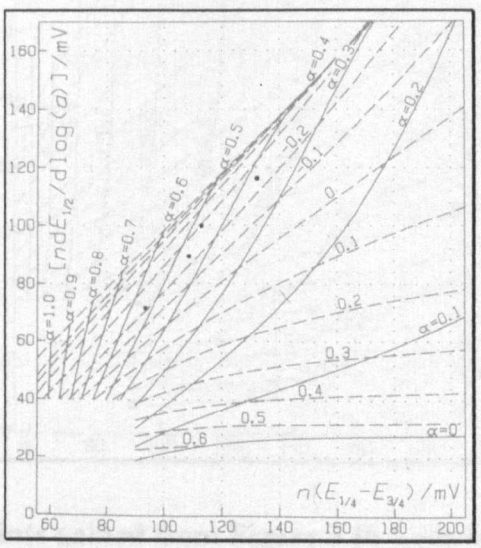

Figure 3.16. Points of $dE_{1/2}/d\log(a)$ vs. $(E_{1/4} - E_{3/4})$ located on kid2.

Each value of log κ was transformed to k^0. Values of between 2.9 x 10^{-3} cm s^{-1} and 52 x 10^{-3} cm s^{-1} were calculated, which were consistent with the results produced via analysis using the Mirkin and Bard method (Table 3.17). From Figure 3.16 it can be seen that in addition to this large range of k^0 values, the points do not lie on a line of constant α, nevertheless transfer was made to kid1 in order to elucidate $E^{0'}$, as shown as Figure 3.17. Knowledge of ($E^{0'}$ – $E_{1/2}$) allowed $E^{0'}$ to be estimated. From the points shown in Figure 3.17 values of $E^{0'}$ = -0.3370, -0.3116, -0.2873 and –0.2431V, all vs. Fc/Fc^+, were obtained for the LSVs recorded at a = 12.5, 5.0, 2.5 and 1.0 μm, respectively. These values are not consistent with each other but are rather similar to those obtained via analysis using the Mirkin and Bard method (Table 3.17). Therefore, of all the protocols that may be employed as part of the Oldham method, this appears to be most appropriate.

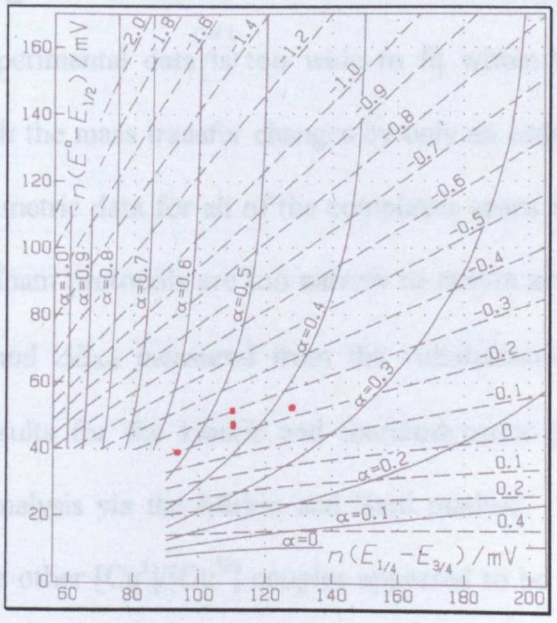

Figure 3.17. The points gained from Figure 3.16 were transferred to kid1 to elucidate $E^{0'}$.

In order to draw some conclusions about the Oldham method, the results obtained by these various protocols are shown in Table 3.18.

Protocol	α	k^0 / (10^{-3}cm s^{-1})	$E^{0'}$ / (V vs. Fc/Fc$^+$)
III.1	Not possible as plot was curved rather than linear.		
III.2	0.82 to 0.6	0.86 to 2.0	-0.395
IV	0.38 to 0.52	2.9 to 52	-0.337 to -0.243

Table 3.18. Kinetic and thermodynamic parameters for the oxidation of CuCl as derived via various protocols of the Oldham method.

Although the Oldham method was initially thought to be more accurate than that of Mirkin and Bard, as it utilised a number of LSVs and hence reduced any error associated with a single measurement, there is little continuity between the various protocols, as the experimental data is too wide to fit within the range of a single protocol, even though the mass transfer changes by only an order of magnitude. It is likely that the voltammetric data for all of the complexes spans a number of protocols and, as such, the Oldham protocols are too narrow to ensure accurate analysis across the range of $\Delta E_{1/4}$ and $\Delta E_{3/4}$ measured from the voltammetric data. Protocol IV appeared to give results for the kinetic and thermodynamic parameters that were closest to those of analysis via the Mirkin and Bard method. The values of ($E_{1/4}$ – $E_{3/4}$) observed for the other [Cu^I]/[Cu^{II}] couples appeared to be of comparable size to that for CuCl and so no further analysis via the Oldham method was carried out. Rather, the Mirkin and Bard method was considered to be simpler to use and as it

yielded similar results to the Oldham IV protocol, all further analyses presented here utilised the Mirkin and Bard method. Three further $[Cu^{I}]/[Cu^{II}]$ were examined voltammetrically.

3.3.2.3 Voltammetric studies of [1_Cu].

Typical data for this system are shown in Table 3.19, these were subjected to analysis by the Mirkin and Bard method. Table 3.20 shows values of D, $\Delta E_{1/4}$ and $\Delta E_{3/4}$, while Table 3.21 shows the kinetic and thermodynamic parameters obtained for the oxidation of this complex (0.5 mM) in a solution of DCE, with TEACl (50 mM) present as supporting electrolyte.

a/ (μm)	i_{lim} / *(nA)*	$E_{1/4}$/ (V vs. Fc/Fc^{+})	$E_{1/2}$/ (V vs. Fc/Fc^{+})	$E_{3/4}$/ (V vs. Fc/Fc^{+})
12.5	1.83	-0.362	-0.323	-0.282
5.0	0.79	-0.334	-0.285	-0.231
2.5	0.41	-0.285	-0.227	-0.158
1.0	0.14	-0.228	-0.163	-0.084

Table 3.19. Voltammetric parameters for the $[1\_Cu^{I}]/[1\_Cu^{II}]$ couple, obtained via LSVs recorded in a solution of CuCl (0.5 mM), ligand 1 (1.25 mM) in DCE that contained THACl (50 mM) as supporting electrolyte.

a / (μm)	$D^{\dagger}$ / (10^{-5} cm^2 s^{-1})	$\Delta E_{1/4}$ / (mV)	$\Delta E_{3/4}$ / (mV)	$E_{1/4}$ - $E_{3/4}$ / (mV)
12.5	0.76	38.0	41.0	79.0
5.0	0.82	49.0	54.0	103.0
2.5	0.85	58.0	69.0	127.0
1.0	0.74	65.0	79.0	144.0

Table 3.20. Interquartile separations for the oxidation of [1_Cu].

a / (μm)	α	λ	$n\Delta E^{0'}$ / (mV)	k^0 / (10^{-3} cm s^{-1})	$E^{0'}$ / (V vs. Fc/Fc$^+$)
12.5	0.69	0.54	43.30	3.3	-0.367
5.0	0.55	0.33	69.90	5.4	-0.355
2.5	0.42	0.47	69.40	16	-0.296
1.0	0.37	0.47	77.50	35	-0.241

Table 3.21. Resultant kinetic and thermodynamic parameters for the oxidation of [1_Cu].

3.3.2.4 Voltammetric studies of [7_Cu].

Typical data for this system are shown in Table 3.22, whilst Table 3.23 shows values of D, $\Delta E_{1/4}$ and $\Delta E_{3/4}$, which were calculated and Table 3.24 shows the kinetic and thermodynamic parameters obtained for this complex.

---

† The value of D was found to be 0.86 ± 0.13 from 10 measurements, according to solution preparation method 2.

a /(μm)	i_{lim} /(nA)	$E_{1/4}$/(V vs. Fc/Fc$^+$)	$E_{1/2}$/(V vs. Fc/Fc$^+$)	$E_{3/4}$/(V vs. Fc/Fc$^+$)
12.5	1.81	-0.346	-0.302	-0.255
5.0	0.80	-0.329	-0.281	-0.227
2.5	0.41	-0.302	-0.252	-0.195
1.0	0.15	-0.257	-0.199	-0.124

Table 3.22. Voltammetric parameters for the [7_Cu^I]/[7_Cu^{II}] couple, obtained via LSVs recorded in a solution of CuCl (0.5 mM), ligand 7 (1.25 mM) in DCE that contained THACl (50 mM) as supporting electrolyte.

a / (μm)	$D^{\ddagger}$ / (10^{-5} cm^2 s^{-1})	$\Delta E_{1/4}$ / (mV)	$\Delta E_{3/4}$ / (mV)	$E_{1/4}$ - $E_{3/4}$ / (mV)
12.5	0.75	43.5	47.5	91.0
5.0	0.80	48.0	54.0	102.0
2.5	0.82	50.0	57.0	107.0
1.0	0.73	57.5	75.0	132.5

Table 3.23. Interquartile separations for the oxidation of [7_Cu].

a / (μm)	α	λ	$n\Delta E^{0'}$ / (mV)	k^o / (10^{-3}cm s^{-1})	$E^{0'}$/(V vs. Fc/Fc$^+$)
12.5	0.62	0.38	60.88	2.3	-0.363
5.0	0.53	0.43	60.50	6.9	-0.341
2.5	0.51	0.45	61.80	15	-0.314
1.0	0.38	0.65	58.95	47	-0.258

Table 3.24. Resultant kinetic and thermodynamic parameters for the oxidation of [7_Cu].

---

‡ The value of D was found to be 0.81 ± 0.08 from 10 measurements, according to solution preparation method 2.

3.3.2.5 Voltammetric studies of [9_Cu].

Typical data are shown in Table 3.25, which was subjected to analysis by the Mirkin and Bard method. Table 3.26 shows values of D, $\Delta E_{1/4}$ and $\Delta E_{3/4}$.

a /(μm)	i_{lim} /(nA)	$E_{1/4}$/(V vs. Fc/Fc^+)	$E_{1/2}$/(V vs. Fc/Fc^+)	$E_{3/4}$/(V vs. Fc/Fc^+)
12.5	1.86	-0.343	-0.297	-0.246
5.0	0.83	-0.323	-0.270	-0.211
2.5	0.39	-0.299	-0.246	-0.185
1.0	0.15	-0.271	-0.217	-0.152

Table 3.25. Voltammetric parameters for the [9_Cu^I]/[9_Cu^{II}] couple, obtained via LSVs recorded in a solution of CuCl (0.5 mM), ligand 9 (1.25 mM) in DCE that contained THACl (50 mM) as supporting electrolyte.

a / (μm)	$D^{\S}$ / (10^{-5} cm^2 s^{-1})	$\Delta E_{1/4}$ / (mV)	$\Delta E_{3/4}$ / (mV)	$E_{1/4}$ - $E_{3/4}$ / (mV)
12.5	0.77	46.5	50.5	97.0
5.0	0.86	53.0	59.0	112.0
2.5	0.80	52.5	61.5	114.0
1.0	0.79	54.5	65.0	119.5

Table 3.26. Interquartile separations for the oxidation of [9_Cu].

---

§ The value of D was found to be 0.88 ± 0.14 from 10 measurements, according to solution preparation method 2.

a / (μm)	α	λ	$n\Delta E^{0'}$ / (mV)	k^0 / (10^{-3}cm s-^{1})	$E^{0'}$ / (V vs. Fc/Fc^{+})
12.5	0.59	0.29	73.43	1.8	-0.370
5.0	0.50	0.33	75.10	5.7	-0.345
2.5	0.47	0.49	61.88	16	-0.308
1.0	0.44	0.51	62.85	40	-0.280

Table 3.27. Resultant kinetic and thermodynamic parameters for the oxidation of [9_Cu].

3.3.2.6 Comparison of voltammetric data.

As identified from the earlier limited analysis, there is a systematic variation in $E^{0'}$ and k^0, as interpreted by the method of Mirkin and Bard. Figure 3.18 shows this in a graphical representation.

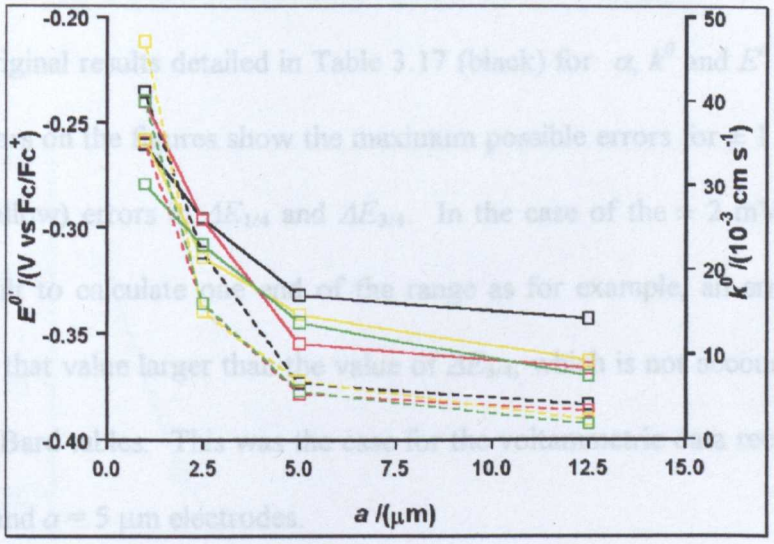

Figure 3.18. Variation of $E^{0'}$ (solid lines) and k^0 (dashed lines), with electrode diameter calculated by the method of Bard and Mirkin. Black lines = [Cu], red lines = [1_Cu], yellow lines = [7_Cu] and green lines = [9_Cu].

As already highlighted, small errors in the quartile potentials could produce large errors in kinetic and thermodynamic parameters. In order to understand the impact of

a small variation in the position of any of the quartile potentials, an error analysis was carried out with the data for the oxidation of CuCl, as detailed previously. The purpose was to determine whether the systematic trend observed could be explained by random errors, or whether a systematic trend prevailed.

3.3.3 Error associated with the method of Mirkin and Bard.

In order to find the maximum range that the three thermodynamic and kinetic parameters may vary over, the above analysis was repeated with errors of either ± 1 mV or ± 2 mV in both $\Delta E_{1/4}$ and $\Delta E_{3/4}$.

From this analysis it was found that even these small uncertainties introduced a significant error in the extracted values of α, k^0 and $E^{0'}$. Figure 3.19 - Figure 3.21 show the original results detailed in Table 3.17 (black) for α, k^0 and $E^{0'}$, respectively. The error bars on the figures show the maximum possible errors for ± 1 mV (red) and ± 2 mV (yellow) errors in $\Delta E_{1/4}$ and $\Delta E_{3/4}$. In the case of the ± 2 mV error, it was often difficult to calculate one end of the range as for example, an error of 2mV in $\Delta E_{1/4}$ made that value larger than the value of $\Delta E_{3/4}$, which is not accounted for in the Mirkin and Bard tables. This was the case for the voltammetric data recorded at the a = 12.5 μm and a = 5 μm electrodes.

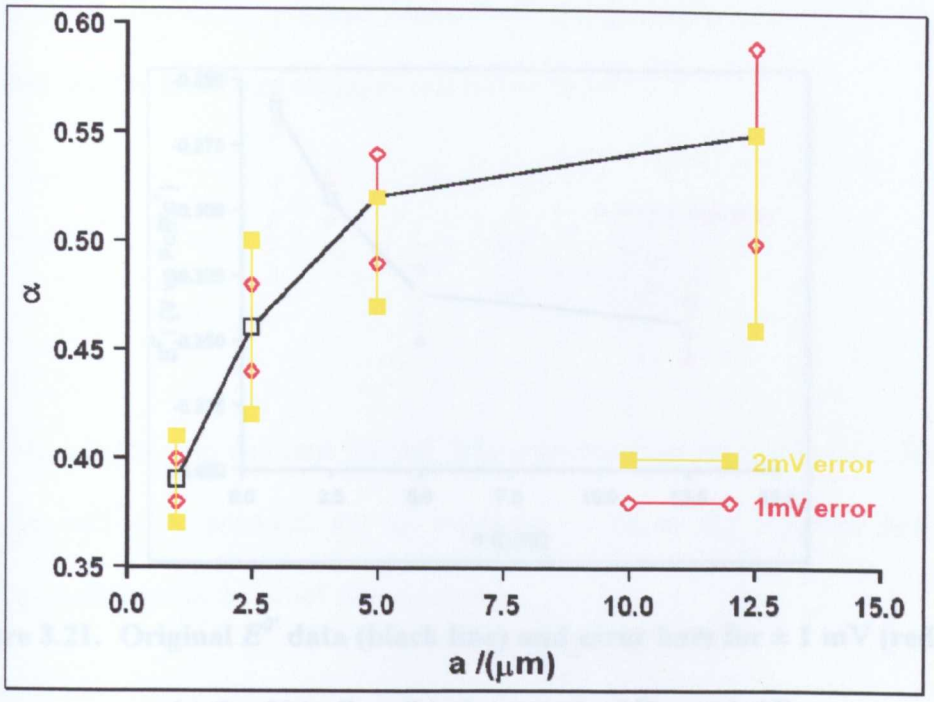

Figure 3.19. Original α data (black line) and error bars for ± 1 mV (red lines) and ± 2 mV (yellow lines) errors in $\Delta E_{1/4}$ and $\Delta E_{3/4}$.

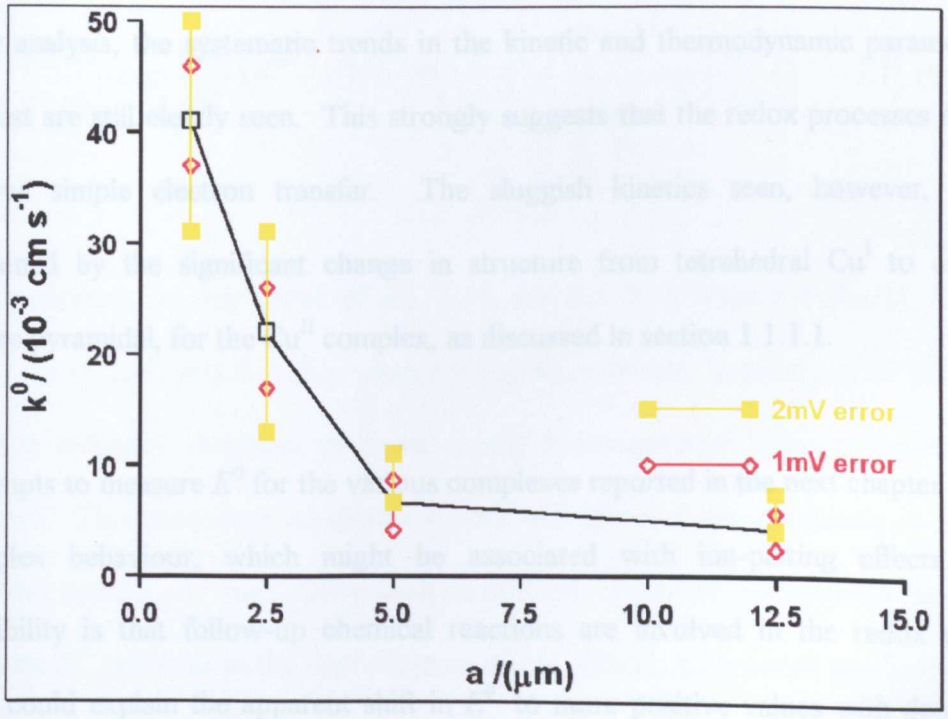

Figure 3.20. Original k^0 data (black line) and error bars for ± 1 mV (red lines) and ± 2 mV (yellow lines) errors in $\Delta E_{1/4}$ and $\Delta E_{3/4}$.

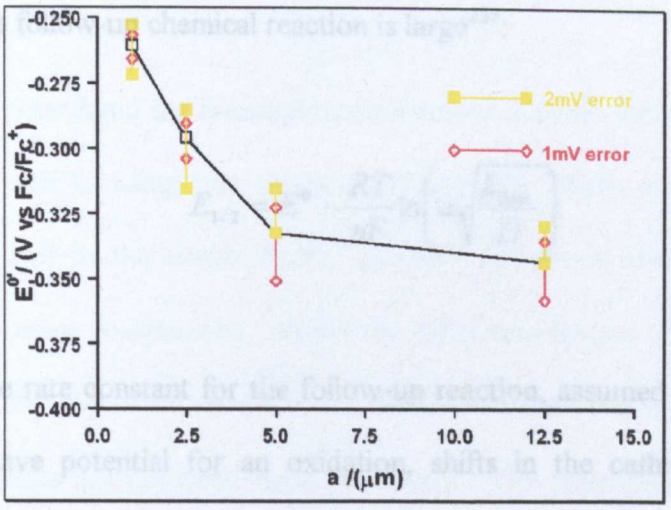

Figure 3.21. Original $E^{0'}$ data (black line) and error bars for ± 1 mV (red lines) and ± 2 mV (yellow lines) errors in $\Delta E_{1/4}$ and $\Delta E_{3/4}$.

Figure 3.19 - Figure 3.21 show that $E^{0'}$ and k^0 were least affected by inaccuracies in the measurement of $\Delta E_{1/4}$ and $\Delta E_{3/4}$ at large electrodes. Nonetheless, even after this error analysis, the systematic trends in the kinetic and thermodynamic parameters of interest are still clearly seen. This strongly suggests that the redox processes may not involve simple electron transfer. The sluggish kinetics seen, however, can be explained by the significant change in structure from tetrahedral Cu^I to distorted square pyramidal, for the Cu^{II} complex, as discussed in section 1.1.1.1.

Attempts to measure E^0 for the various complexes reported in the next chapter suggest complex behaviour, which might be associated with ion-pairing effects. One possibility is that follow-up chemical reactions are involved in the redox process. This could explain the apparent shift in $E^{0'}$ to more positive values with decrease in

electrode size. For an EC process, where the E step (considered to be an oxidation) is reversible and the follow-up chemical reaction is large[223]:

$$E_{1/2} = E^0 - \frac{RT}{nF}\ln\left(a\sqrt{\frac{k_{hom}}{D}}\right) \qquad \text{(Eq. 3.10)}$$

Where k_{hom} is the rate constant for the follow-up reaction, assumed to be first-order. Thus the half-wave potential for an oxidation, shifts in the cathodic direction by 59mV as a changes by an order of magnitude.

Of course the wave shape analysis in this chapter demonstrates that the heterogeneous electron transfer is not reversible. In this case, again for an oxidation, the expression for the wave shape is[223]:

$$\frac{D}{ak^0}\exp\left[\frac{\alpha nF}{RT}\left(E^{0'} - E\right)\right] = \frac{i_{lim} - i}{i} - \frac{1}{1 + a\sqrt{\frac{k_{hom}}{D}}}\exp\left[\frac{nF}{RT}\left(E^{0'} - E\right)\right] \qquad \text{(Eq. 3.11)}$$

By considering limiting forms of Eq. 3.11, for $E = E_{1/2}$, when $i = (i_{lim}/2)$, $E = E_{3/4}$, when $i = (3i_{lim}/4)$ and $E = E_{1/4}$ when $i = (i_{lim}/4)$, it should, in principle, be possible to develop indicator diagrams of those simple heterogeneous kinetics, developed by Oldham. This procedure eliminates k^0, but still leaves three unknowns, a, k_{hom} and $E^{0'}$, thus making any quantitative analysis difficult. With the unsuccessful attempts to measure $E^{0'}$ reported in the next chapter, it was difficult to proceed any further along this line of analysis, but the involvement of coupled chemical processes is a strong possibility.

3.4 Conclusions

This chapter has considered the heterogeneous electron transfer kinetics of a series of Cu^{I} complexes in DCE, using two methods of analysis. Both methods have been shown to apply well to the simple Fc/Fc^{+} process, but reveal that the $[Cu^{I}]/[Cu^{II}]$ redox process is more complicated. When the most appropriate Oldham method is used it provides very consistent results to the Mirkin and Bard method. A comparison of these two methods has not been made previously. The systematic trends in $E^{0'}$, α and k^{0} identified for the analysis suggests the possibility of the involvement of coupled homogeneous reactions. The range of kinetic and thermodynamic parameters determined does, however, provide a guide to the electrochemical behaviour of these complexes.

Chapter 4 - A study of the reaction between electrogenerated Cu^{II} and Cu^{O} in an SECM environment.

This chapter focuses on the comproportionation reaction between Cu^{II} complexes and Cu, which is believed to play a significant role in ATP reactions, as described in Chapter 1. A novel SECM experiment has been designed for investigating this process, in which Cu^{II} is electro-generated from Cu^{I} at a Pt tip UME and diffuses to a Cu UME substrate (unbiased) where the comproportionation reaction occurs. The feedback current transient and corresponding potential-time characteristics are shown to provide information on the etching kinetics underpinning the comproportionation process.

4.1 Introduction

SECM has been shown to be a powerful tool for the elucidation of interfacial reaction kinetics. Chapter 1 described the feedback mode of the SECM, which is well-suited to the study of oxidative dissolution processes promoted by solution species[224,225,226]. Macpherson et al[169] made a study of the oxidative etching kinetics of Cu substrates by $[Ru(bipy)_3^{3+}]$ and Br_2, as well as the general feedback current at small substrates. The effect of substrate size was examined and it was found, in agreement with a previous theoretical prediction[166], that when the substrate was of a size comparable to that of the tip UME, feedback would only occur at an unbiased substrate if a chemical reaction occurred to regenerate the initial solution species.

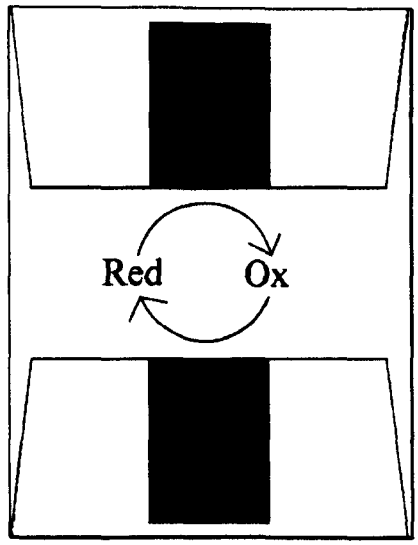

Figure 4.1. Schematic of the SECM feedback mode.

Figure 4.1 shows a schematic of the feedback mode of SECM, illustrating that once electrogenerated at the tip UME, Ox may diffuse through solution to an unbiased substrate. Oxidative etching ensues if Ox is a sufficiently powerful oxidising agent and the kinetics of this process are fast enough. This provides an excellent platform for the investigation of the reaction of Cu^{II} (Ox) with Cu^{0} (substrate). This process is examined in this chapter for a range of Cu^{I} precursor complexes in TEACl (supporting electrolyte, at a concentration of 50 mM) / DCE solution. In addition to tip current-time measurements, simultaneous substrate potential-time curves are shown to provide additional information on the heterogeneous comproportionation reaction.

4.2 Experimental

Solutions were made up as described in chapter 3, with the slight modification that where a ligand was added, it was added in excess (x50) rather than at 2.5 times the

concentration of CuCl. The reasons for this change are connected with the SECM geometry and will become clear later in this chapter, and again in chapter 6.

4.3 Results

In order to use the SECM to determine the kinetics of this heterogeneous process it was necessary to vertically align the two UMEs, in order than the tip resided directly over the substrate, of the same size. By holding the tip at a potential capable of generating [Cu^{II}] from [Cu^{I}] at a diffusion-controlled rate, the reaction of this electrogenerated species with the substrate electrode could then be observed via any feedback current detected for [Cu^{I}] oxidation. For these measurements, a 25μm diameter Pt tip was scanned over a 25μm diameter Cu disc substrate at a velocity of 10μm/s. A data point was typically recorded every 10μm.

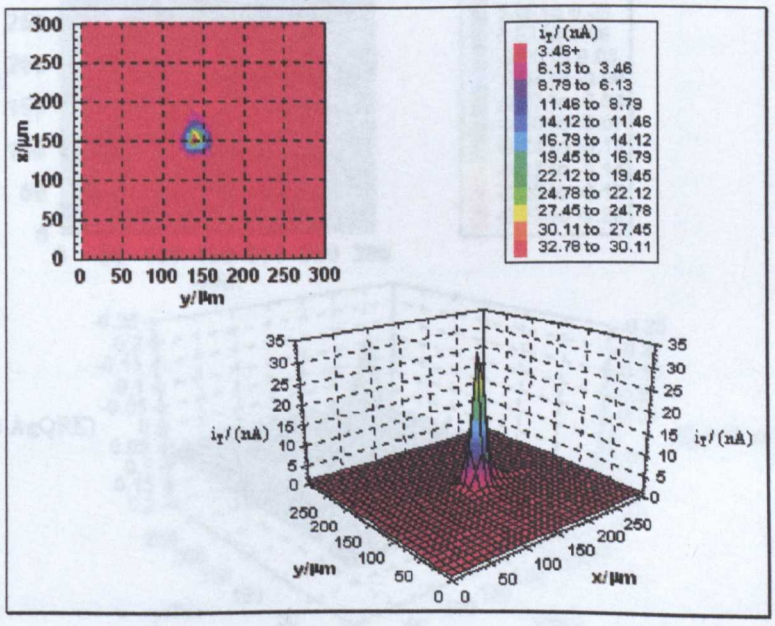

Figure 4.2. An SECM tip current image of a 25μm Cu substrate recorded with a 25μm Pt tip in a solution of CuCl (0.5 mM) in DCE with TBAP (50 mM) present as supporting electrolyte.

When the tip-generated Cu^{II} intercepted the underlying Cu substrate, the reaction of Cu^{II} with the Cu^{0} substrate produced an increase in the flux of Cu^{I} at the tip electrode, causing i_T to increase concomitantly. The production of Cu^{I} from the reaction of Cu^{II} reached a maximum when the tip and substrate were aligned.

The substrate potential was found to change simultaneously with the tip current. A similar shaped trace was observed to the tip response, with the substrate potential swinging to negative values as the tip passed above the Cu electrode surface. These open-circuit potential measurements were made simultaneously with the measurement of i_T. The reasons for the variation in potential will be discussed later.

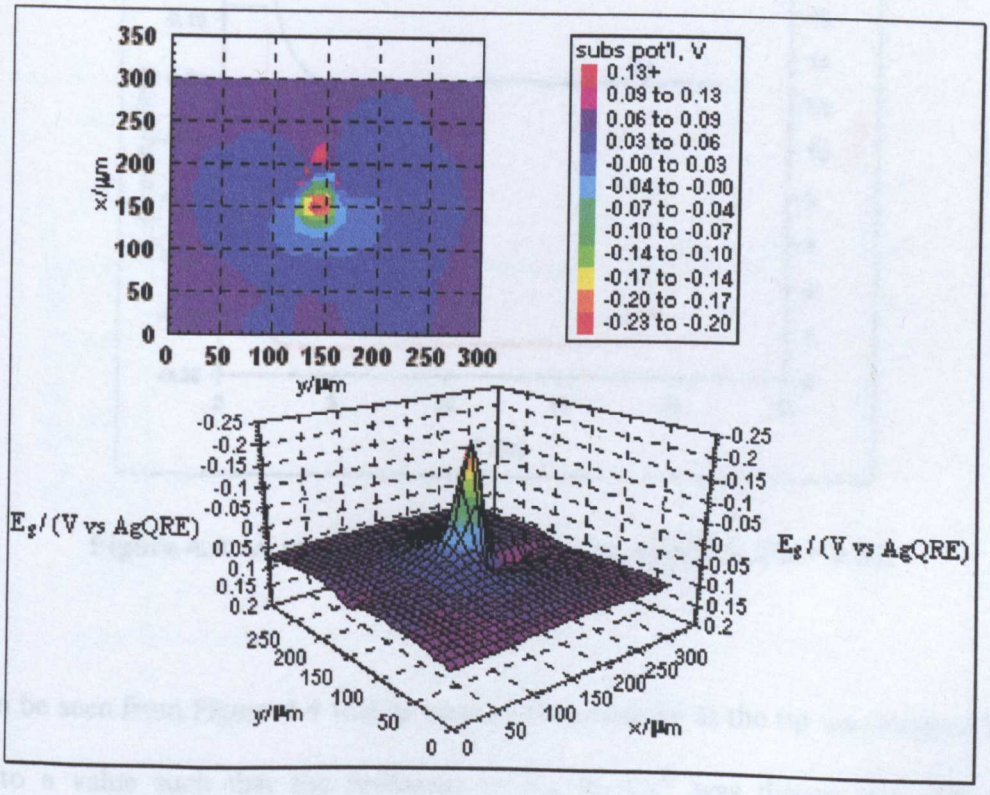

Figure 4.3. The substrate response coincident with the current data of figure 4.2.

4.3.1 Current-time transients

Once aligned, an i_T vs. d approach curve of the tip to the insulating glass sheath part of the substrate was recorded, in order that d could be calibrated. Once the distance of closest approach was known the separation of the two electrodes was then controlled via a piezoelectric element. Current-time transients were recorded at several different separations. Whilst the potential at the tip electrode was "stepped" to drive the oxidation of Cu^{I} to Cu^{II}, the open-circuit potential at the substrate was monitored simultaneously with the tip current. Tip current-time transients were recorded for four [Cu] species: CuCl alone and subsequently with excess of ligand 1, 7 or 9.

4.3.1.1 Current/potential-time transients for CuCl.

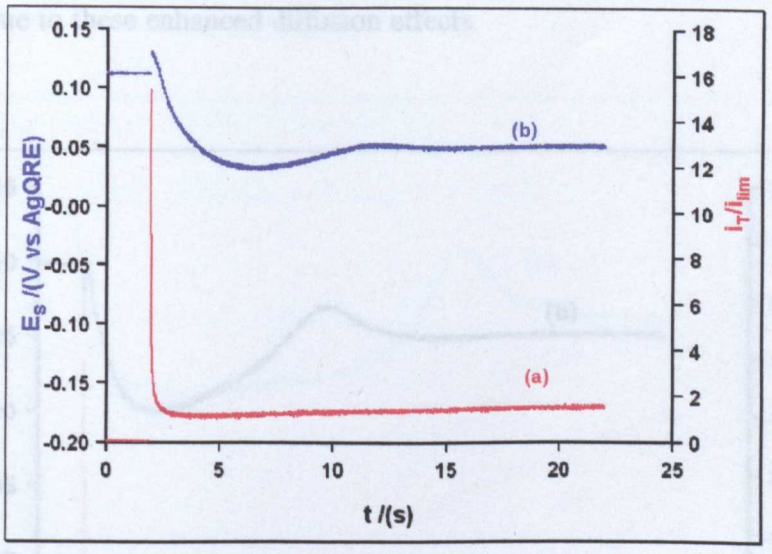

Figure 4.4. A current-time transient recorded at $d/a = 0.83$.

It can be seen from Figure 4.4 that as soon as the potential at the tip was stepped from rest to a value such that the oxidation of Cu^{I} to Cu^{II} was driven at a diffusion-controlled rate, i_T became instantaneously very large, then decreased rapidly until it attained a steady-state value. From the corresponding substrate potential transient, it

was apparent that E_S was grossly affected by the process occurring at the tip. Namely, the potential shifted in the negative direction, reached a minimum, and then increased again peaking slightly before attaining a steady-state value. As d decreased, it was apparent that the minima and maxima in the potential-time transients (see Figure 4.4 - Figure 4.8) increased in magnitude. More significantly, the tip feedback current i_T/i_{lim} is seen to increase significantly. The fact that the current ratio takes values much larger than unity is indicative of a significant heterogeneous reaction producing Cu^I for detection at the tip. The effect of decreasing d is to decrease the tip-substrate separation, which shortens the tip-substrate diffusion time. Consequently, processes are seen most extensively and at shorter times, the smaller the d value. Both the current enhancement and substrate potential effects are larger at smaller tip/substrate separations due to these enhanced diffusion effects.

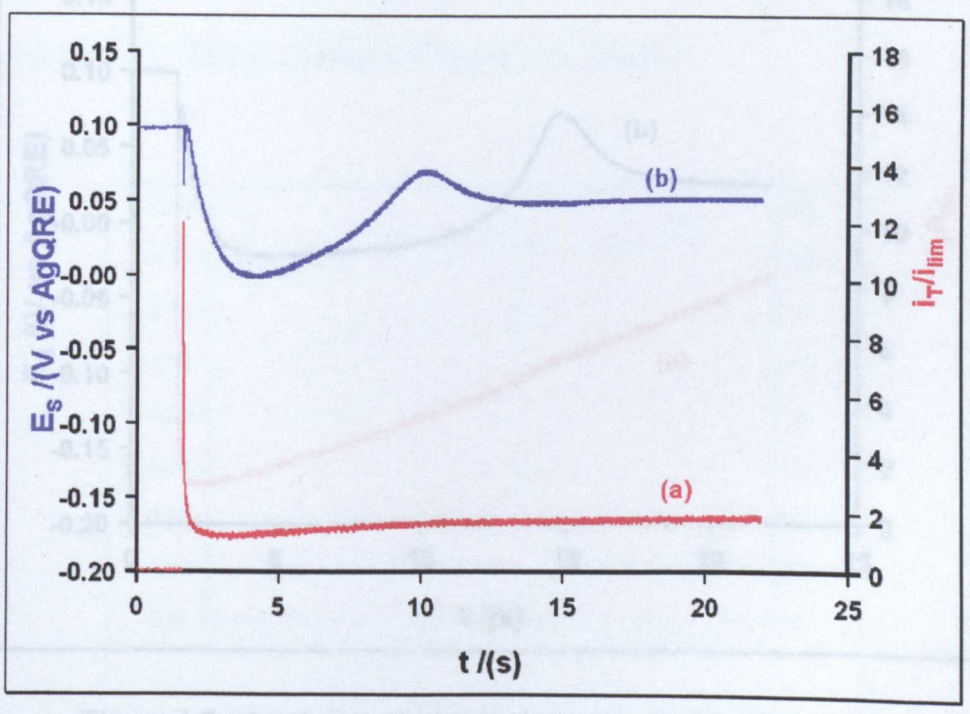

Figure 4.5. A current-time transient recorded at $d/a = 0.63$.

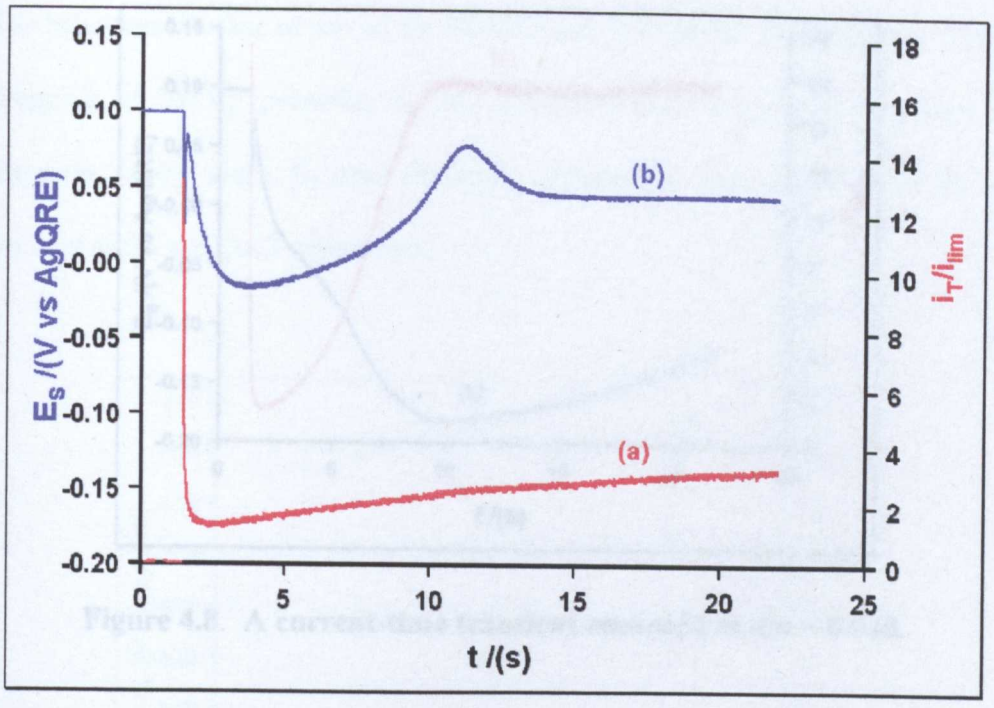

Figure 4.6 A current-time transient recorded at $d/a = 0.43$.

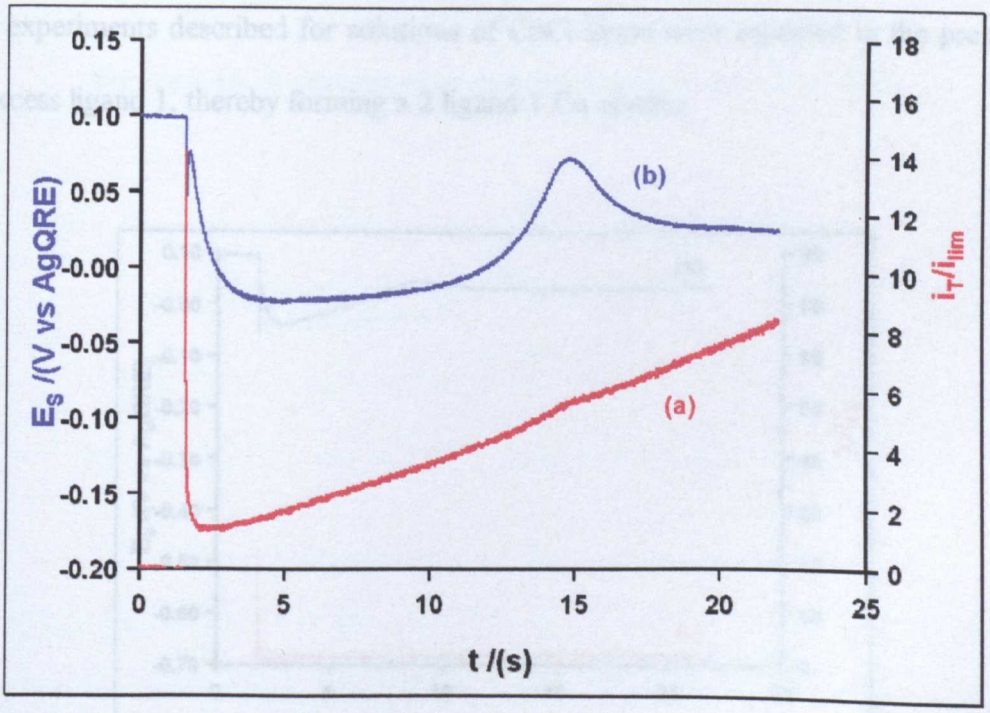

Figure 4.7. A current-time transient recorded at $d/a = 0.23$.

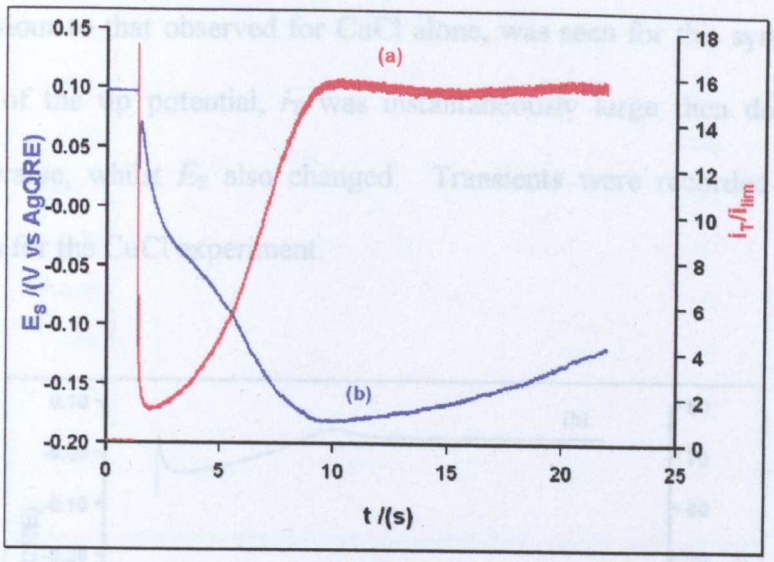

Figure 4.8. A current-time transient recorded at $d/a = 0.028$.

4.3.1.2 Current/potential-time transients for CuCl in the presence of excess ligand 1.

The experiments described for solutions of CuCl alone were repeated in the presence of excess ligand 1, thereby forming a 2 ligand:1 Cu species.

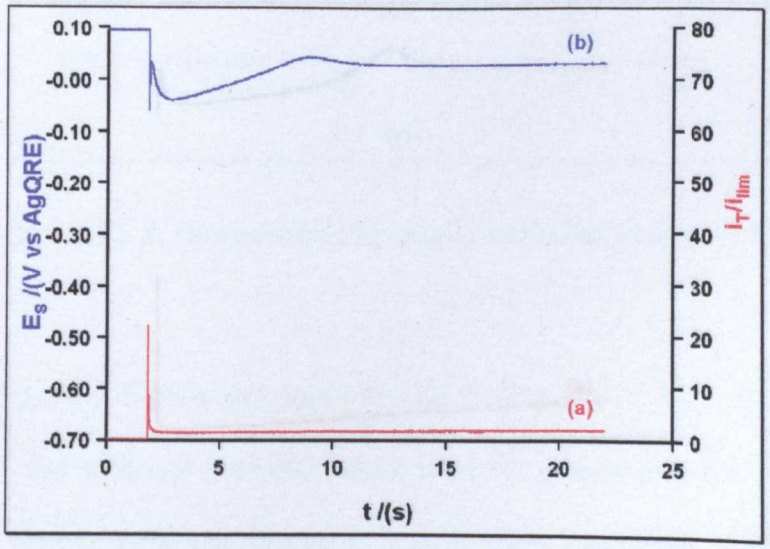

Figure 4.9. A current-time transient recorded at $d/a = 0.83$.

Similar behaviour to that observed for CuCl alone, was seen for this system. Namely, on stepping of the tip potential, i_T was instantaneously large then decreased to a steady-state value, whilst E_S also changed. Transients were recorded at the same values of d as for the CuCl experiment.

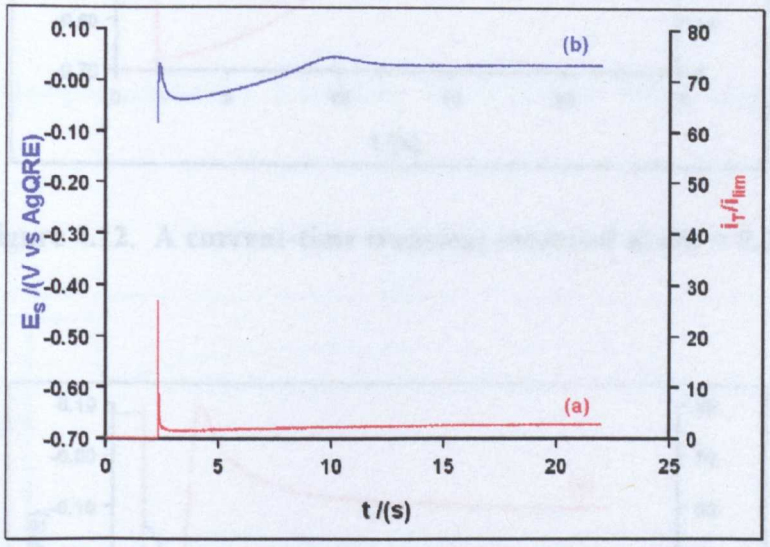

Figure 4.10. A current-time transient recorded at $d/a = 0.63$.

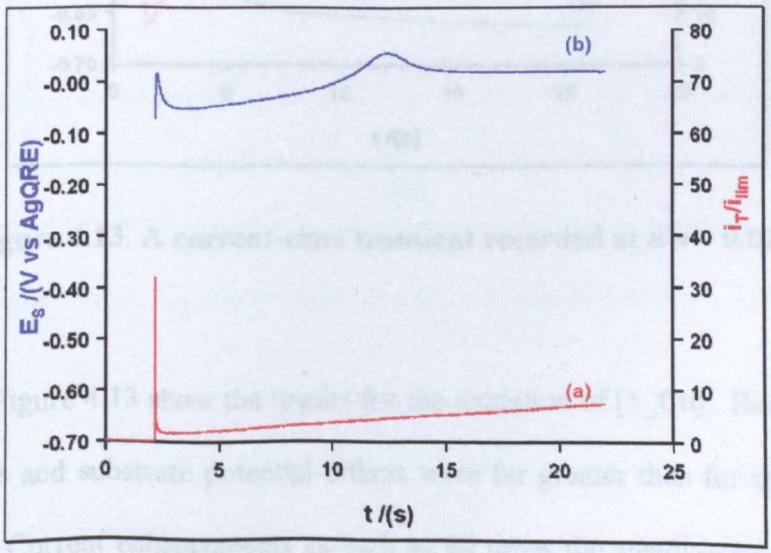

Figure 4.11. A current-time transient recorded at $d/a = 0.43$.

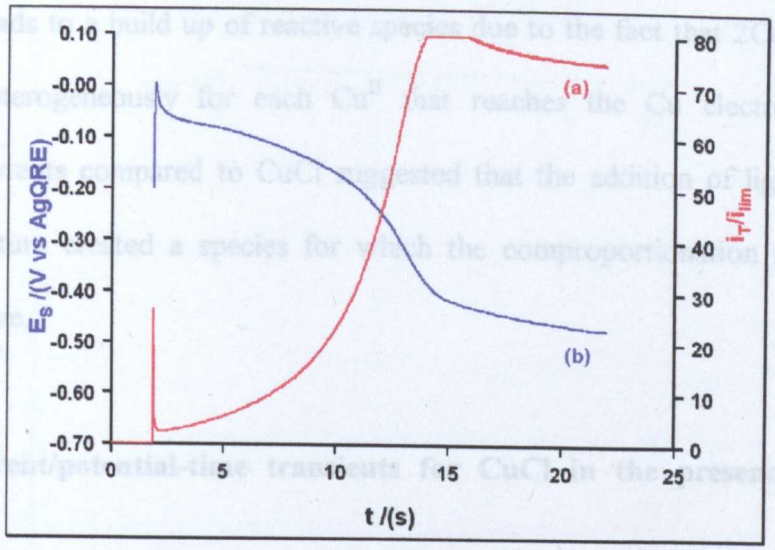

Figure 4.12. A current-time transient recorded at *d*/*a* = 0.23.

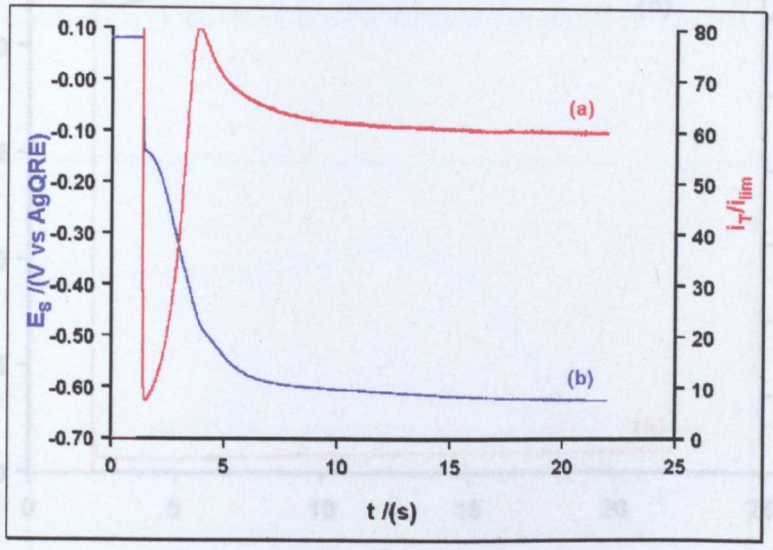

Figure 4.13. A current-time transient recorded at *d*/*a* = 0.028.

Figure 4.9 - Figure 4.13 show the results for the oxidation of [1_Cu]. Both the current enhancements and substrate potential effects were far greater than for the solution of CuCl alone. Current enhancements as high as 80 times the steady-state current were observed at the closest separations examined. Such high activity has never been observed before in SECM and is due to the comproportionation reaction which

essentially leads to a build up of reactive species due to the fact that $2Cu^{I}$ species are produced heterogeneously for each Cu^{II} that reaches the Cu electrode. These enhanced currents compared to CuCl suggested that the addition of ligand 1 to the reaction mixture created a species for which the comproportionation reaction was more extensive.

4.3.1.3 Current/potential-time transients for CuCl in the presence of excess ligand 7.

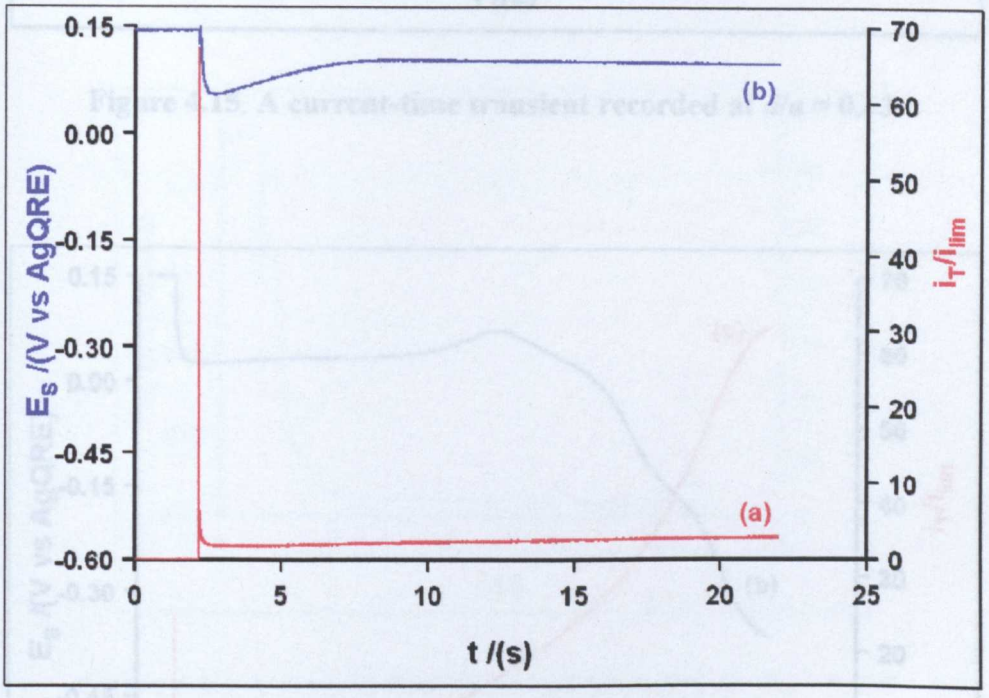

Figure 4.14. A current-time transient recorded at *d/a* = 0.83.

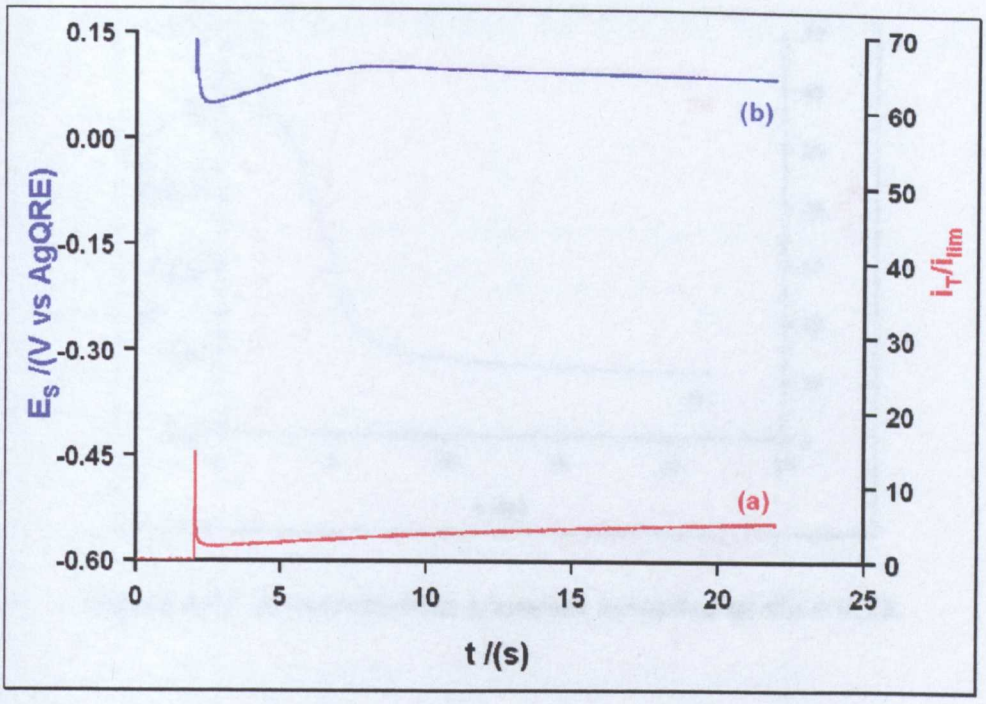

Figure 4.15. A current-time transient recorded at $d/a = 0.63$.

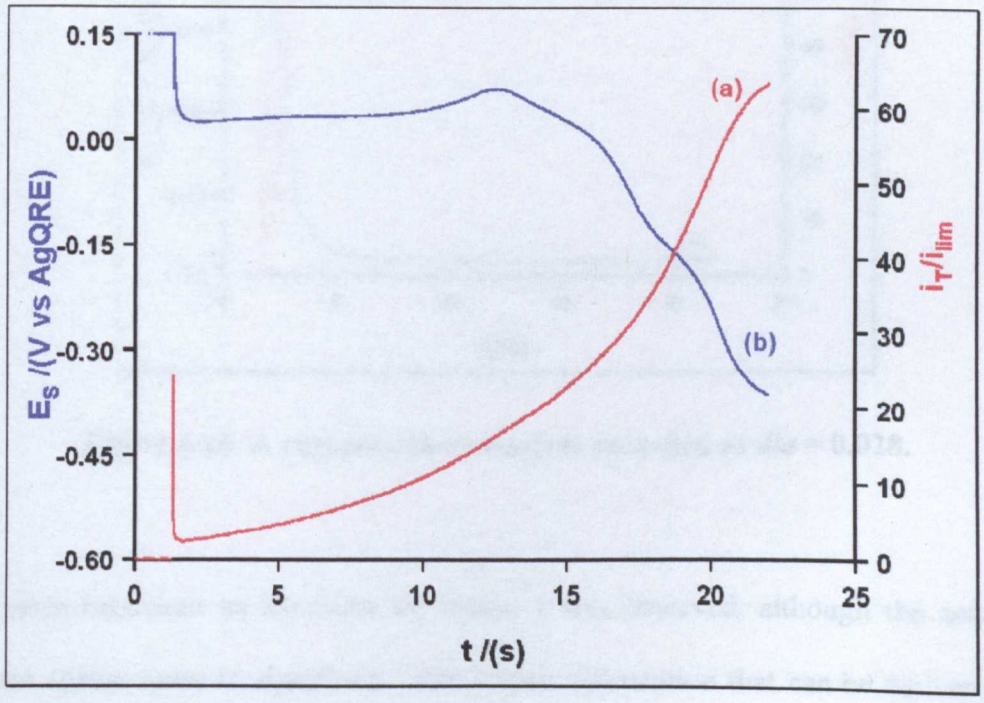

Figure 4.16. A current-time transient recorded at $d/a = 0.43$.

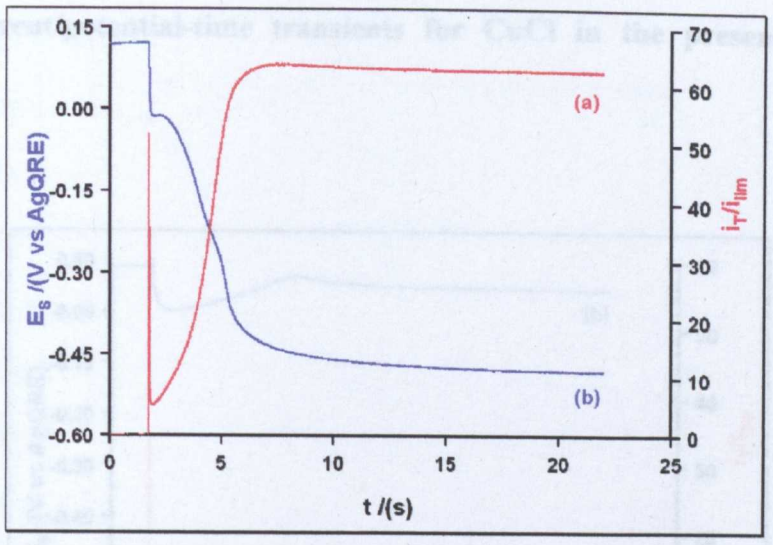

Figure 4.17. A current-time transient recorded at $d/a = 0.23$.

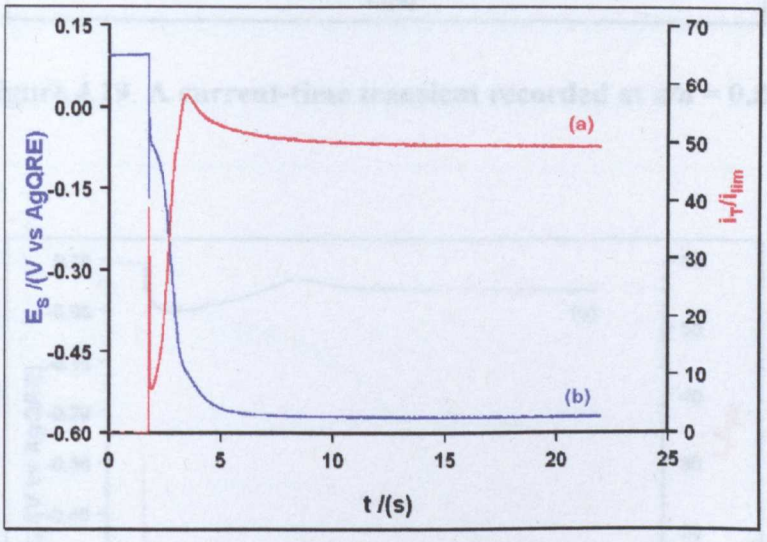

Figure 4.18. A current-time transient recorded at $d/a = 0.028$.

The same behaviour as identified for ligand 1 was observed, although the activities did not appear quite so significant. The kinetic information that can be derived from the transients will be considered in section 4.4

4.3.1.4 Current/potential-time transients for CuCl in the presence of excess ligand 9.

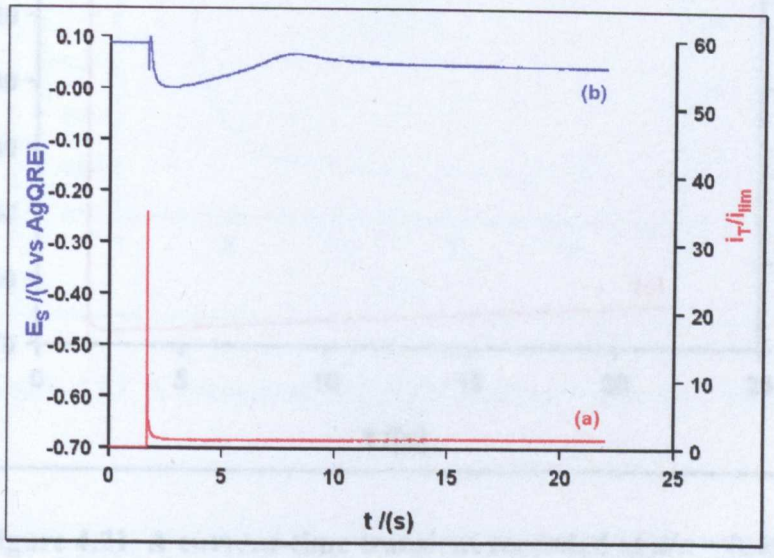

Figure 4.19. A current-time transient recorded at *d/a* = 0.83.

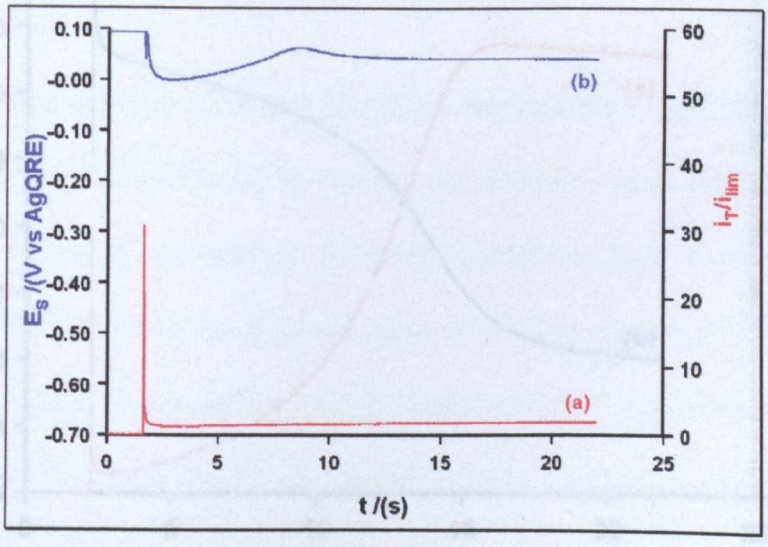

Figure 4.20. A current-time transient recorded at *d/a* = 0.63.

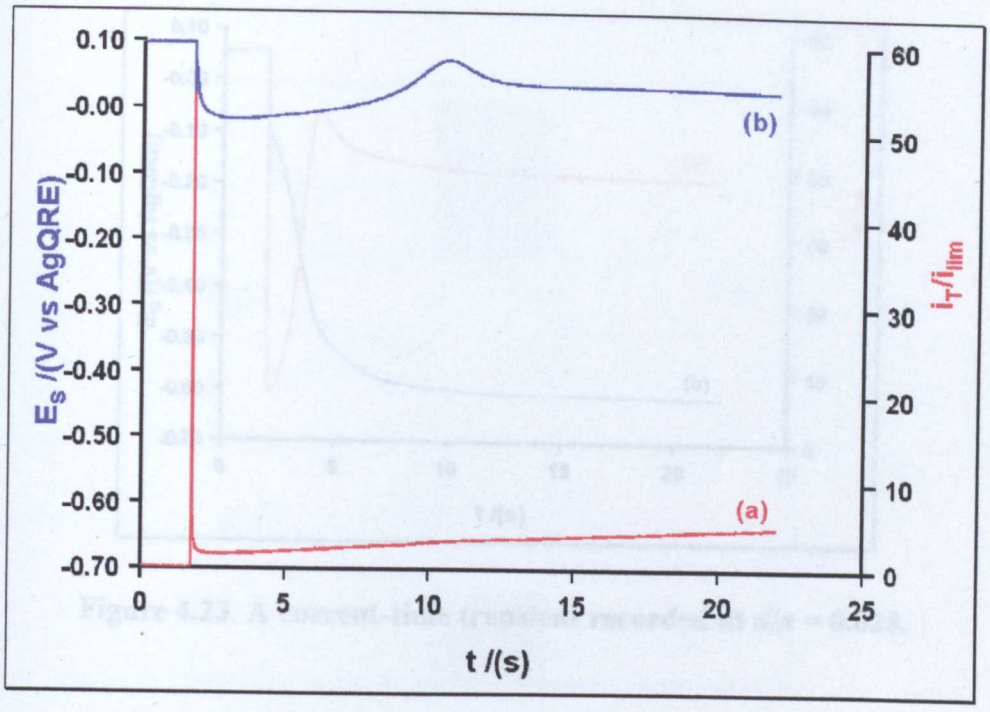

Figure 4.21. A current-time transient recorded at $d/a = 0.43$.

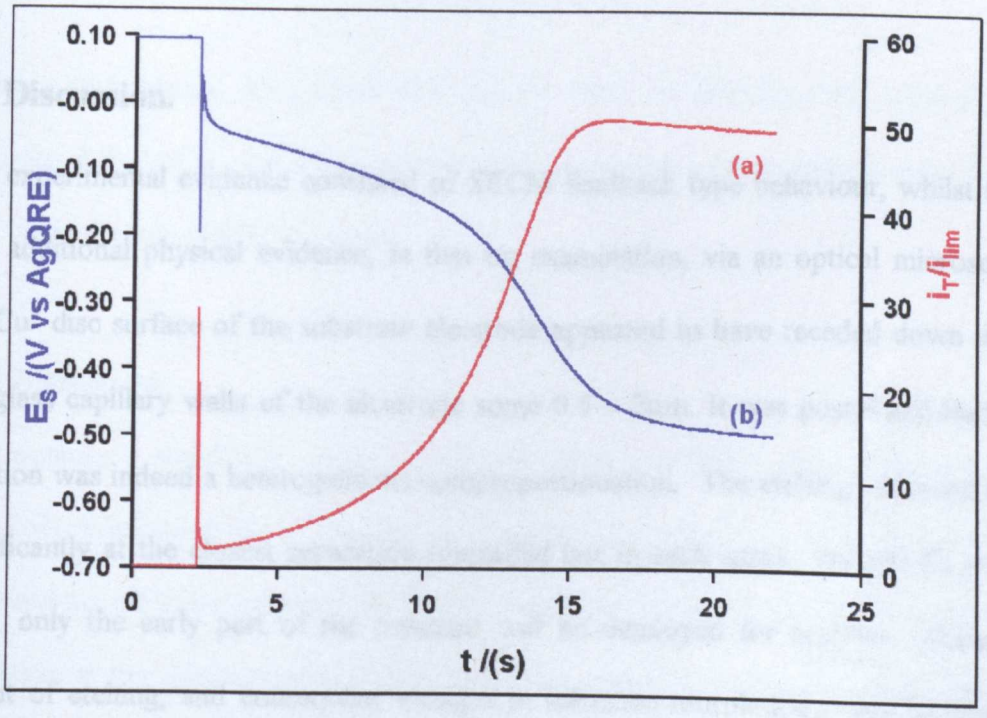

Figure 4.22. A current-time transient recorded at $d/a = 0.23$.

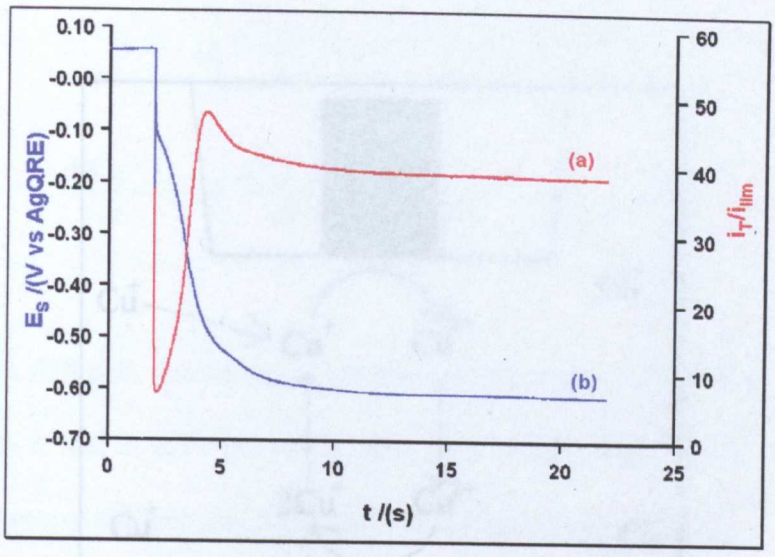

Figure 4.23. A current-time transient recorded at $d/a = 0.028$.

The pattern of activity observed with ligand 9 was somewhat similar to 7. The reasons for the behaviour observed are considered in the next section.

4.4 Discussion.

The experimental evidence consisted of SECM feedback type behaviour, whilst there was additional physical evidence, in that on examination, via an optical microscope, the Cu^0 disc surface of the substrate electrode appeared to have receded down inside the glass capillary walls of the electrode some 0.5 – 2μm. It was postulated that this reaction was indeed a heterogeneous comproportionation. The etching occurred most significantly at the closest separation (recorded last in each case). As will be shown later, only the early part of the transient will be employed for analysis, where the extent of etching, and consequent changes in substrate morphology, will be limited. This type of oxidative etching behaviour could explain the tremendously enhanced currents observed at close tip/substrate separations. Figure 4.24 shows this process as a schematic.

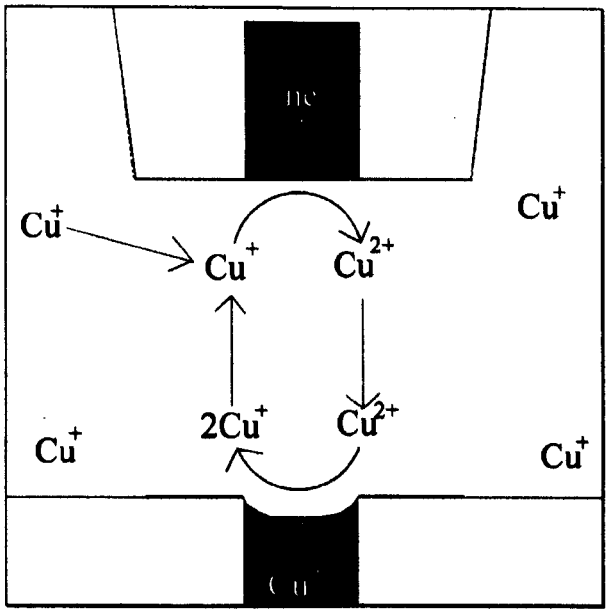

Figure 4.24. Electrogenerated Cu^{II} diffuses to the Cu^{0} substrate, reacts with it to produce $2Cu^{I}$.

At large tip/substrate separations Cu^{II} can be "lost" by diffusion into solution, tip-substrate diffusion is also much slower, and hence the current enhancement is less than when the two UMEs are close.

4.4.1 Simulation

A computer simulation was developed that modeled the heterogeneous comproportionation current behavior at constant potential. In essence, this involved the standard diffusion problem for SECM feedback[195] with an irreversible boundary condition at the substrate electrode surface that considered the comproportionation process. A two species problem was considered in which the diffusion of Cu^{I} and Cu^{II} in the SECM tip/substrate domain was described by:

$$\frac{d[Cu^{I}]}{dt} = D\left[\frac{d^2[Cu^{I}]}{dr^2} + \frac{1}{r}\frac{d[Cu^{I}]}{dr} + \frac{d^2[Cu^{I}]}{dz^2}\right] \quad \text{(Eq. 4.1)}$$

$$\frac{d[Cu^{II}]}{dt} = D\left[\frac{d^2[Cu^{II}]}{dr^2} + \frac{1}{r}\frac{d[Cu^{II}]}{dr} + \frac{d^2[Cu^{II}]}{dz^2}\right] \quad \text{(Eq. 4.2)}$$

where D is the diffusion coefficient of the species of interest (considered to be equal), t is time and r and z are the radial and axial coordinates of the axisymmetric cylindrical geometry defining SECM, as shown in Figure 4.25.

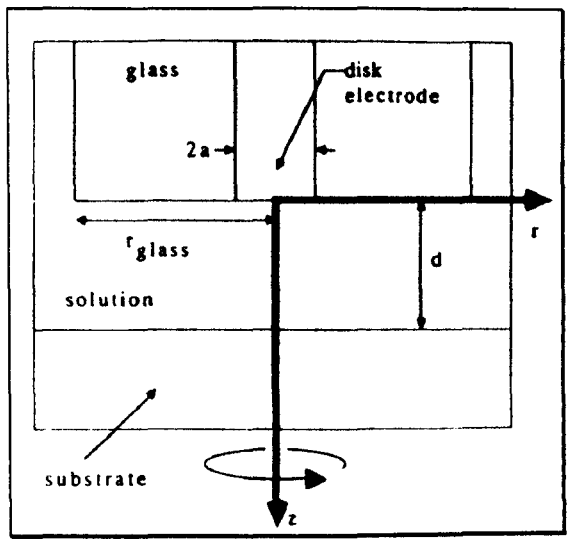

Figure 4.25. A schematic of the SECM geometry.

The boundary conditions applicable to the problem are:

$$0 < r \le a; z = 0 : [Cu^{I}] = 0; \frac{d[Cu^{I}]}{dz} = -\frac{d[Cu^{II}]}{dz} \quad \text{(Eq. 4.3)}$$

$$0 < r \le r_s; z = d : \frac{-d[Cu^{II}]}{dt} = k[Cu^{II}] = \frac{1}{2}\frac{d[Cu^{I}]}{dz} \quad \text{(Eq. 4.4)}$$

$$0 < z \le d; r = 0 : \frac{d[Cu^{I}]}{dr} = \frac{d[Cu^{II}]}{dr} = 0 \quad \text{(Eq. 4.5)}$$

$$0 < z \leq d; r > r_s : [Cu^I] \rightarrow 0; [Cu^{II}] \rightarrow [Cu^{II}]^* \qquad \text{(Eq. 4.6)}$$

where k is the first-order heterogeneous rate constant of the comproportionation reaction between Cu^{II} and Cu and $[Cu^{II}]^*$ is the bulk concentration of $[Cu^{II}]$. In Equs. (4.4) and (4.6), r_s defines the radius of the overall tip end. All the other terms have already been defined. The applicability of an irreversible kinetic model will be considered below.

The problem was cast into the dimensionless form as described elsewhere[171,174], and solved using the program provided as Appendix 2, written by P.R. Unwin. Figure 4.26 shows the behaviour generated by this model.

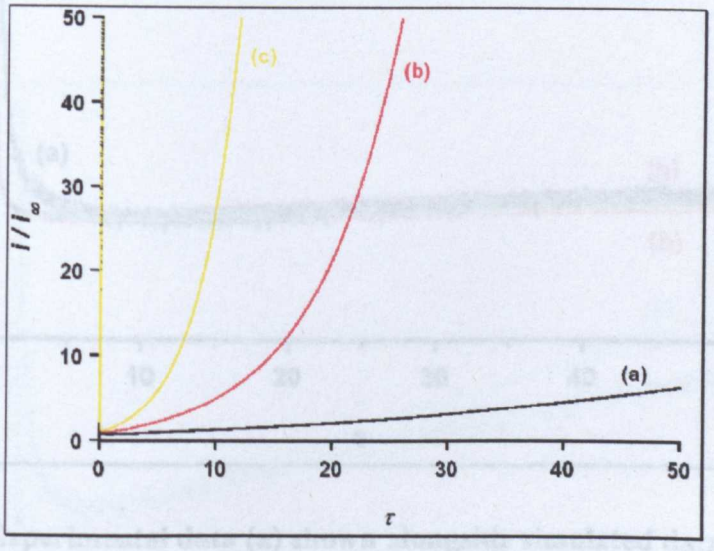

Figure 4.26. Computer simulation output for various normalised rate constants, *K* (=*ka/D*); k is a first order heterogeneous rate constant [cm s^{-1}] and all the other symbols have their usual meaning. The data are for a normalised tip/substrate distance of 0.20 and are shown for K values of: (a) 0.2, (b) 0.3 and (c) 0.4.

This simulation predicted the behaviour of normalised current with respect to normalised time (where $\tau = tD/a^2$). No account was taken of the changing substrate potential and hence attempts to fit such simulated responses to the actual experimental data focused on the short time domain where potential changes were quite small, particularly for the systems involving excess ligand.

Each of the i_T - t curves for the species considered at each value of d, were compared to a range of simulated output at specific values of d/a.

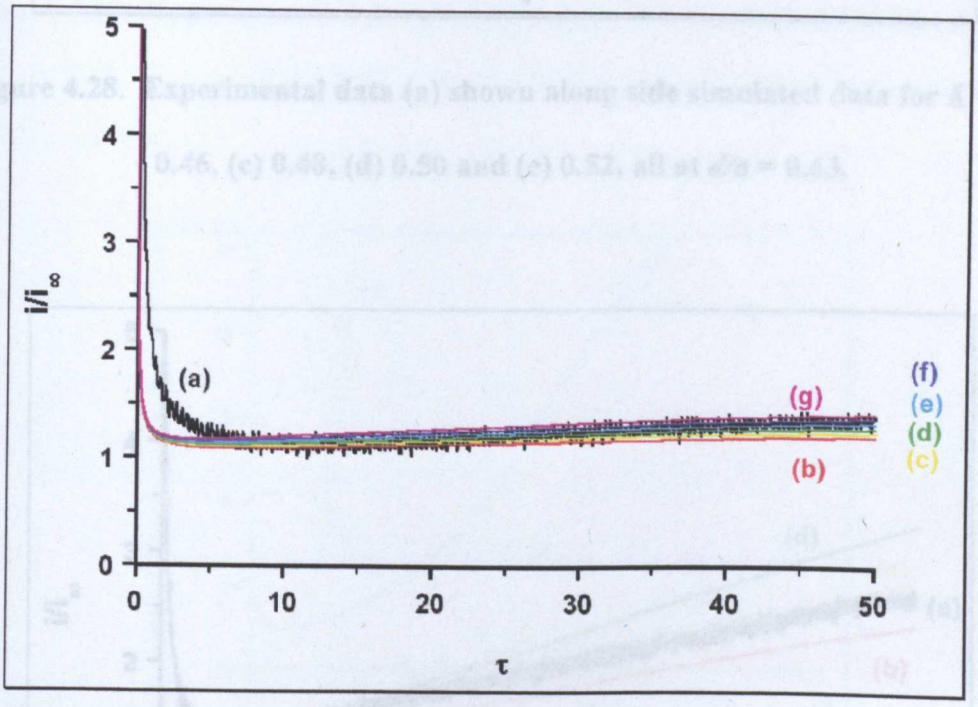

Figure 4.27. Experimental data (a) shown alongside simulated data for K = (b) 0.50, (c) 0.52, (d) 0.54 (e) 0.56 and (f) 0.60, all at d/a = 0.83.

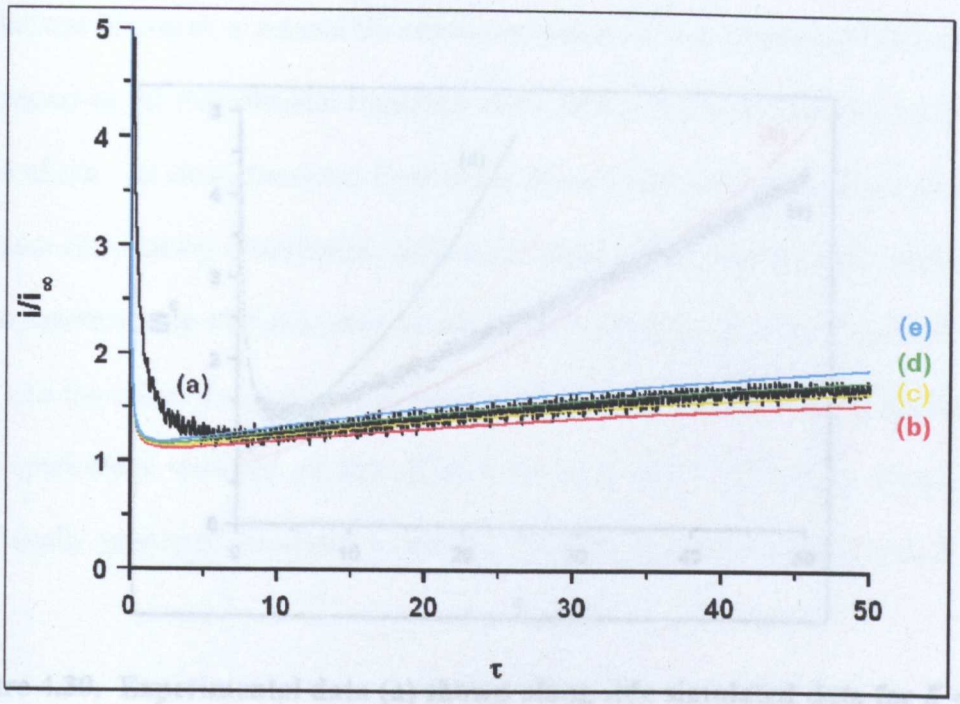

Figure 4.28. Experimental data (a) shown along side simulated data for K = (b) 0.46, (c) 0.48, (d) 0.50 and (e) 0.52, all at d/a = 0.63.

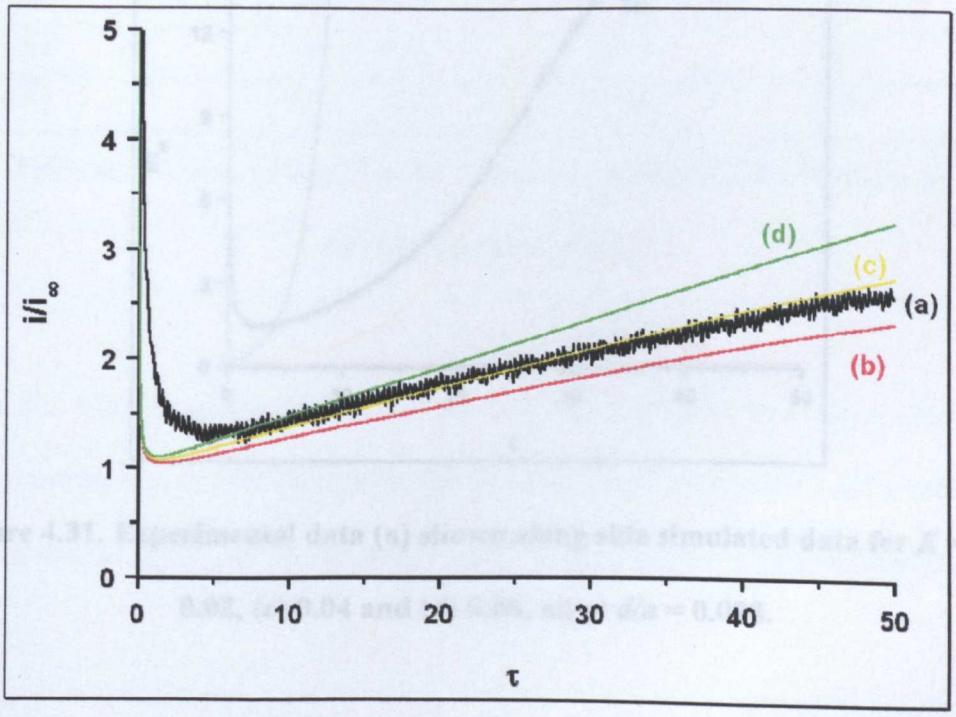

Figure 4.29. Experimental data (a) shown along side simulated data for K = (b) 0.36, (c) 0.38 and (d) 0.40, all at d/a = 0.43.

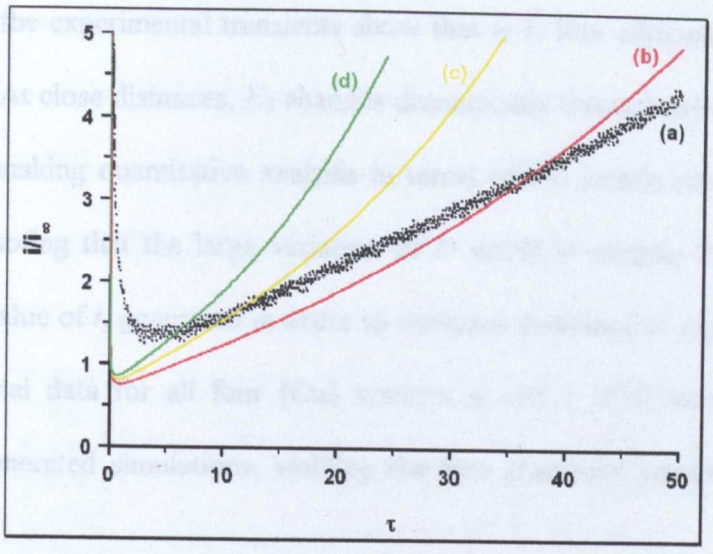

Figure 4.30. Experimental data (a) shown along side simulated data for K = (b) 0.22, (c) 0.24 and (d) 0.26, all at d/a = 0.23.

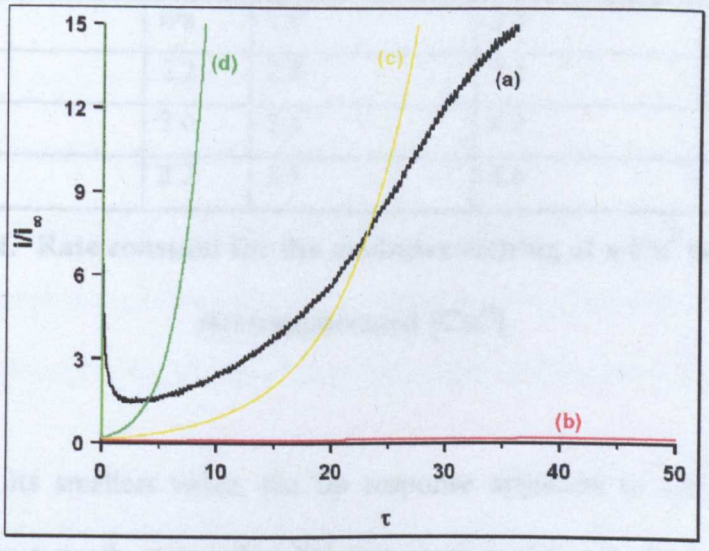

Figure 4.31. Experimental data (a) shown along side simulated data for K = (b) 0.02, (c) 0.04 and (d) 0.06, all at d/a = 0.028.

It can be seen from Figure 4.27 - Figure 4.31 that those transients recorded at large d/a values fitted more readily than those recorded at small d/a values. Moreover, at

the furthest distances a reasonably consistent value of k is obtained. This was not unexpected as the experimental transients show that i_T is less affected by E_S at larger values of d/a. At close distances, E_S changes dramatically throughout the current-time measurement, making quantitative analysis in terms of the simple model difficult. It is also worth noting that the large variation of D noted in chapter 3, will introduce error into the value of t, generated in order to compare simulated to experimental data. The experimental data for all four [Cu] systems at $d/a \geq 0.23$ were compared to theoretically generated simulations, yielding the rate constants summarised in Table 4.1.

Electrode separation	k / (10^{-3} cm s^{-1})			
	CuCl	CuCl/ligand 1	CuCl/ligand 7	CuCl/ligand 9
$d/a = 0.23$	n/a	2.0	2.6	2.1
$d/a = 0.43$	2.2	2.8	3.4	2.3
$d/a = 0.63$	3.0	2.5	4.3	3.3
$d/a = 0.83$	3.3	2.5	4.6	3.3

Table 4.1. Rate constant for the oxidative etching of a Cu^0 surface by electrogenerated [Cu^{II}].

When d/a had its smallest value, the tip response appeared to reach a maximum, before coming to a steady-state value, the perturbation of E_S appeared to be influenced by production of [Cu^{II}] at the tip, which occurred to a greater extent at smaller values of d/a.

In order to investigate the various potentials experienced by the substrate electrode a series of potentiometric measurements were made to elucidate the potentials of the

Cu^0/Cu^I and Cu^I/Cu^{II} couples for each complex. The experiments, although simple, gave a good indication of the range of potentials for the individual couples comprising the systems. The experimental details for these measurements were given in Chapter 2. Both the Cu^0/Cu^I and Cu^I/Cu^{II} (at a Pt indicator electrode) couples were investigated and the results are shown in Figure 4.32 and Figure 4.33 respectively.

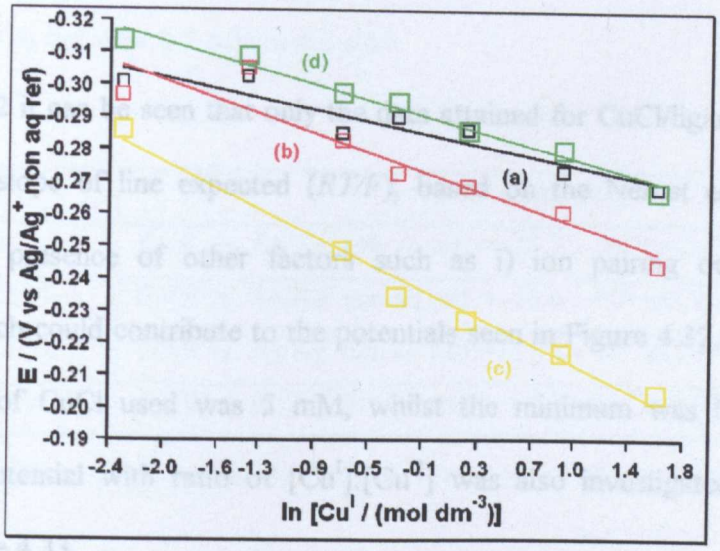

Figure 4.32. Variation of potential with concentration of $[Cu^I]$ for (a) CuCl, (b) CuCl in the presence of ligand 1, (c) CuCl in the presence of ligand 7 and (d) CuCl in the presence of ligand 9. All potentials were recorded in a solution of TEACl (50 mM) / DCE. Errors are indicated via the size of point used.

The equations of each of the linear regression lines, fitted to the data points shown in Figure 4.32 are shown in Table 4.2

Complex	Potential relationship
CuCl	E/ (V vs. Ag/Ag^+ non aq ref) = $8.9 \times 10^{-3} \ln[Cu^I] - 0.28$
CuCl/L 1	E/ (V vs. Ag/Ag^+ non aq ref) = $14.8 \times 10^{-3} \ln[Cu^I] - 0.27$
CuCl/L 7	E/ (V vs. Ag/Ag^+ non aq ref) = $20.1 \times 10^{-3} \ln[Cu^I] - 0.23$
CuCl/L 9	E/ (V vs. Ag/Ag^+ non aq ref) = $12.0 \times 10^{-3} \ln[Cu^I] - 0.29$

Table 4.2. Equations of the best fit regression lines for the Nernst plots shown in Figure 4.32.

From Table 4.2 it can be seen that only the data attained for CuCl/ligand 7 appears to approach the slope of line expected (*RT/F*), based on the Nernst equation. Thus indicating the presence of other factors such as i) ion pairing or ii) Cu oxide formation, which could contribute to the potentials seen in Figure 4.32. The maximum concentration of CuCl used was 5 mM, whilst the minimum was 0.1 mM. The variation of potential with ratio of $[Cu^I]:[Cu^{II}]$ was also investigated, with results shown in Figure 4.33.

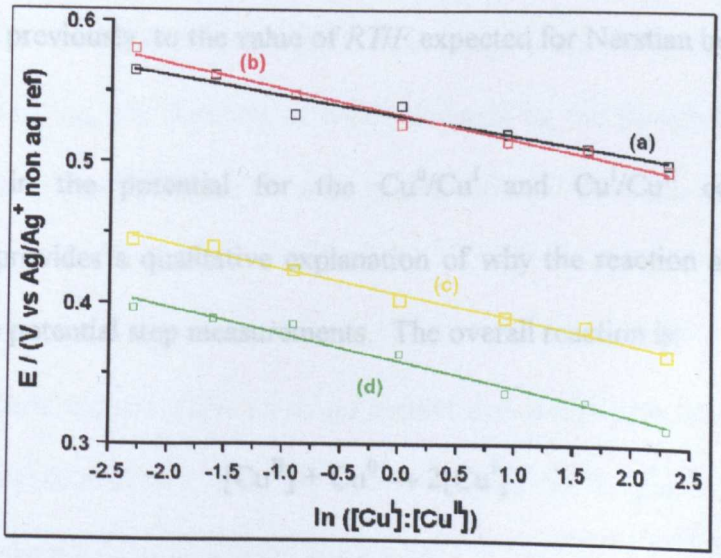

Figure 4.33. Variation of potential with change in ratio $[Cu^I]:[Cu^{II}]$ for (a) $[CuCl]/[CuCl_2]$, (b) $[Cu^I]/[Cu^{II}]$ in the presence of ligand 1, (c) $[Cu^I]/[Cu^{II}]$ in the

presence of ligand 7 and (d) $[Cu^{I}]/[Cu^{II}]$ in the presence of ligand 9. All potentials were recorded in a solution of TEACl (50 mM)/DCE. Error bars are indicated via the size of point used.

Again, the equations of the best-fit regression lines, shown in Figure 4.33 are shown in Table 4.3. Herein the ratios of Cu^{II}:Cu^{I} were made up by altering the concentration of the two species between 0.5 mM and 5 mM.

Complex	Potential relationship
[CuCl]/ [$CuCl_2$]	E/ (V vs. Ag/Ag^+ non aq ref) = $-14.3 \times 10^{-3} \ln[Cu^{I}]/[Cu^{II}] + 0.53$
[CuCl]/ [$CuCl_2$]/L 1	E/ (V vs. Ag/Ag^+ non aq ref) = $-18.0 \times 10^{-3} \ln[Cu^{I}]/[Cu^{II}] + 0.53$
[CuCl]/ [$CuCl_2$]/L 7	E/ (V vs. Ag/Ag^+ non aq ref) = $-17.7 \times 10^{-3} \ln[Cu^{I}]/[Cu^{II}] + 0.41$
[CuCl]/ [$CuCl_2$]/L 9	E/ (V vs. Ag/Ag^+ non aq ref) = $-19.1 \times 10^{-3} \ln[Cu^{I}]/[Cu^{II}] + 0.36$

Table 4.3. Values of the equation for the Nernst plots shown in Figure 4.33.

The slopes of the lines indicated in Table 4.3 are closer, than those for the Cu^{I}/Cu^{0} couples shown previously, to the value of RT/F expected for Nerstian behaviour.

The changes in the potential for the Cu^{0}/Cu^{I} and Cu^{I}/Cu^{II} complexes with concentration provides a qualitative explanation of why the reaction accelerates with time during the potential step measurements. The overall reaction is:

$$[Cu^{II}] + Cu^{0} \leftrightharpoons 2[Cu^{I}] \qquad \text{(Eq. 4.7)}$$

and this involves the two half-reactions:

$$Cu^{I} + e^{-} \leftrightharpoons Cu \qquad E_{Cu^{I}/Cu} \qquad \text{(Eq. 4.8)}$$

$$Cu^{II} + e^{-} \leftrightharpoons Cu^{I} \qquad E_{Cu^{II}/Cu^{I}} \qquad \text{(Eq. 4.9)}$$

The standard potential for the overall comproportionation reaction, (Eq. 4.7), is therefore:

$$E^{\ominus} = E^{\ominus}_{Cu^{II}/Cu^{I}} - E^{\ominus}_{Cu^{I}/Cu} \qquad \text{(Eq. 4.10)}$$

With the SECM experiment, where the substrate is bathed with a solution composition that depends on the tip-substrate distance and time, the substrate potential will be given by:

$$E_{sub} = E_{Cu^{II}/Cu^{I}} - E_{Cu^{I}/Cu} = E^{\ominus}_{Cu^{II}/Cu^{I}} - E^{\ominus}_{Cu^{I}/Cu} + \frac{RT}{F}\ln\frac{[Cu^{II}]}{[Cu^{I}]^2} \qquad \text{(Eq. 4.11)}$$

Initially, there is a small amount of Cu^{II} generated at the tip, which depletes Cu^{I} and enhances Cu^{II} on a very short timescale. According to Eq. 4.11, this explains why, after a diffusional lag, the duration of which depends on the tip-substrate separation ($t_d \approx d^2/D$), the potential begins to shift in the cathodic direction as Cu^{I} gradually builds up.

The potentiometric studies allow us to go further and analyse the likely rate-limiting step. From the potentiometric data, the current-voltage relationships for the two half-cell processes take the form shown in Figure 4.34.

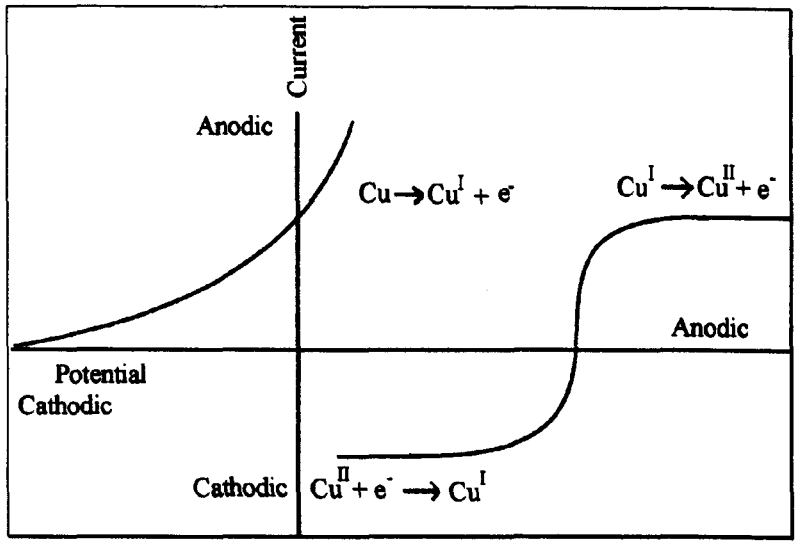

Figure 4.34. Schematic of the current-voltage relationship for the two half cell reactions.

This figure clearly shows that the oxidation of Cu to Cu^{I} will always be driven and the current will be controlled by the redox behaviour of the Cu^{II}/Cu^{I} couple at the substrate. Within the SECM geometry, the tip consumes Cu^{I} and produces Cu^{II} at a diffusion-limited rate, which serves to drive the reaction at the substrate in the direction $Cu^{II} + e^{-} \rightarrow Cu^{I}$. The kinetic data derived thus represents the electron transfer kinetics for the reduction of $[Cu^{II}]$ to $[Cu^{I}]$. The rate constants are similar for all of the complexes studied, which is consistent with the data derived from the voltammetric studies in chapter 3, which showed little difference in the kinetics of the various complexes, even though these were complicated by homogeneous processes.

The hypothesis that the behaviour represents the voltammetric characteristics for the reduction of Cu^{II} to Cu^{I} is borne out when the data at close tip-substrate separations are considered further. In this situation, the SECM approximates most readily to a thin layer cell and the lag in response between the tip current and substrate processes

is at its smallest, making a direct correlation between the two electrode responses most appropriate.

Thus a plot of tip current versus substrate potential should represent a current-voltage curve of the substrate, albeit with the current distorted by the fact that the comproportionation process serves to "inject" reagent with time. Nonetheless, the analysis from Figure 4.17, as an example, bears this out, as shown in Figure 4.35.

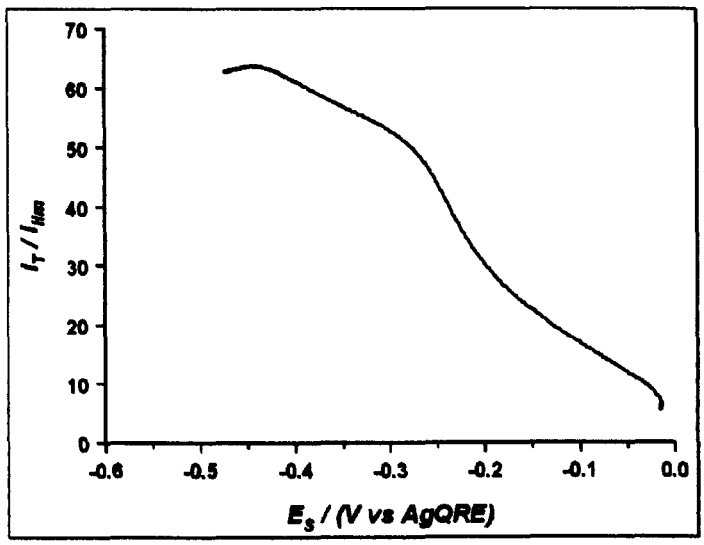

Figure 4.35. Plot of the variation of normalised i_T with E_S, for a separation of d/a = 0.23. Data relate to [Cu_7], taken from Figure 4.17.

At the closest separations (Figure 4.18), the peaks in the current suggests a non-steady state response, indicating transient diffusional effects, which may be due to the reaction proceeding so quickly (potential changing so rapidly) that the hindered diffusion of ligand to co-ordinate to Cu^I produced at the substrate partially limits the reaction at the most driven conditions. This point is taken up briefly in the concluding remarks to this chapter.

4.5 Conclusions

It has been shown that the heterogeneous comproportionation of Cu^{II} complexes with Cu^0, producing Cu^I, can be observed readily with SECM. Addition of ligand causes an increase in the current enhancement due to the reaction of electrogenerated Cu^{II} with Cu^0, which maybe because ligand enhances the solubility of Cu^I in these solutions. A simple model for the SECM reaction at constant potential was applied during the initial stages of reaction and was used to elucidate the rate of the heterogeneous comproportionation. Potentiometric experiments were carried out on a range of $[Cu^I]$ and $[Cu^I]/[Cu^{II}]$ solutions in order to identify the likely rate controlling processes.

It has clearly been shown that the limiting process is effectively the reduction of $[Cu^{II}]$ to $[Cu^I]$ and that this process is similar for all complexes, reasonably consistent with the data in chapter 3. The processes involved in the comproportionation reaction are shown schematically in Figure 4.36.

This applies to most of the tip-substrate distances, where the huge excess of ligand will ensure that the diffusion-limitations of ligand are unimportant. At the closest tip-substrate separations encountered, the picture will change to that shown in Figure 4.37.

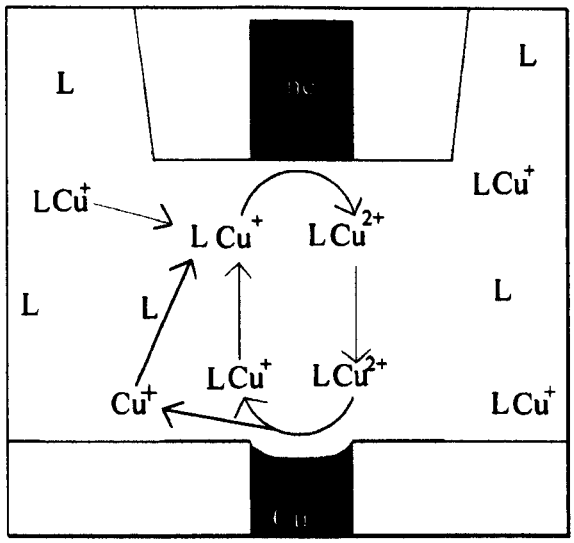

Figure 4.36. Excess ligand (L) in solution will complex Cu^{I}, generated by oxidative etching of the Cu^{0} substrate.

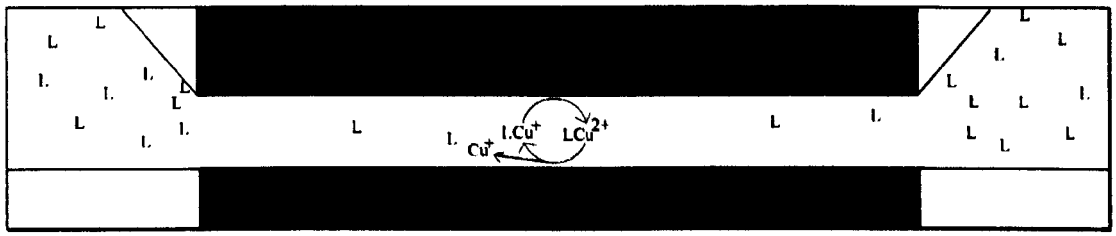

Figure 4.37. When the tip and substrate are very close ligand diffusion into the inter-electrode gap maybe more significant.

In this case ligand diffusion could become important when the reaction is driven. Moreover, if the change in substrate potential with time is rapid, a non steady-state transient response will be expected, as seen in Figures 4.8, 4.13, 4.18 and 4.23. In this situation a more complex analysis is needed than considered in this chapter.

Chapter 5 - Voltammetric studies of [Co(dmgBF$_2$)$_2$] and associated complexes and their reaction with an alkyl halide.

This chapter describes measurements of the kinetics of the reaction of various [Co^I] with an alkyl halide (RX), ethyl-2-isobromobutyrate (E2IBB). The [Co^{II}] described herein and in chapter 6 were originally developed to act as catalytic chain transfer agents (CCTA) in catalytic chain transfer polymerisation (CCTP). They have also been used in ATP, where the initiation reaction involves [Co^I] reacting with E2IBB LSV at UMEs was used to examine the reaction of [Co^I] and E2IBB. Electrochemical measurements were carried out in acetonitrile, DCE and mma. The kinetics of this process are reported.

5.1 [Co] as polymerisation catalysts

Square planar, low spin [Co] can act as either CCTA for monomers with a β hydrogen, for example mma or as catalysts for ATP for monomers without a β hydrogen[28]. The success of these complexes as catalysts is highly dependent on the structure of [Co]. CCTAs assist polymerisation by yielding a product with lower number average molecular weight (M_n) and narrow polydispersity index (PDI); both aspects are highly important in producing commercially useful polymers. The mechanism of this reaction is shown in Scheme 5.1.

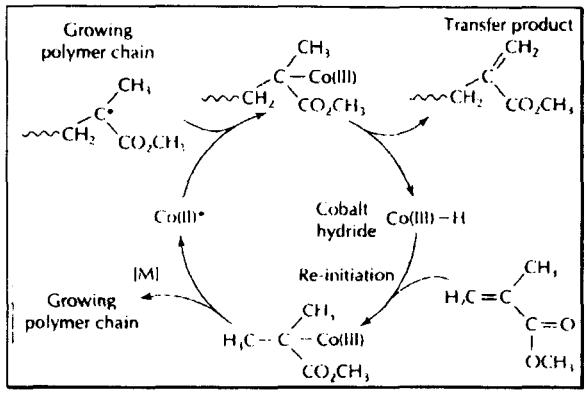

Scheme 5.1. The mechanism of CCTP.

The catalytic cycle shown in Scheme 5.1 indicates that [Co] cycles through a number of redox states during a CCTP. Tada[54] stated that $[Co^{III}]H^-$ may be regarded as an acid form of Co^I, namely, $[Co^I]H^+$ [227,228], although it was stated that $[Co^{III}]H^-$ had not been identified. Further evidence that Tada's assertion was correct came from the ability of $[Co^{III}]H^-$ to add to alkenes, resulting in "hydrocobalation"[229,230], an intermediate step in alkene reduction[231,232,233,234]. Scheme 5.2 shows this reaction in greater detail.

$$[Co(dmgH)_2]H + RCH{=}CH_2 \rightarrow RCH(Me)[Co(dmgH)_2]$$

Scheme 5.2. Hydrocobalation.

5.2 The formation and properties of $R[Co^{III}]$.

Previously, in this thesis the reaction of $[Co^I]$ with n-alkyl halides was described as generally following a S_N2 mechanism, whereas the reaction of more hindered species, such as vicinal dihalides followed an E_2 mechanism. As the former is an addition reaction, it is one way in which $R[Co^{III}]$ may be synthesised. The longevity of such species varies enormously and has provided avenues for researchers to investigate.

Iwunze et al[48] conducted a study of the reactions of cobalt complexes with dihalides. The catalytic reduction of vicinal dibromides via [Co^I] catalysts was investigated. Addition of three different dibromides were found to yield large increases in the [Co^{II}]/[Co^I] wave and no appearance of a [Co^{III}]/[Co^{II}] wave. The reaction of [Co^I] and RBr_2 produced an intermediate of R[Co^{III}] that was either shortlived on the timescale of the measurement or spontaneously decomposed on formation and, as such, could not be detected. The reaction was found to proceed via either a radical or E_2 mechanism, which are kinetically indistinguishable and in the case of [$Co^I(B_{12})$], the rate determining step (rds) was found to be iset from [$Co^I(B_{12})$] to RBr_2. An alternative pathway of β-elimination was proposed[30] and compared to the E_2 pathway, but, in both cases the rds was found to be the reaction of [Co^I] with RBr_2 and hence the pathways were kinetically indistinguishable.

For large reactant (RBr_2):catalyst ([Co^I]) ratios, the rds is psuedo-first order in catalyst and Equ 5.1 applies for steady-state measurements at UMEs.

$$i_c/i_{lim} = 1 + a(\pi/4)(k_c/D)^{1/2} \qquad \text{(Eq. 5.1)}$$

where k_c is the pseudo-first order rate constant of the coupled chemical reaction, i_c is the magnitude of the [Co^{II}]/[Co^I] wave in the presence of RBr_2 and i_{lim} is the magnitude of the diffusion-limited current of the same couple in the absence of RBr_2. In a study of the reaction of $M^{II}PcTS^{6-}$ or MPc^{2-} (where M was Ni or Cu) with RX_n, Kamau and Rusling[235] found the reaction was similar to that of [Co^I] with RBr_2. The reaction proceeded via either a radical or a concerted E_2 process meaning that

whichever pathway was operative, the rds was the same and hence the mechanisms were indistinguishable. The rds was made psuedo first order in catalyst by using a large excess of RX. On addition of RX to solutions containing the catalyst, the single wave for the reduction of [Co^{II}], was seen to increase in magnitude without the appearance of other waves, thus indicating the spontaneous decomposition of any product to yield the original electroactive species. Experimental square wave voltammetry (SWV) results were compared to simulated data for an EC' process and were found to agree well. The waves were used to estimate the apparent pseudo-first order rate constant for the reaction between $M^{II}PcTS^{6-}$ or MPc^{2-} and RX_n. It was concluded that: "the description of the electrochemical catalytic data by EC' simulation is adequate, even though the detailed reaction mechanisms may be more complex".

Zhou et al[242] used Vitamin B_{12}, [Co(PCTA)] and [Co(salen)] as catalysts in the reduction of benzyl bromide (benzyl-Br), which had already been shown to form stable benzyl[Co^{III}] species[242]. The Co-C bond in this species was shown by Schrauzer and Grate[91] to be labile, however, this was found to have little effect on the voltammetric timescale i.e. the Co-C bond was stable during the CV experiment. Sterically unhindered [Co^{I}] generally react with RX via an S_N2 mechanism. Zhou showed that the oxidative addition of benzyl-Br to [$Co^{I}(B_{12})$] in DMF occurred via an iset, as shown in Scheme 5.3.

$$[Co^{I}(B_{12})] + PhCH_2Br \rightarrow [Co^{II}(B_{12})] + PhCH_2^{\cdot} + Br^{-} \quad \text{(iset)}$$

$$[Co^{II}(B_{12})] + PhCH2^{\cdot} \rightarrow PhCH_2[Co^{III}(B_{12})] \quad \text{(coupling)}$$

Scheme 5.3. The reaction of [$Co^{I}(B_{12})$] with benzyl-Br.

The overall process shown in Scheme 5.3 for [$Co^{I}(B_{12})$] and other [Co] investigated were said to be kinetically equivalent and therefore Zhou treated the S_N2 reactions as iset[236]. The systems were examined by cyclic voltammetry and a single peak was reported for the reduction of [Co^{II}] alone, which changed to two peaks on addition of benzyl-Br. The first peak was attributed to the [Co^{II}]/[Co^{I}] couple and was located at a lower over-potential, than for the same couple in the absence of benzyl-Br. The peak remained at the same magnitude as before the addition of benzyl-Br and became more irreversible. The reverse scan peak current of the [Co^{I}]/[Co^{II}] couple also reduced in size and gradually disappeared as a function of scan rate (v) and ratio of reactant to catalyst (ρ). Complete disappearance of the [Co^{I}]/[Co^{II}] wave occurred at different ρ and v for each species. The behaviour was compared to an EC mechanism and computer simulations were shown to qualitatively reproduce the experimental results.

In this study, Zhou found that a plot of i_2/i_1 (where i_1 was the magnitude of the current obtained for the [Co^{II}]/[Co^{I}] couple and i_2 was the current obtained from the benzyl[Co^{III}]/benzyl[Co^{II}] couple) vs. log k_c were different for B_{12} and [Co(salen)]. The conclusion was drawn that the coupling reaction, of benzyl to [Co^{I}], influenced the current by controlling the rate of benzyl[Co^{III}] formation. As such, the rds was not the coupling reaction involving the complex. Rather, reductive cleavage rates were directly related to the strength of the Co-C bond after a one electron reduction[237]. Salen ligand allowed more extensive delocalisation of charge, such that the reductive intermediate was stabilised with salen as equatorial ligand.

With reference to Scheme 5.4, which follows, it was proposed that competition between homolysis, Scheme 5.4(d) and heterolysis, Scheme 5.4 (e), of the Co-C bond should depend on the redox potentials of the $[Co^{II}]/[Co^{I}]$ and the $PhCH_2^{\cdot}/PhCH_2^{-}$ couples which governed the free energy of the electron exchange reaction in Scheme 5.4(g). A further conclusion was that the competition between homolytic and heterolytic cleavage may depend further on the availability of H^+ in solution[238]. The largest values of i_2/i_1, for any complex, were seen in media containing H_2O, which was attributed to either the polarity or the acidity of the medium. Such properties may play a role in the specific catalytic activity. Where the electrochemical reduction of benzyl-Br occurred at a sufficiently negative potential, the initial radical was reduced at a diffusion-controlled rate to benzyl anion. Thus, the radicals were too short lived even if dimerisation was fast[239,240].

In order to carry out controlled potential electrolysis of benzyl bromide, a more positive potential than that of the reduction of B_{12} must be used. As benzyl radicals are stable at the potential of B_{12} reduction, such species may dimerise to give bibenzyl. Zhou showed that despite the complexity, of the mechanism Scheme 5.4, i_2 represented the overall reaction kinetics of the mediated electroreduction of benzyl-Br to stable products[30]. As such, i_2/i_1 was used to make qualitative comparisons of the rates of catalytic benzyl bromide reduction.

Controlled potential electrolysis was also carried out on solutions of $[Co^{II}]$/benzyl-Br. The products of the reaction were either bibenzyl, derived from a radical pathway or toluene, from an anionic route. Scheme 5.4 summarises the range of proposed

pathways. In this scheme HS is solvent and [Co] is either B_{12}, [Co(PCTA)] or [Co(salen)].

Electrode	$[Co^{II}] + e^- \leftrightharpoons [Co^{I}]$	(a)
	$[Co^{I}] + PHCH_2Br \rightarrow PHCH_2[Co^{III}] + Br^-$	(b)
	$PHCH_2[Co^{III}] + e^- \rightarrow PHCH_2[Co^{III}]^{\cdot -}$ or $[Co^{II}]$	(c)
	$PHCH_2[Co^{II}] \rightarrow PHCH_2^{\cdot} + [Co^{I}]$	(d)
	$PHCH_2[Co^{II}] \rightarrow PHCH_2^{-} + [Co^{II}]$	(e)
Electrode	$PHCH_2^{\cdot} + e^- \rightarrow PHCH_2^-$	(f)
	$PHCH_2^{\cdot} + [Co^{I}] \leftrightharpoons PHCH_2^- + [Co^{II}]$	(g)
	$PHCH_2^{\cdot} + HS \rightarrow R + S^{\cdot}$	(h)
	$PHCH_2^- + H^+ \rightarrow RH$	(i)
	$PHCH_2^{\cdot} + PHCH_2^{\cdot} \rightarrow PhCH_2CH_2Ph$	(j)
	$PHCH_2^- + PHCH_2Br \rightarrow PhCH_2CH_2Ph + Br^-$	(k)

Scheme 5.4. Proposed pathways for the reduction of benzyl bromide by $[Co^{I}]$.

Once generated in step Scheme 5.4(b), benzyl$[Co^{III}]$ was shown to breakdown via a complicated series of electrode and chemical reactions[21]. The presence of radical intermediates in these reactions was supported by labelling, stereochemical and theoretical studies as well as ESR spectroscopy and studies of the properties of the C-Co bond in model compounds. It was argued that, in general, electron transfer to $R[Co^{III}]$ weakens the Co-C bond[241]. For example, a one electron reduction of

$R[Co^{III}(B_{12})]$ decreases the Co-C bond strength by 50% and homolysis rates are enhanced by more than an order of magnitude[242]. Electron transfer to $PhCH_2[Co^{III}]$ generated either $PhCH_2[Co^{III}]^{\cdot}$ or $PhCH_2[Co^{II}]^{-}$, depending on the initial electron accepting site. The site was controlled by the relative energies of the Co-C σ^* and ligand delocalised π^* molecular orbitals which, in turn, were related to the nature of the Co bound residue, $PhCH_2$ and ligand. An intramolecular thermal electronic transition from the π^* molecular orbital was proposed to yield the transient species, $PhCH_2[Co^{II}]^{-}$, through which Co-C bond cleavage occurred, Scheme 5.4(d) and (e). However, the pathway described was stepwise and since bond cleavage could either be stepwise or concerted, an alternative pathway involving concerted Co-C breaking, followed by a one-electron reduction, could occur. Any $[Co^{I}]$ and $[Co^{II}]$ produced is this reaction would be available to undergo further alkylation, while any benzyl radical produced was reduced to benzyl anion at the electrode via Scheme 5.4(f) or by $[Co^{I}]$, Scheme 5.4(g).

5.2.1 Summary of $[Co^{I}]$/RBr electrochemistry.

In a general voltammetric experiment, of an initial cobalt species $[Co^{II}]$, a single reduction peak is typically seen for the one-electron transfer to $[Co^{II}]$ producing $[Co^{I}]$. A solution of RX alone may also show a reduction if it is electroactive in the potential window of interest. However, direct electron transfer to RX usually occurs at large cathodic over-potentials and may be difficult to detect. When both [Co] and RX are present, the potential of the $[Co^{II}]/[Co^{I}]$ couple may be more positive than the original wave. Additionally, in a CV experiment the reverse peak due to the $[Co^{I}]/[Co^{II}]$ couple may disappear, indicating that electrogenerated $[Co^{I}]$ has reacted in solution[242]. These peak potential changes are indicative of an E_rC_{ir} reaction mechanism[243]. A

second, new cathodic peak, may also appear, somewhere between that of $[Co^{II}]/[Co^{I}]$ and reduction of RX[242]. This has been assigned to the electro-reduction of $R[Co^{III}]$. However, if $R[Co^{III}]$ is very short-lived, compared to the experimental timescale, then a single catalytic wave/peak (technique dependent) will occur, on addition of greater amounts of RBr, corresponding to an EC' system.

5.3 Effect of BF_2 bridging group

The BF_2 group is strongly electron withdrawing and hence replacement of the –H-bridge in $Co^{II}(dmgH_2)_2$ with $-BF_2-$ in $Co^{II}(dmgBF_2)_2$ decreases the electron density on the central cobalt atom. However, the methyl groups on the pendant arms of the species are electron-donating, countermanding the electron-withdrawing effect of the BF_2 group. These methyl groups may be replaced by other groups[244] as in the case of $[Co^{II}(dmegBF_2)_2]$ and $[Co^{II}(degBF_2)_2]$ and a whole range of other variants. By adjusting the groups on these alkyl arms, the electron density at the central cobalt may be finely tuned, e.g. $[Co(dpgBF_2)_2]$ has a central cobalt atom with very low electron density, as the electron donating ability of the phenyl groups is much lower than that of long alkyl chains. As electron density of the central cobalt atom decreases, so axial co-ordination of ligands is facilitated[244]. Obviously, the solubility of such species is also altered by changing these bridging and equatorial groups.

5.4 BF_2 linked molecules and oxygen interaction

Nonaka and Hamada[244] have stated that because of the reduced electron density at the central cobalt atom, donation from the metal dz^2 orbital to oxygen π^* orbital is diminished. This is because the dz^2 molecular orbital is low-lying when compared to the dz^2 orbital of the central cobalt in $[Co^{II}(dmgH_2)_2]$. Consequently, R[Co]

complexes of $[Co(dmgBF_2)_2]$ and $[Co(dpgBF_2)_2]$ remain stable on exposure to atmospheric oxygen, whereas $[Co(dmgH)_2]$ and $[Co(dpgH)_2]$ are oxidised immediately on exposure to air. It was also shown that BF_2 substituted $[Co^{II}]$ complexes were also stable in an atmosphere of oxygen in a solution of DMF. This anomalous behaviour was attributed to the strength of the bond between cobalt and carbon, thus hindering the exchange of oxygen for alkyl group. This prior work was important in handling and studying the cobalt complexes herein.

5.5 Experimental

The main experimental details were provided in Chapter 2. Solutions of individual [Co] (0.5 mM) and TBAP (50 mM) were made up in an oxygen free atmosphere. The solid was added directly into a volumetric flask, which was placed, via a purgable chamber, into a glove box. Solvent was added once all the components were sealed in the previously purged glove box, which was maintained at a positive pressure to ensure an oxygen free environment.

Where mma was used as solvent, it was filtered through a column of basic alumina immediately prior to use to remove polymerisation inhibitors. All organic solvents were stored over activated 4Å molecular sieves in order to dry them.

5.6 Results and Discussion

The voltammetric characteristics of three $[Co^{II}]$ were examined in three different solvents, DMF, MeCN and mma. A Pt UME (a = 12.5μm) was used unless stated otherwise. After an LSV had been recorded for the reduction of a $[Co^{II}]$ species of interest in a solvent containing supporting electrolyte, a defined quantity of E2IBB

was added to the electrochemical cell. The contents of the cell were then agitated via use of a stream of N_2, which had been plumbed into the glove box. After this thorough mixing of contents a further LSV was recorded, which showed an increase in the diffusion-limited current for the reduction of [Co^{II}]. This process was repeated twice more to give LSVs for the reduction of [Co^{II}] alone, [Co^{II}]:10E2IBB, [Co^{II}]:20E2IBB and [Co^{II}]:40E2IBB. The steady-state LSV results of these experiments form the basis of this chapter.

5.6.1 Voltammetric characteristics in DMF.

It was first necessary to verify that E2IBB was not electroactive in the potential range of interest. LSVs were therefore recorded, first with a solution of supporting electrolyte in solvent and second in the same solution with excess E2IBB (10 mM).

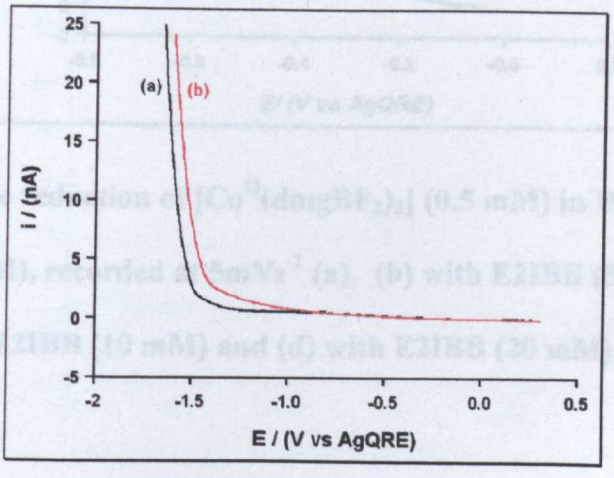

Figure 5.1. Line (a, black), shows the reduction potential window with solvent and supporting electrolyte alone, whilst (b, red) shows the reduction of E2IBB (10 mM) in DMF containing THABr (50 mM). Voltammograms were recorded at 5 mV s^{-1}.

The results in Figure 5.1 indicate that E2IBB is not electroactive within the region of $[Co^{II}]$ reduction (*vide infra*).

LSVs were obtained for each of the three $[Co^{II}]$. Figure 5.2 shows four LSVs for the reduction of $[Co^{II}(dmgBF_2)_2]$, recorded with various amounts of E2IBB. Figure 5.3 shows results of analogous experiments for $[Co^{II}(megBF_2)_2]$, while Figure 5.4 shows results for $[Co^{II}(degBF_2)_2]$.

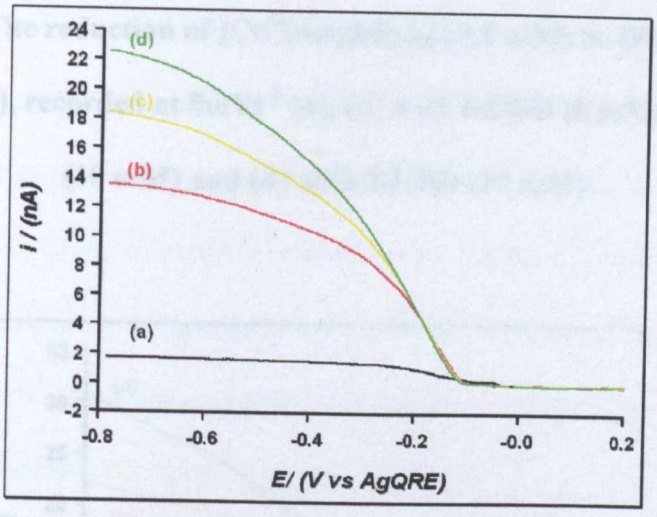

Figure 5.2. The reduction of $[Co^{II}(dmgBF_2)_2]$ (0.5 mM) in DMF containing THABr (50 mM), recorded at $5mVs^{-1}$ (a), (b) with E2IBB (5 mM), (c) with E2IBB (10 mM) and (d) with E2IBB (20 mM).

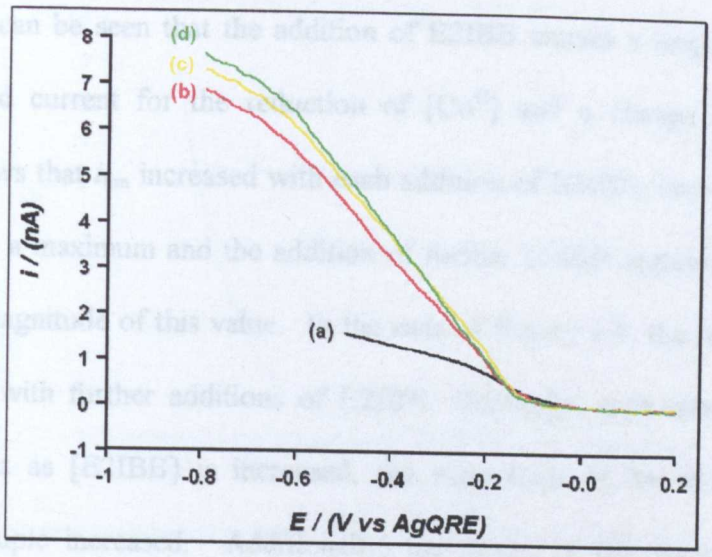

Figure 5.3. The reduction of $[Co^{II}(megBF_2)_2]$ (0.5 mM) in DMF containing THABr (50 mM), recorded at $5mVs^{-1}$ (a), (b) with E2IBB (5 mM), (c) with E2IBB (10 mM) and (d) with E2IBB (20 mM).

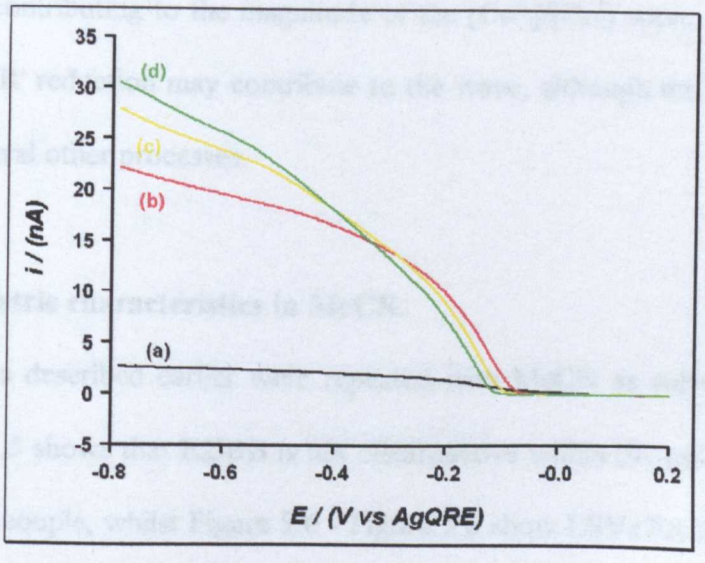

Figure 5.4. The reduction of $[Co^{II}(degBF_2)_2]$ (0.5 mM) in DMF containing THABr (50 mM), recorded at $5mVs^{-1}$ (a), (b) with E2IBB (5 mM), (c) with E2IBB (10 mM) and (d) with E2IBB (20 mM).

In all cases it can be seen that the addition of E2IBB causes a large increase in the diffusion-limited current for the reduction of [Co^{II}] and a change in wave shape. Figure 5.2 shows that i_{lim} increased with each addition of E2IBB, however, for Figure 5.3 i_{lim} reaches a maximum and the addition of further E2IBB appeared to have little effect on the magnitude of this value. In the case of Figure 5.4, the magnitude of i_{lim} also increased with further additions of E2IBB. Generally, such trends support the supposition that as [E2IBB] is increased, the magnitude of the wave due to the [Co^{II}]/[Co^{I}] couple increased. Additionally, the shape of the waves indicate that although there is an increase in current in the potential region of the voltammogram without E2IBB, a further process at higher over potential leads to a drawn out wave shape. It may be assumed that such a contribution could be due to the formation of R[Co^{III}], which is being reduced at higher over-potentials than [Co^{II}] and thus distorting and contributing to the magnitude of the [Co^{II}]/[Co^{I}] wave. There is also a possibility that $R^{\cdot}$ reduction may contribute to the wave, although this species may be involved in several other processes.

5.6.2 Voltammetric characteristics in MeCN.

The experiments described earlier were repeated with MeCN as solvent, rather than DMF. Figure 5.5 shows that E2IBB is not electroactive within the potential region of the [Co^{II}]/[Co^{I}] couple, whilst Figure 5.6 - Figure 5.8 show LSVs for the reduction of the three different [Co^{II}].

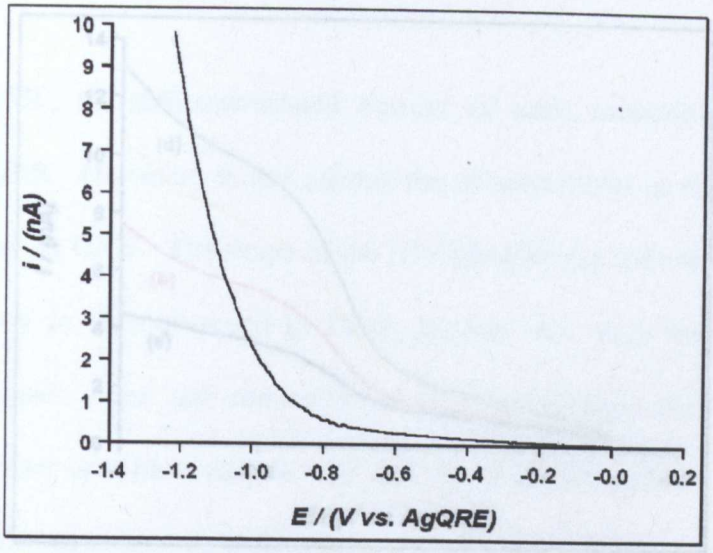

Figure 5.5. Reduction of E2IBB (0.5 mM) in MeCN containing THAP (50 mM) at a 25 μm diameter Pt UME, recorded at 100 mV s^{-1}.

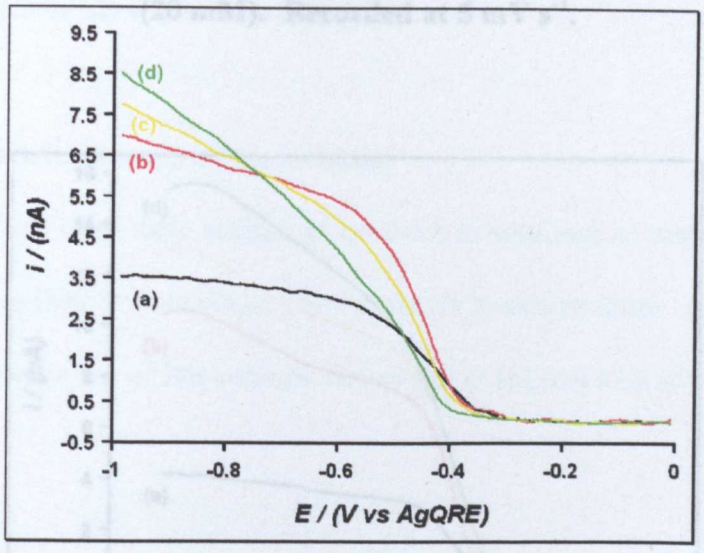

Figure 5.6. The reduction of [$Co^{II}(dmgBF_2)_2$] (0.5 mM) in MeCN with TBAP (50 mM) (a), (b) with E2IBB (5 mM), (c) with E2IBB (10 mM) and (d) with E2IBB (20 mM). Recorded at 5 mV s^{-1}.

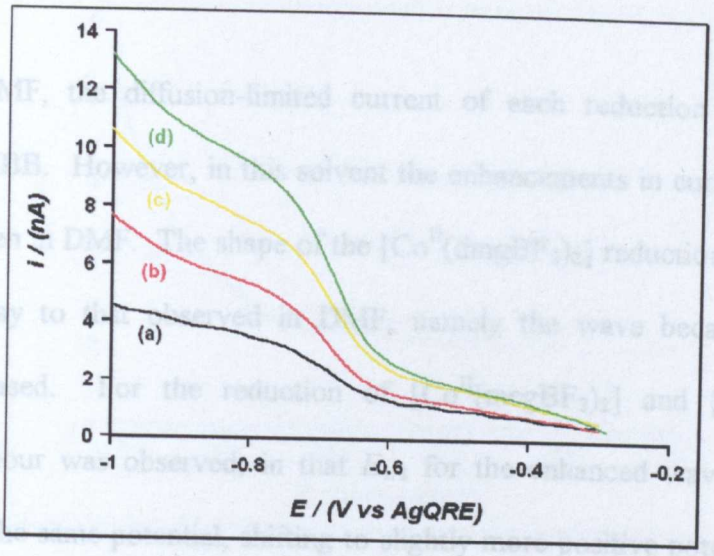

Figure 5.7. The reduction of $[Co^{II}(megBF_2)_2]$ (0.5 mM) in MeCN with TBAP (50 mM) (a), (b) with E2IBB (5 mM), (c) with E2IBB (10 mM) and (d) with E2IBB (20 mM). Recorded at 5 mV s^{-1}.

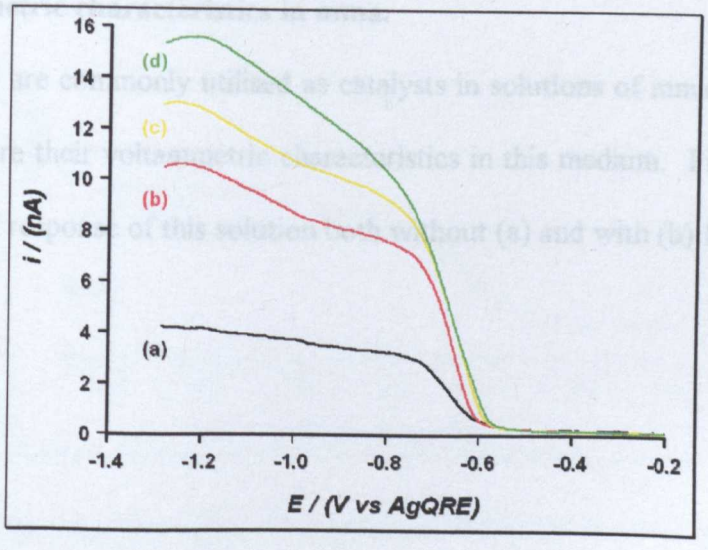

Figure 5.8. The reduction of $[Co^{II}(degBF_2)_2]$ (0.5 mM) in MeCN with TBAP (50 mM) (a), (b) with E2IBB (5 mM), (c) with E2IBB (10 mM) and (d) with E2IBB (20 mM). Recorded at 5 mV s^{-1}.

As seen in DMF, the diffusion-limited current of each reduction increased with addition of E2IBB. However, in this solvent the enhancements in current were much smaller than seen in DMF. The shape of the $[Co^{II}(dmgBF_2)_2]$ reduction wave changed in a similar way to that observed in DMF, namely the wave became broader as [E2IBB] increased. For the reduction of $[Co^{II}(megBF_2)_2]$ and $[Co^{II}(degBF_2)_2]$ different behaviour was observed, in that $E_{1/2}$ for the enhanced waves remained at approximately the same potential, shifting to slightly more positive potentials, whilst a second wave became evident at a potential more negative than the first wave. However, converse to the behaviour observed in DMF, the $[Co^{II}]/[Co^{I}]$ waves are distinct for $[Co^{II}(megBF_2)_2]$ and $[Co^{II}(degBF_2)_2]$, with the later wave appearing at more negative potentials than observed in DMF.

5.6.3 Voltammetric characteristics in mma.

As these $[Co^{II}]$ are commonly utilised as catalysts in solutions of mma, attempts were made to measure their voltammetric characteristics in this medium. Figure 5.9 shows the background response of this solution both without (a) and with (b) E2IBB.

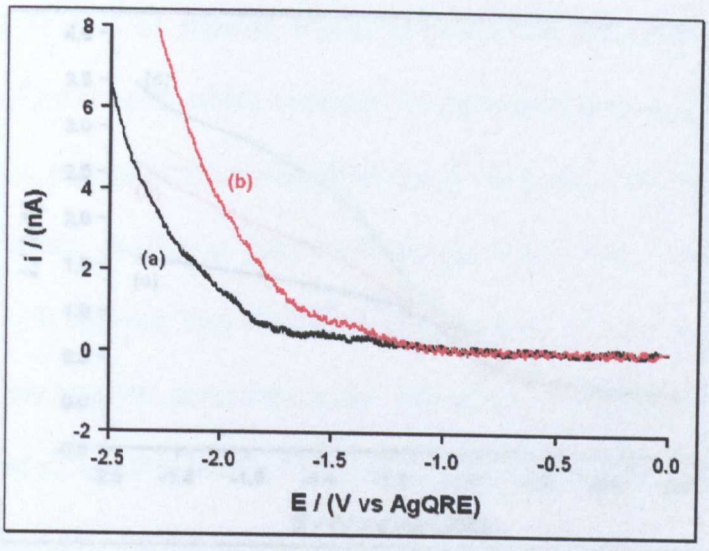

Figure 5.9. Line (b, red) shows the reduction of E2IBB (10 mM) in mma containing THAP (50 mM), while (a, black) shows the potential window without added E2IBB. Both voltammograms were recorded at $5mVs^{-1}$.

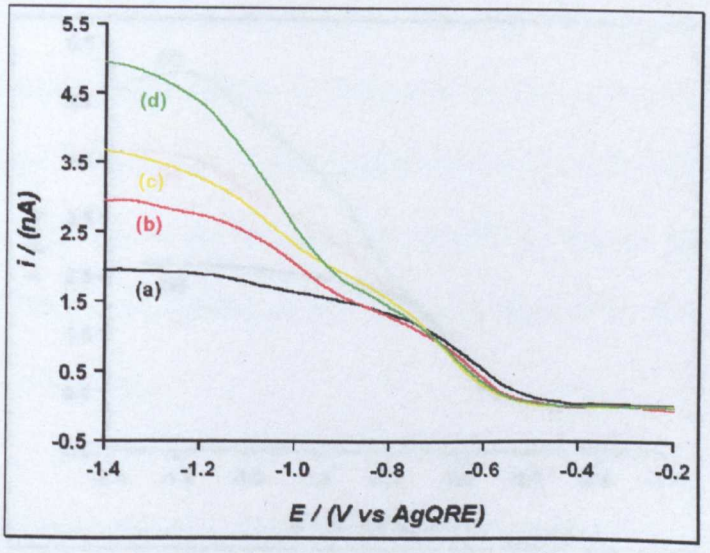

Figure 5.10. The reduction of $[Co^{II}(dmgBF_2)_2]$ (0.5 mM) in mma with TBAP (50 mM) (a), (b) with E2IBB (5 mM), (c) with E2IBB (10 mM) and (d) with E2IBB (20 mM). Recorded at 5 mV s^{-1}.

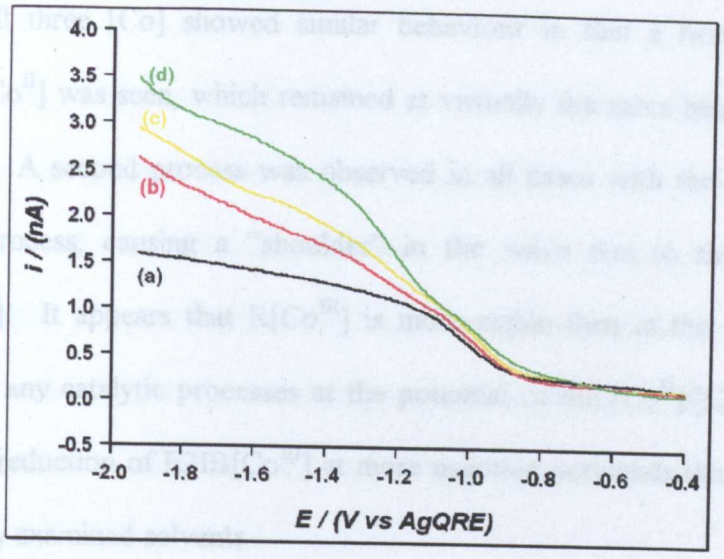

Figure 5.11. The reduction of $[Co^{II}(megBF_2)_2]$ (0.5 mM) in mma with TBAP (50 mM) (a), (b) with E2IBB (5 mM), (c) with E2IBB (10 mM) and (d) with E2IBB (20 mM). Recorded at 50 mV s^{-1}.

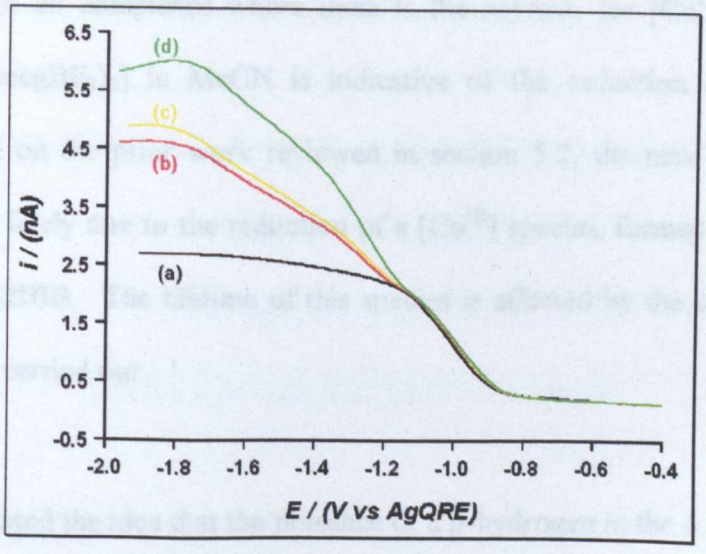

Figure 5.12. The reduction of $[Co^{II}(degBF_2)_2]$ (0.5 mM) in mma with TBAP (50 mM) (a), (b) with E2IBB (5 mM), (c) with E2IBB (10 mM) and (d) with E2IBB (20 mM). Recorded at 500 mV s^{-1}.

In this case all three [Co] showed similar behaviour in that a first wave for the reduction of [Co^{II}] was seen, which remained at virtually the same height as [E2IBB] was increased. A second process was observed in all cases with the possibility of a third, minor process, causing a "shoulder" in the wave due to the reduction of [$Co^{II}(degBF_2)_2$]. It appears that R[Co^{III}] is more stable than in the other solvents. This prevented any catalytic processes at the potential of the [Co^{II}]/[Co^{I}] couple and resulted in the reduction of E2IB[Co^{III}] at more negative potentials than in any of the other previously examined solvents.

5.6.4 Interpretation

Qualitatively, conclusions may be drawn about the processes occurring from the shapes of the waves observed in the three different solvents. The second redox process seen for all complexes where mma is the solvent, for [$Co^{II}(degBF_2)_2$] and possibly [$Co^{II}(megBF_2)_2$] in MeCN is indicative of the reduction of a new [Co] species. Based on the prior work reviewed in section 5.2, the new electrochemical process is most likely due to the reduction of a [Co^{III}] species, formed by the reaction of [Co^{I}] with E2IBB. The lifetime of this species is affected by the solvent in which the reduction is carried out.

Chapter 1 presented the idea that the presence of a β-hydrogen in the R group attached to the central atom in a R[Co^{III}] species aids stabilisation. Thus any complex formed where the axial ligand positions are occupied by mma molecules is likely to be more stable than a complex without a β-hydrogen containing alkyl group. Thus, it is most likely that an R[Co^{III}] complex is formed directly after reduction of [Co^{II}] to [Co^{I}], and that this complex then undergoes reduction at the UME.

In MeCN there were two waves for the reduction of $[Co^{II}(degBF_2)_2]$ and perhaps $[Co^{II}(megBF_2)_2]$ and a single wave for $[Co^{II}(dmgBF_2)_2]$. For all of these complexes, however, the overall pattern is that the first wave is significantly enhanced with increasing [E2IBB], with the second wave rather minor in comparison. In DMF this trend is found more significantly, with huge enhancements in the first wave, which shows some "tailing" in the presence of [E2IBB], which could be due to a second, very minor process.

The evidence suggests that the $R[Co^{III}]$ species formed is most stable in mma followed by MeCN, with breakdown of the Co-C bond occurring most readily in DMF. As the LSVs for the three species in DMF and MeCN show increases in the size of i_{lim} the process maybe likened to an EC' mechanism, as shown in Scheme 5.5.

Electrode	$[Co^{II}] + e^- \rightarrow [Co^{I}]$	(a)
Solution	$[Co^{I}] + R \rightarrow R[Co^{III}]$	(b)
	$R[Co^{III}] \rightarrow [Co^{II}] + R^{\cdot}$	(c)

Scheme 5.5. The $[Co^{II}]$ EC' mechanism.

The shapes and separation of the two waves may be taken as a qualitative indicator of $R[Co^{III}]$ stability in each of the three solvents. The formation of the catalytic cycle depends on two solution steps (b and c of Scheme 5.5). Clearly, Scheme 5.5 (c) is fastest in DMF as a separate wave due to $R[Co^{III}]$ reduction is not seen, rather any contribution to i_{lim} from $R[Co^{III}]$ serves to distort the $[Co^{II}]/[Co^{I}]$ wave. Where MeCN is the solvent, a second wave becomes more pronounced, yet the $[Co^{II}]/[Co^{I}]$ wave

increased in magnitude as [E2IBB] increased, indicating that some [Co^{II}] was regenerated due to Scheme 5.5 (c). With mma as the solvent, the [Co^{II}]/[Co^{I}] wave remained at a constant height whilst a second wave simultaneously formed and increased with increase in [E2IBB], thus indicating the apparent differences between the rate of Scheme 5.5 (c). Scheme 5.5 (b) was shown to be the rds by Iwunze[48] and hence by using the changes in magnitude of current as a function of [E2IBB], the rate constant, k_c for step (b) of Scheme 5.5 may be determined.

5.6.4.1. Quantitative interpretation of voltammetric data.

In the case of the EC' mechanism the following chemical reaction causes a large increase in i_{lim}, as the original electroactive species is regenerated by the coupled chemical reaction. There is also an effect on the position of the wave, but the magnitude of the change is depends on the reversibility of the redox couple. Variations in i_{lim} and $E_{1/2}$ may be used to determine k_c for the catalytic reaction. Monitoring changes in i_{lim} with change in substrate concentration is most accurate, as changes in $E_{1/2}$ are small, and precision is thus susceptible to errors, such as the stability of the reference electrode. Such effects are unimportant for i_{lim} measurements. The limiting current in the presence of substrate compared to that without (i_o/i_{lim}) is a measure of the effective number of electrons transferred (N_{eff}).

Rusling[30] studied the reaction of three vicinal dihalides with B_{12}, concluding that for large [substrate]/[catalyst] ratios (ρ) the reaction was pseudo-first order and therefore Eq. 5.1 applied. This expression was proposed by Fleischmann[245], assuming that a microdisc was equivalent to a hemisphere[246].

Several papers have been published that enable the dimensionless rate constant ($K_{EC'}$) to be determined from N_{eff}. Denuault[247,248] derived an expression for $K_{EC'}$ ($= k_c a^2/D$) at a spherical electrode for the second-order case. By using a large excess of substrate, many researchers have arrived at expressions for the pseudo-first order case. Fleischmann[245], Dayton[249] and Diao[250] each produced an expression for $K_{EC'}$ at a spherical electrode. Once steady-state is reached the characteristic radius of a microdisc may be related to that of either a hemisphere or a sphere by the following:

$$a_{hemi} = 2a_{disc}/\pi \qquad \text{Eq. 5.2}$$

$$a_{sphere} = a_{disc}/\pi \qquad \text{Eq. 5.3}$$

The mass transport equations are 1 dimensional for hemispherical and spherical systems so that mechanistic problems can readily be solved analytically[251] by use of a_{hemi} rather than a_{disc} by way of electrode radius. Phillips[252] presented two expressions for determination of $K_{EC'}$ at an UME under psuedo-first order conditions. The two equations are asymptotic in nature, the first was for large rate constants:

$$Neff = \frac{\pi}{4}\left(1+\sqrt{\rho K_{EC'}}+\frac{1}{4}\left(\rho K_{EC'}\right)^{-1/2}\right) \qquad \text{Eq. 5.4}$$

A slightly different expression was presented for small rate constants:

$$Neff = 1+\frac{2}{\pi}\sqrt{\rho K_{EC'}}+\left(\frac{4}{\pi^2}-\frac{1}{3}\right)\rho K_{EC'} \qquad \text{Eq. 5.5}$$

In addition to analytical solutions, simulations, using numerical methods have been presented by Lavagnini[253], Tutty[254] and Alden[255]. The latter of these is available** on the world wide web for public use. A series of working surfaces/curves is available, that may be used to determine the kinetics of coupled chemical reactions, for a range of different mechanisms, from knowledge of i_{lim}, D and $E^{0'}$.

Alden[256] described working curves that related N_{eff} to $K_{EC'}$. Figure 5.13 – Figure 5.17 show the results of his simulation alongside the analytical expressions of Phillips[252]and the results of application of the equations of Delmastro[257] for pseudo-first order kinetics at a spherical electrode. The results of the application of the analytical expression of Denuault[247,248] for second order kinetics at a spherical electrode were also examined. Alden concurred with Denuault that this method was in error by 2% when $\rho = 1$ and 5% when $\rho = 0.1$. Additionally the sphere/disc equivalence broke down at large k_c or ρ.

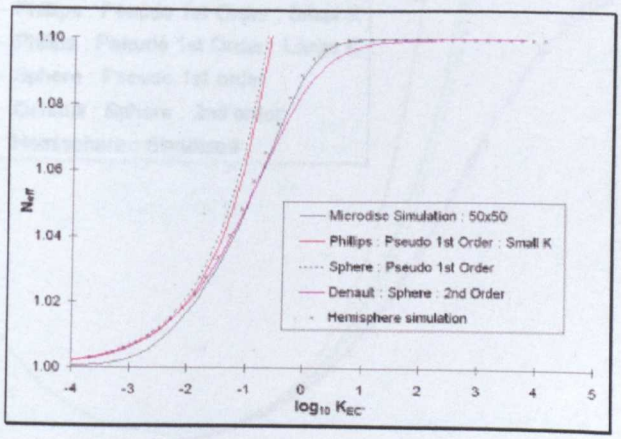

Figure 5.13. Simulated working curve for steady-state, transport limited current at an UME, where $\rho = 0.1$[256].

** www.physchem.ox.ac.uk:8000/wwwda

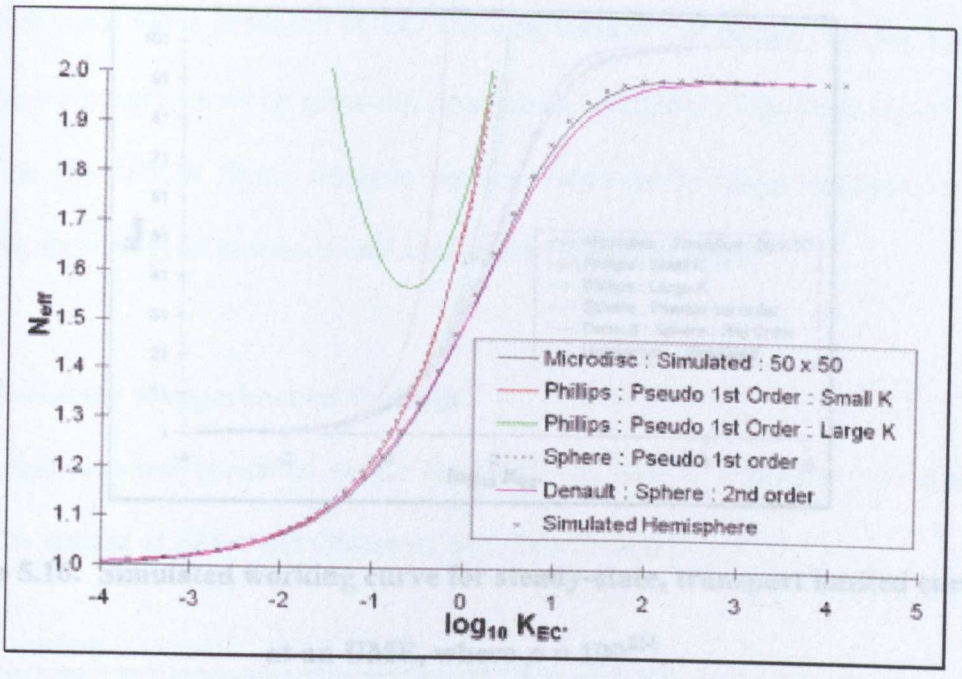

Figure 5.14. Simulated working curve for steady-state, transport limited current at an UME, where $\rho = 1^{256}$.

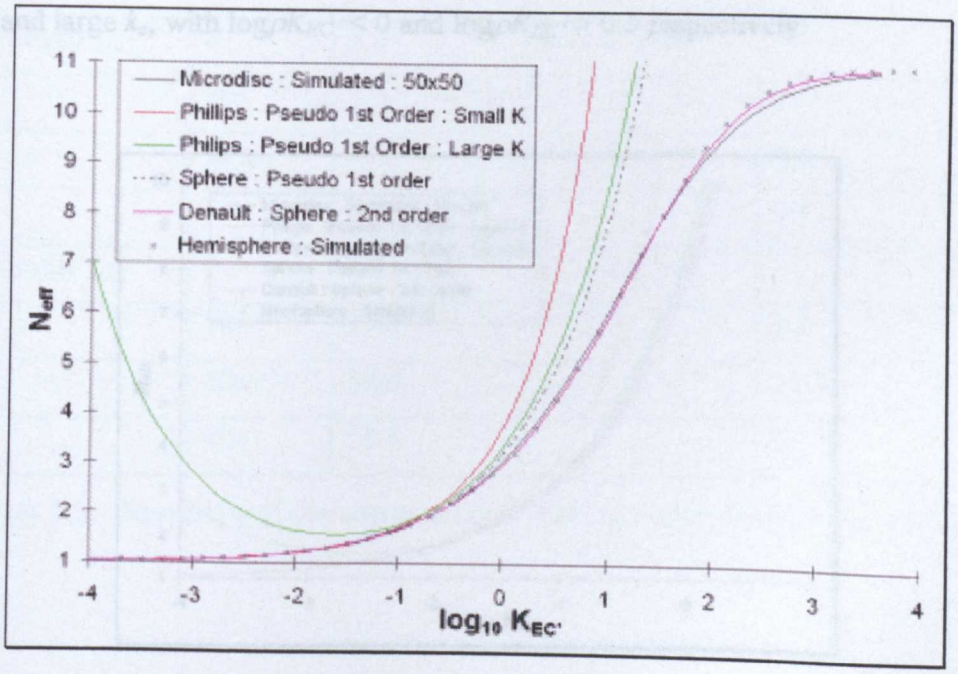

Figure 5.15. Simulated working curve for steady-state, transport limited current at an UME, where $\rho = 10^{256}$.

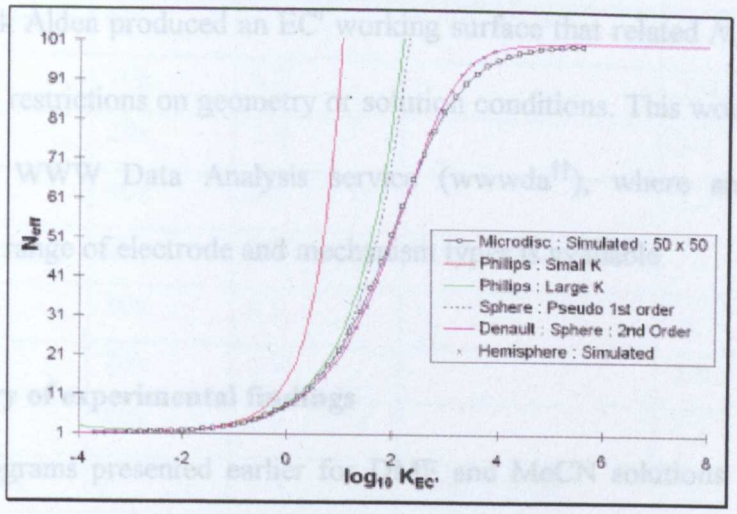

Figure 5.16. Simulated working curve for steady-state, transport limited current at an UME, where $\rho = 100^{256}$.

The pseudo-first order region is depicted in Figure 5.17. This figure shows why Alden concluded that the Phillips' expressions were reliable for ascertaining k_c for small and large k_c, with $\log\rho K_{EC'} < 0$ and $\log\rho K_{EC'} > 0.5$ respectively.

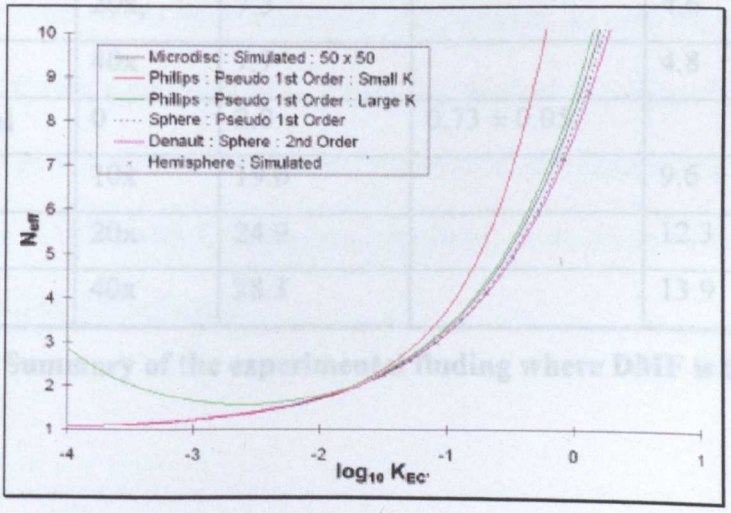

Figure 5.17. Pseudo first order region of the simulated EC' working curve for $\rho = 100^{256}$.

From this work Alden produced an EC' working surface that related N_{eff}, log $K_{EC'}$ and ρ, without any restrictions on geometry or solution conditions. This work provided the basis for the WWW Data Analysis service (wwwda[††]), where analysis of rate constant, for a range of electrode and mechanism types is available.

5.6.5 Summary of experimental findings

The voltammograms presented earlier for DMF and MeCN solutions were analysed using the method of Alden and Compton, and Fleischmann (Eq. 5.1).

Species	E2IBB	i_{lim} / (nA)	D/ (10^{-5} cm^2 s^{-1})	N_{eff} (experimental)
$[Co^{II}(dmgBF_2)_2]$	0	1.6	0.66 ± 0.05	
	10x	13.5		8.5
	20x	18.2		11.5
	40x	22.4		14.2
$[Co^{II}(megBF_2)_2]$	0	1.6	0.63 ± 0.08	
	10x	6.9		4.3
	20x,	7.3		4.6
	40x	7.7		4.8
$[Co^{II}(degBF_2)_2]$	0	2.0	0.73 ± 0.05	
	10x	19.6		9.6
	20x	24.9		12.3
	40x	28.3		13.9

Table 5.1. Summary of the experimental finding where DMF is the solvent.

†† www.physchem.ox.ac.uk/~rgc

Species	E2IBB	i_{lim} / (nA)	D/ (10^{-5} cm^2 s^{-1})	N_{eff} (experimental)
$[Co^{II}(dmgBF_2)_2]$	0	3.1	1.30 ± 0.04	
	10x	6.2		2.0
	20x	7.0		2.3
	40x	8.5		2.7
$[Co^{II}(megBF_2)_2]$	0	2.7	1.13 ± 0.09	
	10x	4.6		1.7
	20x	6.9		2.6
	40x	8.9		3.3
$[Co^{II}(degBF_2)_2]$	0	3.4	1.48 ± 0.08	
	10x	8.2		2.4
	20x	10.4		3.1
	40x	15.5		4.6

Table 5.2. Summary of the experimental finding where MeCN is the solvent.

Values of N_{eff} were measured for the eighteen cases listed in Table 5.1 and Table 5.2. The limiting current, i_{lim}, was measured from the first wave in the case if MeCN and the overall current for DMF. The wwwda program was used to calculate [N_{eff} *(theory)*] for various values of second order rate constant, k_c, until the closest match to the experimental result was obtained. From this method and that of Fleischmann[245], which assumes pseudo-first order kinetics, values of k_c, the second order rate constant for the reaction of [Co^I] with E2IBB were calculated, as shown in Table 5.3 and Table 5.4 for DMF and MeCN solvents.

Species	E2IBB	N_{eff}[‡‡]	k_c/(mol^{-1} cm^3 s^{-1})[§§]	k_c/(mol^{-1} cm^3 s^{-1})[***]
[Co^{II}(dmgBF$_2$)$_2$]	0			
	10x	8.5	5 x 10^8	(7.7 ± 0.6) x 10^7
	20x	11.5	3 x 10^8	(7.5 ± 0.6) x 10^7
	40x	14.2	2 x 10^8	(5.9 ± 0.5) x 10^7
[Co^{II}(megBF$_2$)$_2$]	0			
	10x	4.3	2 x 10^7	(1.4 ± 0.2) x 10^7
	20x	4.6	7 x 10^6	(8.4 ± 1.1) x 10^6
	40x	4.8	3 x 10^6	(4.7 ± 0.6) x 10^6
[Co^{II}(degBF$_2$)$_2$]	0			
	10x	9.6	2 x 10^8	(1.1 ± 0.1) x 10^8
	20x	12.3	4 x 10^8	(9.7 ± 0.7) x 10^7
	40x	13.9	2 x 10^8	(6.3 ± 0.4) x 10^7

Table 5.3. Kinetic parameters for the reduction of three [Co^{II}] (0.5 mM) in DMF containing THABr (50 mM).

Table 5.4 shows how the same methods of analysis were applied to the data obtained in MeCN.

---

‡‡ Experimental value.

§§ Using the method of Alden et al.

*** Using the Fleischmann method (Equ 5.1).

Species	E2IBB	N_{eff}‡‡	k_c /(mol^{-1} cm^3 s^{-1})§§	k_c/(mol^{-1} cm^3 s^{-1})†††
[Co^{II}(dmgBF$_2$)$_2$]	0			
	10x	2.0	5 x 10^6	(2.7 ± 0.1) x 10^6
	20x	2.3	3 x 10^6	(2.3 ± 0.1) x 10^6
	40x	2.7	7 x 10^6	(1.9 ± 0.1) x 10^6
[Co^{II}(megBF$_2$)$_2$]	0			
	10x	1.7	1 x 10^6	(1.1 ± 0.1) x 10^6
	20x	2.6	3 x 10^6	(3.0 ± 0.2) x 10^6
	40x	3.3	4 x 10^6	(3.1 ± 0.2) x 10^6
[Co^{II}(degBF$_2$)$_2$]	0			
	10x	2.4	8 x 10^6	(6.0 ± 0.3) x 10^6
	20x	3.1	9 x 10^6	(6.8 ± 0.4) x 10^6
	40x	4.6	1 x 10^7	(1.0 ± 0.1) x 10^7

Table 5.4. Kinetic parameters for the reduction of three [Co^{II}] (0.5 mM) in MeCN containing TBAP (50 mM).

The method of Alden et al, assumes true second order kinetics, and hence it should be possible to investigate any concentration of RBr. The rate constants are fairly consistent between the two analysis methods for the voltammetric data, in MeCN. In contrast, where DMF is the solvent the value of k_c is not as consistent, between methods, rather the Alden method estimates k_c to be larger than the method of Fleischmann. The use of Eq. 5.1 assumes that the process is pseudo-first order, and it can be seen from Figure 5.13 - Figure 5.17 that the use of pseudo-first order model to determine kinetics from N_{eff} will underestimate the value of the rate constant. This is observed in the analysis presented above, when the kinetics are fast (high N_{eff}).

††† Using the Fleischmann method (Equ 5.1)

In the case of mma as solvent, step (c) in Scheme 5.5 occurs at the electrode surface. The magnitude of the second wave thus depends on the kinetics of step (b). For the second wave, step (a) is driven and so the processes contributing to the current flow at this potential can be written as:

Electrode: $R[Co^{III}] + 2e^- \rightarrow [Co^{I}] + R^-$ (Eq. 5.6)

Electrode: $[Co^{I}] + R \rightarrow R[Co^{III}]$ (Eq. 5.7)

The first wave is thus effectively an EC process, while the second wave is a CEEC' process. In this case the C and C' steps are equivalent and control the magnitude of the overall current flow. For the purposes of a simplified analysis it is reasonable to consider the magnitude of the total current as being due to an EC' process, but recognising that during the second step 2 electrons flow every time $R[Co^{III}]$ is produced by the solution reaction. Thus, to apply existing pseudo-first order EC' models, which is reasonable given the small current enhancements measured, N_{eff} is written:

$$N_{eff} = 1 + \frac{i_{lim}(2)}{2i_{lim}(1)} \quad \text{(Eq. 5.8)}$$

Here, $i_{lim}(2)$ is the total current at the plateau of wave 2 minus the limiting current for wave 1, i.e. the current due only to Eq 5.6 and 5.7.

Table 5.5 shows values of N_{eff} obtained from the voltammograms shown as Figure 5.10 - Figure 5.12, with the corresponding second-order rate constant derived from Eq. 5.8.

Species	E2IBB	i_{lim} / (nA)	D/ (10^{-6} cm^2 s^{-1})	N_{eff}	k_c/(10^5 mol^{-1} cm^3 s^{-1})†††
[Co^{II}(dmgBF$_2$)$_2$]	0	1.7	7.6 ± 0.6		
	10x	3.0		1.7	7.8 ± 0.6
	20x	3.7		1.4	1.3 ± 0.1
	40x	5.0		2.0	4.0 ± 0.2
[Co^{II}(megBF$_2$)$_2$]	0	1.3	5.1 ± 0.7		
	10x	2.0		1.2	0.4 ± 0.06
	20x	2.4		1.4	0.9 ± 0.1
	40x	2.9		1.7	1.3 ± 0.2
[Co^{II}(degBF$_2$)$_2$]	0	2.3	9.2 ± 0.2		
	10x	4.4		1.8	12 ± 0.4
	20x	4.7		1.9	7.7 ± 0.2
	40x	5.8		2.3	8.1 ± 0.2

Table 5.5. Elucidation of k_c for the reaction of [Co^I] with E2IBB in mma.

The reaction examined in this work was of [Co^I] with E2IBB, the [Co] examined herein are used as CCTA and thus relation must be made to studies of their activity as CCTAs. Davis and co-workers[28] observed two basic trends in terms of catalytic activity for CCTAs: increased steric crowding decreases the Co-C bond strength, whilst increasing the electron donating ability of the axial ligands, increases the strength of the Co-C bond. Side reactions were investigated by Gridnev et al[258] who found that the reaction of [Co^I] with [Co^{III}]H could be used to regenerate the polymerisation active [Co^{II}] species and that this regeneration might also be promoted by use of polar aprotic solvents. Davis also noted that the use of aprotic solvents should be avoided as polymerisation media as they could act as radical sinks. Suddaby et al[259] found that the free radical polymerisation of mma, where DMF was used as a solvent, was inhibited by the addition of [Co^{II}(dmgBF$_2$)$_2$] to the reaction

††† Via the application of the pseudo-first order model (Eq. 5.1).

mixture. These points together with the data presented in this thesis lead to a number of conclusions as outlined below.

5.7 Conclusions

The voltammetric characteristics of three different [Co^{II}] have been ascertained in DMF, MeCN and mma. Each solvent offers a distinctly different environment for the formation and stability of R[Co^{III}]. In particular, mma was found to promote the formation of R[Co^{III}], but this species was too short-lived in DMF to enable electrochemical detection. The kinetics of the reaction between [Co^{I}] and E2IBB have been measured. For each solvent considered [$Co^{II}(degBF_2)_2$] showed the fastest reaction rate with E2IBB, followed by [$Co^{II}(dmgBF_2)_2$] and finally [$Co^{II}(megBF_2)_2$]. Values for k_c in the range 10^8 mol^{-1} cm^3 s^{-1}, 10^6 mol^{-1} cm^3 s^{-1} and 10^5 mol^{-1} cm^3 s^{-1} were observed for the reaction of [Co^{I}] with E2IBB in DMF, MeCN and mma respectively. As discussed earlier, the pseudo-first order model (Eq. 5.1) was shown only to agree well with the full second-order analysis afforded by the wwwda, at low values of N_{eff}.

Although the behaviour of the three complexes is not dissimilar, there are clear differences in the current enhancements due to the catalytic process, with [$Co^{II}(dmgBF_2)_2$] and [$Co^{II}(degBF_2)_2$] being most similar. [$Co^{II}(degBF_2)_2$] has the highest value of k_c in each solvent, suggesting that it is the most efficient catalyst for C-C bond forming reactions involving RX.

Chapter 6 - An SECM investigation of the reaction of alkyl halides with [Co^I]

SECM is developed as a new approach for studying EC' systems. The feedback and tip generation-substrate collection characteristics are identified and the method is used to investigate two model systems. These are (i) Fe/H_2O_2 where Fe^{II} reacts with H_2O_2 producing Fe^{III} and (ii) Fe/amidopyrine, where Fe^{III} and amidopyrine react together to generate Fe^{II}. The extension of the methodology to biphasic (organic/water) systems is considered.

6.1 Introduction

Double electrode methods including, interdigitated channel array electrodes[260], paired microband electrodes[261], double channel/tubular electrodes[262], twin electrodes in a thin layer cell[263] and the rotating ring disk electrode (RRDE)[264] have found considerable application in the measurement of heterogeneous electron transfer and coupled solution kinetics. In such set ups, one electrode is set to generate an electroactive species, e.g. Red, whilst the other acts as collector, in that it is set at a potential such that Ox will be regenerated from Red. Any intervening chemical reactions will affect the size of the collection current, and more specifically the collection efficiency (ratio of collector to generator current).

SECM can be configured with two electrodes facing each other, as used in Chapter 4. The potential of each electrode can be controlled independently and the resulting currents measured, by the use of a bipotentiostat. For the measurement of coupled

homogeneous kinetics, the range of rate constant accessible is much greater than the other double electrode geometries listed, especially at the upper limit. This is due to the high rate of mass transfer that can be generated at very closely aligned electrodes. In addition, the precision with which kinetics may be measured is much greater[265]. In the TG-SC and closely related feedback mode, the tip is set at a potential such that it will drive the reaction of interest, e.g. the reduction of Ox and the substrate is conversely set to drive the oxidation of Red. This establishes a generator/collector configuration. If a chemical system includes no coupled homogeneous reactions, Equs. 6.1 and 6.2 illustrate the processes that occur at tip and substrate.

$$Ox + ne^- \rightarrow Red \qquad \text{(Eq. 6.1)}$$

Species Red diffuses away from the tip UME (generator), to a substrate (collector) microelectrode, where it undergoes diffusion-controlled oxidation back to Ox, leading to diffusional feedback.

$$Red - ne^- \rightarrow Ox \qquad \text{(Eq. 6.2)}$$

The choice of substrate size is an important issue when operating the SECM in the TG-SC mode. The substrate should be small enough to eliminate any unnecessary background noise (which is proportional to electrode area) but it must be sufficiently large to ensure that all tip-electrogenerated species would be collected for a kinetically stable species. The size of the substrate needed is governed by the normalised separation of the two electrodes. At large separations a greater area acts as collector, but as the tip is moved closer this area tends to the diameter of the tip.

Empirically, the minimum dimensionless radius of substrate that may be used is given by Eq. 6.4[266].

$$b/a = 1 + 1.5(d/a) \qquad \text{(Eq. 6.3)}$$

where b is the radius of the substrate required for 100% *CoEf.*

A theoretical model for the TG-SC mode of SECM has been developed using the numerical alternating direction implicit finite difference method (ADIFDM)[171]. Typical feedback and TG-SC curves of normalised current plotted against normalised time (τ) are shown in Figure 6.1[171,267]. These are for the simple kinetically-uncomplicated case defined by Eq. 6.1 and 6.2. In the limit of long times it can be seen that the tip and substrate currents coincide, indicating a collection efficiency of 100%.

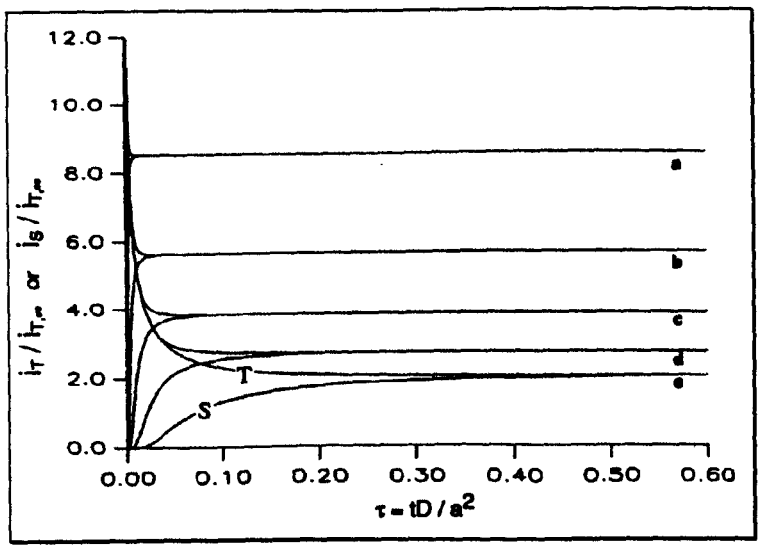

Figure 6.1. Tip and substrate chronoamperometric characteristics for the TG/SC mode[265]. For log(d/a) of (a)-1, (b) –0.8, (c) –0.6, (d) –0.4 and (e) –0.2.

In an EC_i system, Red may react with solution species, B, during transport from the tip to the substrate. For a first order irreversible chemical process, with rate constant, k_c, this process is defined by Eq. 6.4.

$$\text{Red} + \text{B} \xrightarrow{k_c} \text{C} \qquad \text{(Eq. 6.4)}$$

Any fraction of Red that remains in solution is collected at the substrate electrode (collector), giving an indication of the extent of reaction of Red with the solution species. The TG-SC mode is a particularly effective method of measuring k_c because very high collection efficiencies (*CoEf*) can be attained and these are particularly sensitive to changes in k_c when compared to the other dual electrode methods mentioned earlier[265].

The simulation that generated the response of i_T and i_S shown in Figure 6.1 was modified to include an irreversible chemical reaction in solution, following electron transfer[265]. Typical SECM tip diameters are in the range 25 – 2μm, and the range of rate constants that may be measured[265] is 640 – 1.6 x 10^4 s^{-1}, assuming d = 200nm and $D = 10^{-5}$ cm^2 s^{-1}.

Steady-state measurements have been used to determine homogeneous kinetics in solution via the TG-SC and feedback modes. As with other SECM measurements, the most precise measurements are facilitated by close tip-substrate separations. *CoEf*, for SECM is: the diffusion-limited current at the substrate electrode, (i_S) divided by

that at the tip electrode, (i_T). It has been shown that *CoEf* depends on a dimensionless parameter, K[198]:

$$K = k_c d^2/D \qquad \text{(Eq. 6.5)}$$

This parameter is related to *CoEf* by Eq. 6.6.

$$K = 5.608 + 9.347exp(-7.527CoEf) - 7.616exp(-0.307/CoEf) \qquad \text{(Eq. 6.6)}$$

This empirical equation describes the relationship to within 1% and shows the expected limiting behaviour i.e. as $K \rightarrow 0$, $CoEf \rightarrow 1$; as $K \rightarrow \infty$, $CoEf \rightarrow 0$. The determination of kinetic parameters from *CoEf* measurements alone are most accurate when *CoEf* is between 0.1 and 0.8[198].

In theory, the above experimental procedures may be applied to the study of an EC' reaction, whereby instead of the C step being described by Eq. 6.4. it is as shown in Eq. 6.7.

$$\text{Red} + \text{A} \xrightarrow{k_c} \text{Ox} \qquad \text{(Eq. 6.7)}$$

Chapter 5 described the application of UMEs and voltammetric techniques to study the EC' mechanism with a focus on [Co^I]/RBr systems. The work described herein utilised SECM as a tool to further investigate such systems.

6.2 Exemplar Systems

To assess the suitability of SECM as a tool for the investigation of EC' systems, a model system was required. Several EC' systems have been examined in the past with voltammetric and double electrode methods. A standard example is the reaction of electrogenerated Fe^{II} with H_2O_2, via this method. Haber and Weiss[268] postulated a mechanism for the decomposition of H_2O_2, as shown in Scheme 6.1.

$Fe^{2+} + H_2O_2 \rightarrow Fe^{3+} + OH^- + OH$	(a)
$OH + H_2O_2 \rightarrow H_2O + HO_2$	(b)
$HO_2 + H_2O_2 \rightarrow O_2 + H_2O + OH$	(c)
$OH + Fe^{2+} \rightarrow Fe^{3+} + OH^-$	(d)

Scheme 6.1. The four steps of the reaction of Fe^{2+} with H_2O_2.[268]

The mechanism described a free radical chain reaction. Earlier work had suggested a mechanism involving hydrogen peroxide and an iron-oxygen complex[268]. It was assumed that the rate constant should be independent of acidity, but experiments showed a slight dependence of the rate on acidity. Haber and Weiss found that in the presence of a small concentration of Fe^{2+}, other processes which depended on pH became important, namely:

$$Fe^{2+} + HO_2 \leftrightharpoons Fe^{3+} + HO_2^- \qquad \text{(Eq. 6.8)}$$

where HO_2^- is always present in solution due to (the equilibrium constant for this reaction was shown to be 1.2×10^{-12} [268]):

$$HO_2^{\cdot} + H^{\cdot} \leftrightharpoons H_2O_2 \qquad \text{(Eq. 6.9)}$$

Haber and Weiss claimed that it was impossible to quantify the effect of Eq. 6.8 because at the [Fe^{2+}] where this route became important, precise measurements could no longer be carried out. It was concluded that results of experiments showed a "relatively small" dependence on pH, hence Scheme 6.1 (a) – (d) applied with additional complications only at extreme concentration ratios.

Rigg et al[269] made a study of the same system and found that it was independent of acidity over the range 0.05-0.8N. They also measured the rate constant of the reaction to be 63.4 ± 3 $dm^3\ mol^{-1}s^{-1}$ at 25.1^{0}C by means of spectrophotomeric measurements. Pospisil[270] observed that there were differences in the values for the rate of reaction of Fe^{2+} with H_2O_2 when measured by chemical[271] and polarographic[272,,273,274] methods. He attributed this to the assumption of other workers that the layer thickness in a polarographic experiment was finite, whereas this is only true in the case of large k_c. He concluded that of the four Haber and Weiss equations, (b) and (c) apply only in the case of a large excess of H_2O_2 and that at comparable concentrations, (a) and (d) are practically the only applicable ones. In Scheme 6.1, the rate of step (d) was shown to be several orders of magnitude higher than step (a), so the latter is the rate determining step (rds). A substance was added that trapped $^{\cdot}OH$ radicals, formed in step (d), allowing the reaction to proceed via a conventional second order rate law. Pospisil determined that k_c was between 55 – 66 $dm^3\ mol^{-1}\ s^{-1}$.

Electrochemical investigations of this system have been made by many methods, but are complicated by the decomposition of H_2O_2 on Pt[275,276]. Klatt and Blaedel[277] used a gold tubular electrode to increase mass transfer by forced convection. This enabled steady-state measurements of rate constants greater than 0.1 s^{-1} to be measured. The rotating disc electrode was used by Opekar and Beran to study both the reaction of Fe^{2+} with H_2O_2 and with tert-butylhydroperoxide. For the Fe^{2+}/H_2O_2 system, rate constants of 48.1 ± 2.3 dm^3 mol^{-1} s^{-1} and 55.5 ± 3.9 dm^3 mol^{-1} s^{-1} were obtained via two different methods of analysis. Aoki et al[276] used a channel electrode to elucidate k_c for the Fe^{2+}/H_2O_2 reaction to be 40 dm^3 mol^{-1} s^{-1}. A lower value for the rate constant was obtained and assigned to the fact that a large excess of H_2O_2 was used, causing a change in the pathway along which the reaction proceeded

Perhaps the most comparable work to any SECM experiment was that carried out by Herrmann et al[278], who use a turbulent pipe flow method with two electrodes separated by a small distance (50μm in this case). The first was held at a potential such that Fe^{2+} was electrochemically generated from Fe^{3+} in solution. The second electrode, located downstream in the flow apparatus was set at a potential such that the reverse conversion occured, $Fe^{2+} \rightarrow Fe^{3+} + e^-$. As in the case of SECM, *CoEf* was used to obtain a rate constant for the reaction occurring between electrogenerated Fe^{2+} and H_2O_2 in the inter-electrode gap. A rate constant of 70 dm^3 mol^{-1} s^{-1} was measured.

Fe^{3+} will interact with various organic species in alkaline media in the same way as Fe^{2+} will react with hydrogen peroxide in acidic media. Rashid and Kalvoda[279] examined the reaction of Fe^{3+} with amidopyrine by voltammetric methods using Pt

microdisc electrodes. The concentration of amidopyrine was kept at least ten times higher than that of Fe^{3+} to ensure pseudo-first order kinetics. The reaction was studied in a solution of 1M KOH and first-order dependences with respect to amidopyrine, iron and OH^- concentration were found. The rate constant of the reaction of Fe^{2+} with amidopyrine was found to be approximately 2 x 10^3 dm^3 mol^{-1} s^{-1} in 1M KOH.

Both the Fe^{2+}/H_2O_2 and Fe^{3+}/amidopyrine systems were used as model systems within this study. The former, slower, system was investigated first.

6.3 The Fe^{2+}/H_2O_2 system.

In the SECM configuration, with a large excess of H_2O_2, expressions for the tip, substrate and solutions reactions may be considered as shown in Scheme 6.2:

Tip:	$Fe^{3+} \rightarrow Fe^{2+}$	**(a)**
Substrate:	$Fe^{2+} \rightarrow Fe^{3+}$	**(b)**
Solution:	$Fe^{2+} + H_2O_2 \rightarrow Fe^{3+}$	**(c)**

Where route (a) represents the E step and (c) the C' step.

Scheme 6.2. The electrochemical reduction of Fe^{3+} in the presence of H_2O_2.

6.3.1 Experimental

The majority of experimental protocol was discussed in Chapter 2, however, for clarity the main aspects are recapped here. The tip electrode (Au, a = 5 μm) was

located directly over the centre of the substrate electrode (Au, a = 62.5 μm) by recording an SECM image. Once the position of exact alignment was known, the tip electrode was aligned in the x direction, but positioned 200 μm away from direct alignment in the y direction. Then an approach curve of the tip electrode to the glass sheath of the substrate electrode was recorded, thus giving an indication of the hindered diffusion behaviour, afforded by an inert interface. The tip electrode was subsequently aligned in the y direction such that the tip was positioned directly over the centre of the substrate. An approach curve was recorded with the electrodes so aligned, thus the tip-substrate separation, d, was determined. Once the electrodes had been aligned in this manner, steady-state LSVs were recorded at various tip-substrate separations, with the tip potential (E_T) being swept through a potential range (+0.65 - +0.15 V vs. AgQRE) such as to drive the reduction of $Fe^{3+}$to Fe^{2+}. The substrate electrode was set at a potential such as to collect back Fe^{2+} from solution (+0.8 V vs. AgQRE). As H_2O_2 is decomposed by Pt[277], Au electrodes were used in the study of the Fe^{2+}/H_2O_2 system. A series of voltammograms at a range of values of d/a, as described in Chapter 2, were obtained for each value of Fe^{3+}:H_2O_2, so that the behaviour of i_T and i_S vs. d/a could be determined. Thus, when a value of i_T or i_S is quoted, it is the value of the diffusion-limited current for the redox process occurring at the tip or substrate respectively. In order to clearly see the effect of the coupled chemical reactions on the magnitude of i_T and i_S, all currents have been shown as normalised with respect to the diffusion-limited current for a solution where no chemical substrate is present and where the tip-substrate separation is infinitely large ($i_{T\infty}^{0}$), which is equivalent to the i_{lim} of voltammetric studies without substrate.

The key quantity under examination within this chapter is current, the measurement of which, has a small instrumental error associated with it. Whilst this error is potentially magnified by plotting current as normalised with respect to $i_{T\infty}{}^{0}$, it allows ready comparison between experiments run at different [Fe^{3+}].

6.3.2 Results and Discussion

At infinite separation, the substrate electrode detects no Fe^{2+}, however, when the electrodes are brought close together a current flows at the substrate electrode as it detects Fe^{2+} generated voltammetrically at the tip. The magnitude of i_S reflects the production of Fe^{2+} at the tip electrode. Hence, if an LSV is performed at the tip, the i_T vs. E_T plot is a voltammetric wave. As the substrate electrode is set at a potential to detect the product of the tip redox process, it too shows a wave of i_S vs. E_T, where the height of the wave is indicative of the diffusion-limited oxidation of Fe^{2+} to Fe^{3+}. Figure 6.2 shows a comparison of the behaviour of i_T and i_S at the same value of d/a.

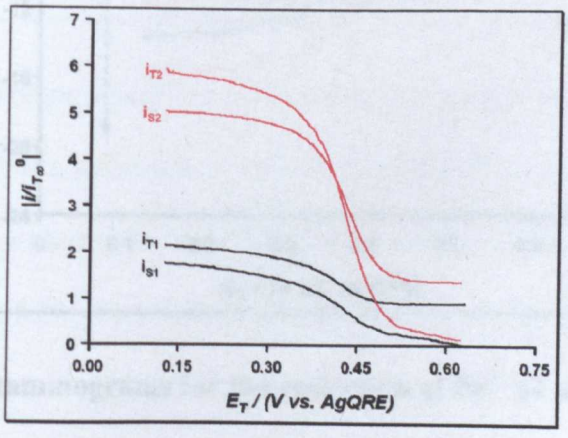

Figure 6.2. Tip (generator) and substrate (collector) voltammograms for the reduction of Fe^{3+}(2 mM) at the tip and collection of Fe^{2+} at the substrate, held at a potential of (0.8 V vs. AgQRE). (1) no H_2O_2 and (2) in the presence of H_2O_2 (120 mM). All voltammograms were recorded at d/a = 0.7 and 20 mV s^{-1}.

The difference in the height of the voltammetric waves is caused by the amount of H_2O_2 present in solution. When H_2O_2 is present, it acts to re-generate Fe^{3+}, hence increasing i_T. The value of i_S also increases, because more Fe^{2+} is generated at the tip, due to the production of Fe^{3+} in solution.

As stated in the experimental section, tip and substrate voltammograms were recorded at a range of values of d/a and $[H_2O_2]$. Figure 6.3 shows a number of voltammograms recorded at different values of d/a for a solution of constant composition. It can be seen that as d/a decreased [(a) → (m)] the magnitude of the diffusion-limited tip current increased.

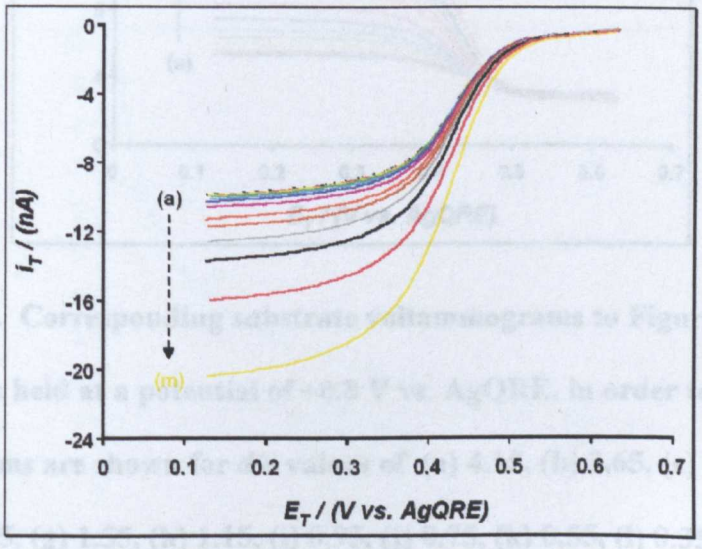

Figure 6.3. Tip voltammograms for the reduction of Fe^{3+} (2 mM) in the presence of H_2O_2 (120 mM), with H_2O as solvent and KCl (0.2 mol dm^3) as supporting electrolyte. Voltammograms were recorded at a scan rate of 20 mV s^{-1} and are shown for d/a values of (a) 4.15, (b) 3.65, (c) 3.15, (d) 2.75, (e) 2.35, (f) 1.95, (g) 1.55, (h) 1.15, (i) 0.95, (j) 0.75, (k) 0.55, (l) 0.35 and (m) 0.15.

The substrate electrode was held at a constant potential, such as to drive the collection of Fe^{2+}. The substrate current was measured simultaneously to i_T as a function of E_T. Figure 6.4 shows that the substrate current also increased as d/a was decreased [(a) → (m)]. When i_S was divided by i_T the result was a value of $CoEf$, which was found to be close to unity at small tip-substrate separations and then decreased as d/a decreased.

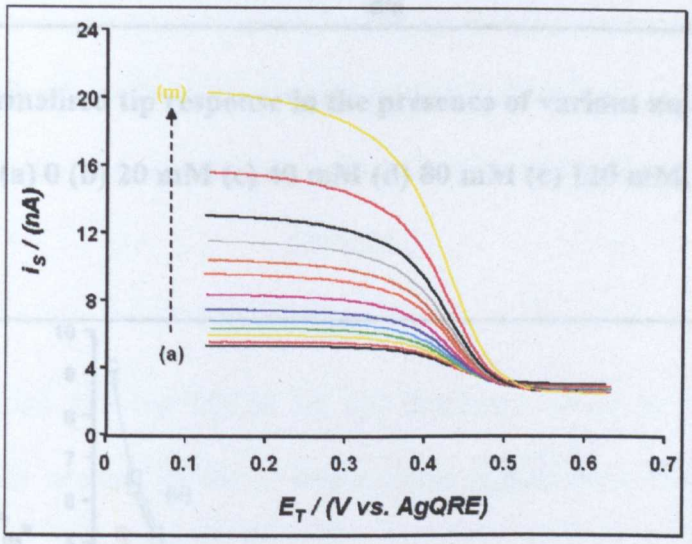

Figure 6.4. Corresponding substrate voltammograms to Figure 6.3. The substrate was held at a potential of +0.8 V vs. AgQRE, in order to collect Fe^{2+}. Voltammograms are shown for d/a values of (a) 4.15, (b) 3.65, (c) 3.15, (d) 2.75, (e) 2.35, (f) 1.95, (g) 1.55, (h) 1.15, (i) 0.95, (j) 0.75, (k) 0.55, (l) 0.35 and (m) 0.15.

The value of the diffusion-limited current for both the tip and substrate electrodes were measured from each voltammogram. The effect of tip/substrate separation on the normalised tip current is shown in Figure 6.5, while Figure 6.6 shows how the substrate current changed as a function of distance.

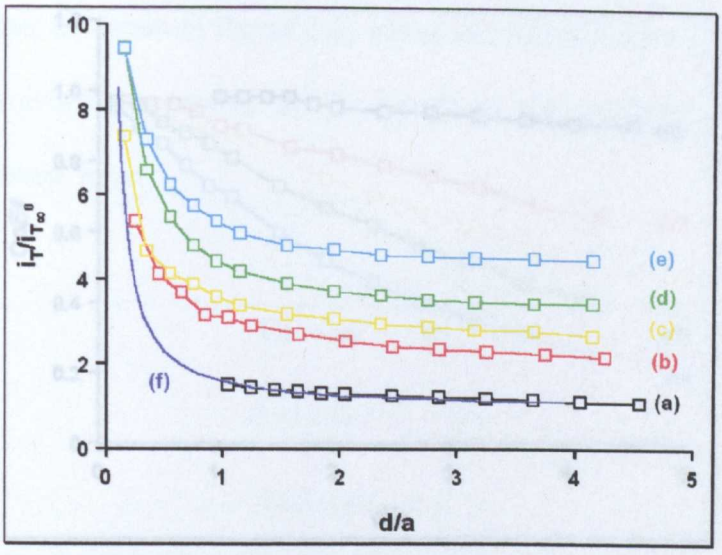

Figure 6.5. Normalised tip response in the presence of various amounts of H_2O_2 - (a) 0 (b) 20 mM (c) 40 mM (d) 80 mM (e) 120 mM.

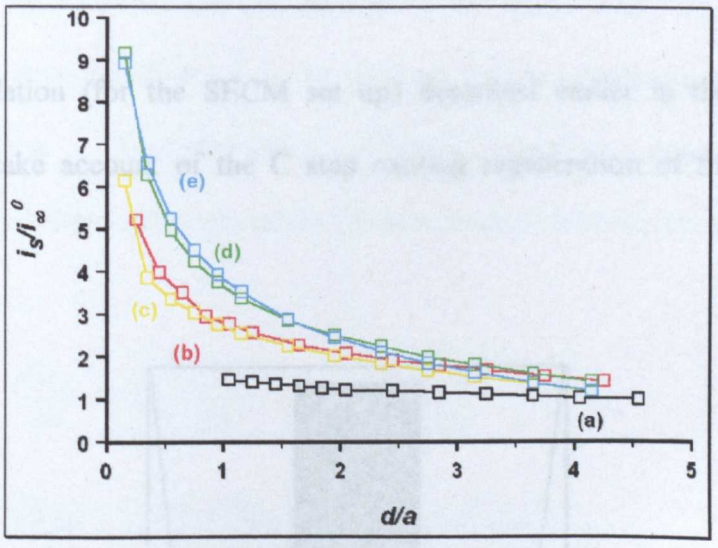

Figure 6.6. Normalised substrate response in the presence of various amounts of H_2O_2 - (a) 0 (b) 20 mM (c) 40 mM (d) 80 mM (e) 120 mM.

By a simple process of dividing i_S by i_T a relationship of *CoEf* vs. *d/a* was determined as shown in Figure 6.7.

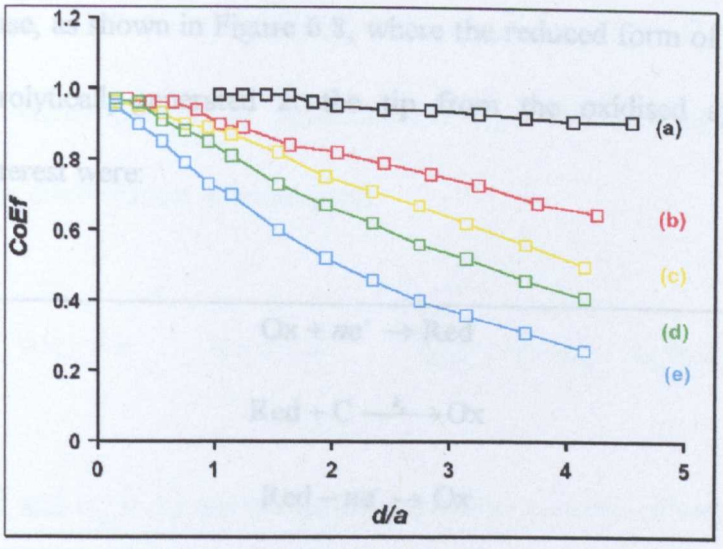

Figure 6.7. Collection efficiency as a function of tip/substrate separation for the $Fe^{3+/2+}$ couple in the presence of H_2O_2 - (a) 0 (b) 20 mM (c) 40 mM (d) 80 mM (e) 120 mM.

The EC_i simulation (for the SECM set up) described earlier in this chapter was developed to take account of the C step causing regeneration of the electroactive species, Ox.

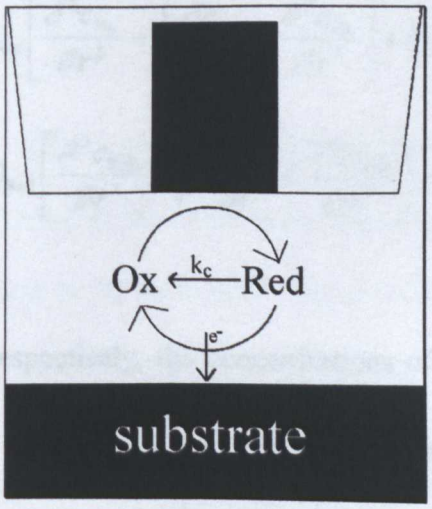

Figure 6.8. A schematic of the EC' mechanism.

For the EC' case, as shown in Figure 6.8, where the reduced form of a redox species, Red, is electrolytically-generated at the tip from the oxidised species, Ox, the reactions of interest were:

Tip:	$Ox + ne^- \rightarrow Red$	(a)
Solution:	$Red + C \xrightarrow{k_c} Ox$	(b)
Substrate:	$Red - ne^- \rightarrow Ox$	(c)

Scheme 6.3. The EC' mechanism.

where Red and Ox denote, respectively, the reduced and oxidised form of the redox couple, C is the substrate (which remains at the same initial bulk concentration throughout the experiment) and k_c is the apparent first order rate constant (s^{-1}) for the solution reaction. Time-dependent diffusion equations, appropriate to the axisymmetric cylindrical geometry of the SECM can be written for Ox and Red.

$$\frac{\partial c_{Ox}}{\partial t} = D_{Ox}\left[\frac{\partial^2 c_{Ox}}{\partial r^2} + \frac{1}{r}\frac{\partial c_{Ox}}{\partial r} + \frac{\partial^2 c_{Ox}}{\partial z^2}\right] + k_C c_{Red} \qquad \text{(Eq. 6.10)}$$

$$\frac{\partial c_{Red}}{\partial t} = D_{Red}\left[\frac{\partial^2 c_{Red}}{\partial r^2} + \frac{1}{r}\frac{\partial c_{Red}}{\partial r} + \frac{\partial^2 c_{Red}}{\partial z^2}\right] - k_C c_{Red} \qquad \text{(Eq. 6.11)}$$

where c_{Ox} and c_{Red} are, respectively, the concentrations of the oxidised and reduced species and D_{Ox} and D_{Red} are the diffusion coefficients, r and z are the co-ordinates in the directions radial and normal to the electrode surface measured from the centre of

the electrode and t is time. In the development of the model, the diffusion coefficients of Ox and Red are considered to be equal, i.e., $D_{Ox} = D_{Red}$ with only the reactant, Ox, initially present, at concentration c^*_{Ox}. This assumption allows the principle of mass conservation to be invoked:

$$0 \le r \le r_s, \qquad 0 < z < d: \qquad c_{Red}(r,z) = c^*_{Ox} - c_{Ox}(r,z) \qquad \text{(Eq. 6.12)}$$

where $c_{Red}(r,z)$ and $c_{Ox}(r,z)$ are the spatial-dependent concentrations of Red and Ox, respectively, within the region of interest (see Figure 6.8), defined in terms of r and z. The parameters d and r_s, respectively, denote the location of the substrate and the edge of the glass sheath surrounding the UME. The use of Eq. 6.12 simplifies the problem to the consideration of species Ox alone. In order to calculate the current response of the tip and substrate electrodes, Eq. 6.10 must be solved subject to the boundary and initial conditions of the system. Prior to the potential step only Ox is present. The initial condition is thus,

$$t = 0; \qquad 0 \le r \le r_s, \ 0 \le z \le d \ : \ c_{Ox} = c^*_{Ox}, c_{Red} = 0 \qquad \text{(Eq. 6.13)}$$

At time $t > 0$, the potential of the UME tip is stepped from a value where no electrode reaction occurs, to one sufficient to drive the reduction of Ox at a diffusion-controlled rate. Species Ox is assumed to be inert with respect to the insulating glass sheath surrounding the electrode and to remain at bulk concentration values beyond the radial edge of the tip. Species Ox is regenerated from Red at the substrate at a

diffusion-controlled rate. Consequently, the exterior boundary conditions may be summarised as follows:

$$0 \le r \le a, \quad z = 0, \quad : \quad c_{Ox} = 0 \qquad \text{(Eq. 6.14)}$$

$$a < r \le r_s, \quad z = 0, \quad : \quad D_{Ox} \frac{\partial c_{Ox}}{\partial z} = 0 \qquad \text{(Eq. 6.15)}$$

$$r > r_s, \quad 0 < z < d, \quad : \quad c_{Ox} = c_{Ox}^* \qquad \text{(Eq. 6.16)}$$

$$0 < r \le r_s, \quad z = 0, \quad : \quad c_{Red} = 0, c_{Ox} = c_{Ox}^* \qquad \text{(Eq. 6.17)}$$

Eq. 6.16 is a reasonable assumption provided that $RG \ge 10$. The axisymmetric geometry of the SECM implies that there is no radial flux of the species at the cylindrical axis of symmetry:

$$r = 0, \quad 0 < z < d \quad : \quad D_{Ox} \frac{\partial c_{Ox}}{\partial r} = 0 \qquad \text{(Eq. 6.18)}$$

To obtain general solutions, the problem is reformulated in terms of the following dimensionless quantities:

$$\tau = \frac{tD_{Ox}}{a^2} \qquad \text{(Eq. 6.19)}$$

$$R = \frac{r}{a} \qquad \text{(Eq. 6.20)}$$

$$Z = \frac{z}{a} \qquad \text{(Eq. 6.21)}$$

$$C_{Ox} = \frac{c_{Ox}}{c_{Ox}^*} \qquad \text{(Eq. 6.22)}$$

$$K = \frac{k_C a^2}{D_{Ox}} \qquad \text{(Eq. 6.23)}$$

Substituting for c_{Red} using Equ 6.13 into Eq.6.10 and rewriting the diffusion equation in terms of these normalised quantities gives:

$$\frac{\partial C_{Ox}}{\partial \tau} = \left[\frac{\partial^2 C_{Ox}}{\partial R^2} + \frac{1}{R}\frac{\partial C_{Ox}}{\partial R} + \frac{\partial^2 C_{Ox}}{\partial Z^2} \right] + K(1 - C_{Ox}) \qquad \text{(Eq. 6.24)}$$

The UME current is related to the flux of Ox at the electrode surface and hence the dimensionless current ratio for the tip UME is given by

$$\frac{i_T}{i_\infty} = \frac{\pi}{2}\int_0^1 \left(\frac{\partial C_{Ox}}{\partial Z} \right)_{Z=0} R dR \qquad \text{(Eq. 6.25)}$$

where the steady-state diffusion-limited current at an inlaid disc electrode positioned at an effectively infinite distance from the interface is given by Eq. 1.3. The substrate current is related to the flux of Red at the substrate surface given by

$$\frac{i_S}{i_\infty} = \frac{\pi}{2}\int_0^1 \left(\frac{\partial C_{Red}}{\partial Z} \right)_{Z=d/a} R dR \qquad \text{(Eq. 6.26)}$$

Using Eq. 6.13,

$$\frac{i_S}{i_\infty} = -\frac{\pi}{2}\int_0^1 \left(\frac{\partial C_{Ox}}{\partial Z} \right)_{Z=d/a} R dR \qquad \text{(Eq. 6.27)}$$

Numerical solutions, were written by A. L. Barker and P. R. Unwin, using the alternating direction implicit finite-difference method (ADIFDM)[280], the code of which is shown as appendix 3.

The simulation was one that represented a chronoamperometric experiment, whereby the potential, applied to the tip electrode was stepped from rest to a position where the reaction was driven at a diffusion-controlled rate. After a particular amount of time, dependent on the rate of reaction, separation of the tip and substrate electrodes and the diffusion coefficient of the species the i_T response (and hence i_S) attained a steady-state value. By examining the value of the steady-state limiting current of the simulated response, it was possible to compare the experimental results for steady-state currents, recorded by LSV.

Figure 6.9 shows the simulated response of i_S vs. d/a for various normalised rate constants. It can be seen that, for large values of d/a, i_T varies little with change in tip-substrate separation. As d/a decreases, a positive feedback type behaviour is observed with i_T increasing with decrease in d/a. The value of i_T is most similar, for the various rate constants, at large values of d/a and most different at close separations, however, as d/a becomes negligibly small the curves tend to a common point of $i_T \rightarrow \infty$. The simulation reported both i_T and i_S, hence it was possible to determine the theoretical behaviour of *CoEf* vs. d/a as shown in Figure 6.10.

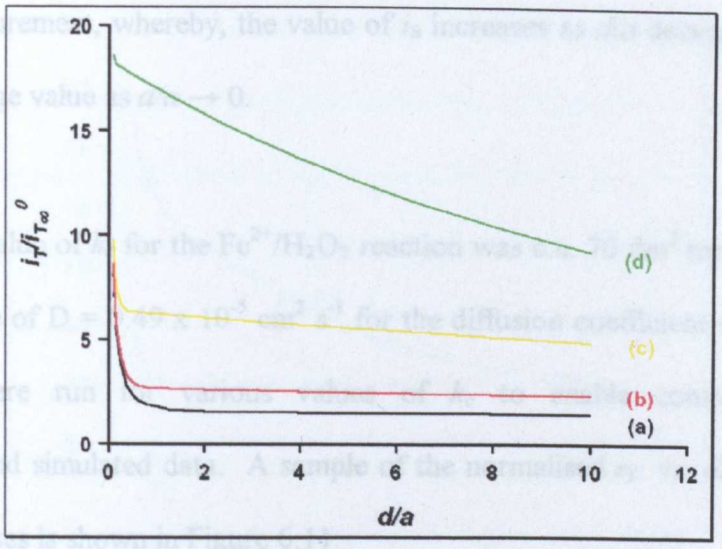

Figure 6.9. Simulated EC' tip responses for K = (a) 1, (b) 10, (c) 100 and (d) 1000 for an EC' reaction.

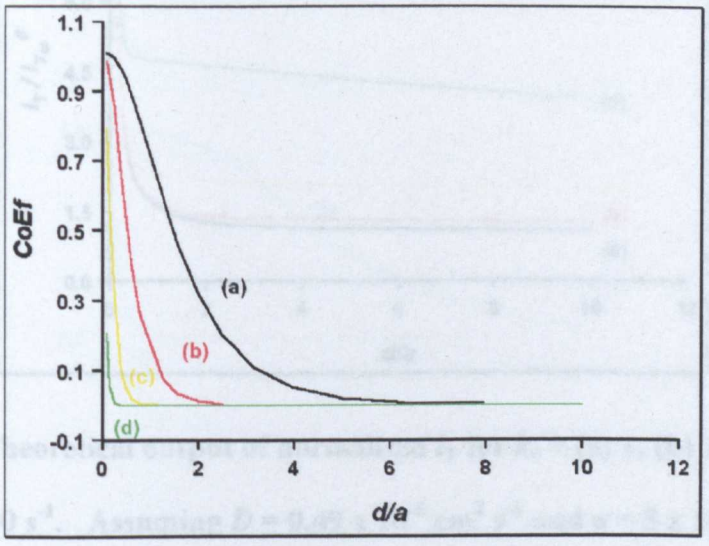

Figure 6.10. Simulated *CoEf* vs. *d/a* response corresponding to Figure 6.9.

It can be seen that i_S, and hence *CoEf*, is very sensitive to both distance and rate constant. At larger values of K ((d), 1000), no current flows at the substrate electrode until d/a is small. Conversely, for a value of K of 1 a response is seen from approximately $d/a = 6$. As was seen in Figure 6.9, the behaviour is akin to that of a

feedback measurement, whereby, the value of i_S increases as d/a decreases, tending to an infinitely large value as $d/a \rightarrow 0$.

The reported value of k_c for the Fe^{2+}/H_2O_2 reaction was c.a. 70 $dm^3\ mol^{-1}\ s^{-1}$. Using a measured value of $D = 0.49 \times 10^{-5}\ cm^2\ s^{-1}$ for the diffusion coefficient of Fe^{3+} in H_2O, simulations were run for various values of k_c to enable comparison of the experimental and simulated data. A sample of the normalised i_T. vs. d/a response for a number of cases is shown in Figure 6.11.

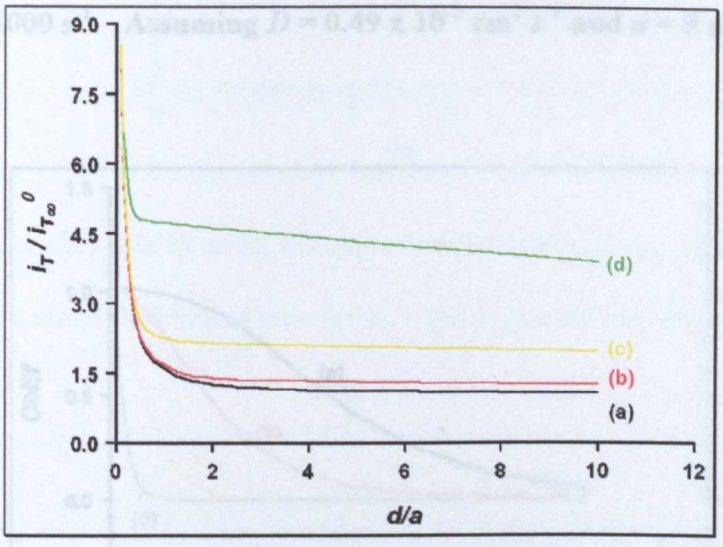

Figure 6.11. Theoretical output of normalised i_T for k_c = (a) 1, (b) 10, (c) 100 and (d) 1000 s^{-1}. Assuming $D = 0.49 \times 10^{-5}\ cm^2\ s^{-1}$ and $a = 5 \times 10^{-6}$ cm.

The substrate response was simulated as part of the program, thereby also allowing comparison of the i_S vs. d/a and hence *CoEf* vs. d/a data. Figure 6.12 and Figure 6.13 respectively, show the corresponding i_S and *CoEf* vs. d/a responses to Figure 6.11.

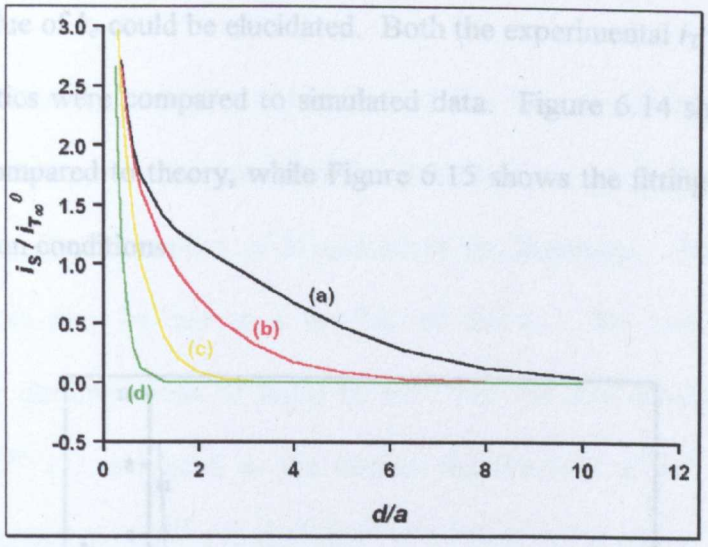

Figure 6.12. Theoretical output of normalised i_S for k_c = (a) 1, (b) 10, (c) 100 and (d) 1000 s^{-1}. Assuming $D = 0.49 \times 10^{-5}$ cm^2 s^{-1} and $a = 5 \times 10^{-6}$ cm.

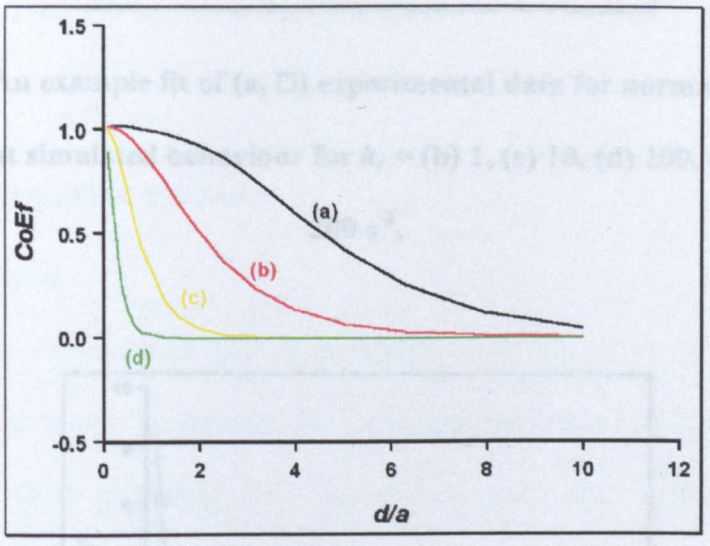

Figure 6.13. Theoretical output of *CoEf* for k_c = (a) 1, (b) 10, (c) 100 and (d) 1000 s^{-1}, corresponds to Figure 6.11 and Figure 6.12.

It can be seen from Figure 6.11 to Figure 6.13 that the measurement of a wide range of rate constants, should be achievable, with high precision, using tip and substrate current measurements. The experimental data were compared to that simulated, in

order that a value of k_c could be elucidated. Both the experimental i_T vs. d/a and i_S vs. d/a characteristics were compared to simulated data. Figure 6.14 shows an example of i_T vs. d/a compared to theory, while Figure 6.15 shows the fitting of i_S vs. d/a for the same reaction conditions.

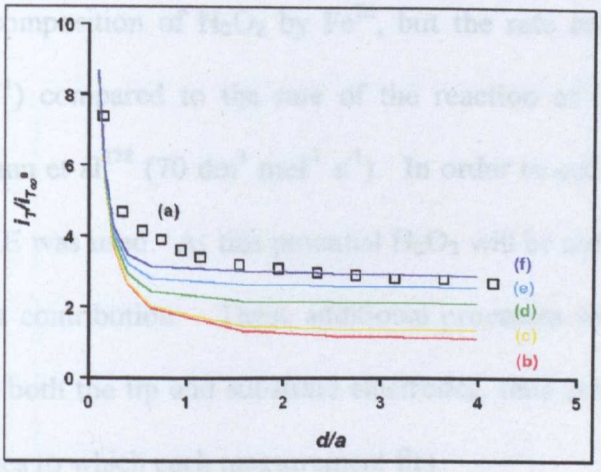

Figure 6.14. An example fit of (a, □) experimental data for normalised i_T vs. d/a, plotted against simulated behaviour for k_c = (b) 1, (c) 10, (d) 100, (e) 200 and (f) 300 s^{-1}.

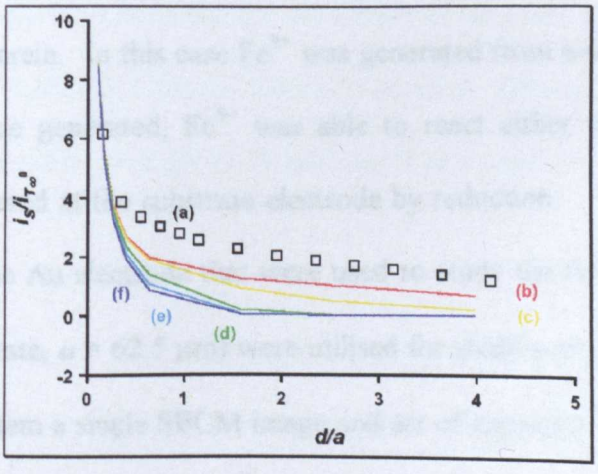

Figure 6.15. An example fit of (a, □) normalised i_S vs. d/a, plotted against simulated behaviour for k_c = (b) 1, (c) 10, (d) 100, (e) 200 and (f) 300 s^{-1}.

It may be seen from Figure 6.14 and Figure 6.15 that the normalised i_T and i_S values do not fit to the same value of simulated k_c. Both currents are higher than predicted by the simulation for the values of k_c quoted in the literature. These higher than expected currents may be due to a number of factors. De Laat and Gallard[281] investigated the decomposition of H_2O_2 by Fe^{III}, but the rate constants found were negligible ($\sim 10^{-4}$ s^{-1}) compared to the rate of the reaction of Fe^{2+} with H_2O_2, as predicted by Herrmann et al[278] (70 dm^3 mol^{-1} s^{-1}). In order to collect Fe^{2+} a potential of 0.80 V vs. AgQRE was used. At this potential H_2O_2 will be oxidised, thus creating an additional current contribution. These additional processes will contribute to the measured current at both the tip and substrate electrodes, thus creating the difference in the simulated values to which each measurement fits.

6.4 Fe^{3+}/amidopyrine system

6.4.1 Experimental

The same basic experimental protocols employed in the study of the Fe^{2+}/H_2O_2 system were used herein. In this case Fe^{3+} was generated from a solution precursor of Fe^{2+} (1 mM). Once generated, Fe^{3+} was able to react either with amidopyrine in solution or be collected at the substrate electrode by reduction. Pt electrodes of the same diameter as the Au electrode that were used to study the Fe^{2+}/H_2O_2 system (tip, a = 5 μm and substrate, a = 62.5 μm) were utilised for studies of the Fe^{3+}/amidopyrine system. For this system a single SECM image and set of approach curves were used to allow alignment and distance calibration of the tip and substrate electrodes. Thereafter, the solution was changed by draining the cell, then adding the next solution, before the experiment re-commenced.

6.4.2 Results and Discussion

Figure 6.16 shows a plot of a series of LSVs recorded at various values of *d/a* for a ratio of amidopyrine:Fe^{2+} of 10:1. Figure 6.17 shows the effect of the changing E_T and hence i_T on i_S.

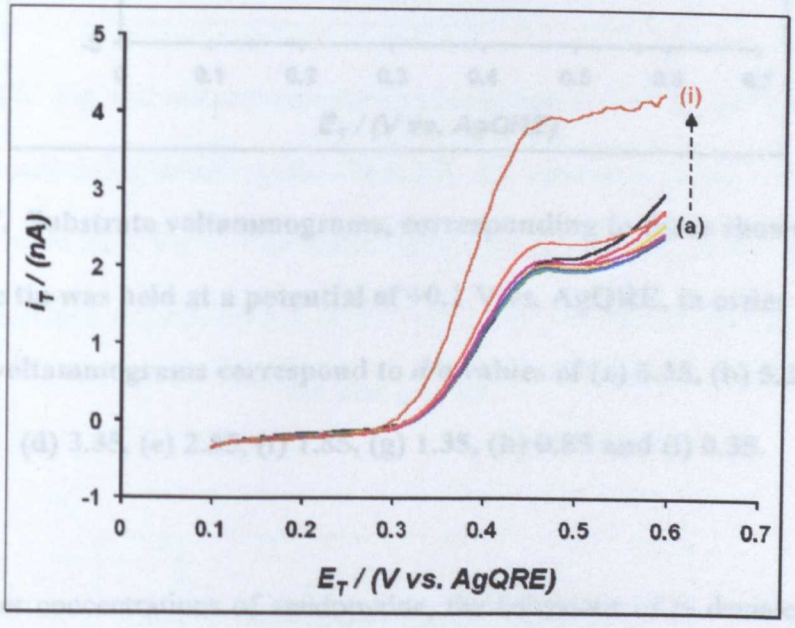

Figure 6.16. Tip voltammograms for the oxidation of Fe^{2+} (1 mM) in the presence of amidopyrine (10 mM), for *d/a* values of (a) 6.35, (b) 5.35, (c) 4.35, (d) 3.35, (e) 2.35, (f) 1.85, (g) 1.35, (h) 0.85 and (i) 0.35. All voltammograms were recorded in a solution of KOH (1 mol dm^{-3}) at a scan rate of 20 mV s^{-1}.

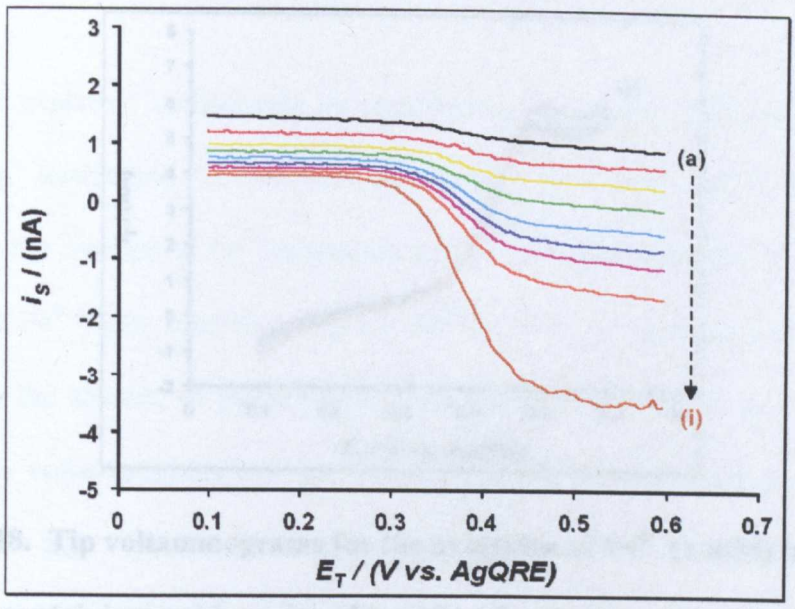

Figure 6.17. Substrate voltammograms, corresponding to those shown in Figure 6.16. The tip was held at a potential of +0.1 V vs. AgQRE, in order to collect Fe^{3+}. The voltammograms correspond to *d/a* values of (a) 6.35, (b) 5.35, (c) 4.35, (d) 3.35, (e) 2.35, (f) 1.85, (g) 1.35, (h) 0.85 and (i) 0.35.

For the higher concentrations of amidopyrine, the behaviour of i_T deviated from that which had been seen for the Fe^{2+}/H_2O_2 system. As can be seen from Figure 6.18, the limiting behaviour of i_T became peaked, rather than showing a plateau. Additionally, there was very little difference in i_T between different values of *d/a*. However, i_S increased with decreasing *d/a* as shown in Figure 6.19.

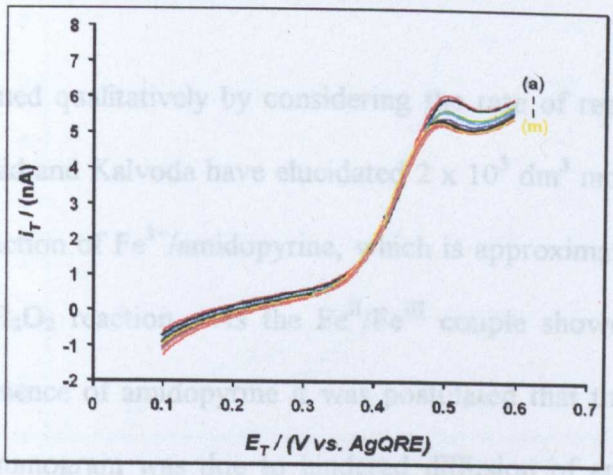

Figure 6.18. Tip voltammograms for the oxidation of Fe^{2+} (1 mM) in KOH (1 mol dm^{-3}), containing amidopyrine (50 mM). All voltammograms were recorded at a scan rate of 20 mV s^{-1}. The voltammograms are shown for *d/a* values of (a) 7.2, (b) 6.2, (c)5.2, (d) 4.2, (e) 3.2, (f) 2,7, (g) 2.2 (h) 1.7 (i) 1.2, (j) 1.0, (k) 0.8, (l) 0.6 and (m) 0.4.

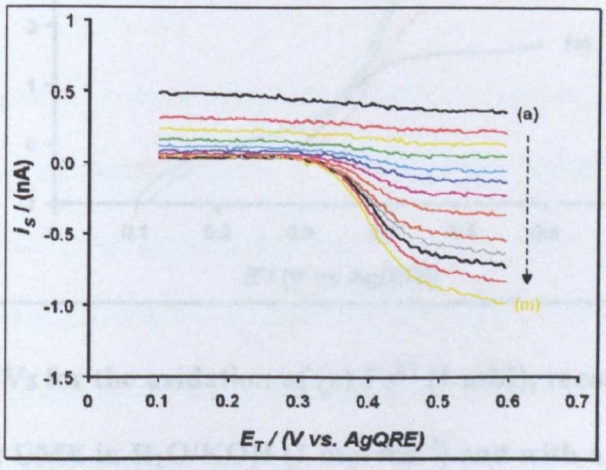

Figure 6.19. Substrate voltammograms, recorded simultaneously to those shown in Figure 6.18. The substrate was held at a potential of +0.1 V vs. AgQRE, in order to collect any Fe^{3+} present in solution. Voltammograms are shown for *d/a* values of (a) 7.2, (b) 6.2, (c)5.2, (d) 4.2, (e) 3.2, (f) 2.7, (g) 2.2 (h) 1.7 (i) 1.2, (j) 1.0, (k) 0.8, (l) 0.6 and (m) 0.4.

This may be explained qualitatively by considering the rate of reaction, as quoted in the literature. Rashid and Kalvoda have elucidated 2 x 10^3 dm^3 mol^{-1} s^{-1} to be the rate constant for the reaction of Fe^{3+}/amidopyrine, which is approximately 30 times larger than for the Fe^{2+}/H_2O_2 reaction. As the Fe^{II}/Fe^{III} couple showed diffusion-limited behaviour in the absence of amidopyrine it was postulated that the peaked nature of the i_T vs. E_T voltammogram was due to hindered diffusion of amidopyrine into the inter-electrode gap. The degree of peak was slight with 10:1 amidopyrine:Fe^{2+} but increased on addition of further amounts of amidopyrine.

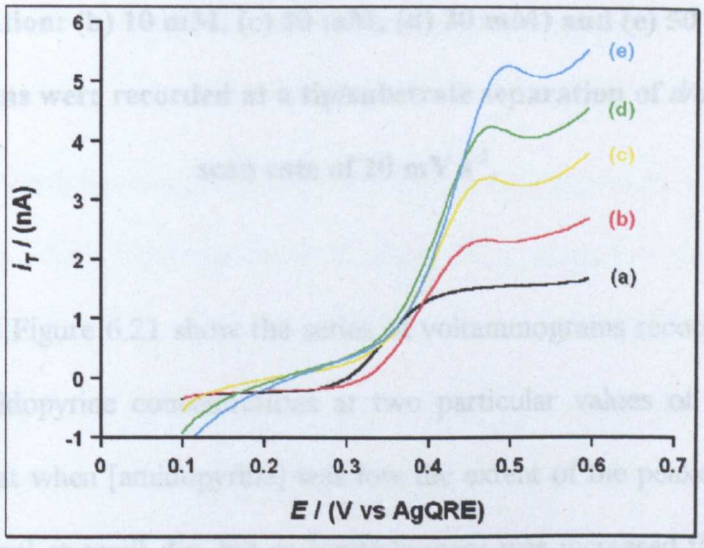

Figure 6.20. LSVs for the oxidation of (a) Fe^{2+} (1 mM), recorded at a 10 μm diameter Pt UME in H_2O/KOH (1 mol dm^{-3}) and with amidopyrine concentrations of: (b) 10 mM, (c) 20 mM, (d) 30 mM and (e) 50 mM. All voltammograms were recorded at a tip/substrate separation of d/a = 1.65 and a scan rate of 20 mV s^{-1}.

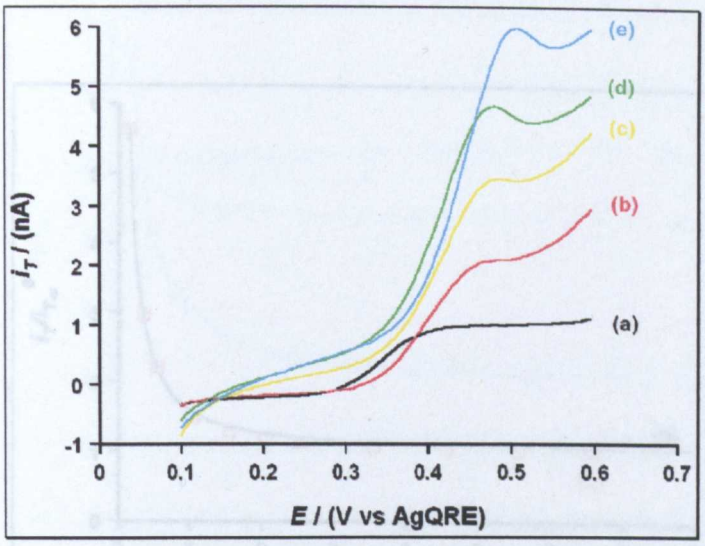

Figure 6.21. LSVs for the oxidation of (a) Fe^{2+} (1 mM), recorded at a 10 μm diameter Pt UME in H_2O/KOH (1 mol dm^{-3}), and with amidopyrine of concentration: (b) 10 mM, (c) 20 mM, (d) 30 mM) and (e) 50 mM. All voltammograms were recorded at a tip/substrate separation of *d/a* = 0.35 and a scan rate of 20 mV s^{-1}.

Figure 6.20 and Figure 6.21 show the series of voltammograms recorded for a range of different amidopyrine concentrations at two particular values of *d/a*. The two figures show that when [amidopyrine] was low the extent of the peaked nature of the wave was minimal at small *d/a*, but as [amidopyrine] was increased the extent of the peaking reached a maximum for all [amidopyrine], at all values of *d/a*. In order to determine the i_T vs. *d/a* behaviour, measurements of wave height were made, with the plateau after the peak used as i_T.

When no amidopyrine was present, the values of i_T that were measured at each point were compared to the Kwak and Bard[151] model of positive feedback, as shown in Figure 6.22, which yielded good agreement.

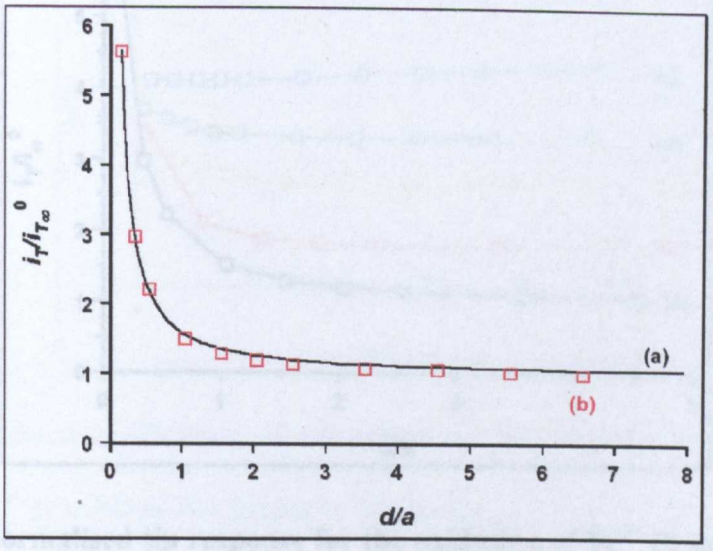

Figure 6.22. (a) The theoretical response for positive feedback compared to (b) i_T vs. *d/a* recorded without amidopyrine present.

LSVs were recorded at a range of values of *d/a*, thus enabling study of $i_T/\ i_{T\infty}{}^0$, $i_S/\ i_{T\infty}{}^0$ or *CoEf* vs. *d/a*. Such plots are shown as Figure 6.23, Figure 6.24 and Figure 6.25 respectively. Qualitatively, it can be seen that, at a particular value of *d/a*, as [amidopyrine] increased i_T increased, whilst i_S and *CoEf* decreased. Specifically, it can be seen that as in the Fe^{2+}/H_2O_2 system, i_T increased with increase in [amidopyrine] and decrease in *d/a*. Each of the different values of [amidopyrine] show markedly different magnitudes of i_T. In the case of the i_S vs. *d/a* measurements, shown as Figure 6.24, it is clear that the values of i_S observed were less dependent on [amidopyrine] than the i_T response. In the case of the *CoEf* measurements, a good range of values was obtained for all [amidopyrine], with the lower concentrations showing the most variation with *d/a*.

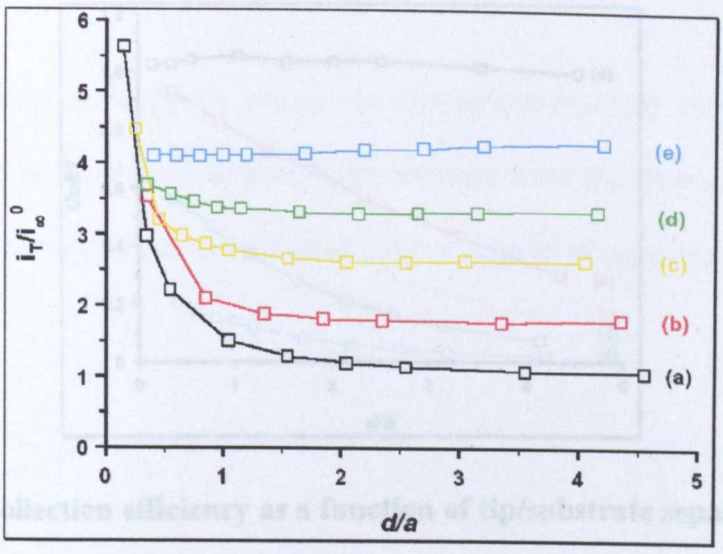

Figure 6.23. Normalised tip response for the oxidation of Fe^{2+} (1 mM) in KOH (1 mol dm^{-3}) the presence of various amounts of amidopyrine - (a) 0 (b) 10 mM, (c) 20 mM, (d) 30 mM and (e) 50 mM.

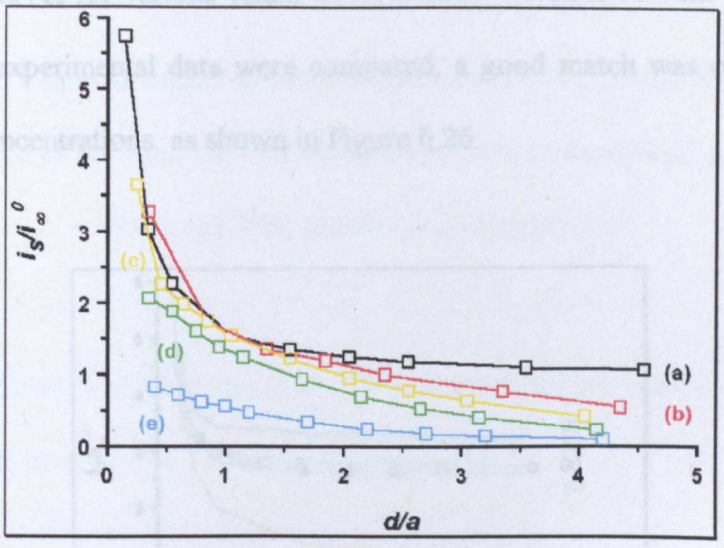

Figure 6.24. Normalised substrate response for the oxidation of Fe^{2+}, corresponding to the tip responses shown in Figure 6.23 in the presence of various amounts of amidopyrine - (a) 0 (b) 10 mM, (c) 20 mM, (d) 30 mM and (e) 50 mM.

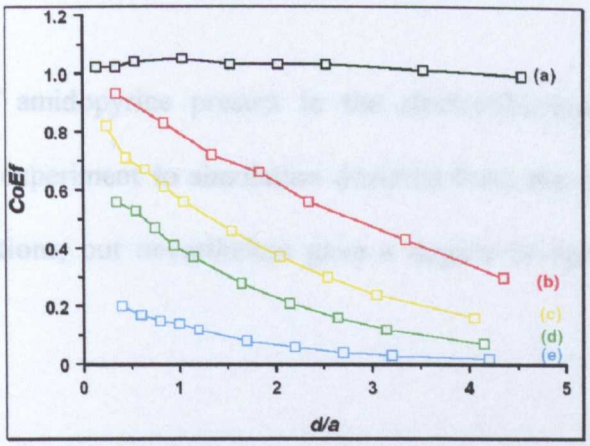

Figure 6.25. Collection efficiency as a function of tip/substrate separation for the oxidation of Fe^{2+} (1 mM) in the presence of amidopyrine - (a) 0 (b) 10 mM, (c) 20 mM, (d) 30 mM and (e) 50 mM.

The same simulation as that described earlier in this chapter was used to obtain a set of theoretical curves for various values of k_c, with $D = 0.62 \times 10^{-5}$ cm^2 s^{-1}. When the simulated and experimental data were compared, a good match was obtained at low amidopyrine concentrations, as shown in Figure 6.26.

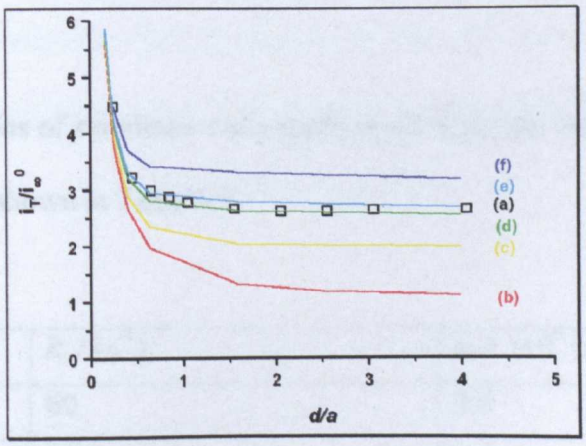

Figure 6.26. Experimental results (a, □) for the TG-SC of the Fe^{III}/Fe^{II} couple in the presence of amidopyrine (20 mM) compared to simulated results for k_c = (b) 1, (c) 100, (d) 250, (e) 300 and (f) 500 s^{-1}.

As the amount of amidopyrine present in the electrochemical cell increased, the correspondence of experiment to simulation deviated from the degree of fit achieved at lower concentrations, but nevertheless gave a degree of agreement, as shown in Figure 6.27.

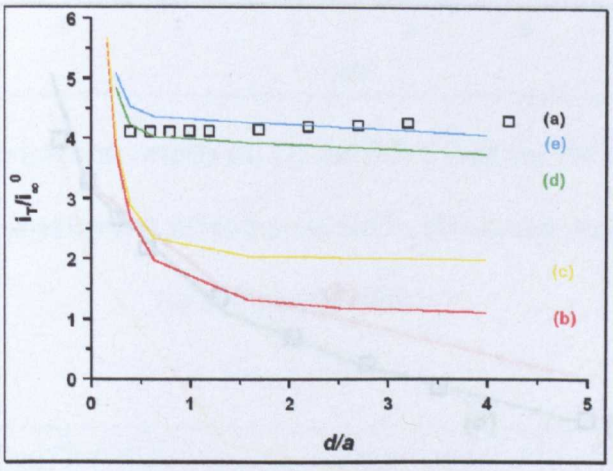

Figure 6.27. Experimental results (a, □) for the TG-SC of the Fe^{III}/Fe^{II} couple in the presence of amidopyrine (50 mM) compared to simulated results for k_c = (b) 1, (c) 100, (d) 800 and (e) 1000 s^{-1}.

From the comparisons of simulated and experimental data, the value of k_c in each case was determined, as shown in Table 6.1.

[amidopyrine]/ mM	k_c / (s^{-1})	k_c / (10^7 mol^{-1} cm^3 s^{-1})
10	60	0.6
20	250	1.3
30	500	1.7
50	800 – 1000	1.6 – 2.0

Table 6.1. Rate constant elucidated for the reaction of Fe^{2+} with amidopyrine.

Further comparison was made between the experimental and simulated data via comparison of the behaviour of $i_S/ i_{T\infty}^{\ 0}$ vs. d/a. From the comparisons of simulated and experimental data the value of k_c in each case was determined, as shown in Table 6.2.

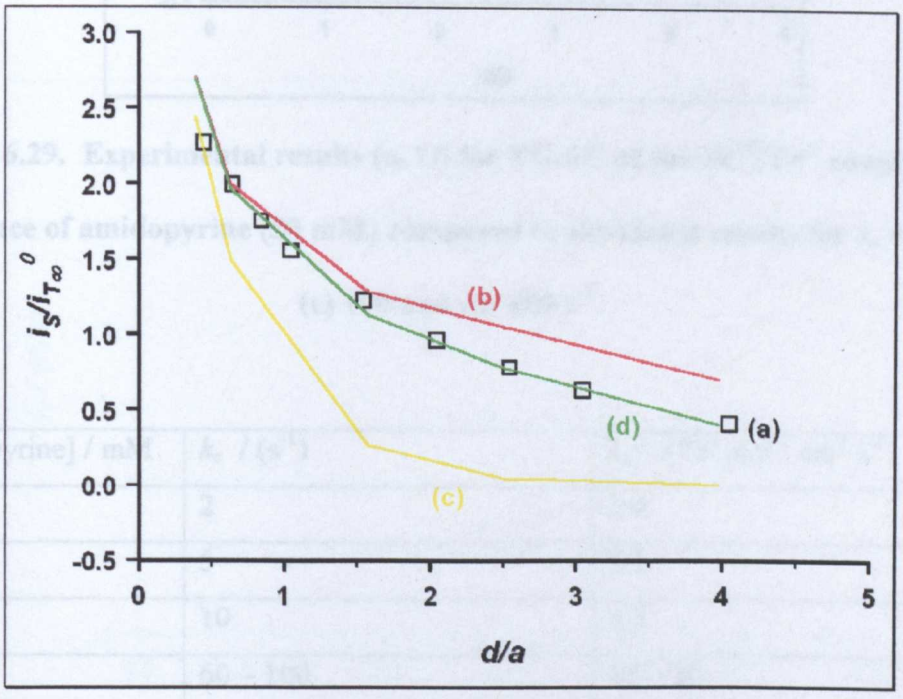

Figure 6.28. Experimental results (a, □) for the TG-SC of the Fe^{III}/Fe^{II} couple in the presence of amidopyrine (20 mM) compared to simulated results for k_c = (b) 1, (c) 100 and (d) 5 s^{-1}.

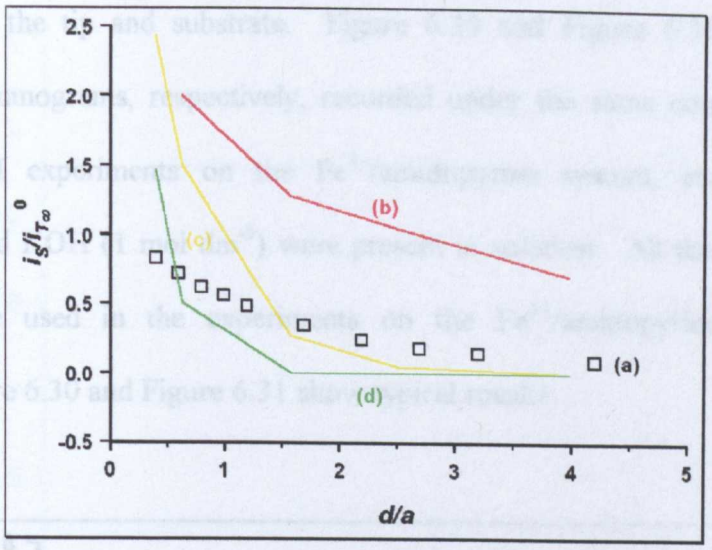

Figure 6.29. Experimental results (a, □) for TG-SC of the Fe^{III}/Fe^{II} couple in the presence of amidopyrine (50 mM) compared to simulated results for k_c = (b) 1, (c) 100 and (d) 800 s^{-1}.

[amidopyrine] / mM	k_c / (s^{-1})	k_c / (10^5 mol^{-1} cm^3 s^{-1})
10	2	2.0
20	5	2.5
30	10	3.3
50	60 – 100	12 – 20

Table 6.2. Rate constants elucidated for the reaction of Fe^{2+} with amidopyrine, as determined via comparison of experimental and simulated values of $i_S/i_{T\infty}^0$ vs. *d/a*.

As previously, it is clear that the EC' simulation constructed is more readily applicable to lower concentrations of amidopyrine. Additionally, the experimental and simulated i_T and i_S data do not yield a consistent rate constant. At +0.1 V vs. AgQRE, the potential used as E_S, amidopyrine is electroactive, thus causing an increase in both i_T and i_S, as amidopyrine, in addition to Fe is cycled between oxidised and reduced

forms between the tip and substrate. Figure 6.30 and Figure 6.31 show tip and substrate voltammograms, respectively, recorded under the same conditions as used for the SECM experiments on the Fe^{3+}/amidopyrine system, except that only amidopyrine and KOH (1 mol dm^{-3}) were present in solution. All the concentrations of amidopyrine used in the experiments on the Fe^{3+}/amidopyrine system were examined; Figure 6.30 and Figure 6.31 show typical results.

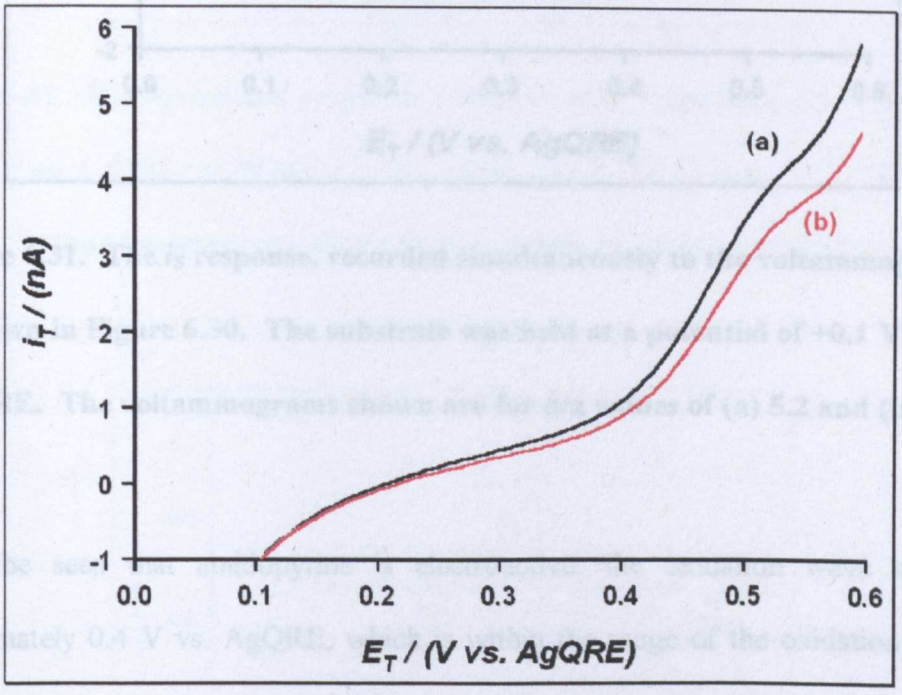

Figure 6.30. The oxidation of amidopyrine (50 mM) in a solution of KOH (1 mol dm^{-3}) at 20 mV s^{-1}. Data correspond to *d/a* values of (a) 5.2 and (b) 0.4.

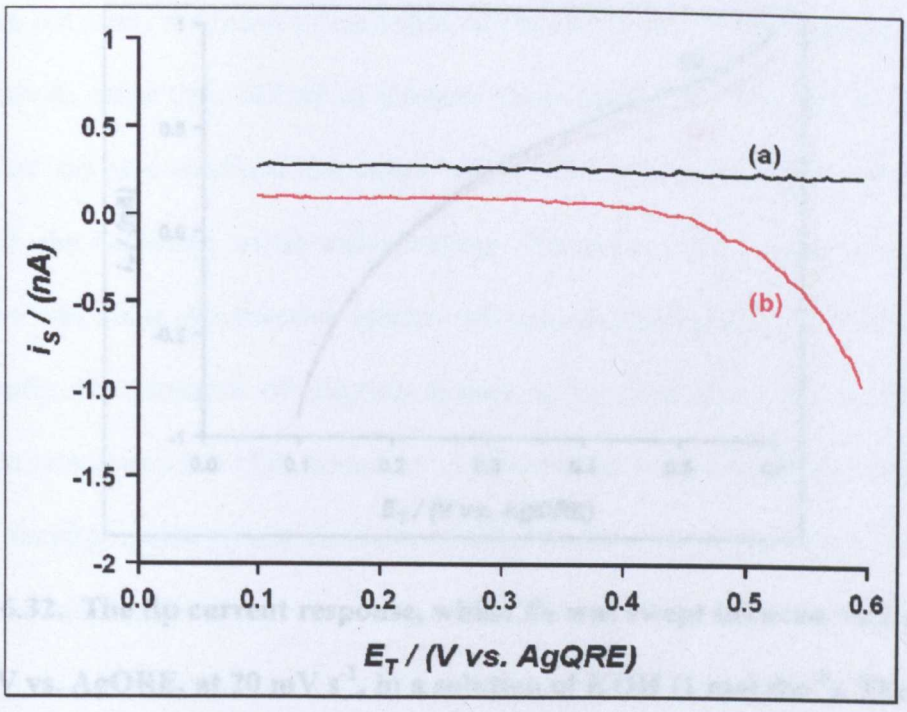

Figure 6.31. The i_S response, recorded simultaneously to the voltammograms shown in Figure 6.30. The substrate was held at a potential of +0.1 V vs. AgQRE. The voltammograms shown are for d/a values of (a) 5.2 and (b) 0.4.

It can be seen that amidopyrine is electroactive, the oxidation wave starts at approximately 0.4 V vs. AgQRE, which is within the range of the oxidation of Fe^{2+} and hence its presence may have interfered with measurements of i_T and i_S.

During examination of the electroactive nature of amidopyrine, a "blank" experiment was run, whereby the solution contained within the electrochemical cell contained only KOH (1 mol dm^{-3}).

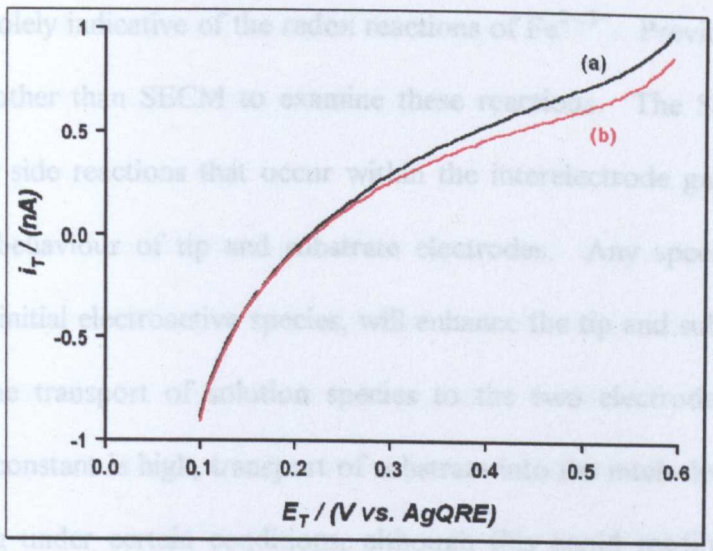

Figure 6.32. The tip current response, whilst E_T was swept between +0.1 and 0.6 V vs. AgQRE, at 20 mV s^{-1}, in a solution of KOH (1 mol dm^{-3}). The voltammograms are shown for d/a values of (a) 5.2 and (b) 0.4

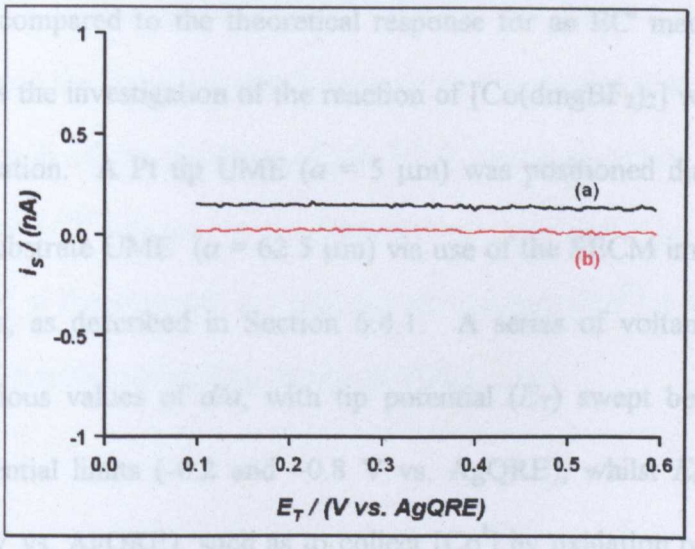

Figure 6.33. The corresponding substrate response to Figure 6.32.

The two systems that were described in the literature as model systems, did not prove to be so under the conditions used for this study. The latter system, in particular, is too complicated to lend itself to use as a model EC' system in that measurements of i_T

and i_S are not solely indicative of the redox reactions of $Fe^{2+/3+}$. Previous studies have used methods other than SECM to examine these reactions. The SECM geometry means that any side reactions that occur within the interelectrode gap make a great impact to the behaviour of tip and substrate electrodes. Any species re-cycled in addition to the initial electroactive species, will enhance the tip and substrate currents. Additionally, the transport of solution species to the two electrodes is important. When the rate constant is high, transport of substrate into the inter-electrode gap may become limiting under certain conditions, although this could readily be taken into account by adapting the model.

6.5 $[Co^{I}]$/RBr reaction studied by the TG-SC mode of the SECM

During Chapter 5 it was demonstrated that under certain conditions, the reaction of $[Co^{I}]$ could be compared to the theoretical response for an EC' mechanism. This section describes the investigation of the reaction of $[Co(dmgBF_2)_2]$ with E2IBB in an SECM configuration. A Pt tip UME (a = 5 μm) was positioned directly above the centre of a Pt substrate UME (a = 62.5 μm) via use of the SECM imaging mode and approach curves, as described in Section 6.4.1. A series of voltammograms were recorded at various values of d/a, with tip potential (E_T) swept between two pre-determined potential limits (-0.2 and –0.8 V vs. AgQRE), whilst E_S was held at a potential (-0.1 V vs. AgQRE), such as to collect $[Co^{I}]$ by oxidation to $[Co^{II}]$. As for the Fe^{2+}/H_2O_2 and Fe^{3+}/amidopyrine systems, the diffusion-limited current, i_T was measured from each voltammogram. As the potential of the substrate was held at a fixed value in order to collect $[Co^{I}]$, a voltammogram was also obtained by measuring i_S as a function of E_T. Here also, a diffusion-limited plateau was observed. As described for the Fe^{2+}/H_2O_2 and Fe^{3+}/amidopyrine systems, i_T and i_S were measured

from a series of voltammograms, recorded at a range of values of *d/a*. Figure 6.34 shows the relationship obtained for i_T vs. *d/a* for this system.

As for the model EC' system described earlier, i_T was seen to increase on addition of substrate (in this case E2IBB). A further observation of note is that the behaviour of i_T vs. *d/a* does not conform to that predicted by positive feedback theory[151]. Rather, i_T was seen to decrease before increasing at lower values of *d/a*. Such behaviour was observed by Demaille et al[196] during study of reactions with the ECE/DISP1 mechanism, although in those cases the i_T vs. *d/a* behaviour was shown to follow the theory for hindered diffusion until *d/a* was very small. The reason for such a shape of approach curve was that the tip process changed from being a two electron process, involving both E steps at large values of *d/a*, to being just that of the first E step at small values of *d/a*, because the diffusion of substrate into the inter-electrode gap was hindered and hence the second E step became hindered. In this case, such behaviour could be as a result of the instability of the [Co^I] supernucleophile. Reaction with solvent or impurities[282] may lead to the formation of a modified [Co] complex, which could be reduced at the potential at which the reduction of [Co^{II}] is diffusion-limited, thus leading to behaviour resembling that of an ECE system.

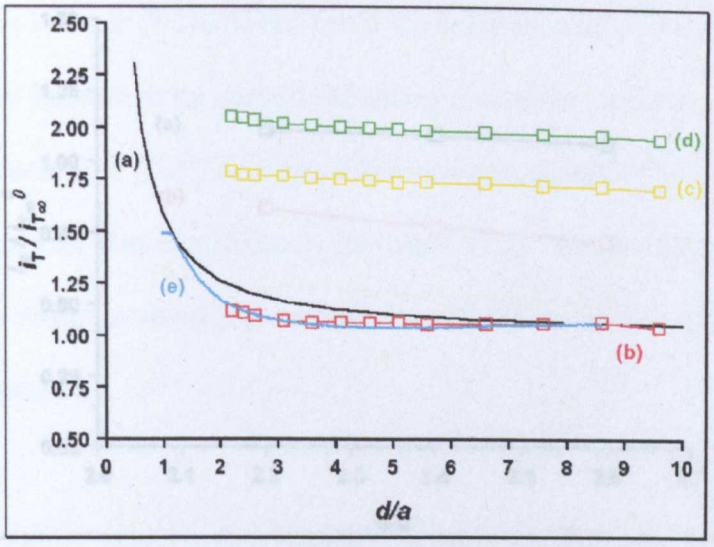

Figure 6.34. Normalised tip current as a function of tip/substrate separation for (a) the theoretical response for positive feedback, (b) reduction of $[Co^{2+}]$ (0.5 mM) alone and in the presence of E2IBB (c) 10 mM and (d) 25 mM. Line (e) shows an approach curve recorded immediately prior to measuring i_T and i_S point wise at specific values of *d/a*.

The substrate current was measured simultaneously in order that the behaviour of i_S vs. d/a, as a function of E_T, could also be studied. It was found that over large distances ($d/a > 3$) i_S fell rapidly, also contributing to the postulation that the $[Co^I]$ species was unstable. Figure 6.35 shows results up to $d/a = 2.6$.

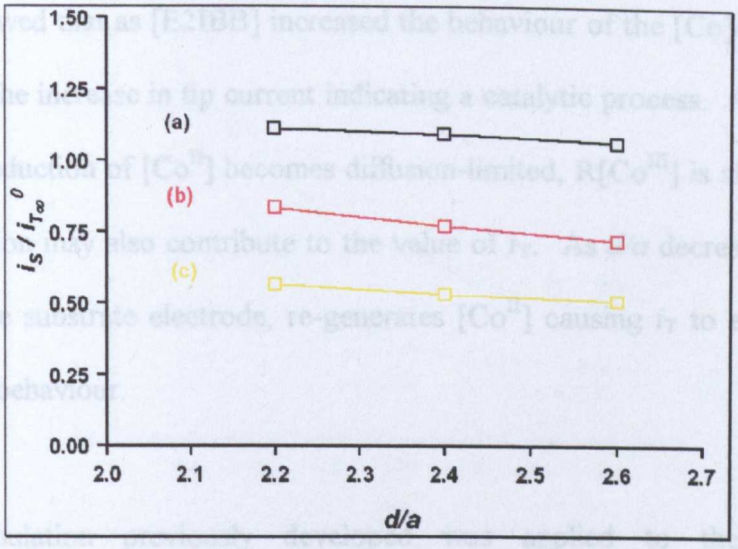

Figure 6.35. The behaviour of i_S, corresponds to the i_T data shown in Figure 6.34. For the reduction of (c) [Co^{II}] (0.5 mM) and in the presence of E2IBB (b) 10 mM and (a) 25 mM. The substrate electrode was maintained at a potential of –0.1 V vs. AgQRE in order to drive the collection of [Co^{I}] at a diffusion-controlled rate, whilst the tip electrode was swept between –0.2 and –0.8 V vs. AgQRE, at a scan rate of 20 mV s^{-1}.

This apparent "loss" of [Co^{I}] may be assigned to the instability of the electrogenerated [Co^{I}] on the SECM timescale. As [Co^{I}] is a supernucelophile it is a highly reactive species and as such is likely to undergo transformation as soon as formed via reduction of [Co^{II}]. Such a decomposition was postulated to have occurred via various routes such as: internal rearrangement or reaction with solvent. In each case a modified [Co] species would be produced.

In this SECM experiment the tip potential was swept to -0.8 V vs. AgQRE, where the reduction of [Co^{II}] was driven at a diffusion-controlled rate. This reduction was accomplished in the presence of an excess of E2IBB of 20 or 50 times that of [Co^{II}].

Figure 5.6 showed that as [E2IBB] increased the behaviour of the [Co]/E2IBB system changed with the increase in tip current indicating a catalytic process. At the potential at which the reduction of [Co^{II}] becomes diffusion-limited, R[Co^{III}] is also present and thus its reduction may also contribute to the value of i_T. As d/a decreases further the presence of the substrate electrode, re-generates [Co^{II}] causing i_T to exhibit positive feedback type behaviour.

The EC' simulation previously developed was applied to the reaction of [$Co(dmg(BF_2)_2)$] with E2IBB. Figure 6.36 shows a typical fit of experimental data for the behaviour of i_T vs. d/a to simulated data for a number of different values of k_c.

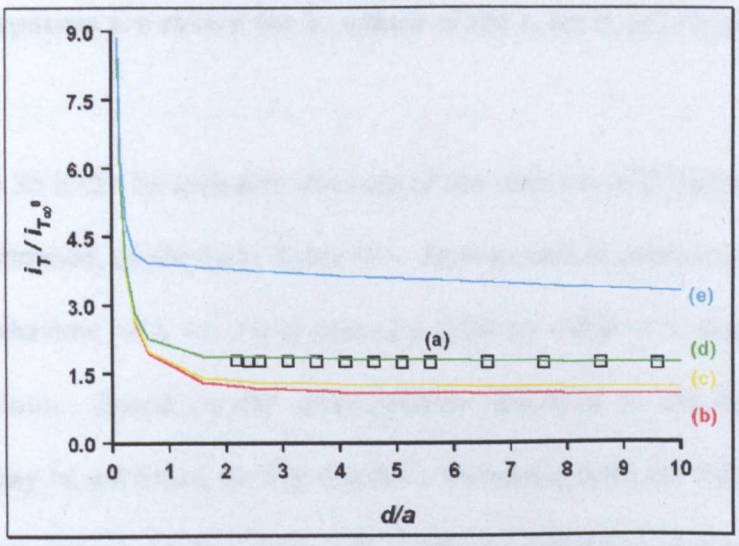

Figure 6.36. Tip response data, (a, □) recorded at various values of d/a for the reduction of [Co^{II}] (0.5 mM) in the presence of E2IBB (10 mM). Comparison is made to simulated i_T vs. d/a behaviour for values of k_c of (b) 1, (c) 10, (d) 100 and (e) 1000 s^{-1}.

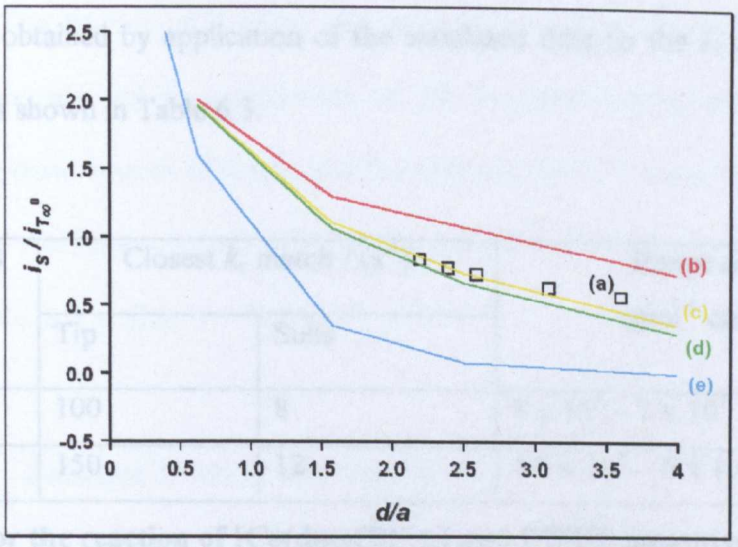

Figure 6.37. The substrate response corresponding to the data shown in Figure 6.36. The substrate was held at a potential of –0.1 V vs. AgQRE, in order to collect [Co^{I}] from solution. Experimental data is shown as (a, □), whilst simulated responses are shown for *kc* values of (b) 1, (c) 8, (d) 10 and (e) 100 s^{-1}.

From Figure 6.36 it can be seen how the rate of the reaction of [$Co(dmg(BF_2)_2)$] with E2IBB was estimated, as shown in Table 6.3. As was seen in previous sections of this chapter, the behaviour of i_S vs. d/a produced a different value of k_c than that of the i_T vs. d/a behaviour. Based on the investigations described at the begining of this chapter, this may be attributed to side reactions increasing both the value of i_T and i_S. The higher than expected values of i_T and i_S may be attributed to the production of R[Co^{III}] as a results of the reaction of E2IBB and [Co^{I}]. Hence, i_T fits to a larger value of k_c than might be expected and i_S fits to a lower value. A better fit might be attainable by developing the simulation to take account of the instability of [Co^{I}] and the contribution of R[Co^{III}] to i_T and hence the slight deviation of i_T vs. d/a from model EC' type behaviour. In spite of this non-ideal behaviour, a range within which

k_c resided was obtained by application of the simulated data to the i_T and i_S vs. d/a behaviour and is shown in Table 6.3.

Excess E2IBB	Closest k_c match / (s^{-1})		Range of k_c / (mol^{-1} cm^3 s^{-1})
	Tip	Subs	
20x (10 mM)	100	8	$8 \times 10^5 - 1 \times 10^7$
50x (25 mM)	150	12	$4.8 \times 10^5 - 6 \times 10^6$

Table 6.3. k_c for the reaction of [Co(dmg(BF_2)$_2$] and E2IBB measured by SECM.

Values of k_c, for the reaction of [Co^I] and E2IBB, of the order of 10^6 mol^{-1} cm^3 s^{-1} were obtained via the voltammetric studies described in chapter 5. Clearly this value agrees with the value of k_c obtained by SECM. Even though both the voltammetric and SECM studies were complicated by non-ideal EC' behaviour, each has been shown to yield a similar value for k_c. Therefore, it may be concluded that k_c for the reaction of [Co^I] and E2IBB in MeCN is of the order of 10^6 mol^{-1} cm^3 s^{-1}.

6.6 Biphasic liquid systems.

6.6.1 Introduction and rationale

[Co^{II}(dmgBF_2)$_2$] was by used Kukulj et al as a catalyst in two phase emulsion[283] or mini-emulsion[284] polymerisation reactions, in addition to the homogeneous reactions described earlier. Emulsion polymerisation is a versatile and widely used commercial process, whilst CCTP reduces the molecular weight of polymers, low molecular weight polymers are commercially important. By combining the two methods, commercially valuable polymers are produced via a versatile and widely utilised reaction[284]. B_{12} and its analogues were also used as phase transfer catalysts in organic

synthesis[95]. The studies of Rusling and co-workers, where microemulsions were used as solvent, has led to examination of the B_{12}/dibromocyclohexane (DBCH) system in a biphasic system of water and benzonitrile (BN)[285] using SECM. Figure 6.38 shows the system employed, where B_{12} is only soluble in the aqueous layer and DBCH is soluble only in BN.

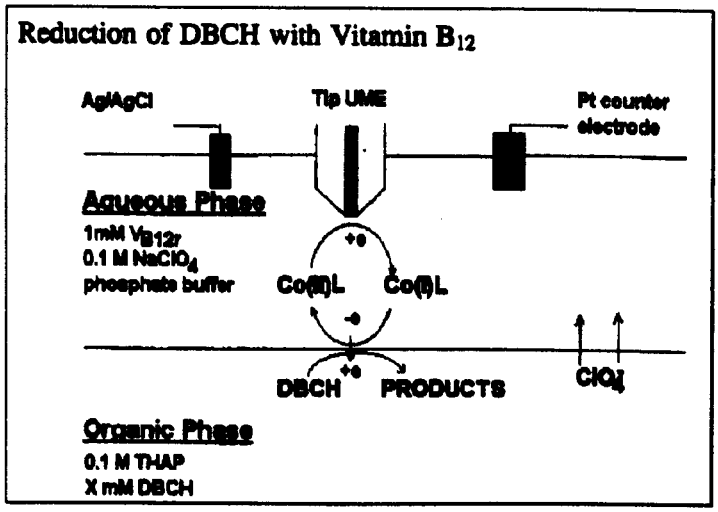

Figure 6.38. The reaction of B_{12} and DBCH across a liquid/liquid interface, taken from ref 285.

A polarisable interface was used, where the polarity was altered by changing the concentration of the common ion (perchlorate in this case) in each layer. $[Co^{I}]H$ was formed at the electrode, which then went on to react with DBCH by either a multistep radical process or a concerted E_2 elimination, as mentioned in chapters 1 and 5. As already discussed, these processes are indistinguishable from a kinetic point of view. Rusling found that all oxygen had to be removed from the system (for reasons discussed earlier) and that $[Co^{III}]$ had to be pre-electrolysed before well defined voltammograms could be seen for the $[Co^{II}]/[Co^{I}]$ transition. The tip electrode was brought close to the interface, whereupon, it was held at a potential to drive the

conversion of [Co^{II}] to [Co^{I}] at a diffusion-limited rate. The tip response, i_T, was measured as a function of the separation between it and the interface to yield approach curves. The reaction was considered to have four stages:

1) mediator diffusion between the tip and the ITIES,

2) the interfacial reaction,

3) diffusion of DBCH in BN,

4) charge compensation by ion transfer.

The motivation behind the experiment was to measure the kinetics of the reaction that occurs between [Co^{I}] and DBCH across the DCE/H_2O interface.

6.6.2 Double Potential Step Chronoamperometry (DPSC)

DPSC[132] was briefly discussed in chapter 1, as a method of initiating and monitoring interfacial reactions. Two sequential potential steps are applied to a tip electrode. First, the forward step, involves stepping the potential at an electrode to a value where a redox event is driven at a diffusion-controlled rate, e.g. generation of Red from Ox. A second potential step, in the reverse direction occurs at a pre-determined time, such that any Red in the vicinity of the electrode will be converted back to Ox and hence "collected". Each potential is maintained for a preset amount of time, thus allowing the current-time characteristics to be measured. In the SECM configuration, where the tip electrode is positioned close to an interface, the current-time characteristics reveal the nature and extent of interaction of Red with the interface[194].

6.6.3 Theory

Where investigations are carried out near an interface, there are a number of possible scenarios. Either 1) the electroactive species, in both the oxidised and reduced forms remains entirely in one of the phases, or 2) one form of the redox couple is soluble, to some extent in both phases or 3) both species are soluble in both phases. The extent of a species solubility in each phase is described by its partition coefficient (K_e). Where:

$$K_e = \frac{c^*_1}{c^*_2} \qquad \text{(Eq. 6.28)}$$

where c^*_1 is the bulk concentration of species in phase 1 and c^*_2 is the bulk concentration of species in phase 2.

For simplicity, the experiments described herein were considered as belonging to one of the three possible regimes shown in Figure 6.39 - Figure 6.41.

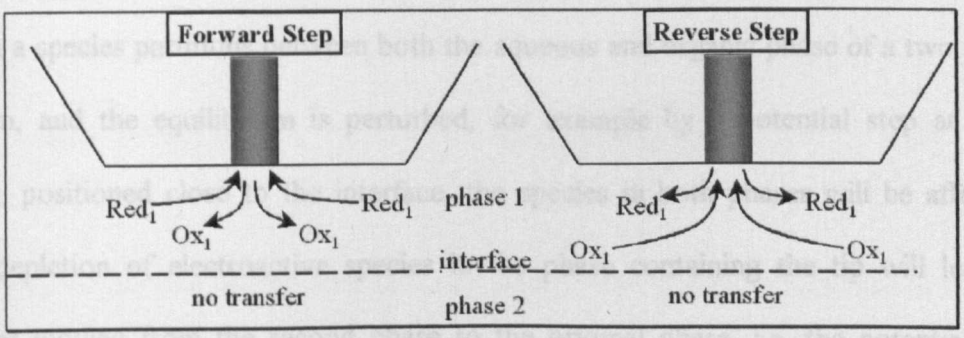

Figure 6.39. Neither the initial or final redox state of the electroactive species is soluble in either phase.

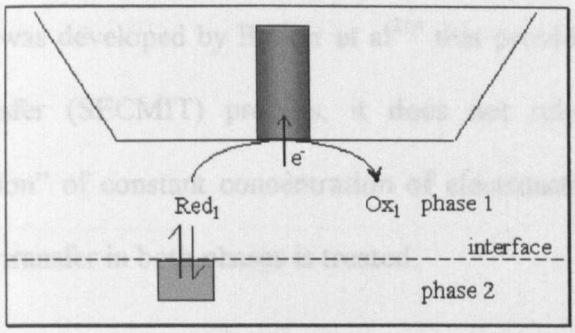

Figure 6.40. The initial redox state of the electroactive species is soluble in both phases.

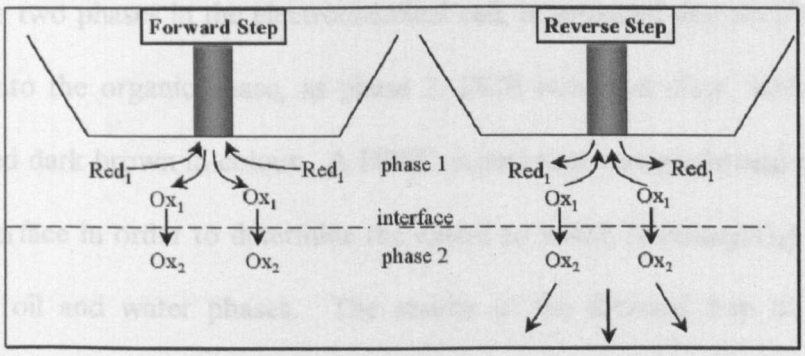

Figure 6.41. The initial redox state of the electroactive species is soluble only in phase 1, but the product is soluble in both phases.

When a species partitions between both the aqueous and organic phase of a two phase system, and the equilibrium is perturbed, for example by a potential step at a tip UME, positioned close to the interface, the species in both phases will be affected. The depletion of electroactive species in the phase containing the tip will lead to species moving from the second phase to the original phase, i.e. the potential step induces the transfer of species from phase 2 to phase 1. The ability of SECM to elucidate detailed information about a particular system is based upon the availability of good quality simulations, that faithfully reproduce experimental results. A

numerical simulation was developed by Barker et al[214] that provides the theory for an SECM induced transfer (SECMIT) process, it does not rely on the "constant composition assumption" of constant concentration of electroactive species in phase 2, as diffusional mass transfer in both phases is treated.

6.6.4 Results and discussion

6.6.4.2 DPSC of [Co(dmgH)$_2$]

The reaction of [Co(dmgH)$_2$] with E2IBB was examined in a liquid/liquid set up. On mixing of the two phases in the electrochemical cell, it appeared that no [Co(dmgH)$_2$] transferred into the organic phase, as phase 2, DCE remained clear, whilst phase 1, H_2O remained dark brown in colour. A DPSC experiment was performed close to the water/oil interface in order to determine the extent to which [Co(dmgH)$_2$] partitioned between the oil and water phases. The results of the forward step of the DPSC experiment are shown in Figure 6.42. The corresponding reverse steps of the DPSC experiment are shown in Figure 6.43. The method of Shoup and Szabo[286] was used to gain D by comparison of the i/i_{lim} vs. $t^{1/2}$ relationship in bulk solution, for a single potential step:

$$i/i_{lim} = 0.4431[(D/a^2)^{-0.5}]t^{1/2} + 0.2146exp(-0.3911(D/a^2)^{-0.5})\, t^{1/2} \quad \text{(Eq. 6.29)}$$

The Shoup-Szabo line on the bulk (i.e. not close to the interface) response in Figure 6.42 indicated that [Co(dmgH)$_2$] had a diffusion coefficient of 3.8×10^{-6} cm^2 s^{-1} in H_2O/LiClO$_4$ (0.1 mol dm^{-3}). Qualitatively, at close distances, the shape of the current/time transients resembled those of a species that resided entirely in the water phase and hence the interface with the oil phase acted as an inert interface.

Experimental data were compared to theoretical data for such transient measurements obtained close to an inert interface.

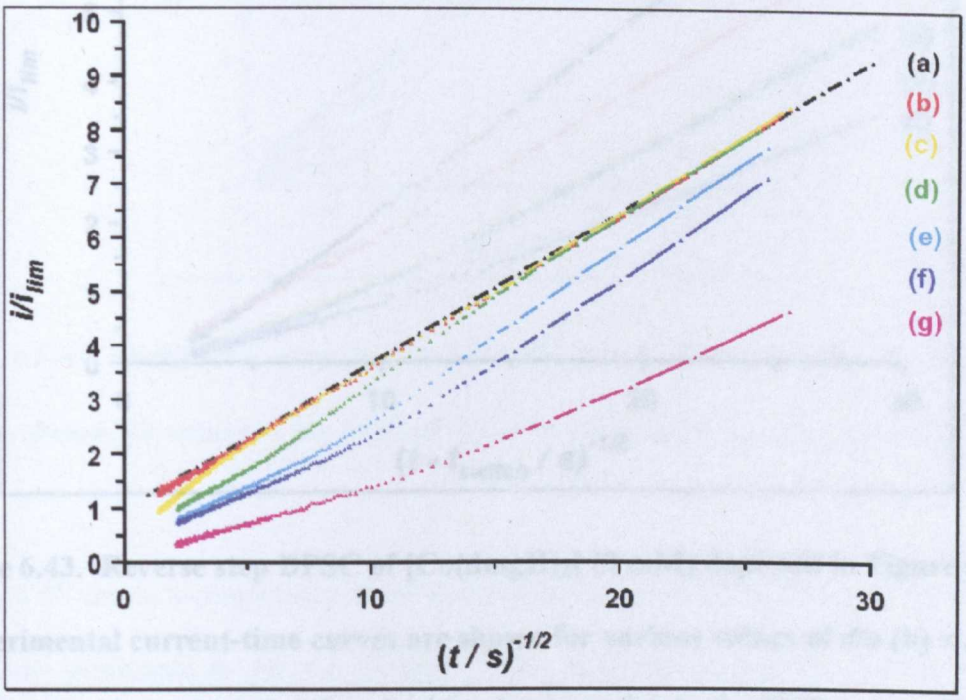

Figure 6.42. Forward step of DPSC of $[Co(dmgH)_2]$ (2 mM) in the aqueous [$LiClO_4$ (0.1 mol dm^{-3}) present as supporting electrolyte] layer of a biphasic liquid solution at various distances from an interface with DCE (containing THAP (0.1 mol dm^{-3}) as supporting electrolyte). Fitting of the Shoup-Szabo equation to (a) yields $D = 3.8 \times 10^{-6}$ cm^2 s^{-1}. Experimental current-time curves are shown for various values of d/a (b) ∞, (c) 0.9, (d) 0.28, (e) 0.14 (f) 0.1 and (g) having passed into the DCE layer. The forward step was c.a. 0.5 s in duration.

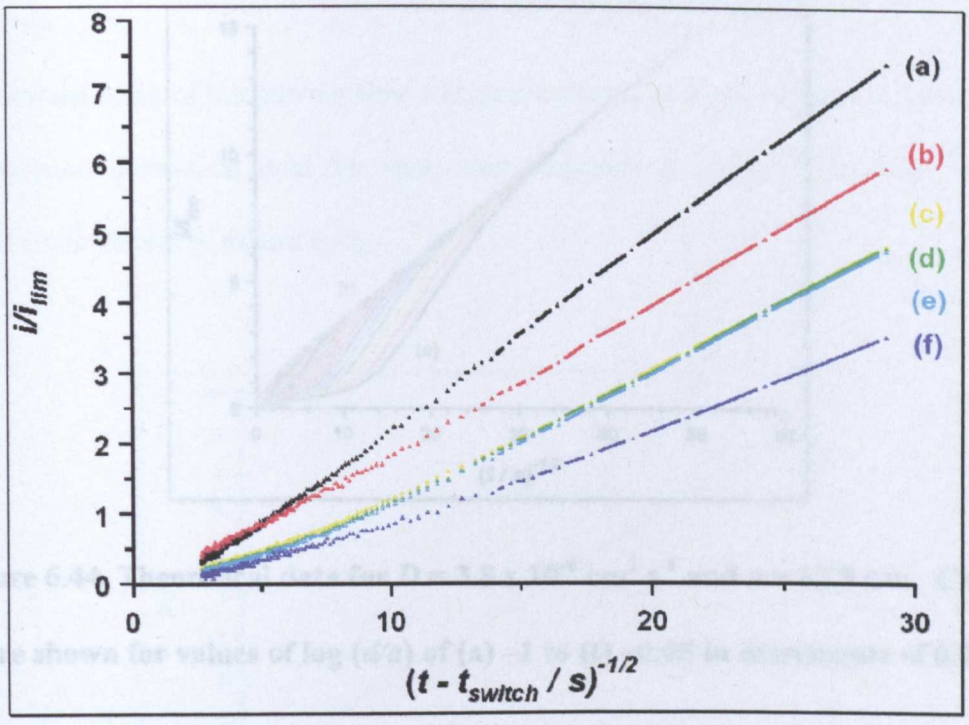

Figure 6.43. Reverse step DPSC of $[Co(dmgH)_2]$ (2 mM) depicted in Figure 6.42. Experimental current-time curves are shown for various values of *d/a* (b) ∞, (c) 0.9, (d) 0.28, (e) 0.14 (f) 0.1 and (g) having passed into the DCE layer. The reverse step was c.a. 0.5 s in duration.

A simulation of the current-time behaviour at a UME for a redox process close to an inert interface, has previously been developed[132]. This computer model was used to simulate the behaviour for the present case (a = 12.5μm and D = 3.8 x 10^{-5} cms^{-1}).

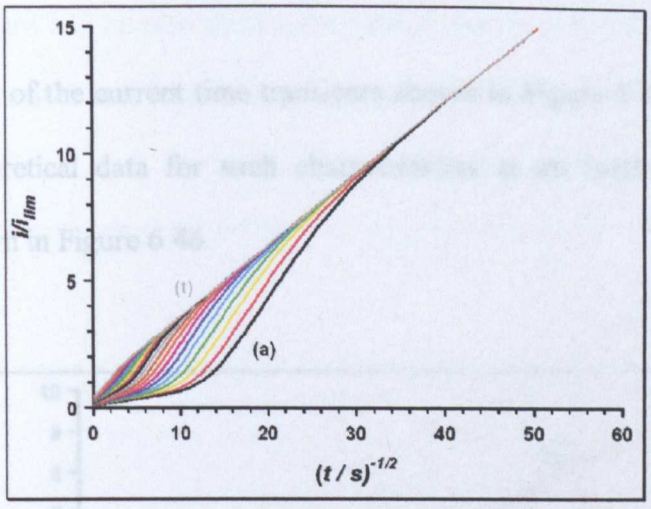

Figure 6.44. Theoretical data for D = 3.8 x 10^{-6} cm^2 s^{-1} and a = 12.5 μm. Curves are shown for values of log (d/a) of (a) –1 to (t) –0.05 in increments of 0.05.

Figure 6.45 shows a comparison of the theoretical response for an UME of radius 12.5 x 10^{-4} cm positioned at d/a = 0.1 from an inert interface. For different D it can be seen that the smaller the D value, the later the hindered diffusion deviation occurs, and that the response is sensitive to D.

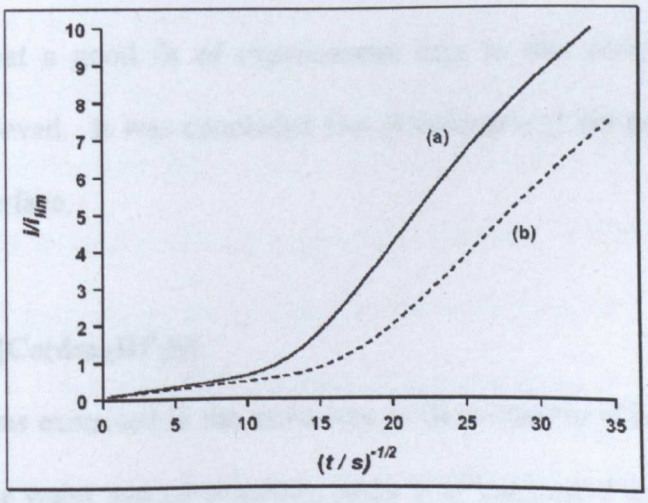

Figure 6.45. The effect of D on the theoretical response of a tip electrode, close to an inert interface (d/a =0.1), D = (a) 3.8 x 10^{-6} cm^2 s^{-1} and (b) 6.4 x 10^{-6} cm^2 s^{-1}.

The forward steps of the current time transients shown in Figure 6.42 were compared to simulated theoretical data for such characteristics at an inert interface, with a typical result shown in Figure 6.46.

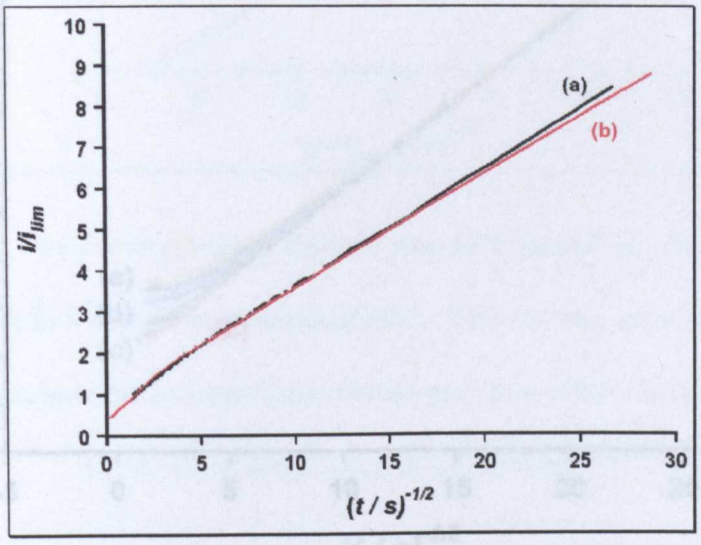

Figure 6.46. Experimental data for the reduction of $[Co(dmgH)_2]$ (a) fitted to simulated data for d/a = 0.9.

It can be seen that a good fit of experimental data to that simulated for an inert interface was achieved. It was concluded that $[Co(dmgH_2)_2]$ did not partition across the H_2O/DCE interface.

6.6.4.3 DPSC of $[Co(dmgBF_2)_2]$

$[Co(dmgBF_2)_2]$ was examined in the same way as described for $[Co(dmgH)_2]$. In this case on mixing the water and oil solutions, some $[Co^{II}]$ appeared to transfer to the oil phase, as the colourless DCE phase became straw coloured, to resemble that of the

H_2O phase. Forward and reverse steps were carried out via a DPSC experiment, these are shown in Figure 6.47 and Figure 6.48, respectively.

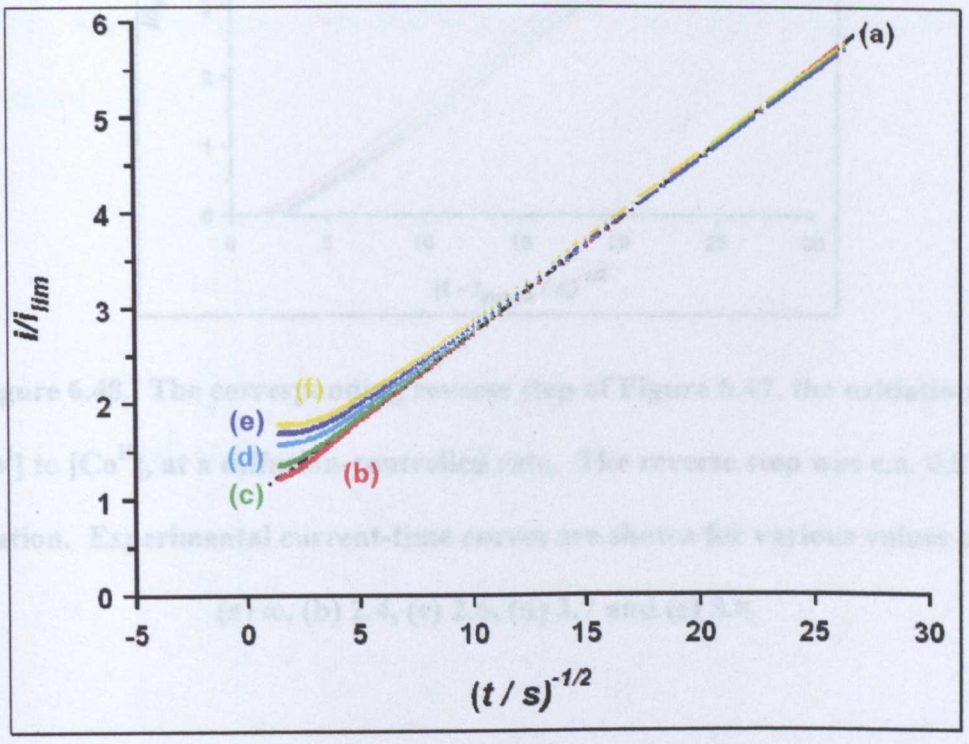

Figure 6.47. The forward step of a DPSC experiment of $[Co(dmgBF_2)_2]$, showing the reduction of $[Co^{II}]$ (0.5 mM) to $[Co^{I}]$ at a diffusion-controlled rate. The forward step was c.a. 0.5 s in duration. Fitting of the Shoup-Szabo equation to (a) yielded $D = 8.5 \times 10^{-6}$ cm^2 s^{-1}. Experimental current-time curves are shown for various values of d/a (b) ∞, (c) 2.4, (d) 2.6, (e) 3.7 and (f) 5.8. The tip electrode was located in the H_2O phase (0.1 mol dm^{-3} $LiClO_4$ present as supporting electrolyte) layer, close to the interface with DCE (containing TBAP, 0.1 mol dm^{-3} as supporting electrolyte).

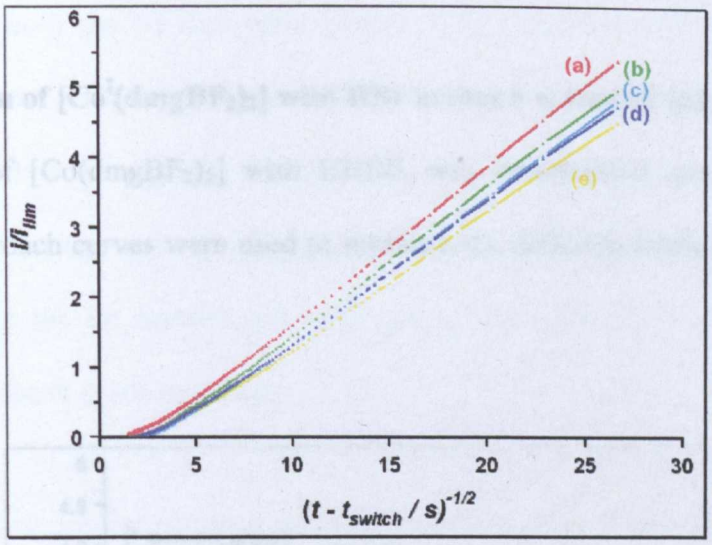

Figure 6.48. The corresponding reverse step of Figure 6.47, the oxidation of $[Co^{I}]$ to $[Co^{II}]$, at a diffusion-controlled rate. The reverse step was c.a. 0.5 s in duration. Experimental current-time curves are shown for various values of *d/a* (a) ∞, (b) 2.4, (c) 2.6, (d) 3.7 and (e) 5.8.

Figure 6.47 appears completely different to that observed for Figure 6.42. In this case as the water/oil interface was approached, the normalised current at small $t^{-1/2}$ (long times), was above that of the transient recorded in bulk solution. This behaviour indicated that $[Co(dmgBF_2)_2]$ resided in the oil phase and as $[Co^{II}]$ was depleted from the water area around the tip electrode, further $[Co^{II}]$ passed through the oil/water interface in an attempt to correct the perturbation to the equilibrium across the interface, i.e. as for the schematic shown in Figure 6.40. Hence, rather than $[Co(dmgBF_2)_2]$ becoming depleted with time, the concentration and thus current, is higher than would be expected for an inert interface. The transients shown above show that $[Co^{II}(dmgBF_2)_2]$ partitions between the water and oil phases, whilst $[Co^{I}(dmgBF_2)_2]$ does not.

6.6.4.4 Reaction of $[Co^{I}(dmgBF_2)_2]$ with RBr across a water/oil interface.

The reaction of $[Co(dmgBF_2)_2]$ with E2IBB was investigated across a water/oil interface. Approach curves were used to measure the diffusion-limited current as *d/a* was reduced.

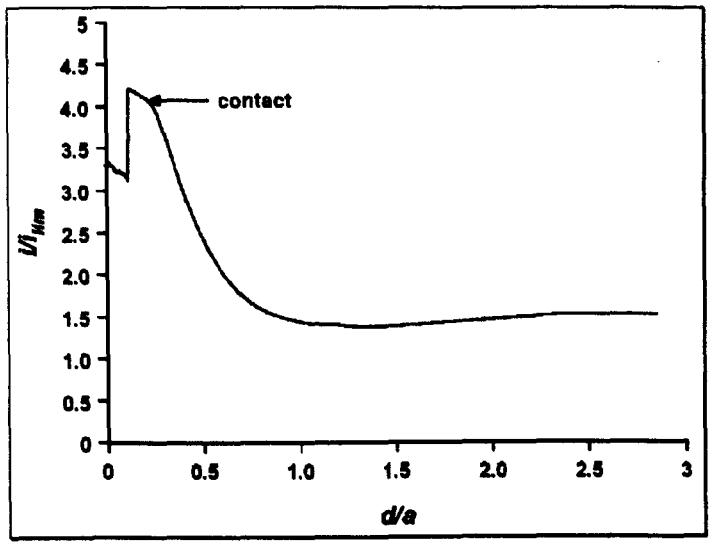

Figure 6.49. An approach curve recorded at a Pt UME tip (a = 12.5 μm) located in the water phase, approaching a water/DCE interface for the reduction of $[Co^{II}(dmgBF_2)_2]$ (2 mM) in the presence of E2IBB (20 mM). The water phase contained LiClO4 (0.1 mol dm^{-3}) and the DCE phase contained TBAP (0.1 mol dm^{-3}), respectively, as supporting electrolytes.

When there was no E2IBB present, the diffusion-limited current took the shape of a hindered diffusion approach curve for d/a ≤ 1. Conversely, when E2IBB was present in the electrochemical cell, the approach curve resembled that for positive feedback. Figure 6.49 shows that the rate of reaction of $[Co^{I}(dmgBF_2)_2]$ with E2IBB increased as the tip electrode approached the water/oil interface. However, as $[Co^{II}(dmgBF_2)_2]$

was present in both the oil and water phases, it is impossible to say whether this increase in current was due to the reaction of $[Co^{I}(dmgBF_2)_2]$ with E2IBB alone, which would follow the process shown in Figure 6.50, or whether there was some contribution to the tip current via induced transfer of $[Co^{II}(dmgBF_2)_2]$ across the interface so that the tip current was made up of contributions both from induced transfer and feedback at the interface.

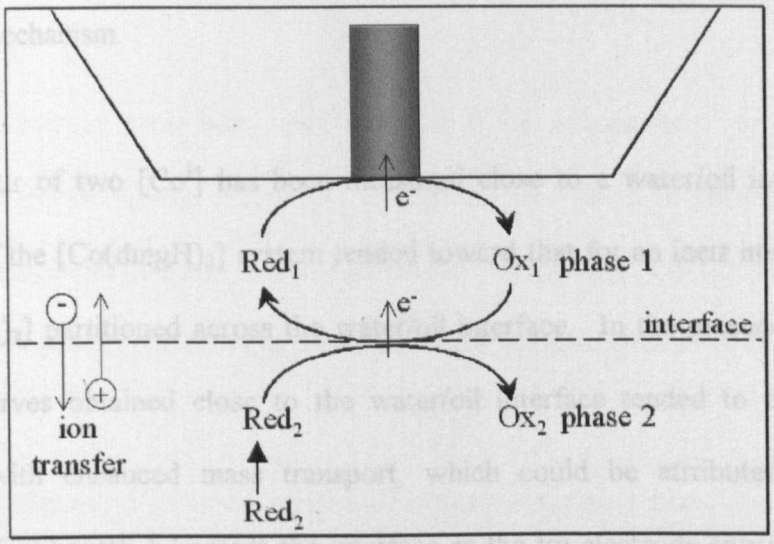

Figure 6.50. SECM feedback experiments at liquid/liquid interfaces.

The approach curve shown in Figure 6.49 bears a great resemblance to that shown in Figure 6.34 (b) and (e), for the TG-SC measurements. Therefore, it could be concluded that there could be an additional complication due to the generation of $R[Co^{III}]$.

These preliminary data illustrate the possibility of using SECM to measure partitioning of redox catalysts in two-phase systems and measurement of the interfacial reactivity in such systems.

6.7 Conclusions

Two model EC' systems have been studied in the TG-SC mode of the SECM and have been shown to be non-ideal for SECM studies, although a guide as to the catalytic reaction rates can be obtained. A computer model was applied for the EC' reaction in the TG-SC mode of the SECM. The $[Co(dmgBF_2)_2]$/RBr system has been studied by the TG-SC mode of the SECM and found to be more complicated than described by a simple EC' mechanism.

The behaviour of two $[Co^I]$ has been measured close to a water/oil interface. The behaviour of the $[Co(dmgH)_2]$ system tended toward that for an inert interface, whilst $[Co(dmgBF_2)_2]$ partitioned across the water/oil interface. In the presence of E2IBB, approach curves obtained close to the water/oil interface tended to the behaviour associated with enhanced mass transport, which could be attributed to induced transfer of $[Co(dmgBF_2)_2]$ across the interface as the tip electrode approaches and/or to the reaction of $[Co(dmgBF_2)_2]$ with E2IBB.

Chapter 7 - Summary and future work

The purpose of the work described in this thesis was to measure standard electrode potentials and rate constants for various systems, based around cobalt and copper centred catalysts. The intention was to increase understanding of these two different types of complexes, with the knowledge described herein aiding in catalyst and system design.

Two main techniques have been used, those of UME voltammetry and SECM. The UME measurements proved technically simple and were used to provide information on redox kinetics and coupled solution reactions. Conversely, the SECM experiments were more complex to perform but allow more complicated systems to be studied.

The results obtained in Chapter 3 provide further information about the properties of [Cu] ATP catalysts. Enhanced information could be obtained with better knowledge of the values of $E_{1/2}$ or $E^{0'}$, but the work has shown that in organic solvents even simple parameters are difficult to obtain due to complexities such as ion pairing.

The theme of Chapter 4; the reaction of $[Cu^{II}]$ with Cu^0 had previously been unexamined. This reaction has been characterised and provides new information of the processes involved in adding Cu^0 to ATP reaction mixtures. A computer simulation was applied that described the theoretical behaviour of an oxidative etching event. A good fit was obtained between experiment and theory at large values of d/a and at short times. The potentials of a number of $[Cu^I]/[Cu^{II}]$ and $[Cu^I]/[Cu^0]$

redox couples have been measured in order to understand the substrate potential response during the SECM etching process.

The rate of reaction of a number of different [Co^{I}] with E2IBB has been measured in a range of solvents, as described in Chapter 5. The solvent was seen to have a great effect on the behaviour of each system, stabilising the formation of R[Co^{III}], such that two reduction processes became evident where mma was the solvent. Such [Co] species are commonly used as C – C bond forming reagents and therefore knowledge of their behaviour in certain solvents is invaluable. Additionally the [Co]/ E2IBB system may be used as an initiator/catalyst system for polymerisation reactions, either in homogeneous or emulsion solutions.

The EC' system was examined via SECM for the first time in Chapter 6. Two EC' systems that had previously been investigated by other methods were used as models, although each proved to be non-ideal. The newly developed model was applied to the reaction of [Co^{I}] with RBr, however, this reaction was found not to be an ideal EC' reaction, under the conditions of study. The EC' simulation developed as part of this work could be used to examine other catalytic systems using SECM.

DPSC experiments were carried out on both [$Co(dmgH)_2$] and [$Co(dmgBF_2)_2$] in biphasic liquid/liquid systems. The former appeared to show no partitioning into the DCE phase, whilst the latter appeared to partition between the water and DCE phases. Further studies of this system must be made to measure the partition coefficients of both species and hence apply theoretical models of induced transfer. The reaction of [$Co(dmgBF_2)_2$] and E2IBB was also examined across a water/oil interface in a two-

phase SECM experiment. The behaviour observed tended towards positive feedback, either due to the partitioning of $[Co(dmgBF_2)_2]$ into the oil phase and/or due to the reaction of $[Co^I]$ with E2IBB. Further work could reveal the nature of the reaction, which would be valuable in the future use of $[Co(dmgBF_2)_2]$ in organic syntheses and emulsion polymerisations.

Appendix 1 – Chemical structures.

A1.1 [Cu] Complexes

The term [Cu] is used to identify a copper complex when the actual identity of the ligand is unimportant. However, when the structure of the ligand is important the following number abbreviations were used.

Number	Name	Structure
1	tbutyl	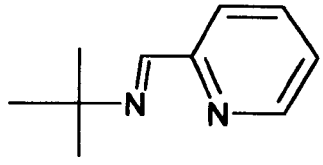
2	sub bpy	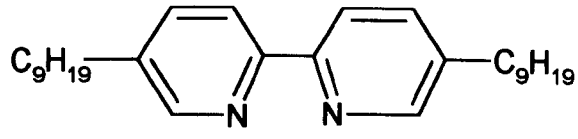
3	pmeda	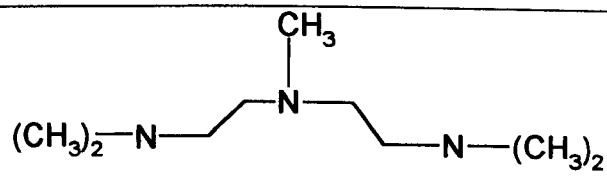
4	Tren	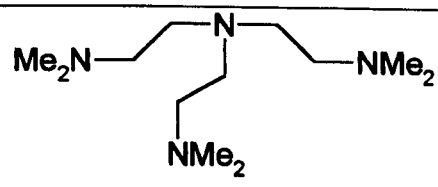
5	Bpy	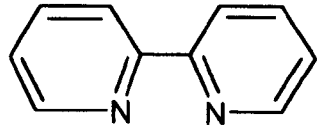
6	D59	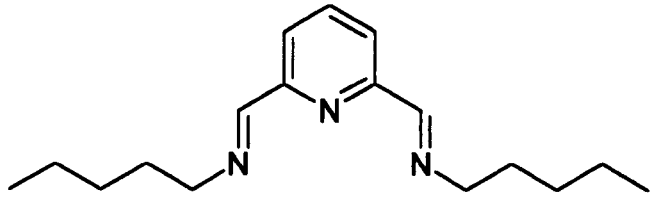

7	Tmeda	
8	Octo	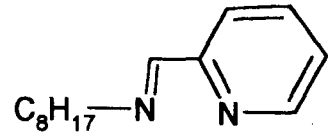
9	Penta	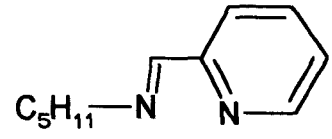
10	Tris	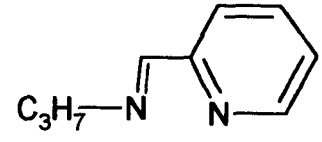

Table A.1.1. Structures of ligands used in conjunction with CuCl to generated [Cu] in situ.

A1.2 [Co] Complexes

Abbreviation	Explanation	Example
[Co]	a cobalt centred macrocycle, the structure being irrelevant.	
[Co(ligand)]	As above but where the structure of the equatorial ligand is relevant.	[Co(salen)]
U[Co]B	A cobalt centred macrocycle with one upper and one basal axial ligand (were the nature of the either axial ligand is relevant).	R[Co]B, (1 axial ligand = R group, 1 general base ligand)
R[Co]	A cobalt centred macrocycle with one alkyl group as axial ligand (assumes that the other axial ligand is irrelevant).	$CH_3CH_2[Co^{III}]$, (1 axial ligand = CH_3CH_2, $[Co^{III}]$ in oxidation state III.

Table A.1.2. Nomenclature used in this thesis‡‡‡.

Abbreviation	Structure
$[Co(dmgH)_2]$	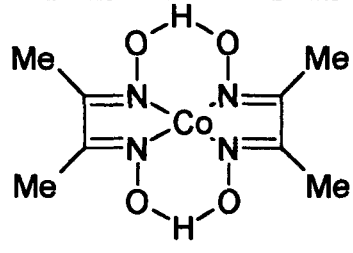

‡‡‡ In all cases it is assumed that each [Co] is surrounded by an appropriate number of axial and equatorial ligands, if non are displayed then their structure is irrelevant to the property under discussion.

$[Co(dmgBF_2)_2]$	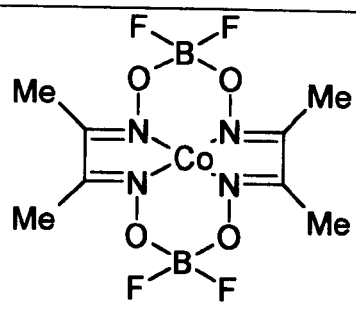
$[Co(megBF_2)_2]$	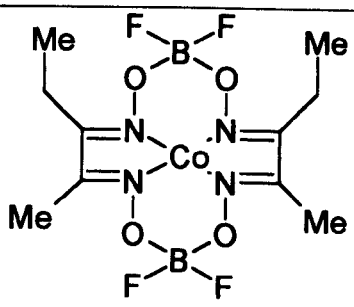
$[Co(degBF_2)_2]$	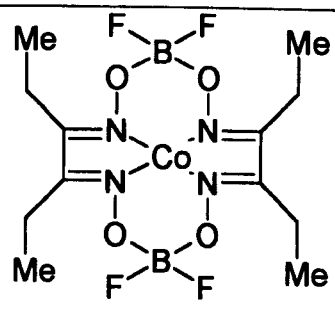
Co(salen)[95]	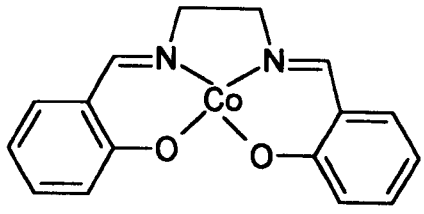
[Co(salophen)][65]	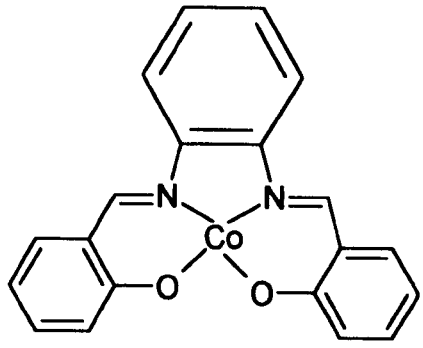

Vitamin B_{12}	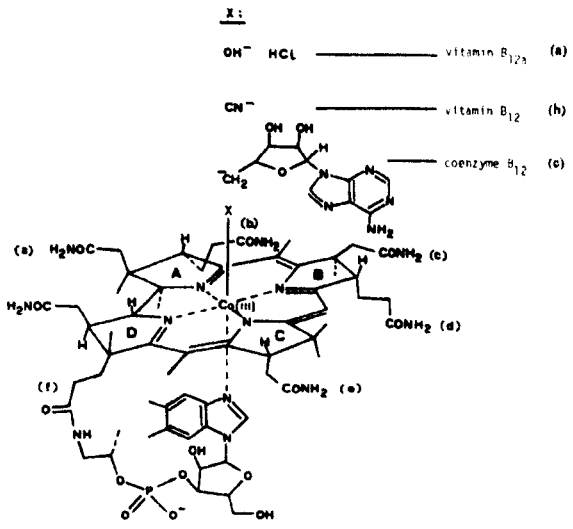
Co(DPD)	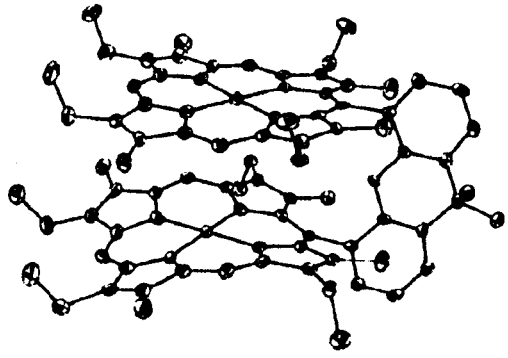
Co(DPX)	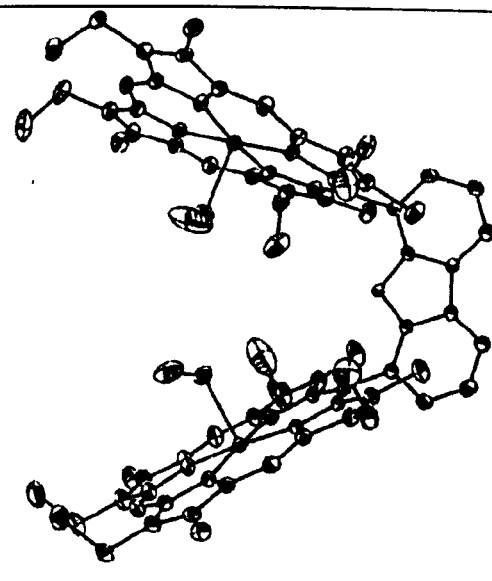

Table A.1.3. [Co] structures.

Appendix 2 – Model for SECM feedback with an irreversible surface comproportionation reaction.

```
C  SECM-bex1.f  TREATS  FEEDBACK  RESPONSE  FOR  Cu  ETCHING
EXPERIMENT
C WITH ALIGNED MICROELECTRODES
C MODIFIED SECM PROGRAM
C CONDUCTOR (POSITIVE FEEDBACK SIMULATION)
C WITHOUT K SPACE COMPRESSION
C INCLUDING TWO SPECIES
C WITH DIFFERENT DIFFUSION COEFFICIENTS
      IMPLICIT DOUBLE PRECISION(A-H,O-Z)
      DOUBLE PRECISION LL,LLOG,LAMP(500),LAMQ(500),LAMZ
     >,DIFFA,DIFFB,CAS,CBS
     >,GAM,LAMZB,LAMPB(500),LAMQB(500)
      INTEGER NP,NZ,NQ,NUM
      CHARACTER*20 FNAM

      DIMENSION
COA(0:500,0:500),FA(500),ALRA(500),BERA(500)
     >,ALZA(500),BEZA(500),ALZGA(500),BEZGA(500),DA(500)
     >,HA(500),CNA(0:500,0:500),RRS(500),CCOMPA(0:500)

      DIMENSION
COB(0:500,0:500),FB(500),ALRB(500),BERB(500)
     >,ALZB(500),BEZB(500),ALZGB(500),BEZGB(500),DB(500)
     >,HB(500),CNB(0:500,0:500),RRT(500),ccompb(0:500)
     >,surfcomb(0:500),surfcoma(0:500)
C.....SORTING OUT FILENAMES
      PRINT*, 'ENTER FILENAME: '
      READ*, FNAM

C.....DIFFERENT DIFFUSION COEFFICIENTS
c      PRINT*,'ENTER DIFFUSION COEFFICIENT FOR SPECIES A:'
c      READ*, DIFFA
c      PRINT*,'ENTER DIFFUSION COEFFICIENT FOR SPECIES B: '
c      READ*, DIFFB
c      GAM=DIFFB/DIFFA
c to start with assume equal D
      GAM=1.

C SET UP KINETICS
      PRINT*,'ENTER NORMALISED RATE CONSTANT'
      READ*,RC

C.....CREATION OF THE INITIAL GRID

C.....VALUE OF THE HALF TIMESTEP
      DELTIN=1.E-6
      DELT=DELTIN
C.....NUMBER OF POINTS OVER ELECTRODE IN J SPACE (NQ)
      NQ=40
C.....NUMBER OF POINTS OVER GLASS IN J SPACE (NP)
      NP=40
C.....NUMBER OF POINTS IN K SPACE (NZ)
      NZ=60
C.....VALUE OF ELECTRODE RG
      RG=10.
C.....VALUE FOR (d/a) IN REAL SPACE (LL)
      PRINT*, 'ENTER normalised TIP/SUBSTRATE DISTANCE: '
      READ*,LL

c      LL=10.**LLOG

c      PRINT*, 'TIP-SUBSTRATE SEPARATION: ', TSD
c      PRINT*, 'LOG(d/a) = ', LLOG
c      PRINT*, 'GAM = ', GAM
C.....SET VALUE FOR CONSTANT (F)
      FF=10.
      QT=LOG(1.+FF)
C.....DELQ IS (RHO) OVER THE ELECTRODE
      DELQ=QT/NQ
C.....SET VALUE FOR (1-R) OVER THE ELECTRODE (REXT)
      REXT=(1.-EXP(-DELQ))/FF
C.....SET VALUE FOR 'G' OVER THE GLASS TO MATCH GRIDS
      GG=0.1
      DIFF=0.1
 138  RES=NP*LOG(1.+(REXT*GG))-LOG(1.+((RG-1.)*GG))
      IF(RES.GT.0.0000001)THEN
      GG=GG-DIFF
      DIFF=DIFF/10.
      GOTO 138
      ENDIF
      IF(RES.LT.-0.0000001)THEN
      GG=GG+DIFF
      GOTO 138
      ENDIF
      PT=LOG(1.+(GG*(RG-1.)))
C.....DELP IS (RHO) OVER THE GLASS
      DELP=PT/NP
C.....SET GRID CONSTANTS OVER K SPACE
      DELZ=LL/NZ
      CURROLD=(DELZ**-1.)*3.142

C.....OPEN DATA FILE
C      OPEN (67, FILE='f1.dat', STATUS='unknown')
      OPEN (67, FILE=FNAM, STATUS='unknown')
C.....SETTING INITIAL BULK CONCENTRATION VALUES
      DO 201 J=0,NQ+NP
      DO 202 K=0,NZ
      COA(J,K)=1.
      COB(J,K)=0.
 202  CONTINUE
 201  CONTINUE
C.....SETTING   INITIAL   SURFACE   CONCENTRATIONS   (OVER
ELECTRODE)
      DO 30 J=0,NQ
      COA(J,0)=0.
      COB(J,0)=1./GAM
      CCOMPA(J)=1.
 30   CONTINUE

C.....CALCULATING LAMQ, LAMP, LAMZ CONSTANTS
C.....LAMZ (K SPACE)
 500  DO 150 K=1,NZ-1
      LAMZ=0.5*DELT/(DELZ*DELZ)
      LAMZB=LAMZ*GAM
 150  CONTINUE
C.....LAMP (GLASS AREA) (J SPACE)
      DO 151 J=1,NP-1
      LAMP(J)=(0.5*GG*GG*DELT*(EXP(-2.*DELP*J)))/(DELP**2.)
      LAMPB(J)=LAMP(J)*GAM
 151  CONTINUE
C.....LAMQ (ELECTRODE AREA) (J SPACE)
      DO 190 J=1,NQ
      LAMQ(J)=0.5*FF*FF*DELT*(EXP(2.*(-QT+(J*DELQ))))/
     >(DELQ*DELQ)
      LAMQB(J)=LAMQ(J)*GAM
 190  CONTINUE

C.....CONSTANTS FOR THE THOMAS ALGORITHM
C.....CONSTANTS WHEN VECTORS ARE RADIAL
C.....BOUNDARY (J=1) VALUES
      ALRA(1)=1.+LAMQ(1)*(1.+(DELQ/2.)+(0.5*DELQ*
     >(EXP(QT-DELQ))/
     >(FF+1.-(EXP(QT-DELQ)))))
      BERA(1)=-LAMQ(1)*(1.+(DELQ/2.)+(0.5*DELQ*
     >(EXP(QT-DELQ))/
     >(FF+1.-(EXP(QT-DELQ)))))/ALRA(1)
      ALRB(1)=1.+LAMQB(1)*(1.+(DELQ/2.)+(0.5*DELQ*
     >(EXP(QT-DELQ))/
     >(FF+1.-(EXP(QT-DELQ)))))
      BERB(1)=-LAMQB(1)*(1.+(DELQ/2.)+(0.5*DELQ*
     >(EXP(QT-DELQ))/
     >(FF+1.-(EXP(QT-DELQ)))))/ALRB(1)


C.....J SPACE OVER THE ELECTRODE
      DO 100 J=2,NQ
      ALRA(J)=1.+(2.*LAMQ(J))+
     >(LAMQ(J)*(1.-(0.5*DELQ)-
     >(0.5*DELQ*(EXP(QT-(DELQ*J)))/(FF+1.-EXP(QT-
     >(J*DELQ))))))*BERA(J-1))
      BERA(J)=-LAMQ(J)*(1.+(0.5*DELQ)+(0.5*DELQ*
     >(EXP(QT-(J*DELQ)))/
     >(FF+1.-(EXP(QT-(J*DELQ))))))/ALRA(J)

      ALRB(J)=1.+(2.*LAMQB(J))+
     >(LAMQB(J)*(1.-(0.5*DELQ)-
     >(0.5*DELQ*(EXP(QT-(DELQ*J)))/(FF+1.-EXP(QT-
     >(J*DELQ))))))*BERB(J-1))
      BERB(J)=-LAMQB(J)*(1.+(0.5*DELQ)+(0.5*DELQ*
     >(EXP(QT-(J*DELQ)))/
     >(FF+1.-(EXP(QT-(J*DELQ))))))/ALRB(J)
 100  CONTINUE

C.....J SPACE OVER THE INSULATOR
      DO 160 J=NQ+1,NQ+NP-2
      ALRA(J)=1.+(2.*LAMP(J-NQ))+(LAMP(J-NQ)*BERA(J-1)*
     >(1.+(DELP/2.)-(DELP*0.5*EXP((J-NQ)*DELP))*
     >(((EXP((J-NQ)
     >*DELP))-1.+GG)**-1.)))
      BERA(J)=LAMP(J-NQ)*(-1.+(DELP/2.)-(0.5*DELP*
     >(EXP((J-NQ)*DELP))
     >*(((EXP((J-NQ)*DELP))-1.+GG)**-1.)))/ALRA(J)

      ALRB(J)=1.+(2.*LAMPB(J-NQ))+(LAMPB(J-NQ)*BERB(J-1)*
     >(1.+(DELP/2.)-(DELP*0.5*EXP((J-NQ)*DELP))*
     >(((EXP((J-NQ)
     >*DELP))-1.+GG)**-1.)))
      BERB(J)=LAMPB(J-NQ)*(-1.+(DELP/2.)-(0.5*DELP*
     >(EXP((J-NQ)*DELP))
     >*(((EXP((J-NQ)*DELP))-1.+GG)**-1.)))/ALRB(J)
 160  CONTINUE
```

```
C.....J SPACE AT ELECTRODE EDGE
      ALRA(NQ+NP-1)=1.+(LAMP(NP-1)*(2.+(BERA(NQ+NP-2)*
     >(1.+(DELP/2.)-
     >(DELP*0.5*(EXP((NP-1)*DELP)))*(((EXP((NP-1)*DELP))-
     >1.+GG)**-1.)))))

      ALRB(NQ+NP-1)=1.+(LAMPB(NP-1)*(2.+(BERB(NQ+NP-2)*
     >(1.+(DELP/2.)-
     >(DELP*0.5*(EXP((NP-1)*DELP)))*(((EXP((NP-1)*DELP))-
     >1.+GG)**-1.)))))

C.....CONSTANTS WHEN VECTORS ARE DOWN (K)
C.....BOUNDARY (K=1) OVER THE ELECTRODE
      ALZA(1)=(2.*LAMZ)+1.
      BEZA(1)=-LAMZ/ALZA(1)

      ALZB(1)=LAMZB+1.
      BEZB(1)=-(LAMZB)/ALZB(1)

C.....K SPACE OVER THE ELECTRODE
      DO 300 K=2,NZ-2
      ALZA(K)=((2.*LAMZ)+1.)+(LAMZ*BEZA(K-1))
      BEZA(K)=-LAMZ/ALZA(K)

 ALZB(K)=((2.*LAMZB)+1.)+(LAMZB*BEZB(K-1))
      BEZB(K)=-LAMZB/ALZB(K)
 300  CONTINUE

C.....K SPACE AT SUBSTRATE BOUNDARY (ELECTRODE)
      ALZA(NZ-1)=1.+LAMZ+(LAMZ*BEZA(NZ-2))
      ALZB(NZ-1)=1.+LAMZB*2.-lamzb/(1.+rc*delz)
     >+(LAMZB*BEZB(NZ-2))

C.....BOUNDARY (K=1) OVER THE GLASS
      ALZGA(1)=LAMZ+1.
      BEZGA(1)=-LAMZ/ALZGA(1)
      ALZGB(1)=LAMZB+1.
      BEZGB(1)=-LAMZB/ALZGB(1)

C.....K SPACE OVER GLASS
      DO 301 K=2,NZ-2
      ALZGA(K)=((2.*LAMZ)+1.)+(LAMZ*BEZGA(K-1))
      BEZGA(K)=-LAMZ/ALZGA(K)
      ALZGB(K)=((2.*LAMZB)+1.)+(LAMZB*BEZGB(K-1))
      BEZGB(K)=-LAMZB/ALZGB(K)
 301  CONTINUE

C.....K SPACE AT SUBSTRATE BOUNDARY (GLASS)
      ALZGA(NZ-1)=1.+LAMZ+(LAMZ*BEZGA(NZ-2))
      ALZGB(NZ-1)=1.+LAMZB+(LAMZB*BEZGB(NZ-2))

C.....FIRST HALF TIMESTEP CALCULATION
C.....(K=OLD) AND (J=NEW)
C.....
      DO 1 K=1,NZ-1
      DO 2 J=1,NQ+NP-1
      DA(J)=(LAMZ*COA(J,K-1))-(((2.*LAMZ)-1.)
     >*COA(J,K))+(LAMZ*COA(J,K+1))
      DB(J)=(LAMZB*COB(J,K-1))-(((2.*LAMZB)-1.)
     >*COB(J,K))+(LAMZB*COB(J,K+1))
 2    CONTINUE
C.....
      DA(NQ+NP-1)=DA(NQ+NP-1)+(LAMP(NP-1)*(1.-(DELP/2.)+
     >(0.5*DELP*(EXP((NP-1)*DELP))*(((EXP((NP-1)*DELP))
     >-1.+GG)**-1.))))
C.....
      FA(1)=DA(1)/ALRA(1)
      FB(1)=DB(1)/ALRB(1)
      DO 3 J=2,NQ
      FA(J)=(DA(J)+(LAMQ(J)*(1.-(DELQ/2.)-(0.5*DELQ*
     >(EXP(QT-(J*DELQ)))
     >/(FF+1.-(EXP(QT-(J*DELQ))))))*FA(J-1)))/ALRA(J)
      FB(J)=(DB(J)+(LAMQB(J)*(1.-(DELQ/2.)-(0.5*DELQ*
     >(EXP(QT-(J*DELQ)))
     >/(FF+1.-(EXP(QT-(J*DELQ))))))*FB(J-1)))/ALRB(J)
 3    CONTINUE
C.....
      DO 41 J=NQ+1,NQ+NP-1
      FA(J)=(DA(J)+((LAMP(J-NQ)*(1.+(0.5*DELP)-
     >((0.5*DELP*(EXP((J-NQ)*DELP)))
     >*(((EXP((J-NQ)*DELP))-1.+GG)**-1.))))*FA(J-1)))
     >/ALRA(J)
      FB(J)=(DB(J)+((LAMPB(J-NQ)*(1.+(0.5*DELP)-
     >((0.5*DELP*(EXP((J-NQ)*DELP)))
     >*(((EXP((J-NQ)*DELP))-1.+GG)**-1.))))*FB(J-1)))
     >/ALRB(J)
 41   CONTINUE
C.....
      CNA(NQ+NP-1,K)=FA(NQ+NP-1)
      CNB(NQ+NP-1,K)=FB(NQ+NP-1)
      DO 4 J=NQ+NP-2,1,-1
      CNA(J,K)=FA(J)-(BERA(J)*CNA(J+1,K))
      CNB(J,K)=FB(J)-(BERB(J)*CNB(J+1,K))
 4    CONTINUE
 1    CONTINUE

C.....UPDATING BOUNDARY CONDITIONS

      DO 555 J=0,NQ
      COA(J,0)=0.
      COB(J,0)=CNB(J,1)+CNA(J,1)/GAM
      COB(J,NZ)=CNB(J,NZ-1)/(1.+RC*DELZ)
      COA(J,NZ)=2.*gam*(cnb(j,nz-1)-cob(j,nz))+CNA(j,NZ-1)
 555  CONTINUE

      DO 101 J=NQ+1,NP+NQ-1
      COA(J,0)=CNA(J,1)
      COB(J,0)=CNB(J,1)
      COA(J,NZ)=CNA(j,NZ-1)
      COB(J,NZ)=CNB(J,NZ-1)
 101  CONTINUE

      DO 777 K=1,NZ-1
      COA(0,K)=CNA(1,K)
      COB(0,K)=CNB(1,K)
 777  CONTINUE

C.....UPDATING REST OF CONCENTRATION VALUES
      DO 103 J=1,NP+NQ-1
      DO 104 K=1,NZ-1
      COA(J,K)=CNA(J,K)
      COB(J,K)=CNB(J,K)
 104  CONTINUE
 103  CONTINUE

C.....CALCULATIONS IN OTHER DIRECTION
C.....(J=NEW OLD) AND (K=NEW NEW)

C.....
      DO 50 J=1,NQ
      CBS=COB(J,NZ-1)
      CAS=COA(J,1)
 899  DO 51 K=1,NZ-1
      HA(K)=(LAMQ(J)*(1.-(0.5*DELQ)-(0.5*DELQ*
     >(EXP(QT-(DELQ*J)))/
     >(FF+1.-(EXP(QT-(DELQ*J))))))*COA(J-1,K))+(COA(J,K)*
     >(1.-(2.*LAMQ(J))))
     >+(LAMQ(J)*(1.+(0.5*DELQ)+(0.5*DELQ*
     >(EXP(QT-(J*DELQ)))/
     >(FF+1.-EXP(QT-(J*DELQ)))))*COA(J+1,K))

      HB(K)=(LAMQB(J)*(1.-(0.5*DELQ)-(0.5*DELQ*
     >(EXP(QT-(DELQ*J)))/
     >(FF+1.-(EXP(QT-(DELQ*J))))))*COB(J-1,K))+(COB(J,K)*
     >(1.-(2.*LAMQB(J))))
     >+(LAMQB(J)*(1.+(0.5*DELQ)+(0.5*DELQ*
     >(EXP(QT-(J*DELQ)))/
     >(FF+1.-EXP(QT-(J*DELQ)))))*COB(J+1,K))
 51   CONTINUE

      HA(NZ-1)=HA(NZ-1)+2.*LAMZ*GAM*(CBS-cbs/(1.+rc*delz))
      HB(1)=HB(1)+(LAMZB*CAS/GAM)

C.....
      FA(1)=HA(1)/ALZA(1)
      FB(1)=HB(1)/ALZB(1)
      DO 53 K=2,NZ-1
      FA(K)=(HA(K)+(LAMZ*FA(K-1)))/ALZA(K)
      FB(K)=(HB(K)+(LAMZB*FB(K-1)))/ALZB(K)
 53   CONTINUE
      CNA(J,NZ-1)=FA(NZ-1)
      CNB(J,NZ-1)=FB(NZ-1)
      DO 54 K=NZ-2,1,-1
      CNA(J,K)=FA(K)-(BEZA(K)*CNA(J,K+1))
      CNB(J,K)=FB(K)-(BEZB(K)*CNB(J,K+1))
 54   CONTINUE

      IF (ABS((CBS-CNB(J,NZ-1))/CNB(J,NZ-1)).GT.0.000000001
     >.OR.
     >ABS((CAS-CNA(J,1))/CNA(J,1)).GT.0.000000001)THEN
      CAS=CNA(J,1)
      CBS=CNB(J,NZ-1)
      GOTO 899
      ENDIF
 50   CONTINUE

C.....
      DO 60 J=NQ+1,NQ+NP-1
      DO 61 K=1,NZ-1
      HB(K)=(LAMPB(J-NQ)*(1.+(DELP*0.5)-(DELP*0.5*
     >(EXP((J-NQ)*DELP))*((EXP((J-NQ)*DELP))-1.
```

```
     >+GG)**-1.))
     >*COB(J-1,K))+(COB(J,K)*(1.-(2.*LAMPB(J-NQ))))
     >+(LAMPB(J-NQ)*(1.-(0.5*DELP)+
     >(0.5*DELP*EXP((J-NQ)*DELP)*((EXP((J-NQ)
     >*DELP))-1.+GG)**-1.))*COB(J+1,K))
 61   CONTINUE

      FB(1)=HB(1)/ALZGB(1)
      DO 63 K=2,NZ-1
      FB(K)=(HB(K)+(LAMZB*FB(K-1)))/ALZGB(K)
 63   CONTINUE
      CNB(J,NZ-1)=FB(NZ-1)
      DO 64 K=NZ-2,1,-1
      CNB(J,K)=FB(K)-(BEZGB(K)*CNB(J,K+1))
 64   CONTINUE
 60   CONTINUE

      DO 70 J=NQ+1,NQ+NP-1
      DO 71 K=1,NZ-1
      HA(K)=(LAMP(J-NQ)*(1.+(DELP*0.5)-(DELP*0.5*
     >(EXP((J-NQ)*DELP))*((EXP((J-NQ)*DELP))-1.
     >+GG)**-1.))
     >*COA(J-1,K))+(COA(J,K)*(1.-(2.*LAMP(J-NQ))))
     >+(LAMP(J-NQ)*(1.-(0.5*DELP)+
     >(0.5*DELP*EXP((J-NQ)*DELP)*((EXP((J-NQ)
     >*DELP))-1.+GG)**-1.))*COA(J+1,K))
 71   CONTINUE

      FA(1)=HA(1)/ALZGA(1)
      DO 73 K=2,NZ-1
      FA(K)=(HA(K)+(LAMZ*FA(K-1)))/ALZGA(K)
 73   CONTINUE
      CNA(J,NZ-1)=FA(NZ-1)
      DO 74 K=NZ-2,1,-1
      CNA(J,K)=FA(K)-(BEZGA(K)*CNA(J,K+1))
 74   CONTINUE
 70   CONTINUE

C.....
      DO 360 J=1,NQ
c      IF(CURRT.GT.2.)THEN
c      COMA=0.95*CCOMPA(J)
c      ELSE IF(CURRT.GT.1.)THEN
c      COMA=0.98*CCOMPA(J)
c      ELSE IF(CURRT.GT.0.5)THEN
c      COMA=0.995*CCOMPA(J)
c      ELSE
c      COMA=0.999*CCOMPA(J)
c      ENDIF
c      IF(CNA(J,1).GT.COMA)THEN
c      KLMA=KLMA+1
c      ENDIF
      If(ABS((CNA(j,1)-CCOMPA(J))/CNA(J,1)).lt.0.01)THEN
      KLMA=KLMA+1
      endif
      if(ABS((CNb(j,1)-CCOMPB(J))/CNB(j,1)).lt.0.01)then
      klmb=klmb+1
      endif
      If(ABS((CNA(j,1)-CCOMPA(J))/CNA(J,1)).gt.0.05)THEN
      nwarn=1
      endif
      if(ABS((CNb(j,1)-CCOMPB(J))/CNB(j,1)).lt.0.05)then
      nwarn=1
      endif
 360  CONTINUE

C.....

      DO 890 J=0,NQ
      COA(J,0)=0.
      COB(J,0)=CNB(J,1)+(CNA(J,1)/GAM)
      COB(J,NZ)=CNB(J,NZ-1)/(1.+RC*DELZ)
      COA(J,NZ)=2.*gam*(cnb(j,nz-1)-cob(j,nz))+CNA(j,NZ-1)
 890  CONTINUE

      DO 402 J=NQ+1,NQ+NP-1
      COA(J,0)=CNA(J,1)
      COB(J,0)=CNB(J,1)
      cob(j,nz)=cnb(j,nz-1)
      coa(j,nz)=cna(j,nz-1)
 402  CONTINUE

      DO 888 K=1,NZ-1
      COA(0,K)=CNA(1,K)
      COB(0,K)=CNB(1,K)
 888  CONTINUE

      DO 403 J=1,NQ+NP-1
      DO 404 K=1,NZ-1
      COA(J,K)=CNA(J,K)
      COB(J,K)=CNB(J,K)
 404  CONTINUE
 403  CONTINUE

C.....
      DO 900 J=1,NQ
      CCOMPA(J)=CNA(J,1)
      CCOMPB(J)=cnb(j,1)
c      surfcoma(j)=cna(j,nz-1)
c      surfcomb(j)=cnb(j,nz-1)
c      IF(COA(J,1).LT.0.0.AND.IIIA.EQ.0)THEN
c      IIIA=1
c      ENDIF
 900  CONTINUE

C.....CALCULATING TIP(RRT) AND SUBSTRATE(RRS) CURRENTS

      DO 880 J=1,NQ-1
      RRT(J)=1.-((EXP(QT-(J*DELQ)))-1.)/FF
 880  CONTINUE

      RRT(NQ)=1.

      FLUXT=CNA(1,1)*(RRT(1)**2.)/DELZ

      DO 689 J=2,NQ
      FLUXT=FLUXT+((RRT(J)**2.)-(RRT(J-1)**2.))*
     >(CNA(J,1))/DELZ
 689  CONTINUE

C.....NORMALISED CURRENT - CALCULATION
      CURRT=FLUXT*(3.1419/4.)

      T=T+DELT
      PRINT 11, T,CURRT

c      print*,'concentrations'
c      do 999 j=0,nq,10
c      do 998 k=0,nz,10
c      print*,coa(j,k),cob(j,k),j,k
c 998  continue
c 999  continue

      IF(KLMA.EQ.Nq.and.klmb.eq.nq)THEN
      DELT=DELT*1.2
      ELSE IF(nwarn.EQ.1) THEN
      DELT=DELT*0.5
      ENDIF
c      IF(IIIA.EQ.1.)THEN
c      DELT=DELT/2.
c      ENDIF
      CURROLD=CURRT
c      IIIA=0
      KLMA=0
      KLMB=0
      nwarn=0
      FLUXT=0.
c      FLUXS=0.

      if(delt.gt.0.1)then
      delt=0.1
      endif

C.....SAVING THE DATA
      WRITE (67,11) T, CURRT

C.....CONTINUING THE CYCLE
      IF (T.LT.200) GOTO 500
      CLOSE (67)

C.....INCREASING GRID POINTS OVER K SPACE
c      NZ=NZ+5

C.....LOOPING BACK TO CALCULATE CURRENT AT NEXT (d/a)
c      DELT=DELTIN
c      T=0.
C      LNAM=LNAM+1
C      GAM=GAM+0.1
C      IF (GAM.LT.0.81) GOTO 501
C      TSD=TSD+0.05
c      LLOG=LLOG+0.1
c      LNAM=LNAM+1
c      IF (LLOG.LT.-0.41) GOTO 501

C.....FORMAT STATEMENTS
 11   FORMAT(2X,E12.6,2X,E12.6)
      STOP
      END
```

Appendix 3 – The model for the EC' reaction in an SECM geometry.

```
c     secm-ec-cat3.f
c program to calculate generator collector response
c for a catalytic ec' mechanism in the secm configuration
c 23 May 2000 PRU (based on ece-gc-w.f etc.)
c corrected ALB
c  modified 1 DEC 2000 to calcuate approach curve: input
rate constant

C UNIFORM GRID IN Z DIRECTION

C REACTION IS

C         UME:          A + e ---> B

C         SOLN:         B -->  A

c         SUBSTRATE:    B - e ---> A

c generation collection

      IMPLICIT DOUBLE PRECISION(A-H,O-Z)
      DOUBLE PRECISION LL,LAMP(600),LAMZ,LAMQ(600),LLOG
      integer nr,nz,NQ

      DIMENSION
COA(0:800,0:600),F(800),ALRA(800),BERA(800),

>ALZA(800),BEZA(800),ALZGA(800),BEZGA(800),DA(800),HA(800),
     >CNA(0:800,0:800),CCOMP(800),rrs(800),rrt(800)

      character*40 datfil

c HOMOGENEOUS RATE CONSTANT
c.....electrode radius
      A=5.e-4
c.....diffusion coefficient
      DIFA=1.e-5

      PRINT*,'ENTER APPARENT 1st ORDER RATE CONSTANT/ s^-1'
      READ*, rk
c....conversion to normalise rate constant
      rk=(rk*A*A)/DIFA

      tout=0.01
C     *************************   MIX NQ AND NR *********

      NQ=200
      NR=NQ

C NO POINTS OVER GLASS IN P SPACE
      NP=400

      RG=10.

c z space
c      print*, 'enter nz'
c      read*, nz
      nz=160

c      print*,'log ll='
c      READ*,LLOG
      LLOG=-1

      print*, 'enter datafile'
      read*, datfil
      open(66,FILE=datfil,STATUS='unknown')

 6600 ll=10.**LLOG

      print*, 'rate',ll,rk
      write(66,*) LLOG,rk,(rk*difa/(a*a))

C   SET CONST FOR RADIAL GRID IN ELECTRIDE ZONE
      FF=5.
      Qt=LOG(1.+FF)
      DELQ=QT/NQ
      PRINT*,DELQ
      REXT=(1.-EXP(-DELQ))/FF
      PRINT*, 'REXT=',REXT

C DEFINING THE CONST OF EXPONENTIATION FOR MATCHING OF
GRIDS IN THE R DIR
      AA=0.1
      DIFF=0.1
 138  RES=NP*LOG(1.+(REXT*AA))-LOG(1.+((RG-1.)*AA))
      IF(RES.GT.0.00001)THEN
      AA=AA-DIFF
      DIFF=DIFF/10.
      GOTO 138
      ENDIF
      IF(RES.LT.-0.00001)THEN
      AA=AA+DIFF
      GOTO 138
      ENDIF

      PT=LOG(1.+(AA*(RG-1.)))
      DELP=PT/NP

      DELZ=LL/NZ

c      print*, delz

      delt=5.e-7
      deltin=delt

      CURROLD=(DELZ**-1.)*3.142
      rld=(1./ll)*(rk**-0.5)
      CRIT=0.01
      DELTCO=CRIT/RK

      DO 201 J=0,NQ+NP
      DO 202 K=0,NZ
      COA(J,K)=1.
      CNA(J,K)=1.
 202  CONTINUE
 201  CONTINUE

      DO 30 J=0,NQ
      COA(J,0)=0.
      CCOMP(J)=1.
 30   CONTINUE

 500  LAMZ=0.5*DELT/(DELZ*DELZ)

      DO 151 J=1,NP-1
      LAMP(J)=(0.5*AA*AA*DELT*(EXP(-2.*DELP*J)))/(DELP**2.)
 151  CONTINUE

      DO 190 J=1,NQ
      LAMQ(J)=0.5*FF*FF*DELT*(exp(2.*(-qt+(j*delq))))/
     >(DELQ*DELQ)
 190  CONTINUE

C *****   IN THE FOLLOWING THE SUFFIX FOLLOWING THE NORMAL
NOTATION DENOTES
C                          THE                          SPECIES
*************************************************************
*

C CONSTANTS WHEN VECTORS ARE RADIAL
      ALRA(1)=1.+LAMQ(1)*(1.+(DELQ/2.)+(0.5*DELQ*(EXP(QT-
DELQ))/
     >(FF+1.-(EXP(QT-DELQ)))))+rk*delt/2.


      BERA(1)=-LAMQ(1)*(1.+(DELQ/2.)+(0.5*DELQ*(EXP(QT-
DELQ))/
     >(FF+1.-(EXP(QT-DELQ)))))/alrA(1)

      DO 100 J=2,NQ

      ALRA(J)=1.+(2.*LAMQ(J))+
     >(LAMQ(J)*(1.-(0.5*DELQ)-
     >(0.5*DELQ*(EXP(QT-(DELQ*J)))/(FF+1.-EXP(QT-
(J*DELQ)))))*BERA(J-1))
     >+rk*delt/2.

      BERA(J)=-LAMQ(J)*(1.+(0.5*DELQ)+(0.5*DELQ*(EXP(QT-
(J*DELQ))))/
     >(FF+1.-(EXP(QT-(J*DELQ))))))/ALRA(J)

 100  CONTINUE

      DO 160 J=NQ+1,NQ+NP-2

      ALRA(J)=1.+(2.*LAMP(J-NR))+(LAMP(J-NR)*BERA(J-1)*
     >(1.+(delp/2.)-(delp*0.5*exp((J-NR)*DELP))*(((EXP((J-
NR)
     >*DELP))-1.+AA)**-1.)))+rk*delt/2.

      BERA(J)=LAMP(J-NR)*(-1.+(DELP/2.)-(0.5*DELP*(EXP((J-
NR)*DELP))
     >*(((EXP((J-NR)*DELP))-1.+AA)**-1.)))/ALRA(J)

 160  CONTINUE

      ALRA(NR+NP-1)=1.+(LAMP(NP-1)*(2.+(BERA(NR+NP-
2)*(1.+(DELP/2.)-
     >(DELP*0.5*(EXP((NP-1)*DELP)))*(((EXP((NP-1)*DELP))-
     >1.+AA)**-1.)))))+rk*delt/2.

C CONSTANTS WHEN VECTORS ARE DOWN

      ALZA(1)=2.*LAMZ+1.
      BEZA(1)=-LAMZ/ALZA(1)

      DO 300 K=2,nz-2
      ALZA(K)=2.*LAMZ+1.+LAMZ*BEZA(K-1)
      BEZA(K)=-LAMZ/ALZA(K)
 300  CONTINUE
```

```
      ALZA(NZ-1)=1.+2.*LAMZ+LAMZ*BEZA(NZ-2)

      ALZGA(1)=LAMZ+1.
      BEZGA(1)=-LAMZ/ALZGA(1)

      DO 301 K=2,NZ-2
      ALZGA(K)=2.*LAMZ+1.+LAMZ*BEZGA(K-1)
      BEZGA(K)=-LAMZ/ALZGA(K)
 301  CONTINUE

      ALZGA(NZ-1)=1.+2.*LAMZ+LAMZ*BEZGA(NZ-2)

 200  DO 1 K=1,NZ-1
      DO 2 J=1,NR+NP-1

      DA(J)=(LAMZ*COA(J,K-1))-(((2.*LAMZ)-1.)
     >*COA(J,K))+(LAMZ*COA(J,K+1))+rk*delt/2.

 2    CONTINUE

      DA(NR+NP-1)=DA(NR+NP-1)+(LAMP(NP-1)*(1.-(DELP/2.)+
     >(0.5*DELP*(EXP((NP-1)*DELP))*(((EXP((NP-1)*DELP))-
1.+AA)**-1.))))

      F(1)=DA(1)/ALRA(1)

      DO 3 J=2,NR
      F(J)=(DA(J)+(LAMQ(J)*(1.-(DELQ/2.)-(0.5*DELQ*(EXP(QT-
(J*DELQ)))
     >/(FF+1.-(EXP(QT-(J*DELQ))))))*F(J-1)))/ALRA(J)
 3    CONTINUE

      DO 41 J=NR+1,NR+NP-1
      F(J)=(DA(J)+((LAMP(J-NR)*(1.+(0.5*DELP)-
     >((0.5*DELP*(EXP((J-NR)*DELP)))
     >*(((EXP((J-NR)*DELP))-1.+AA)**-1.))))*F(J-
1)))/ALRA(J)

 41   CONTINUE

      CNA(NR+NP-1,K)=F(NR+NP-1)

      DO 34 J=NR+NP-2,1,-1
      CNA(J,K)=F(J)-BERA(J)*CNA(J+1,K)
 34    CONTINUE
 1    CONTINUE

C UPDATE BCS

      DO 555 J=0,NR
      COA(J,0)=0.
 555  CONTINUE

      DO 101 J=NR+1,NP+NR-1
      COA(J,0)=CNA(J,1)
 101  CONTINUE


      DO 102 J=0,NP+NR-1
      COA(J,NZ)=1.
 102  CONTINUE

      do 777 K=1,NZ-1
      COA(0,K)=CNA(1,K)
 777  CONTINUE

C UPDATE REST C'S

      DO 103 J=1,NP+NR-1
      DO 104 K=1,NZ-1
      COA(J,K)=CNA(J,K)
 104  CONTINUE
 103  CONTINUE

C OTHER DIRECTION

      DO 50 J=1,NR

      DO 51 K=1,NZ-1
      HA(K)=(LAMQ(J)*(1.-(0.5*DELQ)-(0.5*DELQ*(EXP(QT-
(DELQ*J))))/
     >(FF+1.-(EXP(QT-(DELQ*J))))))*COA(J-1,K))+(COA(J,K)*
     >(1.-(2.*LAMQ(J)))-rk*delt/2.)
     >+(LAMQ(J)*(1.+(0.5*DELQ)+(0.5*DELQ*(EXP(QT-
(J*DELQ)))/
     >(FF+1.-EXP(QT-(J*DELQ)))))*COA(J+1,K))+rk*delt/2.
 51   CONTINUE

      HA(NZ-1)=HA(NZ-1)+LAMZ

      F(1)=HA(1)/ALZA(1)
      DO 53 K=2,NZ-1
      F(K)=(HA(K)+(LAMZ*F(K-1)))/ALZA(K)
 53   CONTINUE
      CNA(J,NZ-1)=F(NZ-1)
      DO 54 K=NZ-2,1,-1
      CNA(J,K)=F(K)-(BEZA(K)*CNA(J,K+1))
 54   CONTINUE

 50   CONTINUE

      DO 60 J=NR+1,NR+NP-1

      DO 61 K=1,NZ-1
      HA(K)=(LAMP(J-NR)*(1.+(DELP*0.5)-(DELP*0.5*
     >(EXP((J-NR)*DELP))*((EXP((J-NR)*DELP))-1.+AA)**-1.))
     >*COA(J-1,K))+(COA(J,K)*(-rk*delt/2.+1.-(2.*LAMP(J-
NR))))
     >+(LAMP(J-NR)*(1.-(0.5*DELP)+
     >(0.5*DELP*EXP((J-NR)*DELP))*((EXP((J-NR)
     >*DELP))-1.+AA)**-1.))*COA(J+1,K))+rk*delt/2.
 61   CONTINUE

      HA(NZ-1)=HA(NZ-1)+LAMZ

      F(1)=HA(1)/ALZGA(1)
      DO 63 K=2,NZ-1
      F(K)=(HA(K)+(LAMZ*F(K-1)))/ALZGA(K)
 63   CONTINUE
      CNA(J,NZ-1)=F(NZ-1)
      DO 64 K=NZ-2,1,-1
      CNA(J,K)=F(K)-(BEZgA(K)*CNA(J,K+1))
 64   CONTINUE

 60   CONTINUE

c      print*,'end of 2nd t step'

      DO 360 J=1,NR
      IF(CURRT.GT.2.)THEN
      COMA=0.95*CCOMP(J)
      ELSE IF(CURRT.GT.1.)THEN
      COMA=0.98*CCOMP(J)
      ELSE IF(CURRT.GT.0.7)THEN
      COMA=0.995*CCOMP(J)
      ELSE
      COMA=0.999*CCOMP(J)
      ENDIF
      IF(CNA(J,1).GT.COMA)THEN
      KLM=KLM+1
      ENDIF
 360  CONTINUE


C   BCS
      DO 890 J=0,NR
      COA(J,0)=0.
 890  CONTINUE

      DO 401 J=0,NR+NP-1
      COA(J,NZ)=1.
 401  CONTINUE

      DO 402 J=NR+1,NR+NP-1
      COA(J,0)=CNA(J,1)
 402  CONTINUE

      DO 888 K=1,NZ-1
      COA(0,K)=CNA(1,K)
 888  CONTINUE

      DO 403 J=1,NR+NP-1
      DO 404 K=1,NZ-1
      COA(J,K)=CNA(J,K)
 404  CONTINUE
 403  CONTINUE

      DO 900 J=1,NR
      CCOMP(J)=CNA(J,1)
      if(coA(J,1).LT.0.0.AND.III.EQ.0)THEN
      III=1
      ENDIF
 900  CONTINUE

C CONVERSION OF DELR TO DELQ

      DO 880 J=1,NR-1

      RRT(J)=1.-(((EXP(QT-((J+0.5)*DELQ)))-1.)/FF)
      rrs(j)=1.-(((exp(qt-((J+0.5)*delq)))-1.)/ff)
 880  CONTINUE
```

```
c       print*, rrt(5),rrs(5),qt,delq,ff
        RRT(NR)=1.
        rrs(nr)=1.
        DO 944 J=NR+1,NR+NP-1
        RRs(J)=1.+(((EXP(((J+0.5-NR)*DELp)))-1.)/AA)
c       print*,rrs(j),j
 944    CONTINUE
        RRs(NR+NP)=RG


        FLUXT=CNA(1,1)*(RRt(1)**2.)/DELZ
        FLUXS=(1.-cna(1,nz-1))*(RRs(1)**2.)/DELZ
c          write(66,*) fluxs,rrs(1),cna(1,nz-1),(1.-cna(1,nz-
1)),delz
        DO 689 J=2,NR
        FLUXT=FLUXT+((RRt(J)**2.)-(RRt(J-
1)**2.))*CNA(J,1)/DELZ
        FLUXS=FLUXS+((RRT(J)**2.)-(RRS(J-1)**2.))*
       >(1.-cna(j,nz-1))/DELZ

c       print*, fluxs,rrs(j),rrs(j-1),CNA(j,nz-1),delz
c          write(66,*) fluxs,rrs(j),rrs(j-1),CNA(J,NZ-1),(1.-
CNA(J,NZ-1))
 689    CONTINUE

        DO 693 J=NR+1,NR+NP
        FLUXS=FLUXS+((RRs(J)**2.)-(RRs(J-1)**2.))*(1.-
cna(j,nz-1))
       >/DELZ
c       print*, fluxs,rrs(j),rrs(j-1),cna(j,nz-1),delz
c          write(66,*) fluxs,rrs(j),rrs(j-1),cna(j,nz-1),(1.-
CNA(J,NZ-1))
 693    CONTINUE

        IF(ILK.EQ.1)THEN
        LIK=lik+1
        ENDIF

C NORMALISED CURRENT
        CURRT=FLUXT*(3.1415927/4.)
        CURRS=FLUXS*(3.1415927/4.)
        CE=CURRS/CURRT
        t=t+delt
        if(t.lt.0.01.and.currt.lt.100.)then
        WRITE(66,10)T,CURRT,T,CURRS
        else if((t.gt.tout).AND.(t.Lt.0.1)) then
        write(66,10)T,currt,T,currs
        tout=tout+0.001
        else if ((t.gt.tout).AND.(t.lt.1)) then
        write(66,10) t,currt,t,currs
        tout=tout+0.01
        else if ((t.gt.tout).AND.(t.lt.10)) then
        write(66,10) t,currt,t,currs
        tout=tout+0.1
        else if ((t.gt.tout).AND.(t.lt.100)) then
        write(66,10) t,currt,t,currs
        tout=tout+1.0
        endif
        PRINT*, t,CURRT,CURRS,rk,delt

        IF(KLM.EQ.NR.AND.III.EQ.0)THEN
        DELTFL=DELT*1.002
        IN=1
        ENDIF

        IF(IN.EQ.0)THEN
        DELTFL=DELT
        ENDIF

        IF(III.EQ.1)THEN
        DELTFL=DELT/500.
        ENDIF

        IF(CURRT.LT.0.8.AND.T.GT.0.1)THEN

        CURROLD=CURRT
        III=0
        KLM=0
        IN=0
        FLUX=0.
        FLUXS=0.
        FLUXT=0.
        KK=KK+1
        GOTO 375
        ENDIF

        IF(RK*DELT.GT.CRIT)THEN
        DELTCO=CRIT/RK
        ILK=1
        ENDIF
        IF(LIK.GT.1.AND.III.EQ.0)THEN
        DELTCO=CRIT/RK
        endif

        CURROLD=CURRt
        III=0
        KLM=0
        IN=0
        FLUX=0.
        FLUXS=0.
        FLUXT=0.
        KK=KK+1
        IF(DELTFL.LT.DELTCO.OR.DELTFL.EQ.DELTCO)THEN
        DELT=DELTFL
        ELSE
        DELT=DELTCO
        ENDIF

 375    IF(CURRT.LT.0.8.AND.T.GT.0.1)THEN
        DELT=DELTFL
        ENDIF

        IF(T.LT.10) GOTO 500

c.....increasing grid points over k space
        nz=nz+5

c.....looping back to calculate current at next (d/a)
 8771   DELT=DELTIN
        tout=0.01
        t=0.
        LLOG=LLOG+0.05
        if (LLOG.LT.0.01) goto 6600

        close(66)

 606     FORMAT(1X,2E12.6)
 10      FORMAT(1X,E12.6,1x,e12.6,1x,e12.6,1x,e12.6)
 11      FORMAT(1X,I4)
 5501    format(1x,e12.6)
 5500    format(1x)
 444    STOP
        END
```

Appendix 4 – The model for PSC close to an inert interface.

```
C MODIFIED SECM PROGRAM
C INSULATOR (NEGATIVE FEEDBACK SIMULATION)
C NOW VARIES (d/a) ASWELL
      IMPLICIT DOUBLE PRECISION(A-H,O-Z)
      DOUBLE                                          PRECISION
LL,LLOG,LAMP(400),LAMZ(800),LAMQ(400)
      INTEGER NP,NZ,NQ
      CHARACTER*20 FNAM(20)
      DIMENSION
CO(0:400,0:800),F(800),ALR(400),BER(400),ALZ(800)

>,BEZ(800),ALZG(800),BEZG(800),D(800),H(800),CN(0:400,0:800
)
     >,RR(200),CCOMP(0:800)

C.....SORTING OUT FILENAMES
      LNAM=1
      PRINT*,'ENTER NUMBER OF CYCLES FOR (d/a):'
      READ*, NUM
      DO 502 M = 1,NUM
      PRINT*, 'ENTER FILENAME:'
      READ*, FNAM(M)
 502  CONTINUE

C.....CREATION OF THE INITIAL GRID
C.....VALUE OF THE HALF TIMESTEP
      DELTIN=5.E-7
      DELT=DELTIN
C.....NUMBER OF POINTS OVER ELECTRODE IN J SPACE (NQ)
      NQ=100
C.....NUMBER OF POINTS OVER GLASS IN J SPACE (NP)
      NP=100
C.....NUMBER OF POINTS IN K SPACE (NZ)
      NZ=100
C.....VALUE OF ELECTRODE RG
      RG=10.
C.....VALUE FOR (d/a) IN REAL SPACE (LL)
      PRINT*, 'ENTER INITIAL LOG(d/a) VALUE: '
      READ*, LLOG
 501  LL=10.**LLOG
      PRINT*, LLOG
C.....SET VALUE FOR CONSTANT (F)
      FF=5.
      QT=LOG(1.+FF)
C.....DELQ IS (RHO) OVER THE ELECTRODE
      DELQ=QT/NQ
C.....SET VALUE FOR [1-R] OVER THE ELECTRODE (REXT)
      REXT=(1.-EXP(-DELQ))/FF
C.....SET VALUE FOR 'G' OVER THE GLASS TO MATCH GRIDS
      GG=0.1
      DIFF=0.1
 138  RES=NP*LOG(1.+(REXT*GG))-LOG(1.+((RG-1.)*GG))
      IF(RES.GT.0.00001)THEN
      GG=GG-DIFF
      DIFF=DIFF/10.
      GOTO 138
      ENDIF
      IF(RES.LT.-0.00001)THEN
      GG=GG+DIFF
      GOTO 138
      ENDIF
      PT=LOG(1.+(GG*(RG-1.)))
C.....DELP IS (RHO) OVER THE GLASS
      DELP=PT/NP
C.....SET GRID CONSTANTS OVER K SPACE
      BB=2.
      ZT=LOG(1.+(BB*LL))
      DELZ=ZT/NZ
      CURROLD=(DELZ**-1.)*3.142
C.....OPEN DATA FILE
      OPEN (67, FILE=FNAM(LNAM), STATUS='unknown')
c      OPEN (67, FILE='c2.dat', STATUS='unknown')
C.....SETTING INITIAL BULK CONNCENTRATION VALUES
      DO 201 J=0,NQ+NP
      DO 202 K=0,NZ
      CO(J,K)=1.
 202  CONTINUE
 201  CONTINUE
C.....SETTING   INITIAL   SURFACE   CONCENTRATIONS   (OVER
ELECTRODE)
      DO 30 J=0,NQ
      CO(J,0)=0.
      CCOMP(J)=1.
 30   CONTINUE
C.....CALCULATING LAMQ, LAMP, LAMZ CONSTANTS
C.....LAMZ (K SPACE)
 500  DO 150 K=1,NZ-1
      LAMZ(K)=0.5*BB*BB*(EXP(-2.*DELZ*K))*DELT
     >/(DELZ*DELZ)
 150  CONTINUE
C.....LAMP (GLASS AREA) (J SPACE)
      DO 151 J=1,NP-1
      LAMP(J)=(0.5*GG*GG*DELT*(EXP(-2.*DELP*J)))/(DELP**2.)
 151  CONTINUE
C.....LAMQ (ELECTRODE AREA) (J SPACE)
      DO 190 J=1,NQ
      LAMQ(J)=0.5*FF*FF*DELT*(EXP(2.*(-QT+(J*DELQ))))/
     >(DELQ*DELQ)
 190  CONTINUE

C.....CONSTANTS FOR THE THOMAS ALGORITHM
C.....CONSTANTS WHEN VECTORS ARE RADIAL
C.....BOUNDARY (J=1) VALUES
      ALR(1)=1.+LAMQ(1)*(1.+(DELQ/2.)+(0.5*DELQ*(EXP(QT-
DELQ))/
     >(FF+1.-(EXP(QT-DELQ)))))
      BER(1)=-LAMQ(1)*(1.+(DELQ/2.)+(0.5*DELQ*(EXP(QT-
DELQ))/
     >(FF+1.-(EXP(QT-DELQ)))))/ALR(1)

C.....J SPACE OVER THE ELECTRODE
      DO 100 J=2,NQ
      ALR(J)=1.+(2.*LAMQ(J))+
     >(LAMQ(J)*(1.-(0.5*DELQ)-
     >(0.5*DELQ*(EXP(QT-(DELQ*J)))/(FF+1.-EXP(QT-
(J*DELQ)))))*BER(J-1))
      BER(J)=-LAMQ(J)*(1.+(0.5*DELQ)+(0.5*DELQ*(EXP(QT-
(J*DELQ)))/
     >(FF+1.-(EXP(QT-(J*DELQ))))))/ALR(J)
 100  CONTINUE

C.....J SPACE OVER THE INSULATOR
      DO 160 J=NQ+1,NQ+NP-2
      ALR(J)=1.+(2.*LAMP(J-NQ))+(LAMP(J-NQ)*BER(J-1)*
     >(1.+(DELP/2.)-(DELP*0.5*EXP((J-NQ)*DELP))*(((EXP((J-
NQ)
     >*DELP))-1.+GG)**-1.)))
      BER(J)=LAMP(J-NQ)*(-1.+(DELP/2.)-(0.5*DELP*(EXP((J-
NQ)*DELP))
     >*(((EXP((J-NQ)*DELP))-1.+GG)**-1.)))/ALR(J)
 160  CONTINUE

C.....J SPACE AT ELECTRODE EDGE
      ALR(NQ+NP-1)=1.+(LAMP(NP-1)*(2.+(BER(NQ+NP-
2)*(1.+(DELP/2.)-
     >(DELP*0.5*(EXP((NP-1)*DELP)))*(((EXP((NP-1)*DELP))-
     >1.+GG)**-1.)))))

C.....CONSTANTS WHEN VECTORS ARE DOWN (K)
C.....BOUNDARY (K=1) OVER THE ELECTRODE
      ALZ(1)=(2.*LAMZ(1))+1.
      BEZ(1)=-(LAMZ(1)*(1.-(0.5*DELZ)))/ALZ(1)

C.....K SPACE OVER THE ELECTRODE
      DO 300 K=2,NZ-2

ALZ(K)=((2.*LAMZ(K))+1.)+(LAMZ(K)*(1.+(0.5*DELZ))*BEZ(K-1))
      BEZ(K)=-(LAMZ(K)*(1.-(0.5*DELZ)))/ALZ(K)
 300  CONTINUE

C.....K SPACE AT SUBSTRATE BOUNDARY (ELECTRODE)
      ALZ(NZ-1)=1.+(LAMZ(NZ-1)*(1.+(0.5*DELZ)))+(LAMZ
     >(NZ-1)*(1.+(0.5*DELZ))*BEZ(NZ-2))

C.....BOUNDARY (K=1) OVER THE GLASS
      ALZG(1)=LAMZ(1)+1.-(DELZ*0.5*LAMZ(1))
      BEZG(1)=-(LAMZ(1)*(1.-(0.5*DELZ)))/ALZG(1)

C.....K SPACE OVER GLASS
      DO 301 K=2,NZ-2

ALZG(K)=((2.*LAMZ(K))+1.)+(LAMZ(K)*(1.+(0.5*DELZ))*BEZG(K-
1))
      BEZG(K)=-(LAMZ(K)*(1.-(0.5*DELZ)))/ALZG(K)
 301  CONTINUE

C.....K SPACE AT SUBSTRATE BOUNDARY (GLASS)
      ALZG(NZ-1)=1.+(LAMZ(NZ-1)*(1.+(0.5*DELZ)))+(LAMZ
     >(NZ-1)*(1.+(0.5*DELZ))*BEZG(NZ-2))

C.....FIRST HALF TIMESTEP CALCULATION
C.....(K=OLD) AND (J=NEW)
C.....
 200  DO 1 K=1,NZ-1
      DO 2 J=1,NQ+NP-1
      D(J)=(LAMZ(K)*(1.+(0.5*DELZ))*CO(J,K-1))-
(((2.*LAMZ(K))-1.)
     >*CO(J,K))+(LAMZ(K)*(1.-(0.5*DELZ))*CO(J,K+1))
 2    CONTINUE
C.....
      D(NQ+NP-1)=D(NQ+NP-1)+(LAMP(NP-1)*(1.-(DELP/2.)+
     >(0.5*DELP*(EXP((NP-1)*DELP))*(((EXP((NP-1)*DELP))-
1.+GG)**-1.))))
C.....
      F(1)=D(1)/ALR(1)
      DO 3 J=2,NQ
      F(J)=(D(J)+(LAMQ(J)*(1.-(DELQ/2.)-(0.5*DELQ*(EXP(QT-
(J*DELQ)))
     >/(FF+1.-(EXP(QT-(J*DELQ))))))*F(J-1)))/ALR(J)
 3    CONTINUE
```

```
C.....
      DO 41 J=NQ+1,NQ+NP-1
      F(J)=(D(J)+((LAMP(J-NQ)*(1.+(0.5*DELP)-
     >((0.5*DELP*(EXP((J-NQ)*DELP)))
     >*(((EXP((J-NQ)*DELP))-1.+GG)**-1.))))*F(J-1)))/ALR(J)
 41   CONTINUE

C.....CALCULATION OF NEW CONCENTRATIONS
      CN(INT(NQ+NP-1),K)=F(INT(NQ+NP-1))
C.....
      DO 4 J=NQ+NP-2,1,-1
      CN(J,K)=F(J)-(BER(J)*CN(J+1,K))
 4    CONTINUE
 1    CONTINUE

C.....UPDATING BOUNDARY CONDITIONS
      DO 101 J=NQ+1,NP+NQ-1
      CO(J,0)=CN(J,1)
 101  CONTINUE
      DO 102 J=1,NP+NQ-1
      CO(J,NZ)=CN(J,NZ-1)
 102  CONTINUE

C.....UPDATING REST OF CONCENTRATION VALUES
      DO 103 J=1,NP+NQ-1
      DO 104 K=1,NZ-1
      CO(J,K)=CN(J,K)
 104  CONTINUE
 103  CONTINUE

C.....CALCULATIONS IN OTHER DIRECTION
C.....(J=NEW OLD) AND (K=NEW NEW)
C.....
      DO 12 K=1,NZ-1
      H(K)=((1.-LAMQ(1)-(0.5*DELQ*LAMQ(1))
     >-(0.5*LAMQ(1)*DELQ*(EXP(QT-DELQ))/(FF+1.-(EXP(QT-
DELQ)))

>))*CO(1,K))+(LAMQ(1)*(1.+(0.5*DELQ)+(0.5*DELQ*(EXP(QT-
DELQ))
     >/(FF+1.-EXP(QT-DELQ))))*CO(2,K))
 12   CONTINUE
C.....
      F(1)=H(1)/ALZ(1)
C.....
      DO 13 K=2,NZ-1
      F(K)=(H(K)+(LAMZ(K)*(1.+(0.5*DELZ))*F(K-1)))/ALZ(K)
 13   CONTINUE
      CN(1,NZ-1)=F(NZ-1)
      DO 14 K=NZ-2,1,-1
      CN(1,K)=F(K)-(BEZ(K)*CN(1,K+1))
 14   CONTINUE
C.....
      DO 50 J=2,NQ
      DO 51 K=1,NZ-1
      H(K)=(LAMQ(J)*(1.-(0.5*DELQ)-(0.5*DELQ*(EXP(QT-
(DELQ*J)))/
     >(FF+1.-(EXP(QT-(DELQ*J))))))*CO(J-1,K))+(CO(J,K)*
     >(1.-(2.*LAMQ(J))))
     >+(LAMQ(J)*(1.+(0.5*DELQ)+(0.5*DELQ*(EXP(QT-
(J*DELQ)))/
     >(FF+1.-EXP(QT-(J*DELQ)))))*CO(J+1,K))
 51   CONTINUE
C.....
      F(1)=H(1)/ALZ(1)
      DO 53 K=2,NZ-1
      F(K)=(H(K)+(LAMZ(K)*(1.+(0.5*DELZ))*F(K-1)))/ALZ(K)
 53   CONTINUE
      CN(J,NZ-1)=F(NZ-1)
      DO 54 K=NZ-2,1,-1
      CN(J,K)=F(K)-(BEZ(K)*CN(J,K+1))
 54   CONTINUE
 50   CONTINUE

C.....
      DO 60 J=NQ+1,NQ+NP-1
      DO 61 K=1,NZ-1
      H(K)=(LAMP(J-NQ)*(1.+(DELP*0.5)-(DELP*0.5*
     >(EXP((J-NQ)*DELP))*((EXP((J-NQ)*DELP))-1.+GG)**-1.))
     >*CO(J-1,K))+(CO(J,K)*(1.-(2.*LAMP(J-NQ))))
     >+(LAMP(J-NQ)*(1.-(0.5*DELP)+
     >(0.5*DELP*EXP((J-NQ)*DELP)*((EXP((J-NQ)
     >*DELP))-1.+GG)**-1.))*CO(J+1,K))
 61   CONTINUE
C.....
      F(1)=H(1)/ALZG(1)
      DO 63 K=2,NZ-1
      F(K)=(H(K)+(LAMZ(K)*(1.+(0.5*DELZ))*F(K-1)))/ALZG(K)
 63   CONTINUE
      CN(J,NZ-1)=F(NZ-1)
      DO 64 K=NZ-2,1,-1
      CN(J,K)=F(K)-(BEZG(K)*CN(J,K+1))
 64   CONTINUE
C.....
 60   CONTINUE
      DO 360 J=1,NQ
      IF(CURR.GT.2.)THEN
      COM=0.95*CCOMP(J)
      ELSE IF(CURR.GT.1.)THEN
      COM=0.98*CCOMP(J)
      ELSE IF(CURR.GT.0.5)THEN
      COM=0.995*CCOMP(J)
      ELSE
      COM=0.999*CCOMP(J)
      ENDIF
      IF(CN(J,1).GT.COM)THEN
      KLM=KLM+1
      ENDIF
 360  CONTINUE
C.....
      DO 401 J=NQ+1,NQ+NP-1
      CO(J,0)=CN(J,1)
 401  CONTINUE
      DO 402 J=1,NQ+NP-1
      CO(J,NZ)=CN(J,NZ-1)
 402  CONTINUE
      DO 403 J=1,NQ+NP-1
      DO 404 K=1,NZ-1
      CO(J,K)=CN(J,K)
 404  CONTINUE
 403  CONTINUE

C.....
      DO 900 J=1,NQ
      CCOMP(J)=CN(J,1)
      IF(CO(J,1).LT.0.0.AND.III.EQ.0)THEN
      III=1
      ENDIF
 900  CONTINUE

C.....CONVERSION OF DELR TO DELQ
      DO 880 J=1,NQ-1
      RR(J)=1.-(((EXP(QT-((J+0.5)*DELQ)))-1.)/FF)
 880  CONTINUE
      RR(NQ)=1.
      FLUX=BB*(CN(1,1)/DELZ)*((RR(1))**2.)
      DO 689 J=2,NQ-1
      FLUX=FLUX+(BB*(((RR(J))**2.)-((RR(J-1))**2.))
     >*CN(J,1)/DELZ)
 689  CONTINUE
      FLUX=FLUX+(BB*(((RR(NQ))**2.)-((RR(NQ-1))**2.))
     > *CN(NQ,1)/DELZ)

C.....NORMALISED CURRENT - CALCULATION
      CURR=FLUX*(3.1419/4.)
      T=T+DELT
      PRINT*, T, CURR
      IF(KLM.EQ.NQ.AND.III.EQ.0)THEN
      DELT=DELT*1.2
      ENDIF
      IF(III.EQ.1)THEN
      DELT=DELT/5.
      ENDIF
      CURROLD=CURR
      III=0
      KLM=0
      FLUX=0.
      FLUXA=0.
      KK=KK+1

C.....SAVING THE DATA
      WRITE (67,11) T, CURR

C.....CONTINUING THE CYCLE
      IF (T.LT.200.) GOTO 500
      CLOSE (67)

C.....INCREASING GRID POINTS OVER K SPACE
      NZ=NZ+10

C.....LOOPING BACK TO CALCULATE CURRENT AT NEXT (d/a)
      DELT=DELTIN
      T=0.
      LLOG=LLOG+0.05
      LNAM=LNAM+1
      IF (LLOG.LT.0.51) GOTO 501

C.....FORMAT STATEMENTS (?)
 606  FORMAT(1X,4F12.6)
 11   FORMAT(2X,E12.6,2X,E12.6)
      STOP
      END
```

References

1. Davis T. P., Haddleton D. M. and Richards S. N., *J. M. S. Rev., Macromol. Chem. Phys.*, **1994**, C34, 243.
2. Marsh A., Khan A., Haddleton D. M. and Hannon M. J., *Macromolecules*, **1999**, 32, 8725.
3. Kato M., Kamigaito M., Sawmoto M. and Higashimura T., *Macromolecules*, **1995**, 28, 1721.
4. Wang J.-S. and Matyjaszewski K., *J. Am. Chem. Soc.*, **1995**, 117, 5614.
5. Haddleton D. M., Jasieczek C. B., Hannon M. J. and Shooter A. J., *Macromolecules*, **1997**, 30, 2190.
6. Granel C., Dubois Ph., Jérôme R. and Teyssie Ph., *Macromolecules*, **1996**, 29, 8576.
7. Haddleton D.M., Kukulj D., Duncalf D. J., Heming A. M. and Shooter A. J., *Macromolecules*, **1998**, 31, 5201.
8. Wang J. –L., Grimaud T. and Matyjaszewski K., *Macromolecules*, **1997**, 30, 6507.
9. Matyjaszewski K., Wang, J. -L., Grimaud T. and Shipp D. A., *Macromolecules*, **1998**, 31, 1527.
10. Percec V., Barboiu B. and Kim H. -J., *J. Am. Chem. Soc.*, **1998**, 120, 305.
11. Matyjaszewski, K., *Macromolecules*, **1998**, 31, 4710.
12. Matyjaszewski K. and Woodworth B. E., *Macromolecules*, **1998**, 31, 4718.
13. Haddleton D. M., Crossman M. C., Dana B. H., Duncalf D. J., Heming A. M., Kukulj D. and Shooter A. J., *Macromolecules*, **1999**, 32, 2110.
14. Haddleton D. M., Heming A. M., Kukulj D., Duncalf D. J. and Shooter A. J.,

Macromolecules, **1998**, 31, 2016.

15. Haddleton D. M., Clark A. J., Crossman M. C., Duncalf D. J., Heming A. M., Morsley S. R. and Shooter A. J., *Chem. Commun.*, **1997**, 1173.
16. Matyjaszewski K., Patten T. E., and Xia J., *J. Am. Chem. Soc.*, **1997**, 119, 674.
17. Matyjaszewski, K., Miller, P. J., Shukla, N., Immaraporn, B., Gelman, A., Luokala B. B., Siclovan T. M., Kickelbick G., Vallant T., Hoffmann H. and Pakula T., *Macromolecules,* **1999**, 32, 8716.
18. Kickelbick G., Paik H. -J. and Matyjaszewski K., *Macromolecules,* **1999**, 32, 2941.
19. Clark A. J., Filik R.P., Haddleton D. M., Radigue A. and Sanders C. J., *J. Org. Chem.* **1999**, 64, 8954.
20. Matyjaszewski K., Coca S., Gaynor S. C., Wei M. and Woodworth B. E., *Macromolecules*, **1997**, 30, 7348.
21. Pattenden G. *Chem. Soc. Rev.* **1988** 17 361.
22. Scheffold R., Rytz G. and Walder L., in *Modern Synthetic Methods,* R Scheffold (ed), Wiley, London, **1983**, 3, 355.
23. Marchaj A., Bakac A., and Epsenson J. H., *Inorg. Chem.* **1992**, 31, 4860.
24. Bedioui F., De Boysson E., Devynck J. and Balkus Jr, K. J., *J. Chem. Soc. Faraday Trans.*, **1991**, 87, 3831.
25. Shi M. and Anson F.C., *Anal. Chem.*, **1998**, 70, 1489.
26. Rockenbauer A., Zahonyi E. B. and Simandi L.I., *J. Chem. Soc. Dalton,* **1975**, 1729.
27. Schrauzer G. N. and Deutsch E., *J. Am. Chem. Soc.*, **1969**, 91, 3341.
28. Davis T. P., Kukulj D., Haddleton D. M. and Maloney D. R., *TRIP*, **1995**, 3,

365.

29. Shi C. and Anson F.C., *Inorg. Chim. Acta.*, **1994**, 225, 215.

30. Owlia A., Wang Z. and Rusling J.F., *J. Am. Chem. Soc.*, **1989**, 111, 5091.

31. Shi C. and Anson F.C., *Anal. Chem.*, **1998**, 70, 3114.

32. Barker A. L. and Unwin P. R., *J. Phys. Chem. B.*, **2000**, 104, 2330.

33. Seeber R., Parker Jr W.O., Marzilli P. A. and Marzilli L.G., *Organometallics*, **1989**, 8, 2377.

34. Simandi L. I. and Simandi T. L., *J. Molec. Catal.*, **1997**, A117, 299.

35. Watanabe J. and Setsune J., *J. Organomet. Chem.*, **1999**, 575, 21, and references therein.

36. Jensen F.R., Madan V. and Buchanan D.H., *J. Am. Chem. Soc.*, **1970**, 92, 1414.

37. Tada M. and Ogawa H., *Tetra. Lett.*, **1973**, 2639.

38. Shinozaki H., Ogawa H. and Tada M., *Bull. Chem. Soc. Jpn.*, **1976**, 49, 775.

39. Eckert H., Lenoir D. and Ugi L., *J. Organomet. Chem.*, **1977**, 141, C23.

40. Schrauzer G.N. and Windgassen R.J., *J. Am. Chem. Soc.*, **1967**, 89, 1999.

41. Bigotto A., Casta G., Mestoni G., Pellizer G., Puxeddu A., Reisenhofer E., Stefani L. and Tauzer G., *Inorg. Chim. Acta. Rev.*, **1970**, 4, 41.

42. Tada M., Okabe M., and Miura K., *Chem. Lett.*, **1978**, 1135.

43. Brown K.L. and Ingraham L.L., *J. Am. Chem. Soc.*, **1974**, 96, 7681.

44. Johnson M.D. and Meeks B.S., *J. Chem. Soc., Part B.*, **1971**, 185.

45. Shinozaki H., Kubota M., Yagi O. and Tada M., *Bull. Chem. Soc. Jpn.*, **1976**, 49, 2280.

46. Wade L.G. Jr., *Organic Chemistry*, **1991**, Prentice Hall, New Jersey.

47. Wang K. and Jordan R. B., *Can. J. Chem.*, **1996**, 74, 658.

48. Iwunze M., Hu N. and Rusling J.F., *J. Electroanal. Chem.*, **1992**, 333, 353.

49. Eckert H., Lagerlund I. and Ugi I., *Tetrahedron*, **1977**, 33, 2243.

50. Costa G., Puxeddu A. and Reisenhofer E., *J. Chem. Soc. Dalton*, **1973**, 2034.

51. Halpern J. and Maher J.P., *J. Am. Chem. Soc.*, **1965**, 87, 5361.

52. Schneider P.W., Phelan P.F. and Halpern J., *J. Am. Chem. Soc.*, **1969**, 91, 77.

53. Gupta B.D., Kumar M. and Roy S., *Inorg. Chem.*, **1989**, 28,11.

54. Tada M., *Rev. Het. Chem.*, **1999**, 20, 97.

55. Costa G., Mestoni G. and Cocevar C., *J. Chem. Soc. Chem. Comm.*, **1971**, 706.

56. Zhou D.- L., Tinembart O., Scheffold R. and Walder L., *Helv. Chim. Acta.*, **1990**, 73, 2225.

57. Smalley T.L., Wright M.W., Garmon S.A., Welker S.M. and Rheingold A.L., *Organometallics*, **1993**, 12, 998.

58. Wright M.W., Smalley T.L., Welker M.E. and Rheingold *J. Am. Chem. Soc.*, **1994**, 116, 6777.

59. Wright M.W. and Welker M.E., *J. Org. Chem.*, **1996**, 61, 133.

60. Stokes H.L. and Welker M.E., *Organometallics*, **1996**, 15, 2624.

61. Tada M. and Shimizu T., *Bull. Chem. Soc. Jpn.*, **1992**, 65, 1251.

62. Kang C. and Anson F.C., *J. Electroanal. Chem.*, **1996**, 407, 233.

63. Ouyang J. and Anson F.C., *J. Electroanal. Chem.*, **1989**, 271, 331.

64. Fendler J. H., Nome F. and Van Woert H. C., *J. Am. Chem. Soc.*, **1974**, 96, 6745.

65. Costa G., Puxeddu A. and Stefani L. B., *Inorg. Nucl. Chem. Lett.*, **1970**, 6, 191.

66. Costa G., Mestroni G., Puxeddu A. and Reisenhofer E., *J. Chem. Soc. (A)*, **1970**, 2870.

67. Costa G., Puxeddu A. and Reisenhofer E., *J. Chem. Soc. Dalton,* **1972,** 1519.

68. Bottcher A., Takeucji T., Hardcastle K. I., Meade T. J., Gray H. B., Cwikel D., Kapon M. and Dori Z., *Inorg. Chem.*, **1997**, 36, 2498.

69. Brown K.L, Zou X. and Webb B.M., *Inorg. Chem.*, **1994**, 33, 4189.

70. Al-Akhdar W.A., Belmore K.A. and Kendrick M.J., *Inorg. Chim. Acta.*, **1989**, 165, 15.

71. Braga D., Grepioni F., Birandha K. and Desiraju G.R., *J. Chem. Soc., Dalton.*, **1996**, 3915.

72. Schrauzer G. N. and Windgassen, R. J., *J. Am. Chem. Soc.*, **1966**, 88, 3738.

73. Pailes W. H. and Hogenkamp H. P. C., *Biochemistry*, **1968**, 7, 4160.

74. Jensen F. R. and Kiskis R. C., *J. Am. Chem. Soc.*, **1975**, 97, 5820.

75. Endicott J.F., Lilie J., Kuszaj J.M., Ramaswamy B.S., Sahmonses W.G., Simic M.G., Glick M.D. and Rillema D.P., *J. Am. Chem. Soc.*, **1977**, 99, 429.

76. Patel V. F. and Pattenden G., *J. Chem. Soc., Perkin, Trans.*, 1., **1990**, 2703.

77. Jensen F.R. and Kiskis R.C., *J. Am. Chem. Soc.*, **1975**, 97, 5825.

78. Deniau J. and Gaudemer A., *J. Organomet. Chem.*, **1980**, 191, C1.

79. Hartung J. and Giese B., *Chem. Ber.*, **1991**, 124, 387.

80. Pearce D. J. and Pletcher D., *J. Electroanal. Chem.*, **1986**, 197, 317.

81. Xiang Y., Zhou D.L. and Rusling J.F., *J. Electroanal. Chem.*, **1997**, 424, 1.

82. Schrauzer G.N., Lee L.P. and Silbert J.W., *J. Am. Chem. Soc.*, **1970**, 92, 2997.

83. Geofroy G.L. and Wrighton M.S., *Organometallic Photochemistry*, Academic Press, London, 1979, 319.

84. Golding B.T., Kemp T.J., and Shena H.H., *J. Chem. Res.*, **1981**, S, 34.

85. Golding B.T., Kemp T.J., and Shena H.H., *J. Chem. Res.*, **1981**, M, 0334.

86. Finke R.G., Smith B.L., Meyer B.T. and Malinero A.A., *Inorg. Chem.*, **1983**, 22, 3677.

87. Rao D.N.R. and Symons M.C.R., *J. Chem. Soc. Faraday Trans. 1.*, **1984**, 80, 423.

88. Garr C.D. and Finke R.G., *Inorg. Chem.*, **1993**, 32, 4414.

89. Ohgo Y., Wada H., Ohtera C., Ikarashi M., Baba S. and Takeuchi S., *Bull. Chem. Soc. Jpn.*, **1991**, 64, 2656.

90. Ohgo Y., Takeuchi S., Natori Y., Yoshimura Y., Ohashi Y. and Sasada Y., *Bull. Chem. Soc. Jpn.*, **1981**, 54, 3095.

91. Schrauzer G.N. and Grate J.H., *J. Am. Chem. Soc.*, **1981**, 103, 541.

92. Nome F., Rezende M. C., Saboia C. M. and da Silva A. C., *Can. J. Chem.*, **1987**, 65, 2095.

93. Rillema D. P., Endicott J. F., and Papaconstantinou E., *Inorg. Chem.*, **1971**, 10, 1739.

94. Scheffold R. and Orlinski R., *J. Am. Chem. Soc.*, **1983**, 105, 7200.

95. Gao J., Rusling J.F. and Zhou D., *J. Org. Chem.*, **1996**, 61, 5972.

96. Pagenkopf B.L. and Livinghouse T., *J. Am. Chem. Soc.*, **1996**, 118, 2285.

97. Rangel M., Arcos T. and de Castro B., *Organometallics*, **1999**, 18, 3451.

98. Costa G., Tavagnacco C. and Balducci G., *J. Electroanal. Chem.*, **1991**, 318, 183.

99. Geiger T. and Anson F.C., *J. Am. Chem. Soc.*, **1981**, 103, 7489.

100. Kobayashi N., Janda P. and Lever A.B.P., *Inorg. Chem.*, **1992**, 31, 5172.

101. Bhugun I. and Anson F.C., *Inorg. Chem.*, **1996**, 35, 7253.

102. Shi C., Steiger B., Yuasa M. and Anson F.C., *Inorg. Chem.*, **1997**, 36, 4292.

103. Shi C. and Anson F.C., *Inorg, Chem.*, **1998**, 37, 1037.

104. Collman J.P., Wagenknecht P.S. and Hutchison J.E., *Angew. Chem. Int. Ed. Engl.*, **1994**, 33, 1537.

105. Collman J.P., Denisevich P., Konai Y., Marrocco M., Koval C., and Anson F.C., *J. Am. Chem. Soc.*, **1980**, 102, 6027.

106. Chang C.J., Deng Y., Shi C., Chang C.K., Anson F.C. and Nocera D.G., *Chem. Commun.*, **2000**, 1355.

107. Marchaj A., Bakac A. and Espenson J.H., *Inorg. Chem.*, **1993**, 32, 2399.

108. Steiger B. and Anson F.C., *Inorg. Chem.*, **1997**, 36, 4138.

109. Steiger B., Shi C. and Anson F.C., *Inorg. Chem.*, **1993**, 32, 2107.

110. Yu H.-Z., Baskin S., Steiger B., Anson F.C. and Zewail A.H., *J. Am. Chem. Soc.*, **1999**, 121, 484.

111. Adin A. and Espenson J.H., *Inorg. Chem.*, **1972**, 11, 686.

112. Gupta B.D. and Qanungo K., *J. Organomet. Chem.*, **1997**, 534, 213.

113. Pletcher D. and Thompson H., *J. Chem. Soc., Faraday Trans.*, **1997**, 93, 3669.

114. Resienhofer E. and Costa G., *J. Chem. Soc. Dalton*, **1976**, 521.

115. Oldham K.B. *J. Electroanal. Chem.*, **1992**, 337, 91.

116. Myland J. and Oldham K. B., *J. Electroanal. Chem.*, **1993**, 347, 49.

117. Oldham K. B. *J. Electroanal. Chem.*, **1988**, 250, 1.

118. Bento M. F., Medeiros M. J., Montenegro M. I., Beriot C. and Pletcher D., *J. Electroanal. Chem.*, **1993**, 345, 273.

119. Bond A.M., Fleischmann M., and Robinson J., *J. Electroanal. Chem.*, **1984**, 180, 257.

120. Andrieux C.P., Audebert P., Hapiot P. and Saveant J.M., *J. Am. Chem. Soc.*,

1990, 112, 2439.

121. Wightman R. M., *Science*, **1988**, *240*, 415.

122. Amatore C., Maisonhaute E. and Simonneau G., *Electrochem. Comm.*, **2000**, 2, 81.

123. Saito Y. *Rev. Polarogr. Jpn.* **1968**, *15*, 177.

124. Slevin C. J., Gray N. J., Macpherson J. V., Webb M. A. and Unwin P.R., *Electrochem. Comm.*, **1999**, 1, 282.

125. Penner R. M., Heben M. J., Longin T. L. and Lewis N. S., *Science*, **1990**, 250, 1118.

126. Heinze J., *Angew. Chem. Int. Ed. Engl.*, **1993**, 32, 1268.

127. Shao Y., Mirkin M. V., Fish G., Kokotov S., Palanker D. and Lewis A., *Anal. Chem.*, **1997**, 69, 1627.

128. Lee C., Miller C. J. and Bard A. J., *Anal. Chem.*, **1991**, 63, 78.

129. Wightman R.M., and Wipf D.O., *Acc. Chem. Res.*, 23, **1990**, 64.

130. Andrieux C. P., Hapiot P. and Saveant J. M., *J Phys. Chem.*, **1988**, 92, 5992.

131. Andrieux C. P. and Saveant J. M., *In Investigations of Rates and Mechanisms of reactions*: Bernasconi, C., Ed. Wiley: New York, **1986**, 6, 4/E, Part 2, 305.

132. Slevin C. J., Macpherson J. V. and Unwin P. R., *J. Phys. Chem. B*, **1997**, 101, 10851.

133. Bard A.J. and Faulkner L.R., *Electrochemical Methods: Fundamentals and Applications*, Wiley, New York, **1980**, 220.

134. Macpherson J. V., Macar S. and Unwin P.R., *Anal. Chem.*, **1994**, 66, 2175.

135. Macpherson J. V., Beeston M. A. and Unwin P.R., *J. Chem. Soc., Faraday Trans.*, **1995**, 91, 899.

136. Martin R. D. and Unwin P. R., *J Electroanal. Chem.*, **1995**, 397, 325.

137. Macpherson J.V. and Unwin P. R., *Anal. Chem.*, **1997**, 69, 5045.

138. Macpherson J.V. and Unwin P.R., *Anal. Chem.*, **1999**, 71, 4642.

139. Macpherson J. V., Jones C. E. and Unwin P. R., *J. Phys. Chem. B.*, **1998**, 102, 9891.

140. Macpherson J. V. and Unwin P. R., *Anal. Chem.*, **1998**, 70, 2914.

141. Macpherson J. V. and Unwin P. R., *Anal. Chem.*, **1999**, 71, 2939.

142. Macpherson J. V., *Electroanalysis*, **2000**, 12, 1.

143. Rees N. V., Dryfe R. A. W., Cooper J. A., Coles B. A., Compton R. G., Davies S. G. and McCarthy T. D., *J. Phys. Chem.*, **1995**, 99, 7096.

144. Rees N. V., Alden J. A., Dryfe R. A. W., Coles B. A. and Compton R. G, *J. Phys. Chem.*, **1995**, 99, 14813.

145. Coles B. A., Dryfe R. A. W., Rees N. V., Compton R. G., Davies S. G. and McCarthy T. D., *J. Electroanal. Chem.*, **1996**, 411, 121.

146. Oldham K. B., Myland J. C., Zoski C. G. and Bond A. M., *J. Electroanal. Chem.*, 270, **1989**, 79.

147. Bard A. J., Fan F-R. F., Kwak J. and Lev O., *Anal. Chem.* **1989**, *61*, 132.

148. Engstrom R.C., Weber M., Wunder D.J., Burgess R. and Winquist S., *Anal. Chem.*, **1986**, 58, 844.

149. Engstrom R.C., Meanly T., Tople R. and Wightman R. M., *Anal. Chem.*, **1987**, 59, 2005.

150. Kwak J. and Bard A. J., *Anal. Chem.*, **1989**, 61, 1794.

151. Kwak J. and Bard A. J., *Anal. Chem.* **1989**, *61*, 1221.

152. Unwin P. R. and Bard A. J., *J. Phys. Chem.*, **1992**, 96, 5035.

153. Macpherson J. V. and Unwin P. R., *J. Phys. Chem.*, **1994**, 98, 3109.

154. Bard A. J., Fan F. -R., F., Pierce D. T., Unwin P. R., Wipf D. O. and Zhou F., *Science*, **1991**, 254, 68.

155. Arca M., Bard A. J., Horrocks B. R., Richards T. C. and Triechel D. A., *Analyst*, **1994**, 119, 719.

156. Unwin P. R. and Macpherson J. V., *Chem. Ind.*, **1995**, 21, 874.

157. Mirkin M. V., *Anal. Chem.*, **1996**, 68, 177A.

158. Wei C., Bard A. J. and Mirkin M. V., *J. Phys. Chem.* **1995**, *99*, 16033.

159. Barker A. L., Gonsalves M. J., Macpherson J. V., Slevin C. J. and Unwin P. R., *Analytica Chim. Acta.*, **1999**, 385, 223.

160. Ding Z., Quinn B. M. and Bard A. J., *J. Phys. Chem. B.*, **2001**, 105, 6367.

161. Macpherson J. V., O'Hare D., Unwin P. R. and Winlove C. P., *Biophys. J.*, **1997**, 73, 2771.

162. Slevin C. J., Ryley S., Walton D. J. and Unwin P. R., *Langmuir*, **1998**, 14, 5331.

163. Wipf D. O., Bard A. J. and Tallman D. E., *Anal. Chem.* **1993**, *65*, 1373.

164. Wipf, D. O. and Bard A. J., *Anal. Chem.* **1992**, *64*, 1362.

165. Wipf D. O. and Bard, A. J., *J. Electrochem. Soc.* **1991**, 138, 5, L4.

166. Wipf D. O. and Bard A. J., *J. Electrochem. Soc.* **1991**, 138, 469.

167. Mirkin M. V. and Bard A. J., *J. Electrochem. Soc.* **1992**, *139*, 3535.

168. Mirkin M. V., Richards T. C. and Bard A. J., *J. Phys. Chem.* **1993**, *97*, 7672.

169. Macpherson J. V., Slevin C. J. and Unwin P.R., *J. Chem. Soc. Faraday. Trans.* **1996**, 92, 3799.

170. Andrieux C. P. and Saveant J. M., J. Electroanal. Chem., **1989**, 267, 15.

171. Zhou F., Unwin P. R., and Bard A. J., *J. Phys. Chem.*, **1992**, 96, 4917.

172. Lee C., Kwak J. and Anson F. C., *Anal. Chem.*, **1991**, 63, 1501.

173. Martin R.D. and Unwin P.R., *Anal. Chem.*, **1998**, 70, 276.

174. Martin R. D. and Unwin P.R., *J. Chem. Soc., Faraday Trans.*, **1998**, 94, 753.

175. Andrieux C. P., Hapiot P. and Savéant J. M., *Chem. Rev.*, **1990**, 90, 723.

176. Shao Y. and Mirkin M. V., *J. Electroanal. Chem.*, **1997**, 439, 137.

177. Macpherson J. V. and Unwin P. R., *Anal. Chem.*, **1997**, 69, 2063.

178. Tsionsky T., Bard A. J. and Mirkin M. V., *J. Phys. Chem.*, **1996**, 100, 17881.

179. Tsionsky T., Bard A. J. and Mirkin M. V., *J. Am. Chem. Soc.*, **1997**, 101, 10785.

180. Delville M. –H., Tsionsky T. and Bard A. J., *Langmuir*, **1998**, 14, 2774.

181. Shao Y. and Mirkin M. V., *J. Am. Chem. Soc.*, **1997**, 119, 8103.

182. Taylor G. and Girault H. H. J., *J. Electroanal. Chem.*, **1986**, 208, 179.

183. Macpherson J. V. and Unwin P. R., *J. Chem. Soc. Faraday Trans.*, **1993**, 94, 753.

184. Macpherson J. V. and Unwin P. R., *J. Phys. Chem.*, **1994**, 98, 1704.

185. Macpherson J. V. and Unwin P. R., *J. Phys. Chem.*, **1994**, 98, 11764.

186. Macpherson J. V. and Unwin P. R., *J. Phys. Chem.*, **1995**, 99, 3338.

187. Macpherson J. V. and Unwin P. R., *J. Phys. Chem.*, **1995**, 99, 14842.

188. Macpherson J. V. and Unwin P. R., *J. Phys. Chem.*, **1996**, 100, 19475.

189. Macpherson J. V., Unwin P. R., Hiller A. C. and Bard A. J., *J. Am. Chem. Soc.*, **1996**, 112, 6445.

190. Macpherson J. V. and Unwin P. R., *J. Chem. Soc., Faraday Trans.*, **1993**, *89*, 1883.

191. Slevin C. J., Umbers J. A., Atherton J. H. and Unwin P. R., *J. Chem. Soc., Faraday Trans.*, **1996**, 92, 5177.

192. Slevin C. J. and Unwin P. R., *J. Am. Chem. Soc.*, **2000**, 12, 2597.

193. Slevin C. J. and Unwin P. R., *Langmuir*, **1997**, 13, 4799.

194. Barker A. L., Slevin C. J., Unwin P. R., and Zhang J., in: A. G. Volkov (Ed.) *Liquid Interface in Chemical, Biological and Pharmaceutical Applications*, Marcel Dekker, New York, **2001**, 283.

195. Unwin P. R. and Bard A. J., *J. Phys. Chem.*, **1991**, 95, 7814.

196. Demaille C., Unwin P. R. and Bard A. J., *J. Phys. Chem.*, **1996**, 100, 14137.

197. Richards T. C., Bard A. J., Cusanelli A., and Sutton D., *Organometallics*, **1994**, 13, 757.

198. Treichel D. A., Mirkin M. V. and Bard A. J., *J. Phys. Chem.*, **1994**, 98, 5751.

199. Zhou F. and Bard A. J., *J. Am. Chem. Soc.*, **1994**, 116, 393.

200. Martin R. D., *Ph.D. Thesis*, University of Warwick, **1997**.

201. Wei C., Bard A. J., Nagy G. and Toth K., **Anal. Chem.**, 1995, 67, 1346.

202. Gonsalves, M., Barker A. L., Macpherson J. V., Unwin P. R., O'Hare D. and Winlove C. P., *Biophys. J.*, **2000**, 78, 1578.

203. Gonsalves M., Macpherson J. V., O'Hare D., Winlove C.P. and Unwin P. R., *Biochim. Biophys. Acta*, **2000**, 1524, 66.

204. Mirkin M. V., Yang H. and Bard A. J., *J. Electrochem. Soc.*, **1992**, 139, 2212.

205. Martin R. D. and P.R. Unwin, *J. Electroanal. Chem.*, **1997**, 439, 123.

206. Wightman R.M. and Wipf D. O., in *Electroanalytical Chemistry*, vol 15, A. J. Bard (ed), Marcel Dekker, New York, **1989**, 267.

207. Bard A.J., Fan F. R. and Mirkin M. V., in *Electroanalytical Chemistry*, vol. 18, A.J. Bard (ed), Marcel Dekker, New York, **1994**.

208. Macpherson J. V., *Ph.D. Thesis*, University of Warwick, **1997**.

209. Denault G., Frank Troise M. H. and Peter L. M., *J. Chem. Soc., Faraday Discuss.*, **1992**, 94, 23.

210. Huang H. J., He P. and Faulkner L. P., *Anal. Chem.*, **1986**, 58, 2889.

211. Evans N. J., *Ph.D. Thesis*, University of Warwick, **1999**.

212. Barker A. L., *Ph.D. Thesis*, University of Warwick, **2000**.

213. Barker A.L., Macpherson J. V., Slevin C. J. and Unwin P. R., *J. Phys. Chem. B.*, **1998**, 102, 1586.

214. Barker A.L., Unwin P. R., Amemiya S, Zhou J. F. and Bard A. J., *J. Phys. Chem. B.*, **1999**, 103, 7260.

215. Zhang J, Barker A. L and Unwin P. R., *J. Electroanal. Chem.*, **2000**, 483, 95.

216. Zhang J. and Unwin P. R, *J. Phys. Chem. B.*, **2000**, 104, 2341.

217. Mirkin M. V. and Bard A.J., *Anal. Chem* 64 **1992** 2293.

218. Clark AJ, Battle GM, Heming AM, Haddleton DM and Bridge A., *Tet. Lett.*, **2001**, 42, 2003.

219. Bond A. M., Oldham K. B. and Zoski C. G., *J. Electroanal. Chem.*, 245, **1988**, 71.

220. Tomes J., *Collect. Czech. Chem. Commun.*, 9, **1937**, 150.

221. Oldham K. B. and Zoski C. G., *J. Electroanal. Chem.*, **1988**, 256, 11.

222. Haddleton D. M., Clark A. J., Duncalf D. J., Hemming A. M., Kukulj D. and Shooter A. J., *J. Chem. Soc., Dalton Trans.*, **1998**, 381.

223. Zhuang Q. and Chen H., *J. Electroanal. Chem.*, **1993**, 346, 29.

224. Mandler D. and Bard A. J., *J. Electrochem. Soc.*, **1989**, 136, 3143.

225. Mandler D. and Bard A. J., *J. Electrochem. Soc.*, **1990**, 137, 2468.

226. Mandler D. and Bard A. J., *Langmuir*, **1990**, 6, 1489.

227. Hanzlik J.H. and Vlecek A.A., *Inorg. Chem.*, **1969**, 8, 669.

228. Pasto D.J. and Timmers D.A. and Haung N.Z., *Inorg. Chem.*, **1984**, 23, 4117.

229. Shi S., Daniels L.M. and Espenson J.H., *Inorg. Chem.*, **1991**, 30, 3407.

230. Derenne S., Gaudemer A. and Johnson M.D., *J. Organomet. Chem.*, **1987**, 322, 239.

231. Fischli A. and Daly J.J., *Helv. Chim. Acta.*, **1980**, 63, 1628.

232. Fischli A., *Helv. Chim. Acta.*, **1982**, 65, 1167.

233. Fischli A., *Helv. Chim. Acta.*, **1982**, 65, 2697.

234. Shoenholzer P., Suess D., Wan T.S. and Fischli A., *Helv. Chim. Acta.*, **1984**, 67, 669.

235. Kamau G. N. and Rusling J. F., *Langmuir*, **1996**, 12, 2645.

236. Saveant J. -M., *Adv. Phys. Org. Chem.*, **1990**, 26, 1 and references cited therein.

237. Martin B. D. and Finke R. G., *J. Am. Chem. Soc.*, **1992**, 114, 585.

238. Zhou D. –L., Gao J. and Rusling J. F., *J. Am. Chem. Soc.*, **1995**, 117, 1127.

239. Fry A. J., and Mitnick M. A., *J. Am. Chem. Soc.*, **1969**, 91, 6207.

240. Jacobus J., and Eastham J. F., *J. Chem. Soc., Chem. Commun.*, **1969**, 138.

241. Martin B.D. and Finke R. G., *J. Am. Chem. Soc.*, **1990**, 112, 2419.

242. Zhou D., Carrero H. and Rusling J. F., *Langmuir*, **1996**, 12, 3067.

243. Bard A. J. and Faulkner L. R., in *"Electrochemical Methods (fundamentals and applications"*, Wiley, New York, **1980**, Chapter 11, 429.

244. Nonaka Y. and Hamada K., *Bull. Chem. Soc. Jpn.*, **1981**, 54, 3185.

245. Fleischmann M., Lasserre F., Robinson J., and Swan D., *J. Electroanal. Chem.*, **1984**, 177, 97.

246. Fleischmann M., Pons S., Rolinson D. R., and Schmidt P. P.,

Ultramicroelectrodes, Datatech Systems, North Carolina, **1997**.

247. Denuault G., Fleischmann M., Pletcher D. and Tutty O., *J. Electroanal. Chem.*, **1990**, 280, 243.

248. Denuault G. and Pletcher D., *J. Electroanal. Chem.*, **1993**, 358, 193.

249. Dayton M. A., Ewing A. G. and Wightman R. M., *Anal. Chem.*, **1980**, 52, 2392.

250. Diao G. and Zhang Z., *J. Electroanal. Chem.*, **1997**, 429, 67.

251. Oldham K. B., *J. Electroanal. Chem.*, **1991**, 313, 3.

252. Philips C. G., *J. Electroanal. Chem.*, **1990**, 296, 255.

253. Lavagnini I., Pastore P., and Magno F., *J. Electroanal. Chem.*, **1993**, 358, 193.

254. Tutty O. R., *J. Electroanal. Chem.*, **1994**, 377, 39.

255. Alden J.A. and Compton R.G., *J. Phys. Chem.*, **1997**, 101, 9606.

256. Alden J. A., "*Computational Electrochemistry*", Ph.D. Thesis, Oxford University, 1998.

257. Amore C. A. and Fossett B., *Anal. Chem.*, **1996**, 68, 4377.

258. Gridnev A. A., Ittel S. D., Fryd M. and Wayland B. B., *Organometallics*, **1993**, 12, 4871.

259. Suddaby K. G., O'Driscoll K. F. and Rudin A., *J. Polym. Sci.: Part A: Polym. Chem.*, **1992**, 30, 643.

260. Ou T. Y., Moldoveanu S., and Anderson J. L., *J. Electroanal. Chem.*, **1988**, 247, 1.

261. Varco Shea T., and Bard A. J., *Anal. Chem.*, **1987**, 59, 2101.

262. Unwin P. R., and Compton R. G., *Comp. Chem. Kinet.*, **1989**, 29, 173.

263. Anderson L. B., and Reilly C. N., *J. Electroanal. Chem.*, **1989**, 10, 538.

264. Albery W. J., and Hitchman M.L., *Ring Disc Electrodes*, Clarendon Press,

Oxford, **1971**.

265. P. R. Unwin, in A.J. Bard and M. V. Mirkin (eds), *Scanning Electrochemical Microscopy*, Chapter 7, Marcel Dekker, New York, **2001**, 241.
266. Bard A. J., Mirkin M. V., Unwin P. R., and Wipf D. O., *J. Phys. Chem.*, **1992**, 96, 1861.
267. Peaceman D. W., and Rachford H. H., *J. Soc. Ind. App. Math.*, **1955**, 439, 123.
268. Haber F. and Weiss J., *Proc. R. Soc.*, **1934**, A147, 332.
269. Rigg T., Taylor W. and Weiss J., *J. Chem. Phys.*, **1954**, 22, 575.
270. Pospisil Z., *Collec. Czech. Chem. Comm.*, **1953**, 18, 337.
271. Baxendale E.H., Evans M.G. and Park G.S., *Trans. Faraday Soc.*, **1946**, 42, 155.
272. Kolthoff I.M. and Parry E.P., *Proc. I. Intern. Polarogr. Cong.*, Part I., 145.
273. Kolthoff I.M. and Parry E.P., *Proc. I. Intern. Polarogr. Cong.*, part III, 671
274. Kolthoff I.M. and Parry E.P., *J. Am. Chem. Soc.*, **1951**, 73, 7228.
275. Bianchi G., Mazza F. and Mussini T., *Electrochim. Acta.*, **1963**, 35, 893.
276. Aoki K., Tokuda K. and Matsuda H., *J. Electroanal. Chem.*, **1976**, 76, 217.
277. Klatt L.N. and Blaedel W.J., *Anal. Chem.*, **1968**, 40, 512.
278. Herrmann J., Schmidt H. and Vielstich W., *Z. Phys. Chem. Neu. Fol.*, **1984**, 139, 83.
279. Rashid A. and Kalvoda R., *J. Electroanal. Chem.*, **1970**, 28, 245.
280. Peaceman D. W. and Rachford H. H., *J. Soc. Ind. Appl. Math.* **1955**, *3*, 28.
281. De Laat J. and Gallard H., *Environ. Sci. Technol.*, **1999**, 33, 2726.
282. Kukulj D. and Davies T. P., *Macromol. Chem. Phys.*, **1998**, 199, 1697.
283. Kukulj D., Davies T. P., Haddleton D. M. and Gilbert R. G., *J. Polym. Sci., Part*

A., Polym. Chem., **1997**, 35, 859.

284. Kukulj D., Davies T. and Gilbert R. G., *Macromolecules*, **1997**, 30, 7661.

285. Shao Y., Mirkin M. V. and Rusling J. F., *J. Phys. Chem. B.*, **1997**, 101, 3202.

286. Shoup D., and Szabo A., *J. Electroanal. Chem.*, **1982**, 140, 237.